Carl von Ossietzky
Universität
Oldenburg

Preparation and Characterization of Nanoporous Copper
and its Application in Electrosynthesis of Cyclic Carbonates

Von der Fakultät für Mathematik und Naturwissenschaften
der Carl von Ossietzky Universität Oldenburg
zur Erlangung des Grades und Titels einer
Doktorin der Naturwissenschaften
-Dr. rer. nat.-
angenommene Dissertation
von

Frau **Sawsan Ibrahim,** M.Sc.

geboren am 28.12.1988
in Rostock, Deutschland

Declaration

This work was carried out from December 2017 to January 2021 at the Carl von Ossietzky University of Oldenburg, Faculty of Mathematics and Natural Science, Institute of Chemistry under the supervision of Prof. Dr. Mehtap Oezaslan. Electrochemical experiments were carried out in the Laboratory of the Electrocatalysis Research Group. All electrosynthesis experiments were performed in the laboratories of Prof. Dr. Gerhard Hilt from the Department of Organic Chemistry.

Gutachterin: Prof. Dr. Mehtap Oezaslan
Zweitgutachter: Prof. Dr. Gerhard Hilt

Tag der Disputation: 14.02.2024

Erklärung

Hiermit versichere ich, dass ich diese Arbeit mit dem Titel "Preparation and Characterization of Nanporous Copper and its Application in the Electrosynthesis of Cyclic Carboantes" selbstständig verfasst und keine anderen als die angegebenen Quellen und Hilfsmittel benutzt habe. Des Weiteren erkläre ich, dass die Dissertation weder in ihrer Gesamtheit noch in Teilen einer anderen wissenschaftlichen Hochschule zur Begutachtung in einem Promotionsverfahren vorliegt oder vorgelegen hat.

-----------------------------------   -----------------------------------

Ort, Datum   (Sawsan Ibrahim)

Acknowledgement

I want to begin by conveying my profound appreciation to my advisor, Prof. Dr. Mehtap Oezaslan, for her invaluable guidance, continuous support, and patience. Her knowledge and experience have been a constant source of motivation for my academic research endeavors. Furthermore, I extend my heartfelt gratitude to Prof. Dr. Gerhard Hilt for his exceptional supervision and insightful counsel in the organic chemistry part of this project. I am also grateful for the University of Oldenburg for funding my project. Being part of the Research Training Group 2226 "Chemical Bond Activation" has been an enriching experience. It has not only allowed me to collaborate with peers but also provided access to valuable seminars and aided in the development of essential organizational skills.

I would also like to thank my colleagues in the working groups of Prof. Oezaslan and Prof. Hilt for their constant support and advice, especially Alexandra Dworzak, Sonja Blaseio, Philipp Weber, Björn Mahrt, Marek Janssen, Dr. Burkhard Hecker, Dr. Julia Strehl, Dr. Jan Fähmann, Dr. Luomo Li and Andre Hockmann. Many thanks to Holger Koch and Dr. Vita Solovyena for their technical support on the electron microscopes. I would like to thank Dr. Daniel Crespo and Dr. Eloi Pineda Soler from the Polytechnical niversity of Catalunya for providing the alloy ribbons and for the interesting discussion about melt-spun ribbons.

I would like to express my sincere gratitude to my husband, Giuseppe, for his constant support and encouragement, and for celebrating with me the small achievements and milestones of this journey. I am also deeply thankful to my parents and my brother for being a continuous source of inspiration and for believing in me. Last but not least, many thanks to all my friends who have helped or encouraged me in one way or another throughout this PhD, with a special mention to Hiba Haydar, who has always been a sympathetic listener to my concerns.

This journey has been both captivating and challenging, and I aspire that my research contributes in some small way to the realm of scientific knowledge. Now, the time has come to embark on a new chapter in my life.

Dedication

This dissertation is dedicated to my parents, Prof. Dr. Siham Sayes and Prof. Dr. Ousama Ibrahim, who taught me to aim high and follow my dreams.

Abstract

Nanoporous (np) materials are characterized by a three-dimensional network of solid ligaments and pores with dimensions from a few nanometers to tens of micrometers. Dealloying is a powerful and versatile method to fabricate np-materials with tunable structural and chemical properties for electrochemical synthesis and catalysis. This dissertation consists of two parts, in which the first discusses the dealloying processes of $Zn_{80}Cu_{20}$ alloy ribbons in acidic and alkaline environments. The findings reveal that the nanostructure can be controlled by varying the nature of the electrolyte solution, pH value, dealloying time, and temperature. The species adsorbed on the surface of the alloy greatly influences the surface diffusivity of Cu, with enhanced surface diffusion leading to the formation of larger ligaments which grow in size over time (e.g., chloride anions in HCl). The formation of Cu (hydr)oxide species, with slower diffusivity, in alkaline media results in a smaller ligament-pore structure. Cross-section analysis indicates that the dealloying process is controlled by interfacial processes. Interestingly, local Zn-rich regions were found in np-Cu ribbons dealloyed in 0.1 M HCl.

The second part focuses on the utilization of the prepared np-Cu as a cathode material for the electrosynthesis of cyclic carbonates from carbon dioxide (CO_2) and epoxides under mild conditions. The cathode (np-Cu/GC) was prepared by drop-casting of np-Cu on glassy carbon (GC) substrate. Very good yields were obtained for 1,2-butylene carbonate ($74 \pm 4\%$) and propylene carbonate ($62 \pm 6\%$). When different cathode materials were explored, low yields on bare GC, but similar yields on polycrystalline Cu were achieved. Although the pore-ligament structure is beneficial to enhance the CO_2 reduction reaction (CO_2RR), its impact on the yield of cyclic carbonate is negligible. This implies that the activation of CO_2 to the $CO_2^{\bullet-}$ radical anion is not the rate-limiting step, but rather the ring closure of the final intermediate to form cyclic carbonates. Furthermore, the np-Cu/GC shows very good stability and reusability for this organic electrosynthesis reaction. Altogether, this dissertation provides deeper insights into the reaction mechanism of cyclic carbonates formation on Cu-based electrodes and allows tuning the structural properties of np-Cu.

Zusammenfassung

Nanoporöse (np) Materialien zeichnen sich durch ein dreidimensionales Netzwerk von Ligamenten und Poren mit einer Größe von Nanometern bis zu einigen Mikrometern aus. Entlegieren ist ein effizientes Verfahren zur Herstellung von np Materialien für die elektrochemische Synthese und Katalyse. Diese Dissertation besteht aus zwei Teilen, wobei der erste Teil die Entlegierungsprozesse von $Zn_{80}Cu_{20}$-Legierungsbändern in saurer und alkalischer Umgebung behandelt. Die Nanostruktur kann durch Variation der Elektrolytlösung, des pH-Werts, der Reaktionszeit und der Temperatur gesteuert werden. Zum Beispiel erhöht sich die Diffusionsgeschwindigkeit von Cu Oberflächenflächen, wenn Chloridionen aus HCl auf dieser adsorbiert werden. Dies führt zur Bildung von größeren Ligamenten. Jedoch ist die Oberflächenbeweglichkeit der Cu Atome im alkalischen geringer und es kommt zur Bildung von kleineren Ligament-Poren-Struktur. Die Querschnittsanalyse zeigt, dass der Entlegierungsprozess durch Grenzflächenprozesse gesteuert wird. Interessanterweise fanden sich in den in 0,1 M HCl entlegierten np-Cu-Bändern Bereiche mit hohem Zn-Gehalt.

Der zweite Teil konzentriert sich auf die Verwendung des hergestellten np-Cu als Kathodenmaterial für die Elektrosynthese von cyclischen Carbonaten aus Kohlendioxid (CO_2) und Epoxiden unter milden Bedingungen. Die Kathode (np-Cu/GC) wurde durch Auftropfen einer np-Cu-Suspension auf ein Glaskohlenstoff-Substrat (GC) hergestellt. Sehr gute Ausbeuten wurden für 1,2-Butylencarbonat (74 ± 4%) und Propylencarbonat (62 ± 6%) erzielt. Kathodenmaterialvariation führte zu niedrigen Ausbeuten auf GC, aber vergleichbaren Ausbeuten auf polykristallinem Cu. Obwohl die nanoporöse Struktur die CO_2-Reduktionsreaktion verbessert, ist ihr Einfluss auf die Ausbeute an cyclischen Carbonaten vernachlässigbar. Die Aktivierung von CO_2 ist also nicht der geschwindigkeitsbestimmende Schritt. Außerdem zeigt das np-Cu/GC eine sehr gute Stabilität und Wiederverwendbarkeit. Insgesamt liefert diese Dissertation tiefere Einblicke in den Reaktionsmechanismus der Bildung von cyclischen Carbonaten an Cu-basierten Elektroden und ermöglicht die strukturellen Eigenschaften von np-Cu kontrolliert zu verändern.

Table of Contents

List of Figures

List of Tables

1. Introduction and Motivation

Nanoporous (np) materials present a three-dimensional and self-assembled network of solid ligaments and pores, with scale length ranging from a few nanometers to tens of micrometers.[1] They possess unique properties, including high surface area, large number of low-coordinated surface atoms, and enhanced mass transport properties.[1-3] While nanoporous gold has been extensively studied[4-6], nanoporous copper (np-Cu) has also attracted attention as a cheaper material, with several interesting applications in the fields of catalysis[7], sensors[8], and batteries[9]. Dealloying is considered as a powerful and versatile synthetic route to fabricate np materials, which has been extensively applied in the last two decades.[10-12] The characteristics of np material obtained during dealloying processes can be controlled by varying the dealloying conditions, such as the electrolyte, dealloying temperature, and time.[13,14] Moreover, the tunable residual content of the less noble metal in np materials prepared by dealloying adds the advantage of modifying the electronic and geometric properties of the noble metal-rich materials.[7] For example, it has been reported that residual Ag content strongly influences the surface-enhanced Raman spectroscopy (SERS) effects of np-Au prepared from dealloying of Ag-Au master alloys.[15]

The nature of the dealloying electrolyte is a critical factor that significantly influences the obtained nanoporous structure. It is associated with different dealloying rates and surface mobility of Cu atoms, depending on the specific electrolyte environment.[7,16] Different np-Cu morphologies and dealloying mechanisms have been observed in alkaline and acidic media.[7,14,16-24] The choice of anions in the electrolyte solution also plays a significant role in determining the size of ligaments in the resulting nanoporous structure. For example, adsorbed chloride ions enhance Cu surface diffusivity, leading to an increase of ligament size, whereas the presence of adsorbed phosphate ions shows an inhibition effect and thus much smaller ligament size.[14,19] These variations highlight the sensitivity of the dealloying process to the chemical environment and the specific ions present in the electrolyte, which can lead to diverse structures and properties in np-Cu materials.

In addition to the electrolyte, the choice of alloy employed in the dealloying process also has a great impact on the resulting nanoporous structure. Alloys can be manufactured using different techniques including melt-spinning[25], quenching of molten metals[16], and electrodeposition of less noble metal followed by thermal annealing[7]. These methods can lead to different crystal phase structures, levels of homogeneity, and thicknesses of master alloys, which, in turn, influence the characteristics of the dealloyed structure. For example, the partial dealloying of $Au_{40}Cu_{28}Ag_7Pd_5Si_{20}$ ribbons (25 µm thick) in 1 M HNO_3 showed an inhomogeneous structure between the surface and cross-section of the ribbons.[26] This observation might be attributed to the dealloying front propagation process and its fundamental mechanism for these thick alloy ribbons, compared to thin alloy films prepared by Zn deposition and thermal annealing method.

This dissertation is divided into six chapters, where **Chapter 1** gives a general introduction as well as the motivation and objectives of this work. **Chapter 2** discusses the fundamental principles of porosity evolution by dealloying, carbon dioxide reduction reaction (CO_2RR), and organic electrosynthesis. This basic knowledge is required to fully understand the presented results. In **Chapter 3**, the experimental procedures are explained, including the preparation and characterization of samples, and the electrosynthesis experiment. The chemicals and instruments utilized throughout this work are also mentioned.

The evolution of a three-dimensional porous structure from melt-spun Cu alloy ribbons is not well explored in the literature. Therefore, **Chapter 4** provides deeper insights into porosity evolution in np-Cu ribbons, formed by chemical dealloying of melt-spun $Zn_{80}Cu_{20}$ ribbons in 0.1 M HCl, 5 M and 15 M H_3PO_4, as well as 1.3 M NaOH solutions. Here, the effects of the dealloying conditions on the structure and residual Zn content of np-Cu ribbons have intensively been investigated by varying the nature of electrolyte, de-aeration and agitation of the electrolyte solution, dealloying time and temperature. The dealloyed ribbons were investigated both on top-view as well as the cross-section. This allows us to gain better understanding of the dealloying process for fabricating np-Cu ribbons with tailored structural and chemical properties for applications in electrochemical synthesis[27,28], sensors[8,29] and catalysis[30-32].

Chapter 5 presents the practical application of the prepared np-Cu in the electrosynthesis of cyclic carbonates from CO_2 and epoxides at room temperature and ambient pressure. For this purpose, np-Cu, dealloyed in 0.1 M HCl for 168 h (7 days), was drop-casted on glassy carbon (GC) substrate and evaluated as cathode material, referred to as np-Cu/GC. Cyclic carbonates are typically obtained by the catalytic coupling reaction of CO_2 with epoxides. The catalysts used for this purpose have several drawbacks. For example, homogenous catalysts such as quaternary ammonium salts, phosphonium salts, and ionic liquids, face significant challenges related to the catalyst recovery and reusability, as well as product purification.[33-35] These limitations restrict their practical applicability in industrial processes. On the other hand, heterogeneous catalysts such as metal oxides and metal complexes require more extreme reaction conditions, namely high CO_2 pressure (10 - 200 bar) and temperature (≥100 °C), which reduces the sustainability of the cyclic carbonate synthesis processes.[34-36]

Electrochemical synthesis presents a promising solution to overcome the shortcomings of conventional organic synthesis. For this purpose, copper cathodes have been widely used, producing higher yields of cyclic carbonates compared to other materials such as stainless steel, nickel, or titanium.[37-40] This can be attributed to the excellent activity of copper towards the reduction of CO_2 to $CO_2^{\bullet -}$ radical anion.[41-44] Planar electrodes are typically used in organic electrosynthesis.[45,46] Therefore, the development of cathode materials with higher surface area and superior catalytic activity for the electrochemical CO_2 reduction reaction (CO_2RR) can be a promising approach to enhance the yield of cyclic carbonates. To our knowledge, there is currently no literature available reporting the use of np electrode materials for the cyclic carbonate formation from epoxide and CO_2. Our results show comparable yields of cyclic carbonates on np-Cu/GC to those formed on flat polycrystalline Cu, despite its enhanced electrochemically active surface area and remarkable catalytic performance for CO_2RR. This observation rules out CO_2 activation as the rate-limiting step of the cyclic carbonate formation. The findings of this work enable us to gain a deeper understanding of the role of the cathode in the reaction pathway involving CO_2 and epoxide and to assess the applicability of np materials in organic electrosynthesis. This comprehensive study allows tuning the structural and

chemical properties of np-Cu material for a wide range of possible applications in electrochemical synthesis and catalysis.

2. Background

This work spans across different scientific fields, including corrosion science, electrochemical and organic chemistry. Therefore, this chapter aims to introduce the relevant theoretical background knowledge. First, **Section 2.1** discusses the fundamental principles of the evolution of nanoporous structures through dealloying. Afterwards, **Section 2.2** provides an overview of the fabrication methods of nanoporous copper, and its various applications. Finally, in **Section 2.3**, the field of organic electrosynthesis is introduced as an attractive application of electrochemistry for the synthesis of valuable organic compounds, such as cyclic carbonates.

2.1. Porosity evolution

In general, np materials can be fabricated by templating or dealloying methods. Templating includes the utilization of sacrificial molds or templates with pores that act as a framework for depositing metals. These templates can be either inorganic (hard templating) or polymeric (soft templating). Once the metal is deposited, the templates are then removed to form a metal replica of the template structure.[47,48] This method allows for precise control over the porous structure. However, it can be time consuming and experimentally complex due to the multiple steps involved. Another approach of templating is the dynamic hydrogen bubble template technique which involves the electrodeposition of metal ions onto a substrate, accompanied by numerous hydrogen bubbles.[49,50] Here, hydrogen bubbles are used as a special dynamic template, and metal is deposited around the bubbles to form three-dimensional metal foams.[49,50] Although this method does not require the addition of external templates, achieving precise and uniform pore sizes is still a challenge.

On the other hand, dealloying is a powerful and versatile method for the fabrication of np materials (**Figure 1**).[10,12,51] This process involves the selective dissolution of the less noble component from an alloy chemically[7,14,52,53] or electrochemically[54-56]. Chemical dealloying refers to a free corrosion process, where the sample is immersed in an electrolyte solution (acidic or alkaline)[13], whereas in electrochemical dealloying an external electrical potential is applied to the sample while it is immersed in an electrolyte

5

solution to remove the less noble metal from an alloy.[57] Both techniques offer the possibility to tune the characteristics of the nanostructure (e.g., ligament size) by adjusting the parameters of the dealloying process. While electrochemical dealloying enables more direct control over the corrosion process[58], chemical dealloying offers the advantage of a simple set-up with the need for specific instrumentations. In the last two decades, many efforts have been done to understand the evolution of bicontinuous ligament-pore structures by dealloying.[10-12]
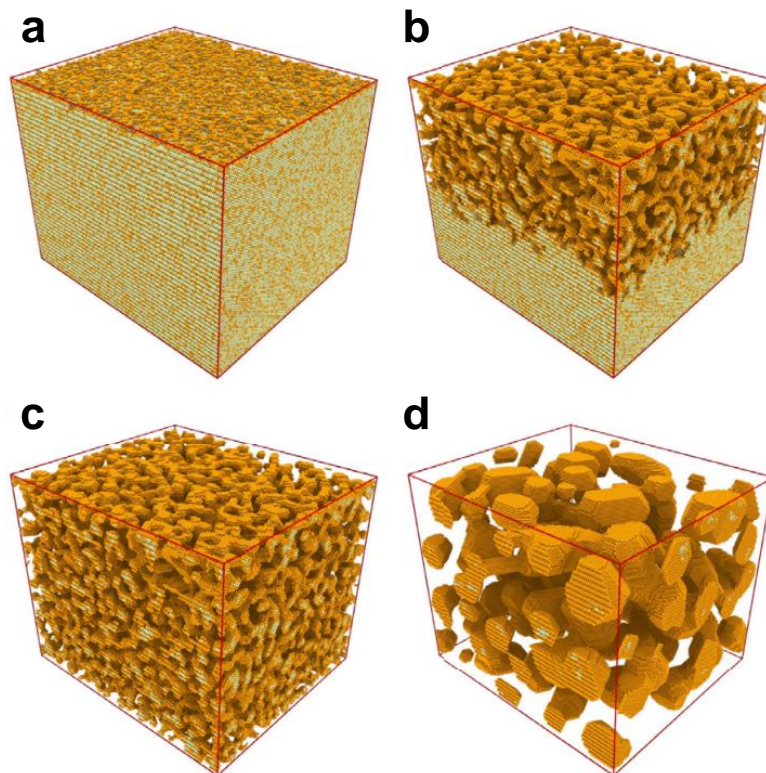
Figure 1: Porosity evolution during dealloying modeled by kinetic Monte Carlo simulation. Primary dealloying (a) with initial surface roughening and partial passivation, (b) formation of small ligaments, (c) proceeding of the corrosion front inward, leaving a high concentration of less noble species in the ligaments' interior. (d) Coarsening of the structure during secondary dealloying and reduction of the residual amount of less noble element. Figure reprinted from ref. 59.

It is suggested that dealloying occurs at two processes or stages: primary and secondary.[58,60] The primary dealloying (**Figure 1a – c**) involves the selective dissolution of the less noble component from the alloy, resulting in the formation of a np structure. It primarily happens at the alloy's surface or near the initial interface exposed to the

corrosive electrolyte. While primary dealloying initiates the formation of porosity, secondary dealloying supplements this process by further dissolving the residuals of the less noble component from the nano-ligaments, potentially enhancing the porosity or modifying the structure. The secondary dealloying can occur during coarsening (**Figure 1d**).

In the following sections, we will give an overview of the proposed models of porosity evolution in the literature and discuss important dealloying parameters, such as dealloying threshold and critical potential.

2.1.1. Models of porosity evolution during dealloying

The main dealloying mechanisms proposed in the literature to explain the microstructure evolution during dealloying are bulk diffusion model[61] and surface diffusion (percolation dissolution) model[11,62,63].

In the bulk diffusion model proposed by Pickering and Wagner[61], it is suggested that the rate-limiting step in the electrolytic dissolution of a binary alloy is the solid state diffusion of the less noble metal element via a divacancy mechanism. This mechanism is illustrated in **Figure 2a** showing the dealloying of a binary alloy, denoted as A_xB_y, where A (in green) represents the more noble metal and B (in orange) represents the less noble metal. Based on the bulk diffusion model, the more noble component A which is the faster diffuser, migrates towards the surface, as indicated by the dark arrows. The lighter arrows represent the combined flux of the less noble atoms B and vacancies moving inward within the alloy. As a result of this process, a negative dendrite-like structure predominantly composed of component A would be generated.

The flux of vacancies can lead to the creation of Kirkendall voids within the interior of the alloy.[64] Kirkendall effect refers to the movement of the bimetallic interface when two attached metals are heated to temperatures where atomic diffusion occurs.[65,66] This shift is caused by the metals having different interdiffusion rates. Consequently, there is also an associated flux of vacancies towards the faster diffusing metal. Void formation is the result of these vacancies clustering at structural defects in the metal, such as grain

boundaries.[65,66] For example, it has been reported that severe Kirkendall voids form in the Cu_3Sn/Cu interface after solid-state aging in solder joints, which greatly weaken the mechanical properties of the joint.[67] Geng et al.[68] also observed the formation of Kirkendall voids during the dealloying of Li-Sn systems. This phenomenon occurred under specific conditions: when the mole fractions of Li were less than 0.5 and at potentials lower than the critical potential (see **Sections 2.1.2** and **2.1.3**). Under conditions, dealloying was rate-limited by the solid-state mass-transport of Li from the alloys.
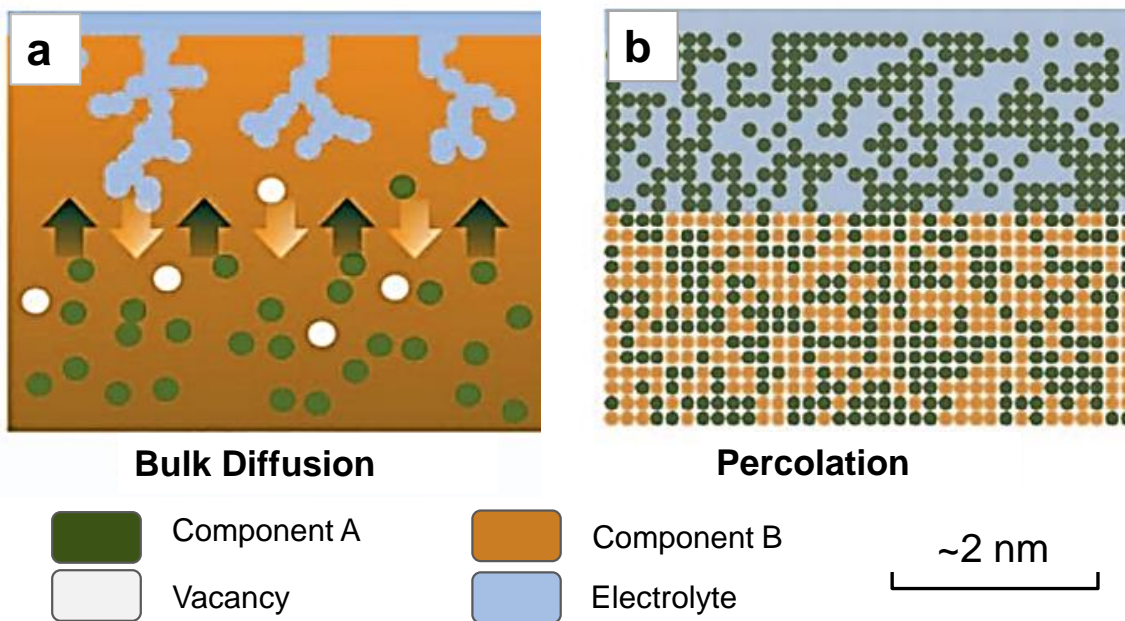
Figure 2: *Proposed models of porosity evolution during dealloying of a binary alloy A_xB_y, where A is the more noble component represented in green color and B is the less noble component in orange color. The atom fractions of the two components are denoted as x and y. (a) Bulk diffusion of component A resulting in a negative dendrite-like structure, and (b) percolation dissolution yielding bi-porosity. The dark arrows signify the movement of component A to the surface, whereas the light arrows show the collective flow of the atoms of component B and vacancies directed toward the interior of the alloy. Figure reprinted from ref. 64.*

The divacancy-mediated lattice diffusion within the alloy is too slow to contribute in any significant manner to the ambient temperature selective dissolution process.[64] Therefore, the subsequent work of Sieradzki[63] and Erlebacher[11,62] lead to the development of an alternative model for porosity evolution, known as the surface

diffusion or percolation dissolution model. This model is based on the concept that when the concentration of the less noble component in an alloy surpasses a critical threshold, continuous atomic-scale pathways form. These pathways effectively eliminate the need for solid-state transport to facilitate selective dissolution and act as routes for the electrolyte to infiltrate the alloy, causing the less noble component to dissolve, as displayed in the scheme in **Figure 2b**.
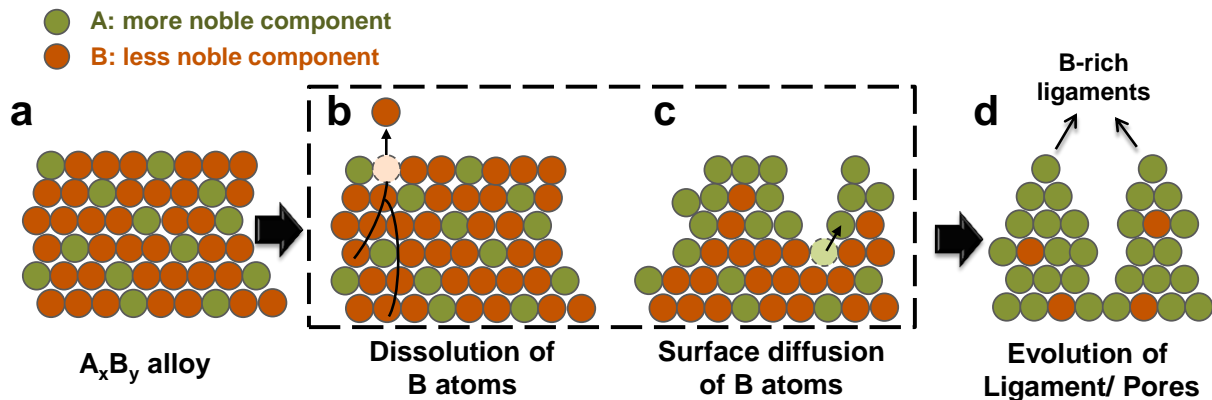
Figure 3: *Schematic of porosity evolution in dealloying of a binary alloy A_xB_y according to the surface diffusion (percolation dissolution) model. (a) A B-rich-A_xB_y alloy system where A is the more noble component represented in green color and B is the less noble component in orange color. The atom fractions of the two components are denoted as x and y. (b) The dissolution of the less noble metal, B, takes place at high-coordinated terrace sites. The black lines indicate the possible interconnected atoms of the less noble metal through the bulk of the alloy, allowing continuous percolation. (c) As dissolution proceeds layer by layer, interfacial uphill surface diffusion of the more noble metal, A, takes place, leading to surface roughening. (d) This process leads to the formation of a bicontinuous ligament-pore structure with B-rich ligaments.*

Porosity evolution by surface diffusion or percolation dissolution model is illustrated in detail in the schematic in **Figure 3** for the dealloying of a binary alloy A_xB_y. The more noble atoms (A) are represented in green circles, whereas the less noble metal atoms (B) in orange (**Figure 3a**). Nanostructure formation is the result of two elementary processes: dissolution of the less noble component, B, and surface diffusion of the more noble component, A. The process starts with the dissolution of a single B atom from the alloy surface, leaving behind a terrace vacancy (**Figure 3b**). The atoms coordinating this vacancy have fewer lateral near-neighbors than other B atoms in the terrace and are

thus more susceptible to dissolution. As a result, the entire terrace is stripped, leaving behind A atoms undercoordinated. To prevent this highly non-equilibrium state, these more noble atoms tend to diffuse and agglomerate into clusters (**Figure 3c**). This exposes the next layer of B atoms to the corrosive electrolyte, leading to the dissolution of more layers of the less noble atoms from the alloy. Consequently, the clusters enriched with more noble atoms transform into three-dimensional hills, denoted as ligaments (**Figure 3d**). The ligaments have base perimeters that grow in diameter as dealloying proceeds, and eventually not enough noble metals atoms are provided to passivate them effectively, allowing them to be undercut. This process causes the pores to split, resulting in an expansion of the surface area and enabling the continued development of porosity into the interior of the original alloy.[11,62]

The dealloying temperature has a remarkable effect on the characteristic length of the np structure.[69-77] This is attributed to correlation of the temperature on the surface diffusivity of the more noble component along the alloy-electrolyte interface (D_s), shown in **Equation (1)**[73,76,77], where $d(t)$ is the ligament size at given dealloying time t, K is the Boltzmann constant, T is the dealloying temperature, γ is the surface energy of the more noble metal, t is the dealloying time and α is the lattice parameter of the more noble metal.

$$D_s = \frac{d(t)^4 KT}{32\ \gamma t \alpha^4} \qquad\qquad \textbf{Equation (1)}$$

Zhang et al.[76] reported surface diffusivity of gold adatoms in 20 wt.% NaOH solutions at −20, 25, and 95 °C to be 2.1 x 10^{-23} , 2.3 x 10^{-21} , and 1.6 x 10^{-19} m^2 s^{-1}, respectively. This increase in the surface mobility of Au leads to the formation of np-Au structures with ligament/channel sizes of 5.3 ± 0.9, 7.7 ± 1.5, 15.0 ± 3.0 nm at dealloying temperatures of −20, 25, and 95 °C, respectively. Similarly, Qian et al.[73] reported surface diffusivity of gold in 70% HNO_3 solution at −20 °C as 9.0 x 10^{-22} compared to 2.0 x 10^{-19} m^2 s^{-1} at 25 °C. The authors found that low dealloying temperature can effectively delay the coarsening of the nanoporous structure, where lowering the dealloying temperature to −20 °C leads to the formation of np-Au with average nanopore sizes four times smaller (7 nm) those formed at 25°C (28 nm).

For the porosity evolution to occur, two criteria should be met. First, the atom fraction (or mole fraction) of the less noble component needs to exceed a minimum value, the dealloying threshold. Second, dealloying potential needs to exceed the critical dealloying potential.

2.1.2. Dealloying threshold

In order for the selective dissolution of the less noble atoms to extend beyond just the alloy's surface exposed to the corrosive electrolyte, there needs to be a continuous and connected cluster of these atoms (**Figure 3b**, black lines). This connected cluster, known as a percolating cluster, serves as an uninterrupted pathway for the dissolution process. Additionally, it facilitates the penetration of the electrolyte into the solid bulk, enabling the corrosion process to persist. Sieradzki et al.[63] defines the dealloying threshold for an alloy system as the lowest atom fraction of the less noble metal element at which this element can be preferentially dissolved from the bulk of an alloy. Below the delaying threshold, at a certain point, the surface will be passivated with the noble metal atoms and the deeper layers of the alloy cannot be fully dealloyed. Above the dealloying threshold, an atomic-scale network of less noble component runs through the entire structure of the alloy, ensuring continuous dissolution. It is reported that for the dealloying of ZnCu alloys, a minimum content of 18 ± 2 at. % of Zn is required[78], whereas Ag content over 55 at. % is needed for dealloying of AgAu alloys.[12]

2.1.3. Critical potential

Another key parameter for porosity evolution by dealloying is the critical potential. This critical potential marks the onset of percolation dissolution in an alloy with a composition exceeding the dealloying threshold, as illustrated in the schematic in **Figure 4**. At potentials below the critical potential, the dissolution exclusively takes place at surface sites with lower coordination such as step edges and these surface sites are rapidly passivated with the remaining more noble atoms. This leads to a passivated, planar morphology.[1,79,80] Above the critical potential, dissolution of the less noble atoms

initiates from highly coordinated terrace sites, which leads to the creation of a terrace vacancy that then grows laterally into a vacancy cluster as lateral near neighbors are subsequently dissolved. The more noble, atoms tend to diffuse with the receding step edge rather than be left as thermodynamically unfavorable adatoms, a kind of interfacial uphill diffusion. This process leads to the formation of bicontinuous structure with a ligament/pore network.[1,62,80]
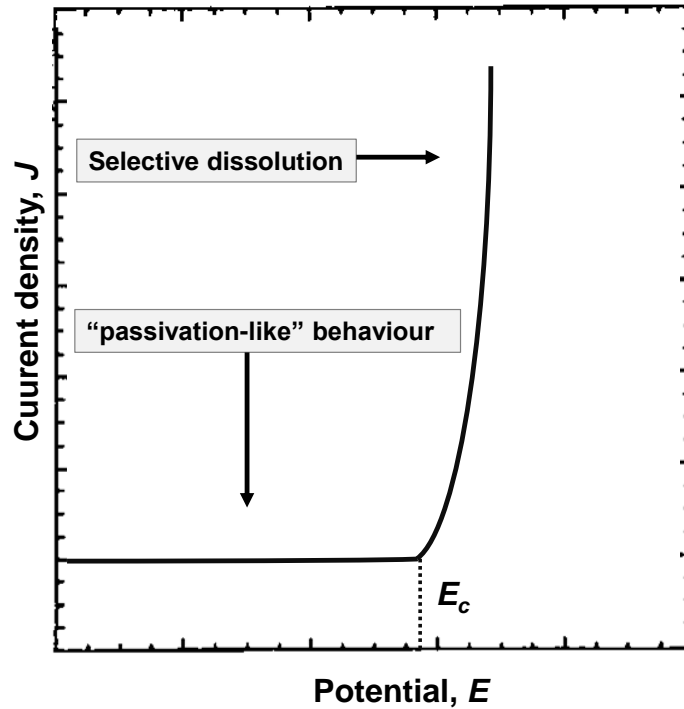
Figure 4: *Schematic illustration of the polarization curve an alloy undergoing selective dissolution. Below the critical potential (E_c), the alloy undergoes a "passivation-like" behavior whereas over the critical potential selective dissolution and the evolution of a bicontineous porous structure occurs. Figure reprinted from ref. 80.*

In general, for an alloy to become nanoporous during dealloying, a difference in potential required to dissolve the alloy component in its pure form must be separated by a few hundred millivolts.[62] The dealloying critical potential, E_c, is given by Sieradzki et al.[80] in **Equation (2)**, where $\bar{E}$ is the reversible potential for the flat surface, K is Boltzmann's constant, T is the absolute temperature, p is the atom fraction of the less noble component in a binary alloy A_pB_{1-p}, $\eta(x)$ is the overpotential for the dissolution process.

$$E_c = \bar{E} - \frac{KT}{nq} [p \ln p + (1 - p)(1 - p)] + \eta(x) \qquad \textbf{Equation (2)}$$

A lower bound critical potential for percolation dissolution, resulting in bi-continuous porosity formation, of 0.55 V vs Li⁺/Li was reported for Li-Sn alloys systems.[68]

2.1.4. Coarsening of np structure

After the formation of np structure by primary dealloying, the process of secondary dealloying occur, driven by curvature and surface-diffusion mediated coarsening (see **Figure 1**). Dealloying and coarsening are distinctly different processes. Dealloying involves chemical or electrochemical driving forces that lead to the dissolution of the less noble component and surface diffusion of the more noble metal, and result in porosity and increase of the surface area over time. In contrast, coarsening, is driven by the endeavor to reduce the net excess surface energy that was introduced during dealloying.[81] In porous metals, coarsening proceeds by ligament pinch-off, in which surface diffusion pulls material away from saddle-point curvature ligaments, which thin to one atom thick and then break. The kinetics of ligament pinch-off are controlled by Rayleigh instabilities and has the geometric effect of reducing the topological genus.[81,82] The genus is a topological concept that describes the number of "handles" or "holes" an object has. For example, a sphere has a genus of 0 whereas a torus has a genus of 1. Bubbles reduce the topological genus of the structures in which they reside. For instance, a bubble inside a sphere has genus of –1.

The Rayleigh instability problem[83] pertains to the spontaneous fragmentation or breakup of a fluid thread or column into smaller droplets or segments due to surface tension effects. The typical scenario involves a cylindrical hat is subjected to small perturbations. When the perturbations reach a critical wavelength, the amplitude will grow because the total surface energy of system decreases, leading to the formation of droplets or smaller segments. This effect would apply to void cylinders as well, meaning that they would break up into a series of bubbles. Erlebacher et al.[82] applied these ideas to open

13

porosity dealloyed metals, where the structure is seen as a network of both solid cylinders and void cylinders. Therefore, Rayleigh instabilities lead to both ligament pinch-off and bubble formation. After a bubble is created, it becomes detached from any mass transport paths for additional morphological changes. Conversely, pinched-off ligaments remain connected to the entire primary external surface of the structure, allowing further potential evolution. As ligament pinch-off, they can destroy nearby bubbles; thus, over longer times the number of bubbles decreases. It is suggested that the coarsening kinetics align with the $t^{1/4}$ power law, that is expected for coarsening mediated by surface transport.[81]

2.2.   Nanoporous copper (np-Cu)

Np-Cu has many interesting properties, such as unique pore structure, high surface area, large number of low-coordinated surface atoms, enhanced mass transport properties, and high electrical and thermal conductivities. These properties make np-Cu a promising material for many applications in energy storage, sensing, and catalytic systems. This chapter will discuss the fabrication methods and distinctive characteristics of np-Cu, as well as its applications.

2.2.1. Fabrication of np-Cu

Various binary alloys have been used to form np-Cu via dealloying, including Zn-Cu[7,14,20,84-87] Al-Cu[18,21], Ti-Cu[22,88], Mn-Cu[16,89,90], and Mg-Cu[91-93], among which Zn-Cu remain one of the most commonly studied dealloying systems. The phase diagram of the copper and zinc alloys is presented in **Figure 5**, showing the relationship between temperature, composition, and the phases present in the alloy. For the different phases, different crystalline brass structures exist: Cu for α-phase, Cu_1Zn_1 for β-phase, Cu_5Zn_8 for γ-phase, $Cu_{0.7}Zn_2$ for δ-phase, Cu_2Zn_8 for ε-phase, and Zn for η-phase. Different brass phases show different dealloying behaviors.[85,94] For example, Egle et al.[14] reported fast dealloying kinetics and formation of homogenous ligament-pore network

when Zn-rich $Zn_{80}Cu_{20}$ alloy (Cu_1Zn_5 single crystal phase) was dealloyed in 5 M HCl, compared to $Zn_{50}Cu_{50}$ (consisting of Cu_5Zn_8, Cu_3Zn_1 and Cu_1Zn_1 crystal phases). The fast dealloying kinetics of the $Zn_{80}Cu_{20}$ alloy is a consequence of the lower critical potential of Zn-rich brasses.
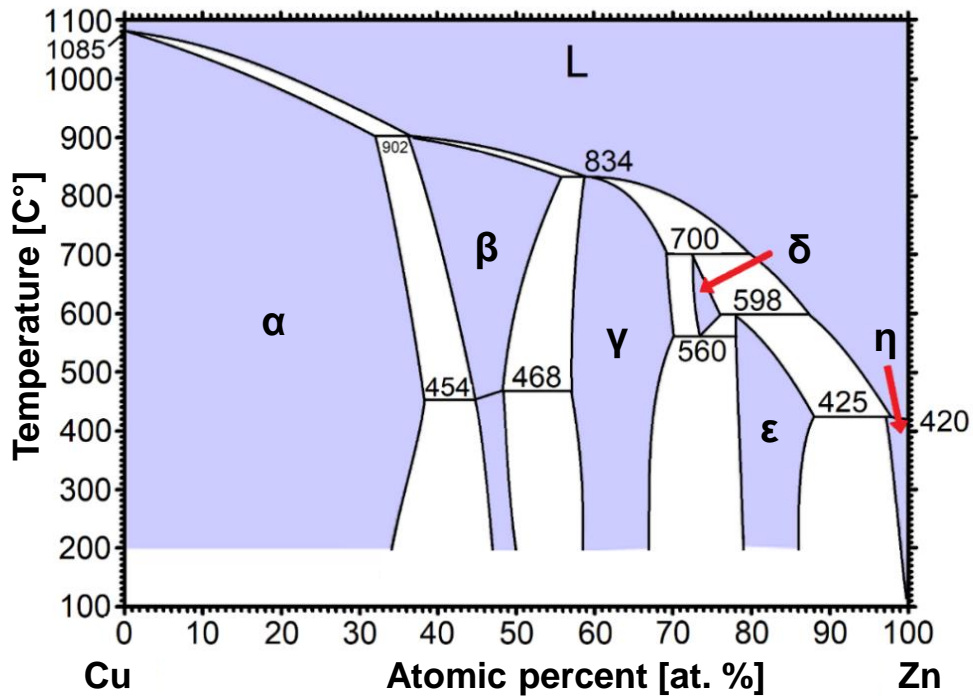
Figure 5: *Cu-Zn binary phase diagram as reported in the ASM Alloy Phase Diagrams Database[95] based on the assessment of Miodownik[96].*

The selective dissolution of Zn from Zn-Cu alloys occurs due to the large equilibrium potential difference of Cu and Zn. The Pourbaix diagrams of copper and zinc are shown in **Figure 6**. It is apparent that the dissolution potentials of copper and zinc exhibit a difference of approximately 1 volt, both in acidic and alkaline conditions. Consequently, this potential difference leads to the selective dissolution of Zn from Zn-Cu alloys when exposed to a corrosive electrolyte.
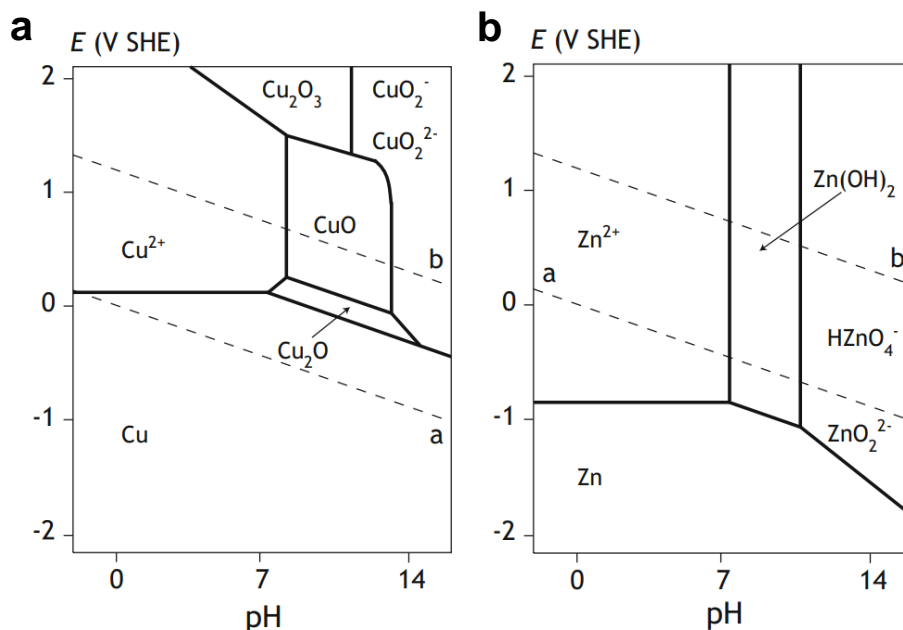
Figure 6: Pourbaix diagram for (a) copper and (b) zinc. Figure reprinted from ref. 97.

An overview of the methods employed in the literature to produce np-Cu can be found in **Table 1**. It is seen that properties of the dealloyed nanoporous structure are greatly affected by the master alloy, as well as the dealloying conditions, such as nature of electrolyte, dealloying temperature, and time. The different techniques used for the preparation of the master alloy, lead to different crystal phase structures, homogeneities and thicknesses, and hence influence microstructure morphology of the dealloyed np-Cu. For example, $Mn_{70}Cu_{30}$ alloys prepared by two different processes, arc and quench melting, have shown different oxide inclusions and second phases, which contribute to different homogeneity of the nanoporous structure.[16] The morphology of np-Cu is also affected by different annealing temperatures used to form Zn-Cu alloy films after electrodeposition of Zn layer on a Cu substrate, where samples with low thermal alloying temperature (100 °C) showed separated nanoparticles instead of forming interconnected porous structure.[20]

The dealloying conditions such as the nature of electrolyte and dealloying temperature influence the Zn dissolution and surface diffusivity of Cu, consequently affecting the resulting ligament-pore structure. Egle et al.[14] investigated the dealloying of $Zn_{80}Cu_{20}$ alloy in different electrolyte solutions of hydrochloric acid (HCl), phosphoric acid

16

(H_3PO_4), sulfuric acid (H_2SO_4) and nitric acid (HNO_3). The oxidation potential of HNO_3 is too positive to allow for selective dissolution of Zn. On the other hand, sulfuric acid forms a thick $ZnSO_4$ surface layer that prevents further dealloying. However, HCl and H_3PO_4 have negative oxidation potentials and thus are able to selectively dissolve Zn forming highly soluble Zn salts. Therefore, the authors investigated the dealloying of $Zn_{80}Cu_{20}$ in the following electrolytes: 5 M H_3PO_4, 15 M H_3PO_4, 5 M H_3PO_4 + 5 M HCl, 5 M H_3PO_4 + 0.25 M NaCl, 5 M HCl, and 5 M HCl + 0.25 M NaCl. Larger ligaments (129 ± 41 nm after 36 h) were observed in HCl compared to ligaments (46 ± 9 nm after 24 h) formed after dealloying in 5 M H_3PO_4. This effect is attributed to the enhanced surface diffusion of Cu by the adsorbed chloride anions on the surface of the alloy. On the other hand, adsorbed phosphate anions suppress Cu mobility, leading to smaller ligaments. Increasing the concentration of H_3PO_4, from 5 to 15 M results in the formation of smaller ligaments (35 ± 8 nm). While the addition of NaCl to 5M HCl led to further increase the ligament size compared to 5 M HCl, the addition of NaCl to 5 M H_3PO_4 only slightly increased the ligament size to 57 ± 16 nm. Dealloying in 5 M H_3PO_4 + 5 M HCl also gave similar ligament size of 51 ± 12 nm. Therefore, when both phosphate and chloride anions are present in the electrolyte, the suppressing effect of phosphate dominates the promoting effect of chloride anions. This effect was reported by other studies, where adsorbed chloride ions enhance the mobility of Cu surface atoms by 2 – 5 magnitudes compared to a chloride free enviroment.[14,19]

Although dealloying in acidic environments is more common, some studies investigated the formation of np-Cu in alkaline media, where ligament sizes ranging between 15 to 43 nm were reported in sodium hydroxide (NaOH) solutions.[7,17,20,72] Here, the dealloying process is mainly restricted by the slow surface diffusion of Cu oxide species, forming in alkaline solutions. It is suggested that the surface diffusivity of Cu oxide species is two to three magnitudes slower than metallic Cu, explaining the remarkably smaller ligament-pore structures compared to those formed in HCl.[7,17-19,72]

Table 1: Comparison of reported literature of np-Cu fabricated by dealloying. Table reprinted with modifications from ref. [52]

starting alloy	alloying method	dealloying conditions	ligaments size [nm]	Ref
$Zn_{80}Cu_{20}$ ribbon (20-40 µm thick)	Melt spinning	0.1 M HCl at 25°C 1.3 M NaOH at 25°C	68 ± 14 (8 h) 73 ± 14 (24 h) 86 ± 19 (48 h) 111 ± 27 (72 h) 115 ± 28 (6 days) 128 ± 27 (13 days) 21 ± 4 (8 - 48 h)	52
$Zn_{80}Cu_{20}$ alloy cubes (3x3x0.3 mm^3)	Purchased from GoodFellow	5 M H_3PO_4 15 M H_3PO_4 5 M H_3PO_4 + 5 M HCl 5 M H_3PO_4 + 0.25 M NaCl 5 M HCl 5 M HCl + 0.25 M NaCl	46 ± 9 (24 h) 53 ± 14 (6 days) 35 ± 8 (24 h) 51 ± 12 (24 h) 57 ±16 (24 h) 129 ± 41 (24 h) 156 ± 76 (24 h)	14
$Zn_{80}Cu_{20}$ film (2 µm thick)	Electrodeposition of Zn and subsequent thermal annealing	0.1 M HCl at RT 1.3 M NaOH at RT	33 ± 6 (8 h) 100 ± 38 (48 h) 33 ± 14 (8 h)	7
ZnCu films	Electrodeposition of Zn and subsequent thermal annealing	5 wt.% NaOH at RT	~15 (24 h)	20
ZnCu films	Co-electrodeposition of ZnCu	1 M HCl at RT	-	84
$Mn_{70}Cu_{20}$ ribbons	Melt-spinning	2 M HCl at RT	114 – 214 (2-17 h)	25
$Mg_{12}Cu_{88}$ ribbons	Melt-spinning	0.3 M HCl at RT	20 ± 5	98
$Al_{15}Cu_{85}$ ribbons	Melt-spinning	1.6 M HCl at 75 °C 2.6 M NaOH at RT	80 - 100 20 - 40	17
$Al_{35}Cu_{65}$ ribbons	Melt-spinning	1.6 M HCl at 90±5 °C	100 – 300 (1-2 h)	21
$Al_{40}Cu_{60}$ ribbons	Melt-spinning	1.6M HCl at 90±5 °C	100 - 300 (1-2 h)	21
$Al_{50}Cu_{50}$ ribbons	Melt-spinning	1.6 M HCl at 90±5 °C	300 – 500 (1-2 h)	21
$Mn_{72}Cu_{28}$ ribbons	Melt-spinning	0.1 M HCl at 25°C	48.7 nm* (3.5 h)	99
$Mn_{70}Cu_{30}$	Metal melting followed by quenching	0.05 M HCl 1 M citric acid 0.01 M H_2SO_4 + 0.001 M $MnSO_4$ 1 M $(NH_4)_2SO_4$	125 ± 30 (8 days) 80 ± 20 (10 days) 45 ± 11 (6 days) 53 ± 8 (6 days)	16

starting alloy	alloying method	dealloying conditions	ligaments size [nm]	Ref
ZnCu films	Electrodeposition of Zn and subsequent thermal annealing	0.1 M HCl at 50 °C 0.1 M HCl at 60 °C 0.1 M HCl at 70 °C 0.1 M HCl at 80 °C 0.1 M HCl at 90 °C	132 (5 h) 140 (5 h) 174 (5 h) 218 (5 h) 265 (5 h)	77
$Al_{67}Cu_{33}$ powders	Melt-spinning	5 wt% HCl at 25 °C 5 wt% HCl at 60 °C 5 wt% HCl at 75 °C 5 wt% HCl at 90 °C	30 ± 5 (10 h) 50 ± 5 (5 h) 90 ± 10 (5 h) 150 ± 10 (5 h)	100
Al_3Cu_{60} ribbons	Mechanical milling	2 M NaOH at 3 °C 2 M NaOH at 25 °C 2 M NaOH at 50 °C 2 M NaOH at 70 °C 2 M NaOH at 90 °C	18 ± 2 21 ± 3 30 ± 3 36 ± 4 43 ± 4	72

*pore size

Dealloying in higher temperature leads to the formation of np-Cu structures with larger ligaments, due to the enhanced Cu surface diffusivity. Zhan et al.[77] reported a significant increase in Cu surface diffusion rates from 8.97 x 10^{-17} to 1.61 x 10^{-15} $m^2 s^{-1}$ in 0.1 M HCl when the dealloying temperature increases from 50 to 90°C. This improved mobility of Cu atoms results in a remarkable coarsening of np-Cu, with a doubling of the size of the ligaments (132 and 265 nm after dealloying for 5 h at 50 and 90°C, respectively). Similar findings were reported by Liu et al.[100], where Cu surface diffusivities of 9.45 x 10^{-20}, 1.63 x 10^{-17}, 1.79 x 10^{-16}, and 1.44 x 10^{-15} $m^2 s^{-1}$ were found in 5 wt.% HCl solutions at 25, 60, 75, and 90°C, respectively. The authors reported a growth in ligament size from 30 ± 5 nm at 25°C to 150 ± 10 nm at 90°C. On the other hand, the same pattern was observed in alkaline environments, with slower Cu diffusivity compared to HCl, where Cu surface diffusion coefficients of 1.7 x 10^{-19}, 6.5 x 10^{-19}, 5.9 x 10^{-8}, 1.6 x 10^{-17} and 3.5 x 10^{-17} $m^2 s^{-1}$ were reported in 5 M NaOH at 3, 25, 50, 70 and 90°C, respectively.[72]

These numerous studies in the literature illustrate that the properties of np-Cu can be adjusted through the control of alloying and dealloying parameters.

2.2.2. Applications of np-Cu

Np-Cu is a material with unique properties, making it suitable for various applications in the fields of sensing, energy storage and catalysis. Among the several advantageous properties of np metals, their intrinsic conductivity and high surface area make them excellent electrode materials for electrochemical sensors.[8,29,101-104] Their versatility as sensor materials lies in its tunable properties and surface functionalization. As a result, np-Cu shows to be promising material for a wide range of sensing applications, including the detection of substances like glucose[102], nitrite[101], glyphosate[29], and carbendazim[103]. Np-Cu also shows excellent properties as a substrate for Surface-Enhanced Raman Spectroscopy (SERS).[105-108] Furthermore, np-Cu foams[109,110] and Cu_xO on nanoporous Cu composites[111] shows to be high-performance electrodes for supercapacitors, offering several benefits like low-cost, the ability to operate under atmospheric conditions, and having minimal ohmic losses during cycling.[109,110] On the other hand, np-Cu is a promising anode for lithium ion batteries, such as np-Cu on Li foil[112], np Si/Cu composites[9], and tin-coated np-Cu[113].

The tunable properties and high reactivity of nanoporous copper make it a versatile material for catalytic applications, with the potential to contribute to the development of more efficient and sustainable chemical processes, such as methanol oxidation[31], hydrogenation of biomass-derived furfural to furfuryl alcohol[32], and the hydrogen evolution reaction in water splitting[114,115]. Np-Cu has been extensively studied for the electrochemical reduction of CO_2 to valuable chemicals and fuels, as it offers a substantial specific surface area and a multitude of under-coordinated sites.[116-122] The electrochemical CO_2 reduction reaction (CO_2RR) involves the cathodic reaction with the general form:

$$X\ CO_2 + n\ H^+ + n\ e^- \rightarrow Product + y\ H_2O \qquad \textbf{Equation (3)}$$

Whereas the anodic reaction is the hydrogen evolution reaction (HER):

$$2\ H_2O \rightarrow O_2 + 4\ H^+ + 4\ e^- \qquad \textbf{Equation (4)}$$

A wide range of products can be produced by CO₂RR including formic acid, carbon monoxide, methanol, methene, oxalic acid, acetic acid, acetaldehyde, ethanol, ethylene, ethane, propionaldehyde, and propanol.[43,123,124] Metal electrodes used for CO₂RR are generally classified based on their selectivity into four groups[43,125], shown in **Figure 7**.

- Group 1: Pb, Hg, Tl, In, Sn, Cd, and Bi produce primarily formate (HCOO⁻).
- Group 2: Au, Ag, Zn, Pd, and Ga produce primarily carbon monoxide (CO).
- Group 3: Ni, Fe, Pt, and Ti reduce very little CO₂ and instead almost exclusively reduce water to H₂.
- Group 4: Cu stands out in uniquely producing a number of hydrocarbons, aldehydes, and alcohols. Cu is thus the only pure metal that reduces CO₂ to products requiring more than two electron (>2e⁻) transfers with substantial Faradaic efficiencies.
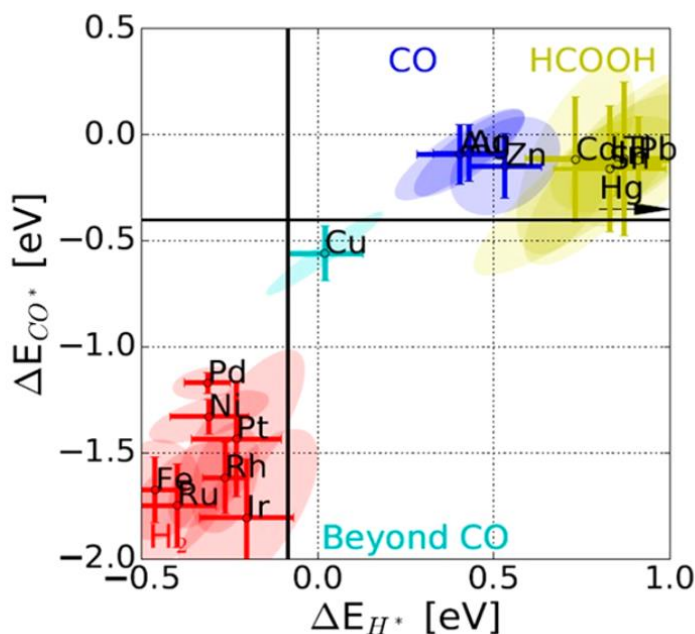
Figure 7: *CO₂ reduction metal classification. Four groups are identified: H₂ (red), formic acid (yellow), CO (blue) and beyond CO* (cyan). The black lines show the thermodynamics of adsorbed or none-adsorbed hydrogen (ΔG_H*=0, for ½ H₂↔H*) or CO (ΔG_CO*=0, for CO↔CO*). Figure reprinted from ref. 125.*

The splitting of the metals into these four groups has been explained as the result of their binding energy to key CO₂RR and HER intermediates, including *H, *OCHO,

*COOH, and *CO. The unique ability of Cu to reduce CO_2 to >2e⁻products may be due to the fact that it is the only metal that has a negative adsorption energy for *CO but a positive adsorption energy for *H (see **Figure 7**).[43,125] The binding energy of adsorbed CO (*CO) on Cu is proposed to be a key descriptor for reduction activity to >2e⁻products.[126,127] Moreover, studies have shown that CO adsorption on Cu suppresses the competing HER due to site blocking effects and changes in *H binding energy.[43,128] This inhibition prevents hydrogen evolution at these active sites, redirecting the electrochemical reactions toward the desired CO_2 reduction instead of hydrogen production.

The ability to reduce CO_2 to valuable hydrocarbons, aldehydes, and alcohols is of great interest, leading to extensive research efforts to better understand the reactivity of Cu and tuning it to achieve greater selectivity, stability, and efficiency.[129-133] Nanostructuring of Cu electrodes has been widely applied in attempts to improve selectivity and energy efficiency for CO$_2$RR.[117,118,121,134,135] For example, Yang et al.[134] tuned the C_2 chemical selectivity by systematically altering the morphology of Cu mesopore electrodes. The authors prepared Cu mesopore electrodes with controlled pore widths and depths by using a thermal deposition process onto a structured template. Pores of 30 nm diameter and 40 nm depth yield mainly C_2H_4 at −1.7 V vs NHE, whereas CH_4 is the main CO$_2$RR product on polycrystalline electrodes. However, electrodes with wider pores (300 nm pore width) give product distributions more similar to polycrystalline Cu. The authors attributed the increase in C_2 products for the electrodes with narrow pores to an increased local pH. Interestingly, as the pore depth was increased from 30 to 70 nm (keeping width 40 nm), the major C_2 product changed to the saturated hydrocarbon, C_2H_6. This change could be caused by re-adsorption and further reduction of the products due to the longer retention time in the catalyst layer.

Another study by Zeng et al.[118] investigated np-Cu films with a ligament size of 35 ± 6 nm for CO$_2$RR. The utilization of np-Cu results in doubling the current density of CO$_2$RR and the Faradaic efficiency of formic acid, compared to that of Cu foils. Increasing the ligament size to 63 nm after a post-annealing treatment leads to an increase of the Faraday efficiency toward formic acid from 29 to 45%. The authors suggest that this enhanced selectivity and Faraday efficiency could be attributed to the presence Cu_2O

formed after the post-annealing step.[116] On the other hand, Hoang et al.[121] reported the fabrication of np-Cu films prepared by electrodeposition of Cu on Au substrate with 3,5-diamino-1,2,4-triazole as additive. This material showed high activity for CO_2 reduction, resulting in facile production of ethylene and ethanol.

In a summary, the unique properties of np-Cu can enhance the selectivity and efficiency of CO_2RR, contributing to the development of sustainable energy conversion technologies. Moreover, these attributes make np-Cu a promising material for other applications in sensing, supercapacitors, and lithium ion batteries.

2.3. Electrosynthesis of cyclic carbonates

After exploring its unique properties and versatile applications, this section focuses on the application of np-Cu in the electrosynthesis of cyclic carbonates. Key concepts like organic electrosynthesis and CO_2 utilization will be introduced. Afterwards, the available literature regarding the synthesis of cyclic carbonates will be discussed.

2.3.1. Organic electrosynthesis

While the origins of electrosynthesis can be traced back to the mid-nineteenth century, with the pioneering contributions of Kolbe[136], it has recently entered a period of renewed expansion and development. This renaissance is driven by the increasing interest of intermittent renewable energy sources, which involves the use of local and temporary excesses of electric energy to produce value-added chemicals.[137] It also reflects the synthetic community's aspiration to transition toward more environmentally friendly and efficient methodologies.[138] Compared to the conventional methods for reduction and oxidation of organic compounds, electrochemistry provides several interesting features.[137-140] It enables the substitution of hazardous and toxic chemicals with electric current, which reduces the amount of generated waste and thereby promoting enhanced cost-effectiveness and environmental compatibility. Additionally, organic electrosynthesis generally takes place under mild conditions, such as atmospheric pressure and room temperature, making it inherently safe process. One of the most

famous examples of the application of organic electrosynthesis is the industrial-scale production of adiponitrile, a key ingredient used in the production of polyamides, such as nylon-6,6.[141] The Monsanto-Baizer process involves the cathodic hydrocoupling of acrylonitrile and currently affords over 300,000 tons per year of adiponitrile.[141,142] Other commercial and pilot electrochemical processes currently used within the chemical industry include the electrosynthesis of acetoin from butanone (BASF) and Calcium gluconate from glucose (Sandoz).[138]

There are two main operational modes to perform electrolytic conversions: galvanostatic (constant current) and potentiostatic (constant voltage).[140,143-145] In galvanostatic electrosynthesis, only two electrodes are required, one serving as the anode for oxidation processes and the other as the cathode for reduction processes. In this mode, a constant current is applied through the electrolyte using a galvanostat, acting as the power supply. Here, the potential of the reaction is not controlled. Initially, the substance with the lowest redox potential undergoes transformation. As time progresses, the starting material is gradually consumed, leading to a decrease in its concentration, while the product continues to form. At a certain point, the mass transport becomes insufficient, leading to an increase in the cell voltage. Continuing the electrolysis beyond this point may lead to the formation of undesired side products (over-electrolysis).[143,144] Galvanostatic operation is a simpler, cheaper, and easier approach compared to the potentiostatic mode.

On the other hand, potentiostatic electrosynthesis includes the use of a third electrode, a reference electrode, that provides a constant reference potential as a fix point. A potentiostat is employed to maintain a constant potential between the working and reference electrodes. The selected potential is usually set to a value 10–20% higher than the redox potential, to ensure a continuous transport of the starting material to the electrode. As the starting material is consumed over time, mass transfer to the electrode becomes the limiting factor. Consequently, the current gradually decreases and electrolysis process reaches its endpoint when the current falls below 5% of the initial current.[143,145] The potentiostatic method allows precise control of the reaction pathways, making it particularly useful for synthesizing complex organic molecules.

Organic electrosynthesis can be carried out in various types of electrochemical cells, depending on the specific requirements of the reaction and desired outcomes. The most common types of cells include the undivided and divided cells. In the undivided configuration, as shown in **Figure 8a**, the anolyte and catholyte are present within the same compartment without any physical barrier between them. This type of cell offers several advantages, including cost-effectiveness, simple design, lower internal resistance, and longer operational lifespan.[138,140] In some cases, the effectiveness of an electrolysis process can be hindered by an unavoidable reaction occurring at the other electrode, leading to issues like a significant reduction in yield or contamination of the desired product. To overcome this limitation, the use of a divided cell with two separate compartments (**Figure 8b**) is necessary. Usually, porous materials like sintered-glass frits or ion-exchange membranes are used to separate the two compartments. Divided cells introduce additional costs, additional seals, and potential maintenance issues.[138,144]
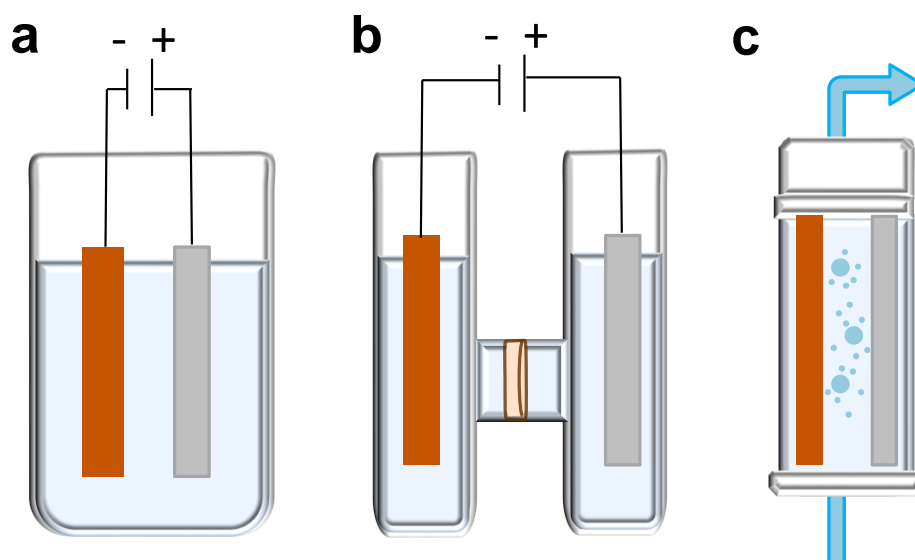
Figure 8: *Schematic representation of (a) undivided, (b) divided, and (c) flow cells for organic electrosynthesis. The blue arrow in (c) represents the flow of the electrolyte into and out of the cell.*

Recently, a third type of cells, the flow cell, **Figure 8c**, has gained interest both in academic and industrial laboratories.[146,147] It allows reactions to be carried out continuously as reactants are fed into the cell and products are removed, throughout the

process. Despite the need for extra electrical equipment and the associated additional costs, flow cells offer the advantage of enabling continuous synthesis under well-defined and standardized conditions. Additionally, flow cells provide the opportunity to reduce the quantities of solvents and starting materials, thereby lowering reagent costs, and minimizing waste generation compared to traditional batch electrosynthesis.[138,148,149]

The choice of electrode material is a crucial aspect of designing electrochemical processes. Ideal electrode materials should possess several key characteristics such as adequate electronic conductivity, corrosion stability, and selectivity.[138,150] However, predicting the best material based solely on theoretical concepts is challenging due to the complex nature of electrode processes.[150] Therefore, the selection of the most suitable electrode material is typically determined through empirical methods and experimentation. For example, Buckley et al.[151] investigated several cathode (Cu, steel, graphite) and anode (Mg, Al, Sn, Zn) materials for the reaction of styrene oxide with CO_2. Under their reaction conditions, Cu Cathode and Mg anode were found to be the optimal electrodes combination which gives the highest yields of styrene carbonates.

2.3.2. Carbon dioxide and its utilization

The carbon atom in CO_2 is in its most oxidized form resulting in a thermodynamically stable molecule, with a standard heat of formation of -394 $kJ \cdot mol^{-1}$. Therefore, CO_2 exhibits low reactivity, and a substantial amount of energy is needed to convert it into other chemical compounds. For the utilization of CO_2 as chemical feedstock, four strategies are suggested in the literature[152-154]: (i) using high-energy starting materials such as small ring compounds (e.g. epoxides), (ii) choosing oxidized low-energy synthetic targets such as organic carbonates, (iii) shifting the equilibrium to the product side by removing a particular compound, or (iv) supplying physical energy such as electricity. During the electrochemical reduction of CO_2, when one electron is transferred, it is transformed into a radical anion ($CO_2^{\bullet -}$). The radical anion has a bent geometry with an angle of 135° and the bond length is extended by approximately 0.08 Å compared to the neutral linear state, clearly indicating the weakening of the carbon-oxygen bond.[155,156] This highly reactive $CO_2^{\bullet -}$ has been identified as the key

intermediate state in many CO_2 transformation reactions such as carboxylation processes[156] or cycloaddition of CO_2 to epoxides[41,42].

Many chemical compounds are commercially produced from CO_2 such as urea, salicylic acid, cyclic carbonates, aliphatic polycarbonate, and methanol.[157,158] The first well-established method for the chemical utilization of CO_2 is urea production from carbon dioxide and ammonia (Bosch–Meiser process), which has been a commercial process since 1922.[157-159] The production of five-membered cyclic carbonates from CO_2 has been industrialized since the 1950s.[152] **Section 2.3.3** provides an overview of the conventional and electrochemical synthesis of cyclic carbonates from CO_2.

2.3.3. Conventional and electrochemical synthesis of cyclic carbonates

Cyclic carbonates are a class of organic compounds that contain a carbonate functional group arranged in a ring structure. They exhibit attractive features that make them a target of interest, including high boiling temperature, low toxicity, minimal odor levels, low evaporation rates, biodegradability, and solubility in a wide range of solvents.[160] Cyclic carbonates are widely used as polar aprotic solvents, green reagents, industrial lubricants, and precursors for polycarbonates.[34,35,160-162] Lately, cyclic carbonates have gained significant attention, particularly in the field of lithium ion batteries, driven by the growing popularity of electric vehicles. They are often employed as electrolytes in lithium ion batteries due to their favorable electrochemical stability, ion conductivity, and ability to form protective films.[163-165]

Cyclic carbonates can be produced by different routes, displayed in **Figure 9**. The reaction of diols with the high toxic carbonyl dichloride, known as phosgene, and ethylene glycol to produce ethylene carbonate (**Figure 9a**) was reported by Nemirowsky et al.[166] in 1883. Since then, several other routes have been discovered including the reaction of diols with dimethyl carbonates, urea, CO, and CO_2 (**Figure 9b – e**).[160] Other starting materials have been employed for the reaction with CO_2 such as halohydrins, propargyl alcohols, alkenes and epoxides (**Figure 9f – i**). However, among these chemical routes, the atom-economic addition of CO_2 to epoxides is currently the most attractive one, especially with respect to sustainability.[160] Catalysts are typically

necessary for the reaction between epoxides and CO_2 to proceed at a reasonable rate. The nature of the catalyst, as well as the specific epoxide and reaction conditions, significantly influence the selectivity between the two potential products of the CO_2-epoxide reaction: cyclic carbonates and polycarbonates. Consequently, the design and development of active and selective catalytic systems is a central topic of research in the domain of the conversion of CO_2 into cyclic carbonates. [33-35,160,161,167,168]
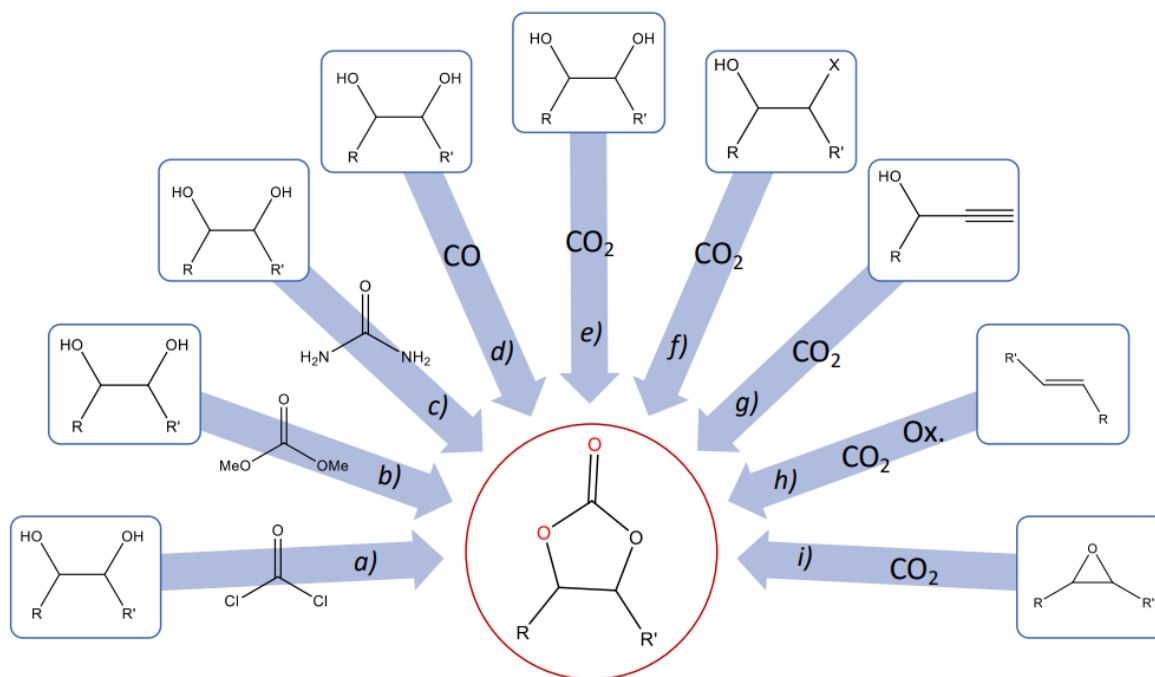
Figure 9: *An overview of the routes used to produce cyclic carbonate in the literature using the following starting materials (a) Phosgene, (b) dimethyl carbonate, (c) urea, (d) CO, and (e) CO_2 have been converted with diols to yield cyclic carbonates. Furthermore, (f) halohydrins, (g) propargyl alcohols, (h) alkenes and (i) epoxides have been used as starting materials for the coupling reaction with CO_2. Figure reprinted from ref. 160.*

The catalysts used for this reaction (e.g., metal complexes[36], metal organic frameworks (MOFs)[169], and silica-based catalysts[170]) typically demand harsh reaction conditions to function effectively, such as high CO_2 pressure (10 - 200 bar) and temperature (≥100 °C). These conditions reduce the sustainability of cyclic carbonate formation processes. Homogeneous catalysts also face significant challenges regarding the catalyst recovery, reusability, and product purification.[33-35] Consequently,

electrosynthesis presents a promising solution to overcome the shortcomings of conventional organic synthesis.

The first electrochemical synthesis of cyclic carbonates from CO_2 and epoxide under room temperature and atmospheric pressure was reported in 1955 by Tascedda and Duniich.[171] The study used a nickel(II) cyclam complex as a catalyst with stainless steel cathode, magnesium anode, dimethylformamide the solvent and potassium bromide as the supporting electrolyte. This was an attractive system for the synthesis of cyclic carbonates in mild conditions. Since then, several studies have explored this reaction using different electrode materials, electrolytes, and different epoxides as starting materials, where a catalyst is not required anymore. A summary of the literature is listed in **Table 2**.

Electrochemically, cyclic carbonates can be obtained through the coupling reaction between CO_2 and epoxides[38,151,172] or diols[45,46] whereas the reaction with alcohols[27,39] produces aliphatic carbonates. Zhang et al. reported a higher yield of cyclic carbonates when epoxides[173] were used as a starting material (86 – 95% yields) in comparison to diols (28 – 58 % yields)[174]. Furthermore, the choice of solvent has an impact on the yield. Acetonitrile performs well in electrochemical settings due to its high dielectric constant and it is a good solvent for CO_2 (0.27 M).[175,176] This was supported by Xiao et al.[172] who reported a higher conversion of epoxides to cyclic carbonates when acetonitrile was used as a solvent compared to dimethylformamide. Ionic liquids were also reported as electrolytes, substituting organic solvents with supporting electrolytes.[38,40,46] However, their use is not widely spread due to their high cost and viscosity.

Table 2: *Comparison of reported literature of electrosynthesis of cyclic carbonates. Table reprinted from the manuscript submitted to a journal.*

Starting material	Temp. (°C)	electrolyte	Cathode	Anode	Current density [mA cm^{-2}]	Charge [F mol^{-1}]	Yield of products		Ref
Epoxides (0.1 M)	RT	0.1 M TEAI-MeCN	np-Cu/GC	Mg	2.0	2.0	PC BC	62 ± 6 % 74 ± 4 %	This study
			Cu				PC BC	63 ± 5 % 76 ± 4 %	
			GC				PC BC	14 ± 3% 20 ± 3%	
Epoxides (0.067 M)	0	0.1 M TEAI-MeCN	SS	Mg	2.9	1.3	PC	70 %	172
Epoxides (0.1 M)	25	0.1 M TEAI-MeCN	Cu NP	Mg	3.0	2.5	PC BC	86 % 68 %	177
Epoxides (0.1 M)	25	0.1 M TEAI-MeCN	Ag NP	Mg	3.0	2.0	PC BC	70 % 57 %	178
Epoxides (0.15 M)	RT	0.1 M TEAI-MeCN	Cu/CS	Mg	4.1	2.0	PC BC	95 % 87 %	173
Epoxides	50	TBAB (1.0 eq.)-MeCN	Cu	Mg	-- [a]	-	PC	94 %	151
Epoxides (0.01 M)	RT	C$_4$MIMBF$_4$	Cu	Mg	-- [b]	-	PC	87 % [c]	179
Diols (0.15 M)	RT	0.2 M TEAI-MeCN	Cu/PC	graphite	12.2	1.0	PC BC	46 % [d] 47 % [d]	174
Diols (0.1 M)	50	C$_4$MIMBF$_4$	Ni	Mg	-- [b]	1.0	PC BC	4 % 12 %	46
Diols (0.1 M)	0	0.1 M TEAI-MeCN	Cu	graphite	17.2	1.0	PC BC	19 % [d] 44 % [d]	45
Diols (0.15 M)	25	0.1 M TBAI-MeCN	Cu	graphite	4.1	1.0	PC BC	21 % 23 %	39
Alcohol	50	C$_4$MIMBF$_4$	NPC-Ag	Pt	-- [b]	1.0	DC	80 %	27

Galvanostatic electrosynthesis in undivided cells using 1 atm CO_2 was used. [a] 60 mA was applied. [b] Potentiostatic electrosynthesis. [c] Conversion %. [d] Divided cell.

Starting material: [Epoxides] propylene oxide and 1,2-butylene oxides were used. [Diols] 1,2-propandiol and 1,2-butanndiol were used. [Alcohol] Methanol was used.

Electrolyte: [TEAI] Tetraethylammonium iodide; [TBAI] Tetrabutylammonium iodide; [TBAB] Tetrabutylammonium bromide; [C$_4$MIMBF$_4$] 1-Butyl-3-methylimidazolium tetrafluoroborate (ionic liquid).

Cathode: [np-Cu/GC] nanoporous copper (ligament size 115 ± 28 nm) on glassy carbon (Cu loading 1 mg cm^{-2}); [SS] Stainless steel; [Cu NP] Cu nanoparticles with particle size of 100 nm; [Ag NP] Ag nanoparticles with particle size of 100 nm; [Cu/Cs] Carbon sphere-loaded Cu nanoparticles with Cu loading of 8 wt%; [Cu/PC] Copper nanoparticles on porous carbon with Cu loading of 19.5 wt%; [NPC-Ag] Silver-coated nanoporous copper.

Cyclic carbonates PC: propylene carbonate, BC: 1,2-butylene carbonate, DC: (aliphatic) dimethyl carbonate.

Other reaction parameters are usually screened for choosing the optimal conditions, including the supporting electrolyte, current density, passed charge, and electrode materials. Sacrificial magnesium anodes and copper cathode materials have been widely used, giving higher yields of cyclic carbonates compared to other cathode materials such as stainless steel, nickel, or titanium.[38-40,180] Recently, nanostructured materials have been developed by some research groups in an attempt to improve the electrosynthesis of cyclic carbonates.[173,174,177,178] Yields between 31 and 86% of different cyclic carbonates were achieved on copper nanoparticles.[177] Moreover, Zhang et al.[173] reported higher yields of propylene carbonate on carbon sphere-loaded Cu nanoparticles (68%) compared to the sheets (44%).

To our knowledge, there is currently no literature available reporting the use of np electrode materials for the cyclic carbonate formation from epoxide and CO_2. However, np materials have been employed in other electrochemical reactions involving CO_2. For example, Wang et al.[27] applied a silver-coated np copper electrode in the CO_2 fixation to methanol in ionic liquid to produce (aliphatic) dimethyl carbonate with a yield of ~80% compared to silver sheet (yield of ~59%).

The reaction pathway of epoxide with CO_2 has not been fully understood. It is suggested that CO_2 activation is necessary for the reaction with epoxides to take place in ambient conditions. This assumption is drawn from experiments in which cyclic carbonates were not detected when the electrolysis was carried out in the absence of external current or potential.[42,46,172] It is proposed that the activation process involves the electro-reduction of CO_2 to form the $CO_2^{\bullet-}$ radical anion.[39,41,172] Distortion of the commonly linear structure of neutral CO_2 towards a bent structure of the radical anion results in a pronounced activation at the electrophilic center of CO_2, consequently enhancing the efficiency of the reaction with epoxide.[42]

Pérez-Gallent et al.[41] performed Fourier transform infrared spectroscopy (FTIR) investigations to explore the rate-limiting step for the synthesis of propylene carbonate on copper electrodes. First, propylene oxide was reduced at –2.5 mA (–2.86 V vs Ag/AgClO$_4$) for 30 minutes. This conditioning step was expected to activate the epoxide and thus lead to the opening of the ring. Then, CO_2 was introduced in the

electrochemical cell (at a current of –0.5 mA at which no propylene carbonate was observed in previous experiments) and absorbance spectra were recorded every 4 minutes for 45 minutes. If the activated propylene oxide was the active species, propylene carbonate should form directly after the addition of CO_2. However, the absence of the band at 1800 cm^{-1} (corresponding with propylene carbonate) when a mild reduction current was applied with CO_2 present in solution, suggests that the reductive ring opening is not a critical step but rather that CO_2 needs to be activated. When a higher current is applied in the presence of CO_2 and propylene oxide, propylene carbonate was formed. These experimental findings suggest that under electrochemical conditions the reaction pathway starts with the activation of CO_2. Therefore, the authors suggest the electroreduction of CO_2 to $CO_2^{\bullet\,-}$ as a key step for the formation of propylene carbonate.

Similarly, theoretical and experimental investigations by Xiao et al.[172] suggest the activation of CO_2 to be the first step of the reaction of epoxides with CO_2. The authors propose that the formed radical anion $CO_2^{\bullet\,-}$ is stabilized via the coordination of its oxygen atom to Mg^{2+} (from the sacrificial Mg anode) and Br^- (from the supporting electrolyte tetrabutylammonium bromide, TBAB). The formed intermediate **I** (**Figure 10**) reacts with the epoxide (**II**), leading to opening of the ring and insertion of CO_2 (**III**, **IV**, **V**). The ring closure of **VI**, leads to the formation of the product **VII** through intramolecular nucleophilic replacement of bromine atom by a negatively charged oxygen atom.
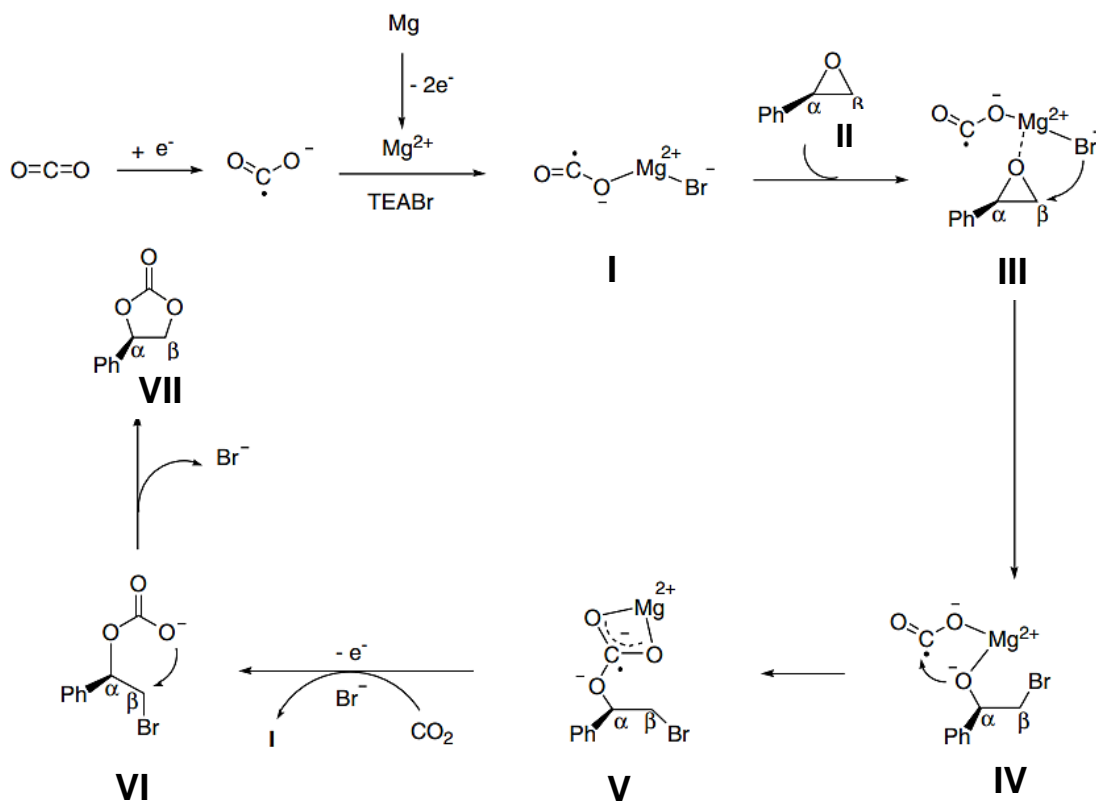
Figure 10: *Proposed mechanism for the synthesis of cyclic carbonates from CO_2 and R(+)-styrene-oxide according to Xiao et al.172.*

Gallardo-Fuentes et al.[42] conducted DFT calculations to theoretically investigate the propylene oxide reaction with CO_2. The study explored the activation of CO_2 by potentiostatic electrolysis (applying a potential of –2.4 V vs Ag/AgCl), incorporation of Mg cations from a sacrificial Mg anode in the electrolyte, and the utilization of the ionic liquid 1-butyl-3 methylimidazolium bromide $[C_4C_1Im][Br]$ as electrolyte. Two possible scenarios were investigated to simulate the ring opening step of the epoxide, shown in **Figure 11a**. The first model (**TS1-C$_4$C$_1$Im**) examines the interaction between the epoxide, the $[C_4C_1Im]^+$ cation, Br$^-$ and CO_2. This pathway involves an energy barrier to open the epoxide of 27.5 kcal/mol. The second scenario (**TS1-Mg**) considers the interaction between the epoxide in the presence of Mg^{2+}, Br$^-$ and CO_2, with an energy barrier of 6.8 kcal/mol to open the epoxide. The energetically preferred pathway,

indicated by **TS1-Mg**, highlights the influence of the ionic liquid's anion as a ring-opening agent and the Lewis acid Mg^{2+} as the catalyst.
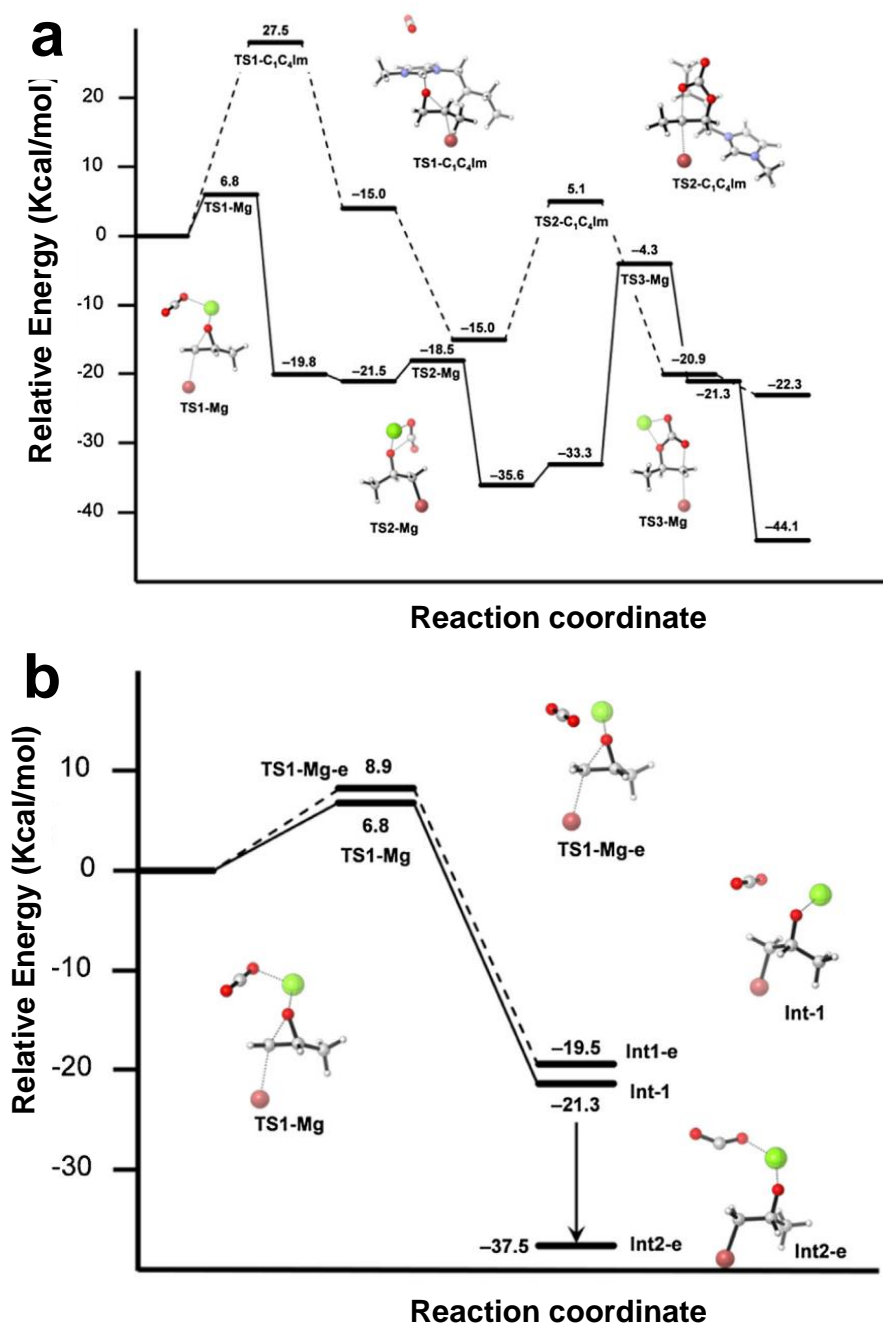
Figure 11: *Free Energy Profiles (a) for the cycloaddition between CO_2 and propylene oxide catalyzed by Mg^{2+} (solid line) and $[C4C1Im]^+$ cation (dashed line), (b) for the reaction between CO_2 and propylene oxide catalyzed by Mg^{2+} with an extra electron ($CO_2^{\cdot -}$ solid line) and without an extra electron (neutral linear CO_2 dashed line). Figure reprinted from ref. 42.*

To understand the influence of overpotential on the ring opening stage, the process was simulated both with and without the introduction of an additional electron. The reaction barriers for these stages were found to be 6.8 kcal/mol for **TS1-Mg** (ring opening without an extra electron) and 8.9 kcal/mol for **TS1-Mg-e** (ring opening with an extra electron). The free energy profile in **Figure 11b** indicates that intermediates **Int-1** and **Int1-e** exhibit similar energy levels, maintaining a linear CO_2 structure. However, the relevant difference appears when $CO_2^{\bullet\,-}$ is in its bent configuration, because in this case the energy of **Int2-e** is almost 17 kcal/mol lower. This outcome reinforces the significance of overpotential (the additional electron in the calculation) in the reaction, facilitating the formation of an electrophilically activated $CO_2^{\bullet\,-}$ species. In this context, the overpotential's role is crucial in bending the CO_2 molecule, thereby stabilizing the system and promoting the nucleophilic attack of oxygen to carbon, subsequently leading to the ring closure steps.[42,172]

The DFT calculations of Gallardo-Fuentes et al.[42] shows that the ring closing as the rate determining when the system is coordinated by Mg^{2+} and it is favored by 5 kcal/mol in the simulation, in the presence of applied overpotential. This is in contrast with the findings from Pérez-Gallent et al.[41] and Xiao et al.[172] that the CO_2 activation is the rate-limiting step of the reaction. Based on their findings, Gallardo-Fuentes et al.[42] proposed the reaction pathway of CO_2 with propylene oxide shown in **Figure 12**.

Although Gallardo-Fuentes et al.[42] and Xiao et al.[172] agree that Mg^{2+} and Br^- are necessary for the reaction to proceed, they propose different intermediates that facilitate the ring opening of the epoxide. Xiao et al.[172] suggest that intermediate **I** (**Figure 10**) formed from the radical anion $CO_2^{\bullet\,-}$, Mg^{2+} and Br^- is responsible for the ring opening, whereas Gallardo-Fuentes et al.[42] propose that the halide species from the ionic liquid or supporting electrolyte (e.g., Br^- from TBAB) are responsible for the ring opening, while Mg^{2+} facilitates this process (**I − II, Figure 12**). CO_2 is activated to form $CO_2^{\bullet\,-}$, which attacks the already open epoxide (**III**) and the product (**IV**) is formed by ring closure. Further investigations are required to gain a deeper understanding of the reaction pathway and identify the intermediates involved.
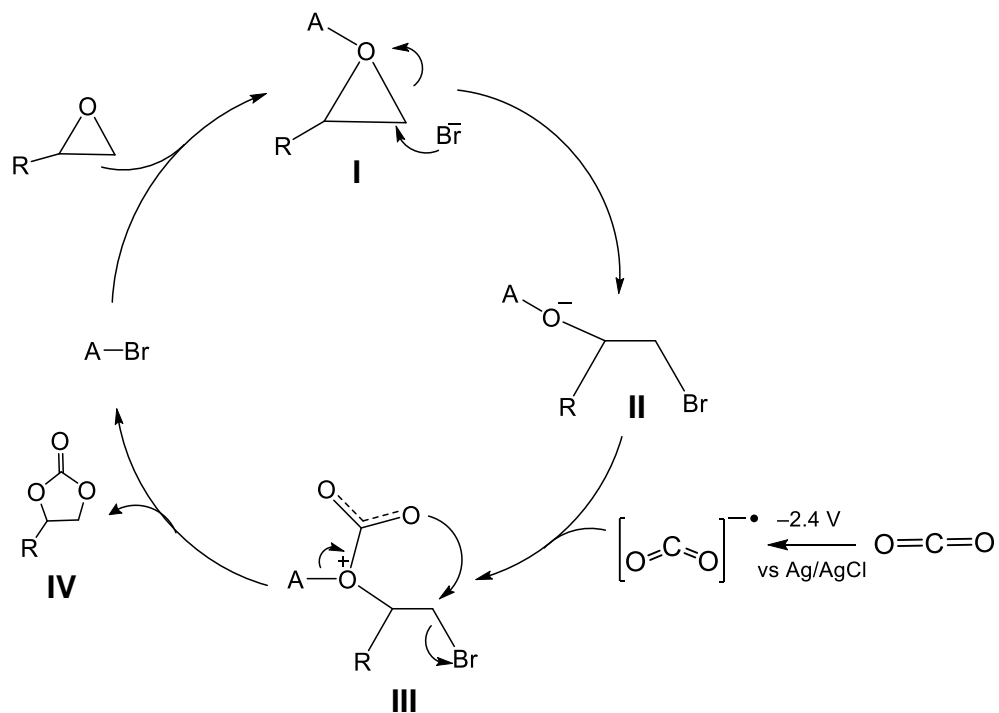
Figure 12: *Proposed mechanism for the reaction of CO$_2$ with propylene oxide according to Gallardo-Fuentes et al.[42]. The species "A" is a general Lewis acid such as Mg^{2+} from the sacrificial Mg anode.*

3. Experimental Procedures

3.1. Samples preparation

3.1.1. Fabrication of $Zn_{80}Cu_{20}$ alloy ribbons

The master alloy ribbons were prepared via melt-spinning technique using an Edmund Buehler Melt-spinner SC (**Figure 13**). Melt-spinning is a rapid solidification process, in which molten metals are expelled out onto a cold rotating wheel to form ribbon-shaped alloys.[181] First, the chamber was evacuated to 10^{-3} mbar and then filled with Ar (99.995%, Nippon Gases) to a pressure of 0.4 bar, to prevent the oxidation of the starting materials. The metals, pure copper (99.99%, Alfa Aesar) and zinc (99.9%, Alfa Aesar) foils, were then inductively melted in a quartz glass crucible at ~850 K for one minute. This temperature was chosen to avoid any Zn evaporation.
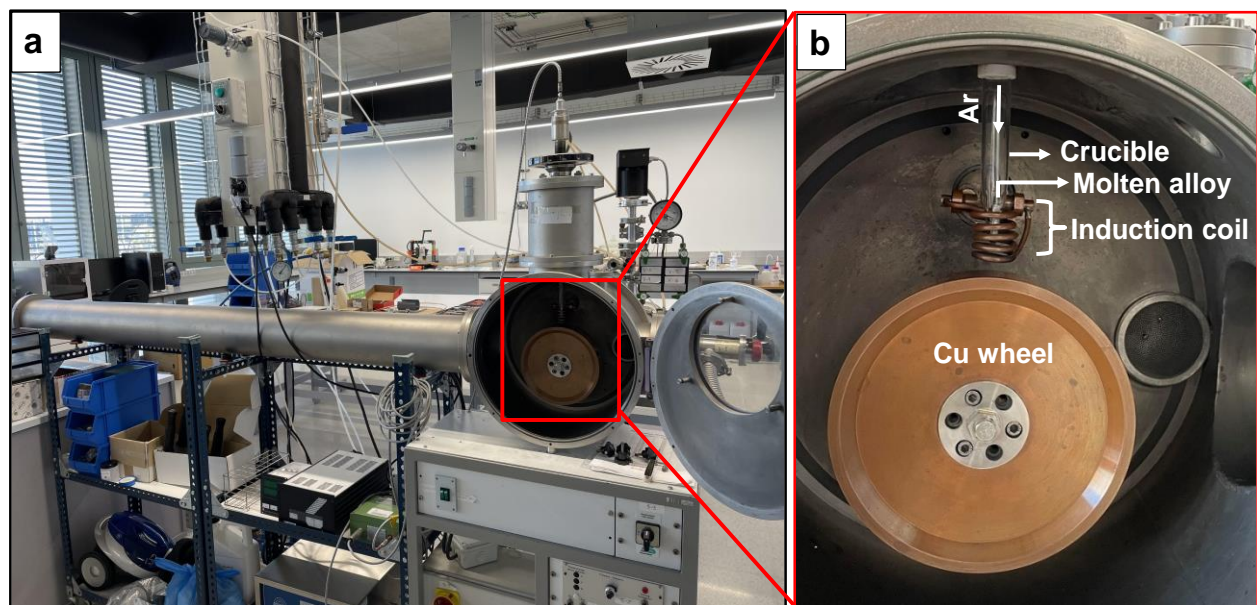
Figure 13: *(a) The melt-spinner device used in this study to fabricate $Zn_{80}Cu_{20}$ master alloy ribbons. (b) A zoom-in of the chamber, consisting of an argon gas inlet, quartz glass crucible, where metals are molten by an induction coil, and a rotating copper wheel.*

In the next step, 5 -10 g of the melt was pressed out of the crucible onto a rotating copper (Cu) wheel. When it hits the wheel, the melt rapidly solidifies at cooling rates of $10^5 - 10^6$ K s^{-1}, forming alloy ribbons. The geometric dimensions of the formed $Zn_{80}Cu_{20}$ ribbons are 4 –10 cm long, 2 – 3 mm wide, and 35 ± 3 µm thick, respectively. The master alloy was prepared and supplied by Dr. Daniel Crespo at the Polytechnic University of Catalonia, Barcelona, Spain.

3.1.2. Chemical dealloying of $Zn_{80}Cu_{20}$ alloy ribbons

The $Zn_{80}Cu_{20}$ alloy ribbons were chemically dealloyed under free corrosion to form nanoporous copper (np-Cu). First, the pristine ribbons were cleaned with highly purified water (18 MΩ cm at room temperature, ElgaPureLab Classic) and propan-2-ol (99.5%, Fisher Scientific) using an ultra-sonication bath. The dealloying electrolytes were 0.1 M hydrochloric acid (HCl), 5 M and 15 M phosphoric acid (H_3PO_4), and 1.3 M sodium hydroxide (NaOH). The electrolyte solutions were prepared by diluting 37% HCl (ACS reagent, VWR Chemicals), 85 wt.% H_3PO_4 (99.99%, Merck) or by dissolving the respective amount of NaOH pellets (99.99%, Alfa Aeser) in highly purified water, respectively. All solutions were saturated with Ar (99.999%, Air Liquide) for at least 30 min before starting the dealloying process.

Ribbons were chemically dealloyed in 25 mL vials under Ar atmosphere at 25°C using a bath thermostat (Lauda, ECO RE620), as shown in **Figure 14**. To investigate the effect of the dealloying temperature on the nanoporous structure, the dealloying in HCl was carried out at 15, 25, and 50 °C. Only in 1.3 M NaOH, the ribbons were attached to a Cu foil (0.1 mm thick, 99.999%, Alfa Aesar), using a Cu wire (99.999%, 1 mm diameter, Alfa Aesar), to accelerate the Zn dissolution (**Figure 14b**). As Zn dissolution occurs during the dealloying process, hydrogen evolution reaction (HER) takes place concurrently on the cathodic site. The hydrogen bubble formation on the sample surface is illustrated in **Figure 14 a´– b´**. Samples were taken out from the solution after different dealloying times (3.5, 8, 24, 48, 72, 168, and 312 h in 0.1 M HCl and 1.3 M NaOH; 3, 5, and 7 h in M and 15 M H_3PO_4). The dealloyed ribbons were washed with highly purified water and propan-2-ol, dried in Ar atmosphere and immediately used for further investigations or

stored in vacuum to avoid air oxidation. All experiments were repeated at least three times.
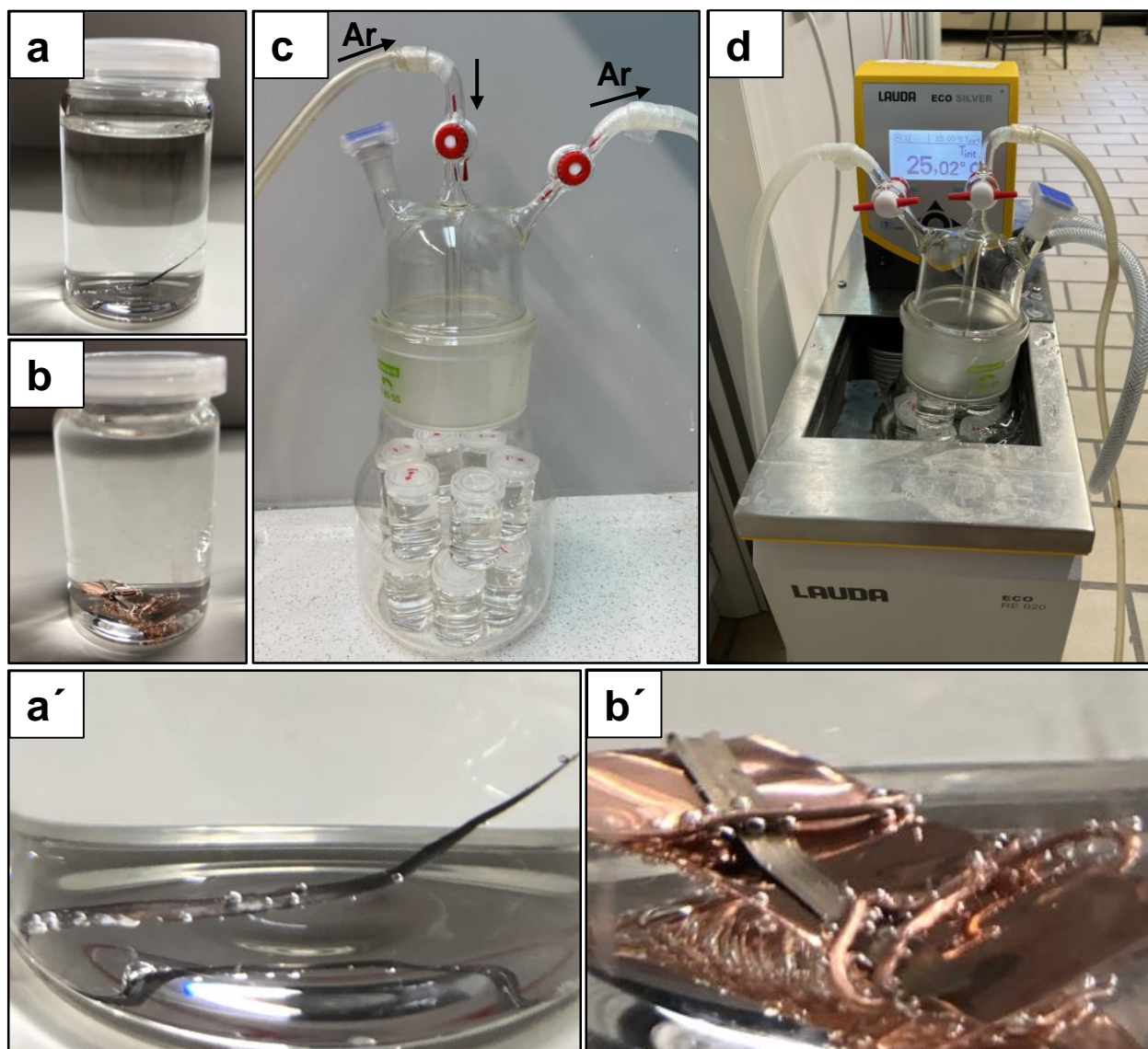
Figure 14: *Setup of the dealloying process, showing the ribbons immersed in vials containing (a, a´) solutions of HCl, H_3PO_4, or (b, b´) NaOH and the hydrogen bubbles formation during the dealloying process; (c) the vials placed in a glass container under an argon atmosphere; (d) the container positioned in a thermostat to maintain a constant temperature of 25°C throughout the dealloying. The image in (b´) was reprinted with permission from ref. 52.*

3.1.3. Drop-casting of np-Cu ribbons on glassy carbon (GC)

A dop casting technique was utilized to prepare a practical electrode, consisting of a thin film of np-Cu ribbons coated on a glassy carbon (GC) plate. This electrode is referred to as np-Cu/GC. The preparation steps are displayed in **Figure 15**. First, a GC plate (dimensions 35 x 20 x 2 mm) was polished with 0.05 µm of aluminum oxide powder (Buehler, Germany) onto a Microcloth polishing paper (Buehler, Germany, #423710). The GC plate was cleaned with highly purified water and propan-2-ol. Second, a dispersion was prepared by mixing and horn sonication (Branson SFX 250 Sonifier) of 8 mg of np-Cu ribbons and 1 mL of propan-2-ol (99.5%, Fisher Scientific) for 20 minutes. To avoid heating the sample, the vial was put in a beaker filled with ice during horn sonication.
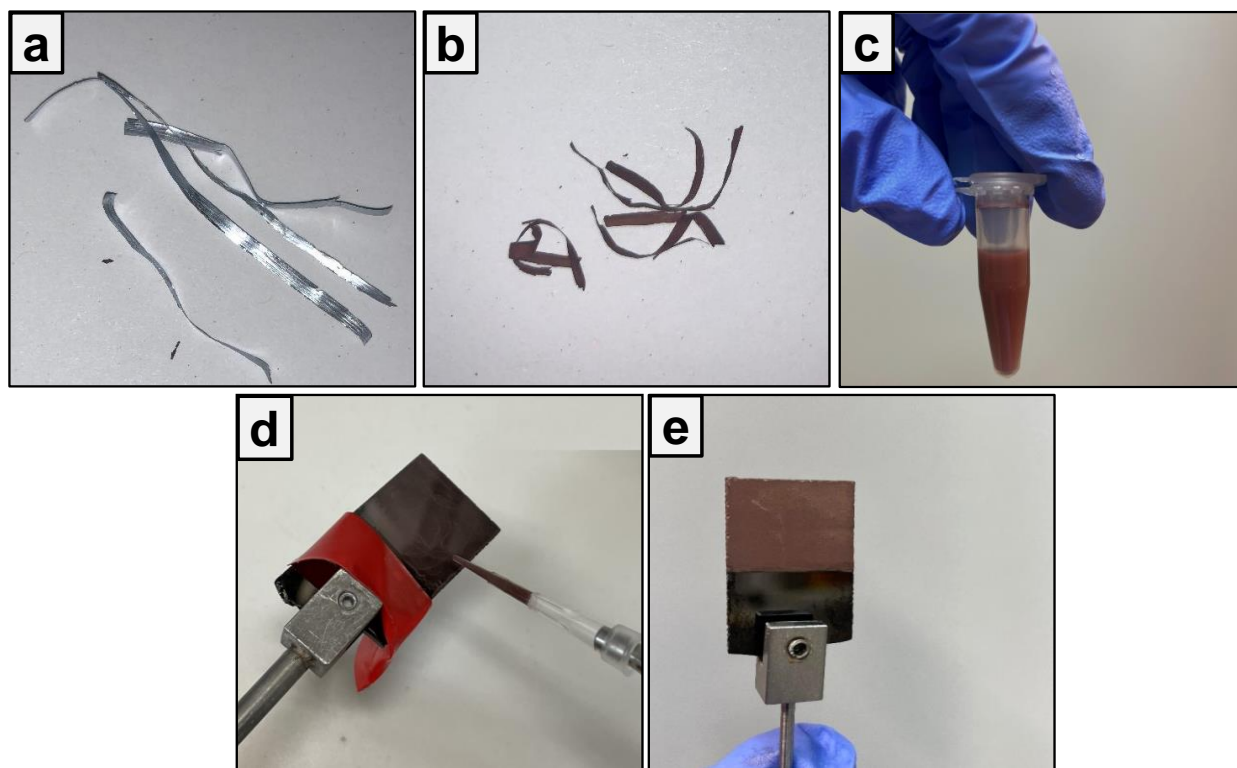
Figure 15: *Preparation steps of the drop-casted np-Cu material on the GC substrate. (a) $Zn_{80}Cu_{20}$ alloy ribbons; (b) np-Cu ribbons after chemical dealloying; (c) suspension of np-Cu material in propan-2-ol after horn sonication; (d) drop-casting of the np-Cu on GC plate under argon; and (e) the resulting np-Cu/GC electrode. Figure reprinted from the manuscript submitted to a journal.*

Subsequently, 10 µL of the dispersion was uniformly pipetted onto the surface of the GC plate and dried at room temperature under Ar. This process was repeated until a loading of 1 mg cm$^{-2}_{geo}$ (per geometric surface area) Cu on GC was achieved. The np-Cu/GC was directly used as a cathode for electrolysis or stored in vacuum to avoid air oxidation. When the np-Cu/GC was reused after electrolysis, it was immersed in concentrated phosphoric acid (85 wt.% H_3PO_4) for 5 seconds as a chemical polishing step, washed with highly purified water and propan-2-ol, and dried under Ar.

3.2. Physicochemical characterization

3.2.1. Scanning Electron Microscopy with Energy-dispersive X-ray Spectroscopy (SEM-EDX)

The structure and morphology of pristine and dealloyed ribbons as well as np-Cu/GC were investigated using a Helios NanoLAB 600i SEM operated at an accelerating voltage of 5 kV and a current of 0.17 nA. For top-view SEM images, aluminum flat FIB pin mounts (12.7 mm diameter) were used to secure the samples (**Figure 16a**).
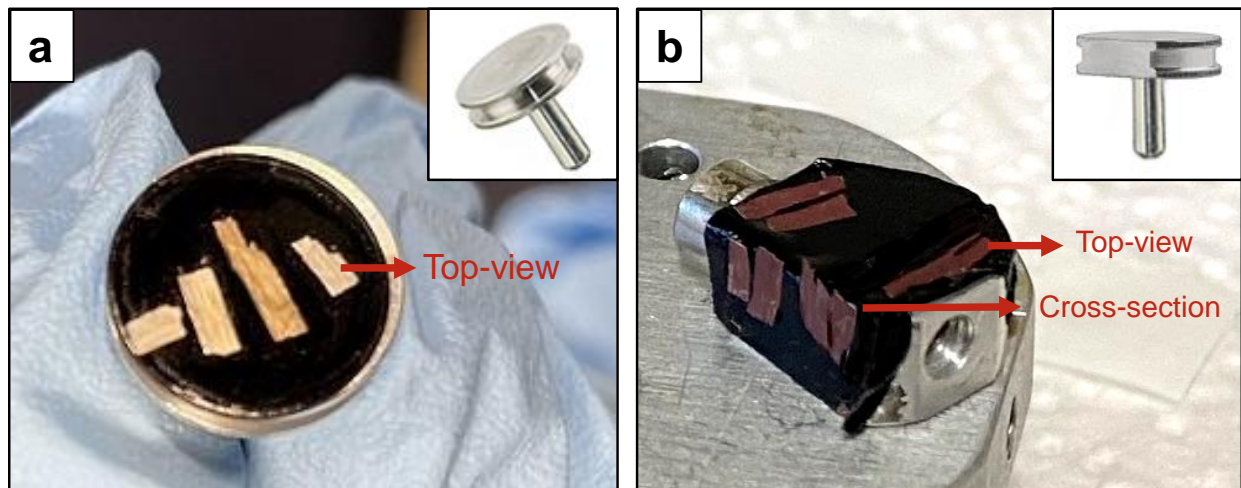
Figure 16: *Sample holders used for SEM measurements. (a) Flat FIB pin mounts for top-view, and (b) 90° FIB pin mounts for cross-section investigations. The flat surface of the 90° pin mounts was simultaneously used for top-view analysis.*

The samples were fixed to the FIB mounts using adhesive carbon tape. The cross-section acquisitions were carried out by putting the samples vertically on a 90° FIB pin

mount so that the cross-section of the samples was parallel to the optical zone of the beam (**Figure 16b**). Micrographs were acquired at a working distance of 4.0 mm and a dwell time of 30 µs. Sample areas were imaged in a magnification range from 1,500x to 200,000x.

ImageJ 1.46r software was then used to establish the ligament sizes of np-Cu ribbons from several SEM micrographs. Ligament size was measured at a minimum magnification of 80,000 kx, with the width of ligaments measured at 1 – 4 positions (**Figure 17a**). Very thin bridges between ligaments, or ligaments that were covered by other ligaments by more than 30 % were excluded from the measurements (**Figure 17b – c**). The mean ligament size was estimated by analyzing more than 200 arbitrary ligaments from at least three different dealloyed samples.
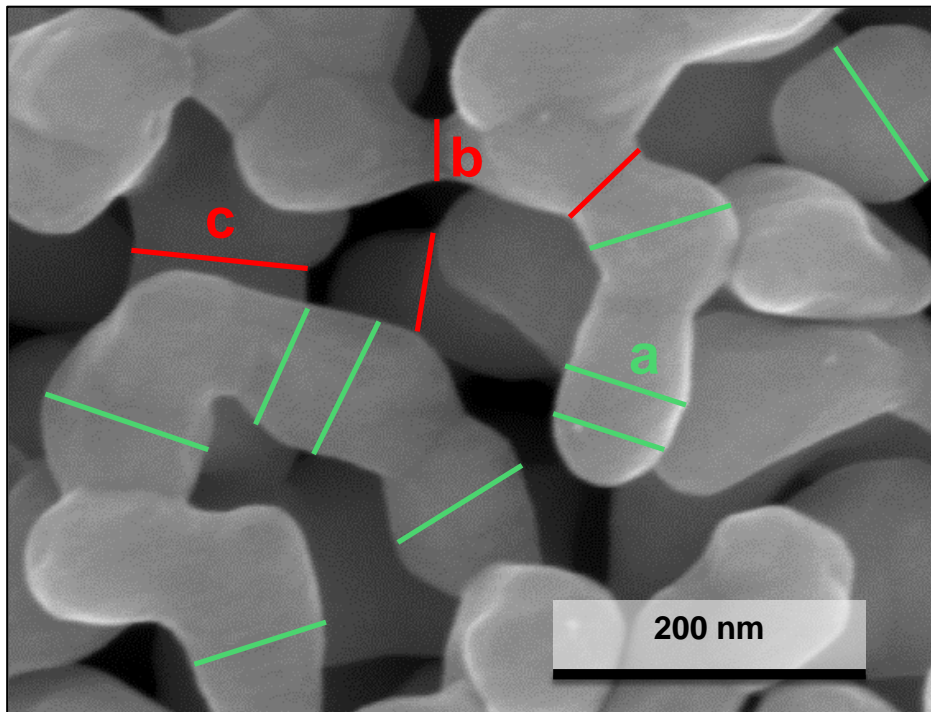
Figure 17: *SEM micrograph of np-Cu at a magnification of 150,000 kx, showing the estimation of ligament size. (a) The measured width of the ligaments is represented by green lines, while unmeasured distances are indicated by red line, including (b) thin bridges, and (c) covered ligaments, respectively.*

The coverage of np-Cu on the GC surface was evaluated using the thresholding method in ImageJ 1.46r software. In the context of this study, the coverage refers to the

percentage of the surface area occupied by np-Cu (ligaments) relative to the total surface area analyzed. SEM micrographs of np-Cu/GC at magnifications of 1,200x, 3,500x, and 6,500x were used for the analysis. In greyscale images, intensity values of 0 and 100 % represent pure black and white, respectively. Therefore, pixels with intensities below threshold values of 45, 52, and 60%, representing the black GC substrate, were replaced by red pixels. The area percentage of np-Cu ligaments and the GC background were then estimated for each threshold value. The mean coverage of np-Cu/GC was calculated from three samples.

Applying too low or too high threshold values would lead to incorrect estimation of the coverage. The impact of using different threshold values (20, 52 and 80%) on the estimation of coverage is highlighted in **Figure 18**. Applying too low threshold values (**Figure 18b**) leads to the inclusion of parts of the background in the estimation of the np-Cu area, resulting in an overestimation of the coverage. Conversely, too high threshold values (**Figure 18d**) lead to an underestimation of the coverage, where parts of the ligaments are incorrectly measured with the background. The coverage of np-Cu/GC for this SEM image was estimated as 78, 65, and 43 % for threshold values of 20, 52, and 80%, respectively. Therefore, the middle values of 45, 52, and 60 % were shown to give the best separation of the grey ligaments from the black background and were used in this study.

The chemical composition of pristine and dealloyed ribbons was investigated using a Helios NanoLAB 600i SEM equipped with an Apollo 10 EDX detector (EDAX AMETEK) and Everhart-Thornley secondary electron detector. The microscope was operated at an accelerated voltage of 20 kV, and a beam current of 0.34 nA. The magnification was set 15,000 kv to measure sample area of approximately 85 μm^2. The acquisition time for each EDX spectrum was about 60 seconds. The characteristic intensities of the K line for O, Cu, and Zn at 0.525, 6.924 and 8.630 keV were evaluated, respectively. The chemical composition was calculated from at least three spectra measured on different positions for at least three samples.
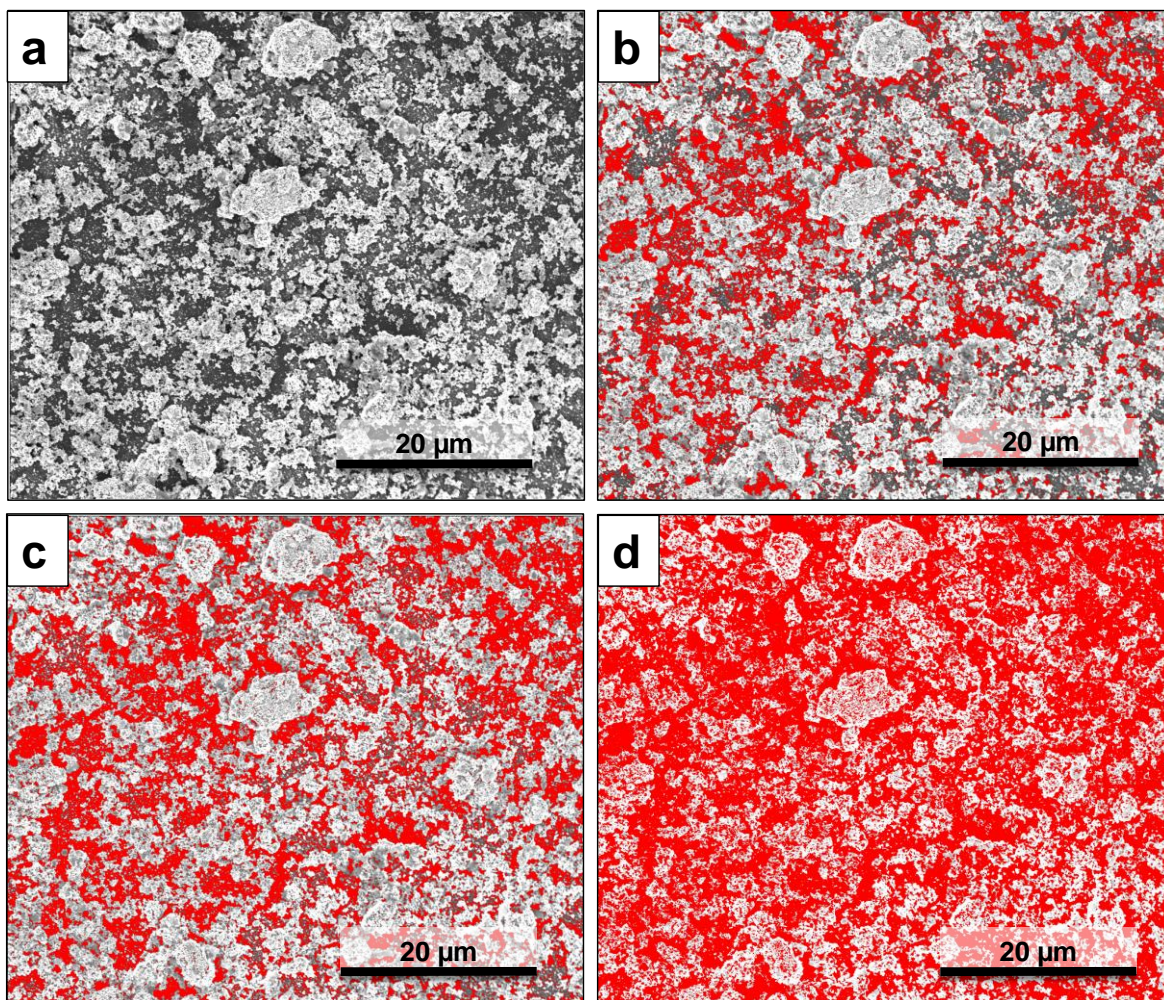
Figure 18: *Estimation of coverage of np-Cu/GC by the thresholding method in ImageJ 1.46r software. (a) SEM micrographs of np-Cu/GC, where a threshold value of (b) 20 %, (c) 52%, and (d) 80 % were used for the adjustment of the background.*

3.2.2. (Scanning) Transmission Electron Microscopy with Energy-dispersive X-ray Spectroscopy ((S)TEM-EDX)

The morphology and chemical composition of np-Cu ribbons at higher magnification was investigated by JEOL JEM2100F microscope equipped with an Oxford INCA Energy TEM250 EDX system with a Silicon Drift Detector (SDD). Np-Cu (1 mg) was dispersed in propan-2-ol (4 mL) by horn sonication for 30 minutes. Then, 5 µL of the dispersion was pipetted on a holey carbon film coated TEM grid (EMS, 300 mesh) and dried at room temperature in air. The TEM images were taken at an accelerating voltage of 200 kV. To better understand the elemental distribution within the ligaments, EDX elemental

mappings of sample areas of up to 1 µm^2 were performed and evaluated using INCA 5.03 software (Oxford Instruments).

3.2.3. X-ray Diffraction (XRD)

To analyze the crystallinity and crystal phases of the pristine and dealloyed ribbons, an X-ray diffractometer Empyrean (PANalytical) equipped with a Cu tube, Bragg-Brentano unit, soller and PIXcel^{1D} detector was employed. The setting parameters were as follows: 2 θ range from 10° to 90°, step size of 0.03°, counting time of 900 s, sample spinning time of 2 s, and total acquisition time of 3 h. The ribbons were positioned on a self-made Plexiglas disc with a centered depth of 1 mm and a diameter of 10 mm.

Data processing and evaluation were performed by Rietveld analysis using TOPAS version 5.0 software. The background was fitted using Chebychev polynomial function, order 5. The crystallographic phases of the samples were identified by utilizing reference patterns of $Zn_{80}Cu_{20}$ (Space group P6$_3$/mmc, ID: #1524894), $Cu_{38}Zn_{62}$ (Space group I-43m, ID: #1100057), and Cu_2O (space group Pn-3m, ID: #1000063) from the International Centre for Diffraction Data (COD)[182]. The quality of the fit between the calculated and experimental XRD patterns was expressed by weighted profile residual (Rwp) values.

3.2.4. X-ray Photoelectron Spectroscopy (XPS)

The surface composition and chemical state of Zn and Cu species in the pristine and dealloyed ribbons were characterized using an ESCLAB 250 Xi spectrometer (Thermo Fisher). The XPS spectra were collected with monochromatic Al Kα radiation with a photon energy of 1486.6 eV. Survey spectra were collected from 0 to 1350 eV with pass energy of 100 eV and resolution step of 1 eV. Experimental parameters for the acquisition of high resolution XPS spectra of C 1s, O 1s, Cu 2p, and Zn 2p as well as Auger spectra of Cu and Zn LMM are summarized in **Table 3**. An Ar ion source (MAGCIS, Thermo Fisher) was used to sputter a geometric surface area of

approximately 2.25 mm^2. Samples were introduced for a short time and not heated to avoid contamination during XPS measurements and sputtering processes.

Table 3: Experimental acquisition parameters for survey and high-resolution spectra for XPS investigations of $Zn_{80}Cu_{20}$ alloy ribbons. Table reprinted with permission from ref. 52.

XPS line	Pass energy [eV]	Number of scans [a.u.]	Dwell time [ms]	Energy step size [eV]
survey	100	10	10	1
C 1s	10	10	50	0.02
O 1s	10	10	50	0.02
Cu 2p	20	30	50	0.035
Cu LMM	20	50	50	0.025
Zn 2p	10	10	50	0.035
Zn LMM	20	10	50	0.02

To determine the elemental depth profile of $Zn_{80}Cu_{20}$ alloy ribbons, a sequence of depth profile measurements was conducted. The measurement sequence consisted of three sputter cycles at 2 kV for 30 s, followed by 5 sputter cycles at 4 keV for 120 s, and finally one cycle at 4 keV for 300 s. The increase in local temperature on the sputtered area of the samples under vacuum accelerates the volatilization rate of Zn. This is related to the differences in temperature dependence of the saturated vapor pressures of zinc and copper.[183-185] For this reason, results from the XPS depth profiles of pristine ribbons were corrected by the standard deviations calculated from commercial ZnCu alloy (Alfa Aesar, Brass foil alloy 260, Cu 69 %, Zn 31%). The commercial alloy showed experimental composition of 84.3 at.% and 15.7 at.% Cu and Zn, respectively (**Figure 19**).

Being a surface sensitive analysis method, XPS was also employed to investigate the formation of a lead monolayer on the surface of np-Cu/GC following an underpotential deposition of lead (Pb-UPD) experiment. After disposition of Pb monolayer, the electrode was washed with highly purified water and propan-2-ol, dried under Ar, and directly measured. The experimental parameters for the acquisition of high resolution XPS spectra of C 1s, O 1s, Cu 2p, Zn 2p, and Pb 4f are summarized in **Table 4**. Data

analysis for all XPS data was performed by Avantage software (Thermo Fischer Scientific, version 5.9911).
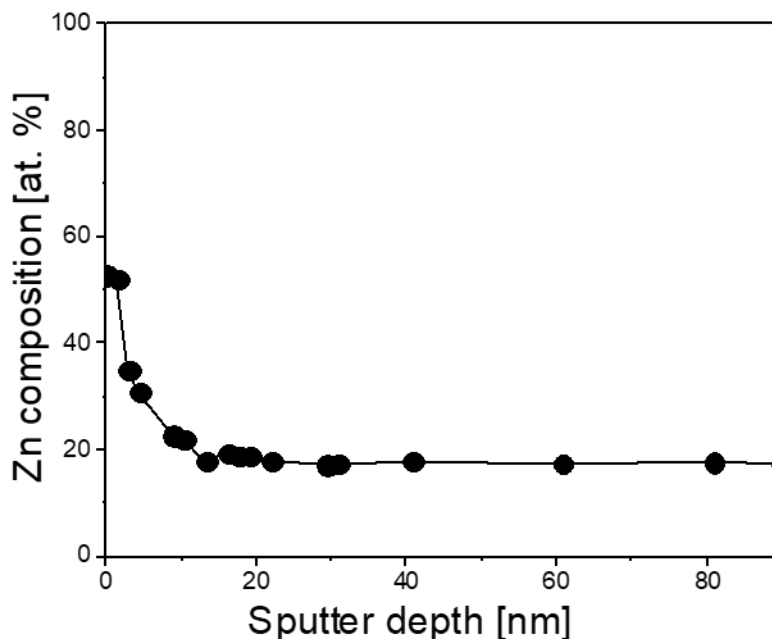
Figure 19: *XPS sputter depth profile of commercial ZnCu alloy (69.4 at.% Cu and 30.5 at.% Zn) up to 90 nm showing the standard deviation of measured composition (84.3 at.% Cu and 15.7 at.% Zn) due to the sputter process and different sublimation temperatures of Zn and Cu. Figure reprinted with permission from ref. 52.*

Table 4: *Experimental acquisition parameters for the survey and high-resolution spectra for XPS analysis of np-Cu/GC after Pb-UPD deposition.*

XPS line	Pass energy [eV]	Number of scans [a.u.]	Dwell time [ms]	Energy step size [eV]
survey	100	10	10	1
C 1s	10	5	50	0.02
O 1s	20	10	50	0.02
Cu 2p	20	30	50	0.035
Zn 2p	20	20	50	0.035
Pb 4f	20	40	50	0.02

3.2.5. Raman spectroscopy

To investigate the chemical state of Cu of different samples, Raman spectroscopy measurements were carried out. Raman mappings were acquired using an alpha300 RSA Raman Imaging Microscope (WITec), equipped with a 532 nm laser, a 600 l/mm grating, and a Zeiss EC Epiplan-Neofluar Dic 50x / 0.8 objective. A spectrum was recorded with an integration time of 2 s every 1 µm. Mappings were collected for a total area of 200x200 µm for np-Cu/GC and 100x100 µm for np-Cu ribbons and polycrystalline Cu foil. The measured spectra were processed in the Witec Project FIVE 5.2 software for cosmic ray removal and baseline subtraction. Spectra were then fitted using Gauss peak fitting function, and Raman peak areas at 218 cm^{-1} and 295 cm^{-1} were used for the estimation of Cu(I) and Cu(II) species, respectively. The ratio of Cu(I) to Cu(II) was calculated for every spectrum, and a mean value was established for the whole mapping area.
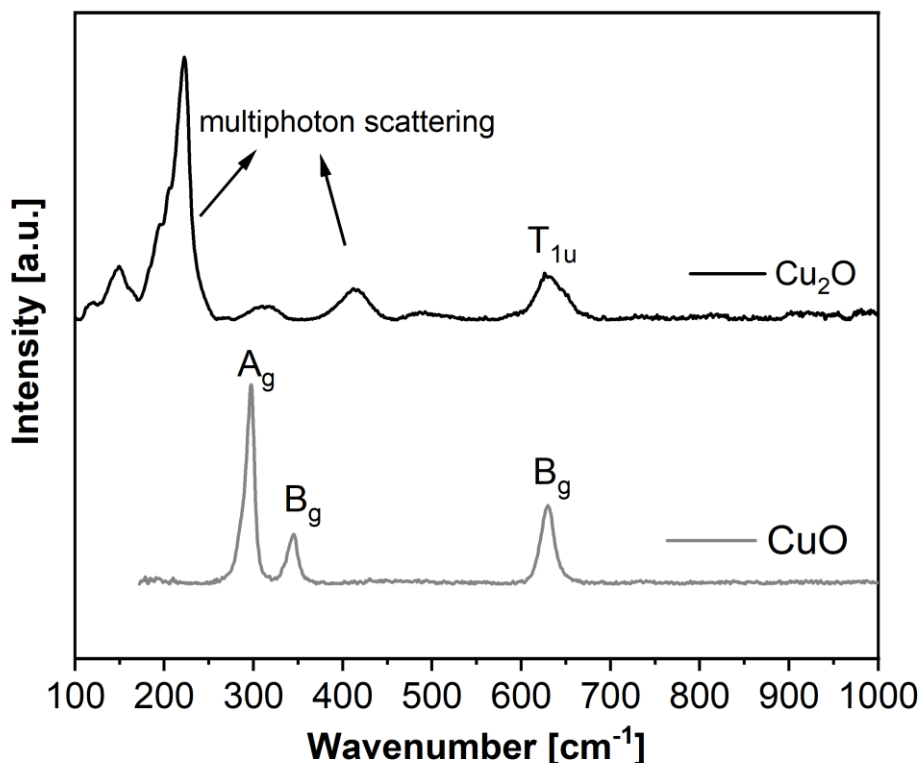
Figure 20*: Reference Raman spectra of Cu$_2$O [ID: #R050384] in black, and CuO [ID: #R060978] in grey, obtained from the RUFF™ project Database[186].*

Figure 20 shows the reference spectra for cupric oxide [CuO, ID: #R060978] and cuprous oxide [Cu_2O, ID: #R050384] from the RUFF™ project Database.[186] The Raman spectrum of CuO shows three Raman peaks corresponding to the Raman-active vibrational A_g (at 295 cm^{-1}), and B_g (at 347 and 630 cm^{-1}) modes.[187-189] On the other hand, the Raman spectrum of Cu_2O shows no Raman-active peaks. The peaks at 218 cm^{-1} and 410 cm^{-1} are assigned to multiphonon Raman scattering and the peak at 623 cm^{-1} corresponds to the IR-active mode T_{1u}.[189-191]

The Cu(I):Cu(II) ratio was investigated for three samples: np-Cu/GC electrode after electrolysis experiments, dealloyed np-Cu ribbons, and unpolished polycrystalline Cu foil (0.25 mm thick, 99.999%, Alfa Aesar). All samples were washed with highly purified water (18 MΩ cm at room temperature) and propan-2-ol. The np-Cu/GC electrode and np-Cu ribbons were dried under Ar and stored in vacuum. Both samples were in contact with air for a few hours during the Raman measurements.

3.3. Electrochemical characterization

3.3.1. Cyclic voltammetry (CV)

To investigate CO_2 reduction reaction (CO_2RR), cyclic voltammetry (CV) profiles were recorded using a potentiostat (Reference 600+, Gamry Instruments) and a home-made undivided glass cell (**Figure 21**). The electrolyte solution was 0.07 M tetraethylammonium iodide in acetonitrile (TEAI-MeCN), saturated with N_2 or CO_2 for at least 30 minutes. A graphite sheet and a silver/silver chloride (Ag/AgCl; in 3 M KCl) electrode were used as counter and reference electrodes, respectively. Different materials were employed as a working electrode: np-Cu/GC, copper wire (99.999%, 1 mm diameter, Alfa Aesar), or bare GC disk (5 mm diameter, Pine Research Instrumentation). For all electrochemical measurements, a rotating disc electrode (RDE) equipped with a GC disk (5 mm diameter, Pine Research Instrumentation) was used as a substrate for np-Cu, with a Cu loading of 1 mg cm^{-2}_{geo} (**Figure 21b, b´**). The freshly prepared np-Cu/GC was directly used for electrochemical measurements. The copper wire was polished with crystalline diamond suspensions of 9, 6, and 3 µm sizes (MetaDi

Supreme, Buehler) onto a Microcloth polishing paper (Buehler, Germany, #423710). The GC disk was polished with 0.05 µm of aluminum oxide powder onto a Microcloth paper.

All CV profiles were recorded with a scan rate of 0.02 V s^{-1} in the potential range from –1.0 to –2.0 V vs Ag/AgCl. Gamry Framework and Echem Analyst software version 7.8.5 were used for data acquisition and analysis, respectively.
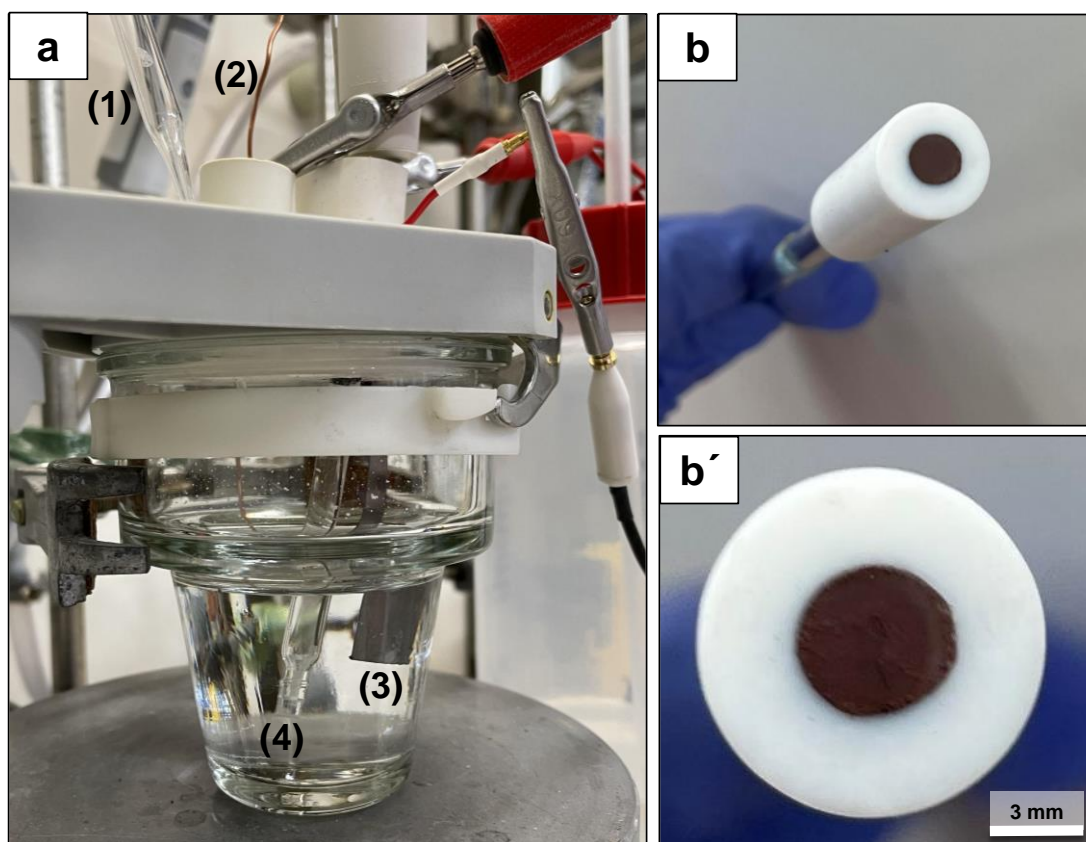
Figure 21: *(a) Experimental set-up for CO$_2$RR in 0.1 M TEAI-MECN, consisting of (1) CO$_2$ gas inlet, (2) Cu wire working electrode, (3) graphite counter electrode, and (4) Ag/AgCl reference electrode. (b, b´) The np-Cu/GC working electrode used for all electrochemical measurements, where np-Cu was drop-casted on a GC disk with diameter of 5 mm.*

3.3.2. Lead under potential deposition (Pb-UPD)

UPD-assisted surface area measurements were carried out by recording CV profiles using a potentiostat (VSP300, Biologic), operated with EC-Lab software (v11.32). The CV profiles were registered in a solution containing 0.01 M perchloric acid (HClO$_4$,

70 vol.%, 99.999%, Sigma-Aldrich), 0.1 M sodium perchlorate ($NaClO_4$, ≥98.0%, Sigma Aldrich), 0.01 M lead(II) perchlorate hydrate ($Pb(ClO_4)_2$, ≥99.995%, Sigma Aldrich), and 0.05 M sodium chloride (NaCl, ≥99.0%, Sigma Aldrich). Solutions were freshly prepared by dissolving/diluting their respective amount in highly purified water (18 MΩ cm at room temperature). Background experiments were performed in the same solution but in the absence of Pb^{2+} ions. The electrochemical experiments were performed in a home-made three-electrode glass cell (see **Figure 23**) with a np-Cu/GC (**Figure 21b, b´**) or polycrystalline Cu disk as working electrodes, platinum mesh (99.95%, Alfa Aesar) as a counter electrode, and a Pb wire (99.9%, Alfa Aesar) as a reference electrode. The polycrystalline Cu disks were polished with crystalline diamond suspensions of 9, 6, and 3 µm sizes (MetaDi Supreme, Buehler) onto a Microcloth polishing paper, washed with highly purified water and propan-2-ol. Directly before use, they were immersed in 85 wt.% H_3PO_4 for 5 seconds, washed again, and dried under Ar. This two-step polishing served to ensure an oxide-free surface. The Pt mesh was flame annealed prior to use, and the reference electrode was pretreated by etching in a diluted nitric acid (1:1 ratio) solution, heated up to 50 °C for 5 minutes. The solution was purged with Ar (99.999%, Air Liquide) at least two hours before UPD experiments.

First, CV profiles were recorded in a potential range from 0.4 to –0.4 vs Pb/Pb^{2+} at scan rate of 0.01 V s^{-1} to identify the regions of bulk deposition and UPD of Pb (**Figure 22**). Then, they were registered in UPD potential region from 0.4 to 0.0 V vs Pb/Pb^{2+} at 0.01 V s^{-1}, where a monolayer of Pb forms on the surface of the working electrode. From the deposition and stripping peaks in the CV profiles, the averaged integrated charge, $\bar{Q}_{\text{dep./strip.}}$ (in A V^{-1}) was estimated, then divided by the scan rate, v (in V s^{-1}) to get the charge, Q (in µC).

$$Q = \frac{\bar{Q}_{dep./strip.}}{v} \qquad \textbf{Equation (5)}$$

The electrochemically active surface area, ECSA (in cm^2), was calculated by normalizing the charge of Pb-UPD by the charge of one monolayer of Pb on pure flat Cu (300 µC cm^{-2})[192,193].

$$ECSA = \frac{Q}{Q_{Pb-ML}} \qquad \text{Equation (6)}$$

The enhancement of the surface area of np-Cu/GC is estimated by the roughness factor (RF), which refers to the ratio between the electrochemically active surface area and, *ECSA*, and the geometric surface area A_{geo} of the electrode. Since it is not possible to determine the A_{geo} for np-Cu/GC, the geometric surface area of the GC substrate (0.195 cm^2) was used for the estimation of *RF*.

$$\mathbf{RF} = \frac{\mathbf{ECSA}}{\mathbf{A_{geo}}} \qquad \textit{Equation (7)}$$
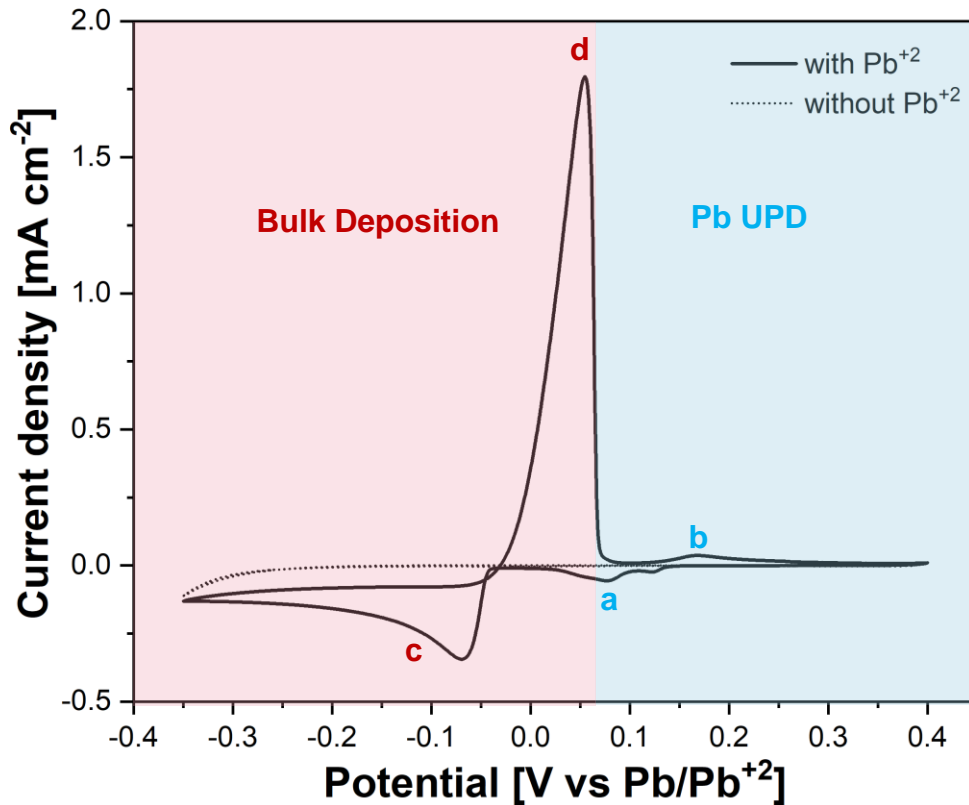
Figure 22: *CV profile of polycrystalline Cu in the potential range from 0.4 to −0.4 vs Pb/Pb^{2+} at a scan rate of 0.01 V s^{-1} in Pb-containing solutions (solid line) using platinum mesh and a Pb wire as counter, and reference electrode, respectively, showing the (a) deposition and (b) stripping peaks of Pb monolayer, as well as the (c) deposition and (d) stripping of multilayers of Pb atoms on the surface of Cu. The background CV profile was recorded in Pb-free solutions (dashed line).*

3.3.3. Double layer capacitance measurements

Double layer capacitance measurements were carried out to estimate the electrochemically active surface area (ECSA) of np-Cu/GC electrode. Electrochemical experiments were performed using a potentiostat (VSP300, Biologic) and a home-made three-compartment glass cell. The electrolyte solution was 0.1 M perchloric acid ($HClO_4$) prepared by diluting 70 vol.% $HClO_4$ (99.999%, Sigma Aldrich) in highly purified water (18 MΩ cm at room temperature) and saturated with Ar for at least 2 h before each experiment. Np-Cu/GC, bare GC disk, or polycrystalline Cu disk were used as working electrodes. All working electrodes have the same geometric area of 0.196 cm^2 (disk diameter of 2 mm). A platinum mesh (99.99% metal basis, Alfa Aesar) and mercury/mercurous sulfate electrode (Hg/HgSO$_4$, AMATEK) were used as counter and reference electrodes, respectively (**Figure 23**). For this experiment, a rotating disk electrode (RDE) equipped with a GC disk (5 mm diameter, Pine Research Instrumentation) was used as a substrate for np-Cu with metal loading of 1 mg cm$^{-2}_{geo}$. CV profiles were recorded in a potential range from –0.1 to –0.2 V vs Ag/AgCl at different scan rates of 0.02, 0.04, 0.05, 0.075, 0.10, and 0.15 V s^{-1}. All potentials were converted into silver/silver chloride (Ag/AgCl) scale. The electrochemical experiments were repeated three times for three independent np-Cu/GC samples.

CV profiles were recorded in the potential range (–0.1 to –0.2 V vs Ag/AgCl) where no apparent Faradaic processes occur, and it is assumed that measured current in this non-Faradaic potential region is due to double-layer charging. The charging current, i_C, is measured from CV profiles at multiple scan rates. The double-layer charging current is equal to the product of the scan rate, v, and the electrochemical double-layer capacitance, C, as given by **Equation (8)**.[173,194,195] Thus, a plot of i_C as a function of v yields a straight line with a slope equal to C (see **Figure 42** in **Section 5.2.2**).

$$i_C = v * C \qquad \textbf{Equation (8)}$$

In order to determine the enhancement of surface area of the np-Cu/GC, the measured capacitance, $C_{np\text{-}Cu/GC}$, is divided by the capacitance of a reference material. In this study, bare GC was used as a reference electrode, therefore, the roughness factor (RF)

of the np-Cu/GC is determined by **Equation (9)** by dividing $C_{np\text{-}Cu/GC}$ by the double-layer capacitance of bare GC, C_{GC}.

$$RF = C_{np\text{-}Cu/GC} / C_{GC} \qquad \textbf{Equation (9)}$$
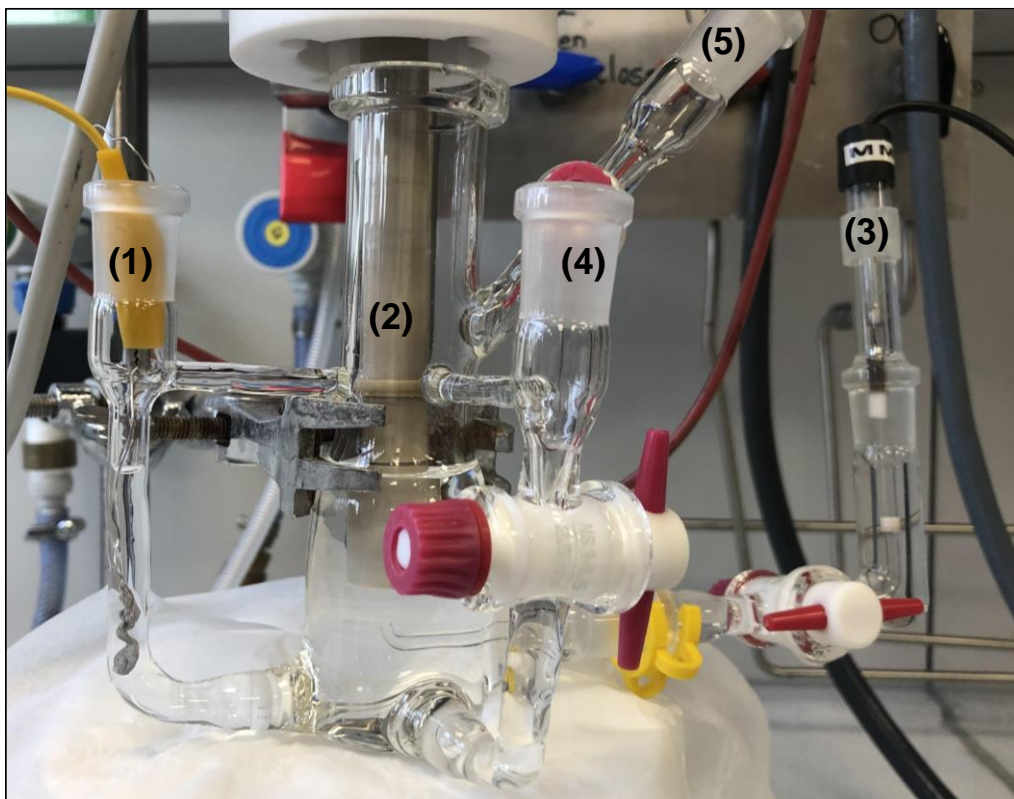
Figure 23: Experimental set-up of double layer capacitance measurement, consisting of a home-made three compartment glass cell with (1) Pt mesh counter electrode, (2) working electrode, (3) mercury/mercurous sulfate electrode ($Hg/HgSO_4$) reference electrode, (4) gas inlet bubbling through frit in the electrolyte, and (5) gas inlet above the electrolyte solution.

Bare GC was chosen as a reference material instead of polycrystalline Cu due to the large difference in the double-layer capacitance between the two materials. **Figure 24** show the CV profiles of np-Cu/GC (in black), bare GC (in grey), and polycrystalline Cu (in orange) in the potential range –0.1 to –0.2 V vs Ag/AgCl at a scan rate of 0.02 V s^{-1} in argon-saturated 0.1 M $HClO_4$ electrolyte. It is obvious that polycrystalline Cu has a much lower double-layer capacitance than that of bare GC. And since the GC substrate was not fully covered with np-Cu, np-Cu/GC also shows high double-layer capacitance

in respect to Cu. Therefore, dividing by the double layer capacitance of polycrystalline Cu in **Equation (9)** would deliver extremely high RF values for np-Cu/GC.
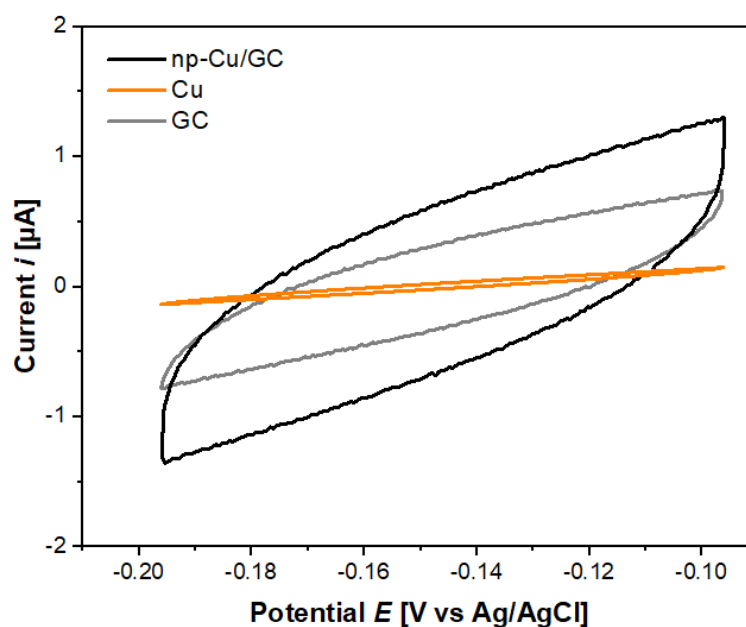
***Figure 24**: CV profiles of the np-Cu/GC (black), polycrystalline Cu (orange) and bare GC (grey) at a scan rate of 0.02 V s^{-1} in argon-saturated 0.1 M HClO$_4$ electrolyte, using platinum mesh and mercury/mercurous sulfate electrode (Hg/HgSO$_4$) as counter and reference electrodes, respectively. Figure reprinted from the manuscript submitted to a journal.*

3.4. Electrosynthesis experiments

3.4.1. General Procedure
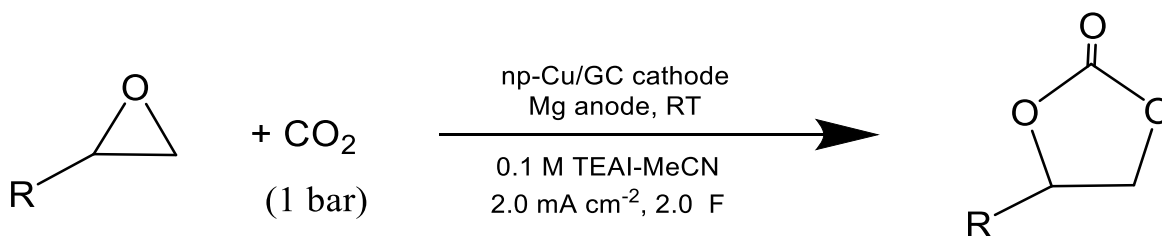
Galvanostatic electrolysis was conducted in an undivided cell (**Figure 25**), with an AIM-TTI MX100T Triple Output Multi-Range DC power supply. The electrolyte was prepared by dissolving 1 g of tetraethylammonium iodide (98%, Sigma Aldrich) in 40 mL acetonitrile (HPLC grade, Merck) to form 0.1 M TEAI-MeCN. The electrolyte was

saturated with CO_2 (99.998 %, Air Liquid) at least 30 minutes before beginning the electrolysis. A gas balloon was used to ensure CO_2 atmosphere during the electrolysis. The electrolyte was agitated with magnetic stirrer at 600 rpm. The electrolysis was carried out at room temperature. The anode was a magnesium (Mg) foil (99.999%, Alfa Aesar, dimensions 35 x 20 mm). Different cathode materials were tested: np-Cu/GC, polycrystalline copper plate (dimensions 35 x 20 mm) and bare GC plate (dimensions 35 x 20 mm). The distance between the anode and cathode was ~ 1 cm. The starting materials for the reaction with CO_2 were propylene oxide (99.5%, Fluka) and 1,2-butylene oxide (1,2-Epoxybutane 99+%, Sigma Aldrich).
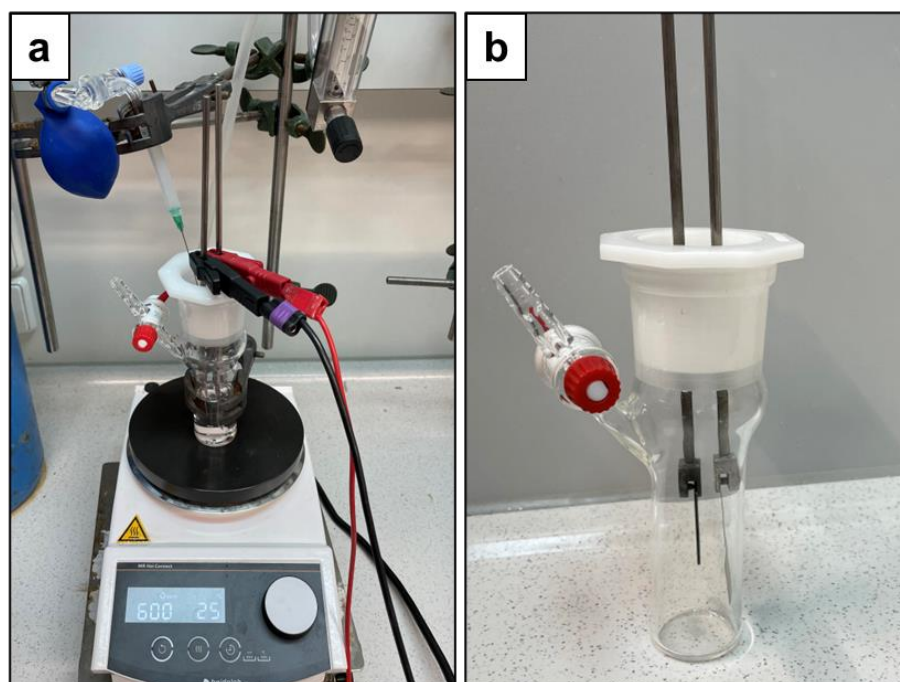
Figure 25: *Experimental set-up of the electrolysis, (a) including a cell, CO_2 balloon and a stirrer, (b) the undivided cell with the cathode and anode.*

The electrodes underwent specific cleaning and polishing procedures prior to the electrolysis experiments. The freshly prepared np-Cu/GC electrode was used directly, while the reused electrode was washed with highly purified water and propan-2-ol, dried under Ar, and stored in vacuum. Before reuse, np-Cu/GC was immersed in 85 wt.% H_3PO_4 for 5 seconds as a chemical polishing step, washed, dried under Ar, and immediately used. The polycrystalline Cu plate was polished with crystalline diamond

suspensions of 9, 6, and 3 μm sizes onto a Microcloth polishing paper (Buehler, Germany, #423710), washed with highly purified water and propan-2-ol. Directly before use, the plate was immersed in 85% H_3PO_4 for 5 seconds, washed again, and dried under Ar. The bare GC was polished with 0.05 μm of aluminum oxide powder onto a Microcloth polishing paper, cleaned with highly purified water and propan-2-ol. The Mg foil, used as an anode, was polished with 0.05 μm of aluminum oxide (Al_2O_3) powder onto Silicon Carbide polishing paper (CarbiMet P120, Buehler, Germany) and cleaned with highly purified water and propan-2-ol.

3.4.2. GC-MS

A Shimadzu GCMS-QP2020 gas chromatography coupled with mass spectrometry (GC-MS) was employed for identification of the reaction products. The capillary column used was an Optima 5 HT (Macherey-Nagel, length 30 m, inner diameter 0.25 mm, film thickness 0.25 μm). Helium was used as the carrier gas. The electron ionization was accomplished by electron impact (EI) with energy of 70 eV.

3.4.3. GC-FID

Yields of the generated cyclic carbonates were determined using gas chromatography with flame ionization detector (GC-FID, Shimadzu GC-2010 Plus) equipped with an Optima 5 MS capillary column (Macherey-Nagel, length 15 m, inner diameter 0.25 mm, film thickness 0.25 μm). The data analysis was conducted with Lab solution software (version 4.5, Shimadzu). For the blank experiment without any current flowing through the cell, magnesium bromide ($MgBr_2$) was dried under high vacuum at 200°C for 8 hours and added to the reaction mixture.

The product yields were determined from the calibration curves using propylene carbonate (PC, 99.5%, Thermo Scientific) and 1,2-butylene carbonate (BC, 98%, BLD Pharmatech Ltd). Mesitylene (98%, Merck) was added to the reaction mixture as an internal standard. A series of known amounts of cyclic carbonates (PC or BC) was added to a solution with a known amount of mesitylene. The ratio of number of moles, n,

of cyclic carbonates/mesitylene was plotted against the peak area ratio of cyclic carbonates/mesitylene from the corresponding peaks in the gas chromatogram (**Figure 26**).
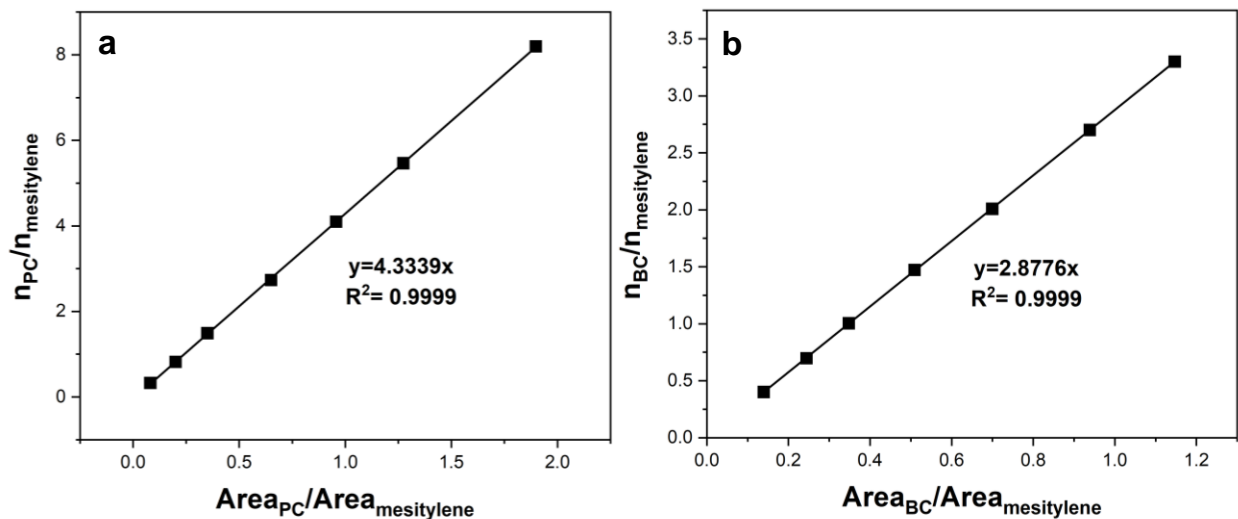
Figure 26*: Gas chromatography calibration curves for (a) propylene carbonates, PC, and (b) 1,2-butylene carbonates, BC, using mesitylene as an internal standard.*

Equation (10) and **Equation (11)** were used for the quantification of propylene carbonates and 1,2-butyleen carbonates from the crude reaction mixtures after electrolysis.

$$\frac{n_{PC}}{n_{mesitylene}} = 4.3339 \frac{Area_{PC}}{Area_{mesitylene}} \qquad \text{Equation (10)}$$

$$\frac{n_{BC}}{n_{mesitylene}} = 2.8776 \frac{Area_{BC}}{Area_{mesitylene}} \qquad \text{Equation (11)}$$

4. Preparation and characterization of nanoporous copper ribbons

This chapter is reprinted in adapted form from ref. 52 with permission from the Journal of Physical chemistry C, copyright 2022 American Chemical Society.

Co-authors' contribution: A. Dworzak performed the TEM measurements. D. Crespo prepared the master alloy. F.U. Renner contributed in the research planning. C. Dosche helped with the XPS analysis. M. Oezaslan supervised the whole work and contributed in the editing of the manuscript.

4.1. Characterization of pristine $Zn_{80}Cu_{20}$ alloy ribbons

The morphology, crystal structure, and chemical composition of initial $Zn_{80}Cu_{20}$ ribbons prepared by melt-spinning were investigated by using SEM, EDX, XRD, and XPS techniques. **Figure 27a** displays a SEM micrograph of as-prepared ribbons with visible grain boundaries. The dots that appear on the ribbon surface are expected to be oxide species, immediately forming on the metal surface by exposure to air. From the EDX data, the elemental quantification was found to be 23 ± 1 at.% Cu and 77 ± 1 at.% Zn on the surface as well as in the cross-section of the as-prepared ribbons. This is in excellent agreement with the crystal structure detected by XRD. The XRD profile in **Figure 27b** shows reflexes at 2θ values of 38.1°, 42.1°, 43.7°, 58.1°, 68.7°, 77.9°, 83.9°, and 84.9°. Rietveld analysis indicated that these reflexes correspond to a hexagonal $Cu_{20}Zn_{80}$ phase with space group of $P6_3/mmc$ (COD[182], pattern ID: #1524894). Other crystal phases, e.g. monometallic metals or oxides were not detected by XRD.

Moreover, the survey and high resolution XPS spectra of Zn 2p, Cu 2p, and O 1s spectra of the ribbon surface are shown in **Figure S1** of the **Supporting information for Chapter 4**. In **Figure S1a – b**, the Cu 2p and Zn 2p XPS spectra were deconvoluted and fitted with a doublet for Cu $2p_{1/2}$ and Cu $2p_{3/2}$ at 953.2 and 933.3 eV as well as for Zn $2p_{1/3}$ and $2p_{3/2}$ at 1045.5 and 1022.1 eV, respectively. The low intensity of the Cu 2p data signifies its minor content on the ribbon surface. To identify the chemical state of Zn, we also analyzed the corresponding Zn Auger spectra (**Figure 27c**), signifying three different oxidation states, namely for metallic Zn (blue

line, at 491.4 and 494.7 eV)[196], for ZnO (green line, at 496.2 and 498.5 eV)[196] and finally for Zn(OH)$_2$ species (red line, at 499.8 eV)[197]. The formation of metal oxide and hydroxide species is confirmed by the O 1s XPS spectrum (peak maxima at 530.9 and 532.5 eV), as shown in **Figure S2c**. The results from the deconvoluted XPS spectra clearly reveal that the top layer of Zn$_{80}$Cu$_{20}$ alloy ribbons is Zn-enriched and strongly oxidizes, forming a passivation layer with a thickness of few nanometers. The segregation of Zn to the surface is likely related to the melt-spinning process and/or its strong oxophilic character, when ribbons are in contact with air. Very likely, during the melt-spinning the liquid ZnCu impregnates a rotating cooled wheel. This quenching might lead to a change in mobility of Cu and Zn atoms based on the different melting temperatures. In other words, zinc shows a lower melting temperature and is therefore more mobile compared to copper with higher melting temperature. Thus, starting from the precipitation of denser ZnCu liquid, Zn atoms tend to segregate to the surface during the quenching process.

In **Figure 27d**, the XPS sputter depth profile of pristine Zn$_{80}$Cu$_{20}$ ribbons shows the chemical distribution of Zn and Cu up to 77 nm of depth. After the first few mild sputter cycles, the amount of overall oxygen was negligible and only the ribbon surface is oxidized. Thus, it is not illustrated in the depth profile plot. The dashed area represents the deviation of the chemical composition due to the inhomogeneous sputter process of Zn and Cu (temperature dependence of the saturated vapor pressures of zinc and copper).[183-185,198] On the top layer, the apparent Zn composition was 93 at.%. After the first 14 nm depth of the ribbons, the Zn content decreases to 72 ± 9 at.%, while the Cu content simultaneously increases from 7 at.% to 28 ± 9 at.%. Deeper layers up to 77 nm show a relatively constant distribution with 77 ± 7 at.% for Zn and 23 ± 7 at.% for Cu. This result is in excellent agreement with the EDX data.

We can sum up that only the first 14 nm depth of alloy ribbons signifies a Zn-rich surface, but in the deeper layers both metals are homogeneous distributed with an atomic Zn:Cu ratio of 77:23 (± 7 at.%).
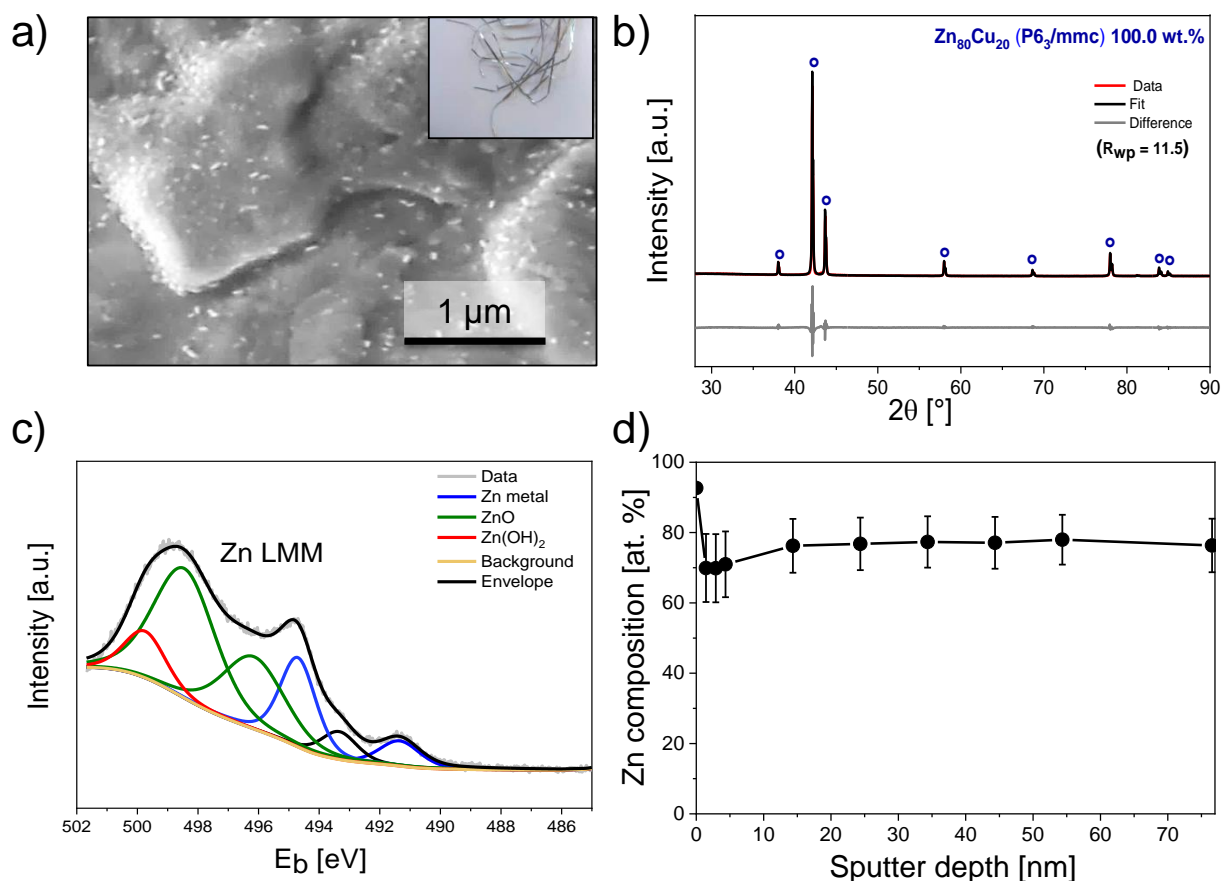
Figure 27: *Structural characterization of pristine $Zn_{80}Cu_{20}$ alloy ribbons prepared by melt-spinning. (a) SEM micrograph at a scale bar of 1 μm; insert: photograph of pristine ribbons. (b) XRD profile with Rietveld analysis signifies the formation of hexagonal $Zn_{80}Cu_{20}$ crystal phase with space group of P63/mmc, lattice parameter of a = 2.734 ± 0.001 Å and c = 4.293 ± 0.001 Å, and crystallite size of 165 ± 4 nm. Difference profile is denoted in grey line. The Rwp is the weighted profile residual as a quality of the fit. Blue hollow circles denote the $Zn_{80}Cu_{20}$ reference pattern (ID: #1524894 from COD[182]). (c) XPS Auger spectra and the corresponding fit of Zn LMM from the ribbon surface. The experimental data are denoted in grey, the resulting envelope is symbolized in black, and the background is indicated in yellow. (d) XPS sputter depth profile up to 77 nm showing the chemical distribution of Zn. The relatively large error bars are due to the inhomogeneous sputter process. Figure reprinted with permission from ref. 52.*

4.2.   Time-resolved ligament evolution of dealloyed $Zn_{80}Cu_{20}$ ribbons

The effects of nature of electrolyte on the ligament evolution over dealloying time were investigated for pristine $Zn_{80}Cu_{20}$ alloy ribbons using a combination of SEM, (S)TEM,

EDX, XRD, and XPS techniques. Thereby, the ribbons were dealloyed in 0.1 M HCl and 1.3 M NaOH for different reaction times (3.5. 8, 24, 48, 72, 92, 168, and 312 h) under free corrosion. We chose 0.1 M HCl and 1.3 M NaOH as electrolyte solutions to compare our results with previous work on np-Cu films[7] and other research works.[20,199,200] Throughout this paper, we will denote the multiple np-Cu samples dealloyed at different electrolytes for different dealloying times as follows: np-Cu (electrolyte, time).

After dealloying, metallic grey ribbons changed color to brown/black (in NaOH) and brown (in HCl), see **Figure S2** of the **Supporting information for Chapter 4**. The dealloyed ribbons had to be carefully handled due to the brittle nature of the material. **Figure 28** displays a series of low and high resolution SEM micrographs of ribbons dealloyed for 3.5, 24, and 312 h in 0.1 M HCl at 25°C under Ar atmosphere. In the first 3.5 h of dealloying time, the surface of the ribbons is only partially dealloyed accompanied by the evolution of pores, as shown in **Figure 28a – a´**. The initial dealloying process takes preferentially place at the grain boundaries of the ribbons. It is well-known that grain boundaries contain defects and under-coordinated surface atoms, where the diffusion rate of atoms along the grain boundaries is higher than the high-coordinated terrace atoms on the grain surfaces.[201,202] The appearance of pits signifies the attack of aggressive electrolyte at defect-rich parts of the ribbon surface, e.g. formed during reduction of the oxide-contained species visible as dots in the SEM micrograph, **Figure 27a**. Micro-cracks are observed in the dealloyed ribbons due to the strong volume changes during the Zn dissolution and the resulting crystal transformation from hexagonal close packed (hcp) to face-centered cubic (fcc).

Over dealloying time, the evolution of pores is more and more pronounced, implying the continuous Zn dissolution from the surface of alloy ribbons. An entire formation of porous network structure, denoted as np-Cu material, is clearly observed after 24 h of dealloying time, displayed in **Figure 28b – b´**. It is well-known that the evolution of pores is controlled by the critical interplay between dissolution rate of less noble metal atoms and surface diffusion rate of remaining noble metal atoms. The np-Cu (HCl, 24 h) consists of self-assembled and homogeneous ligaments. Recently, a loss of ligament structure has been reported for np-Cu films after 72 h of dealloying time in 0.1 M HCl.[7]

For this reason, a very long dealloying period was applied to evaluate the structural and chemical stability of the np-Cu materials in HCl.
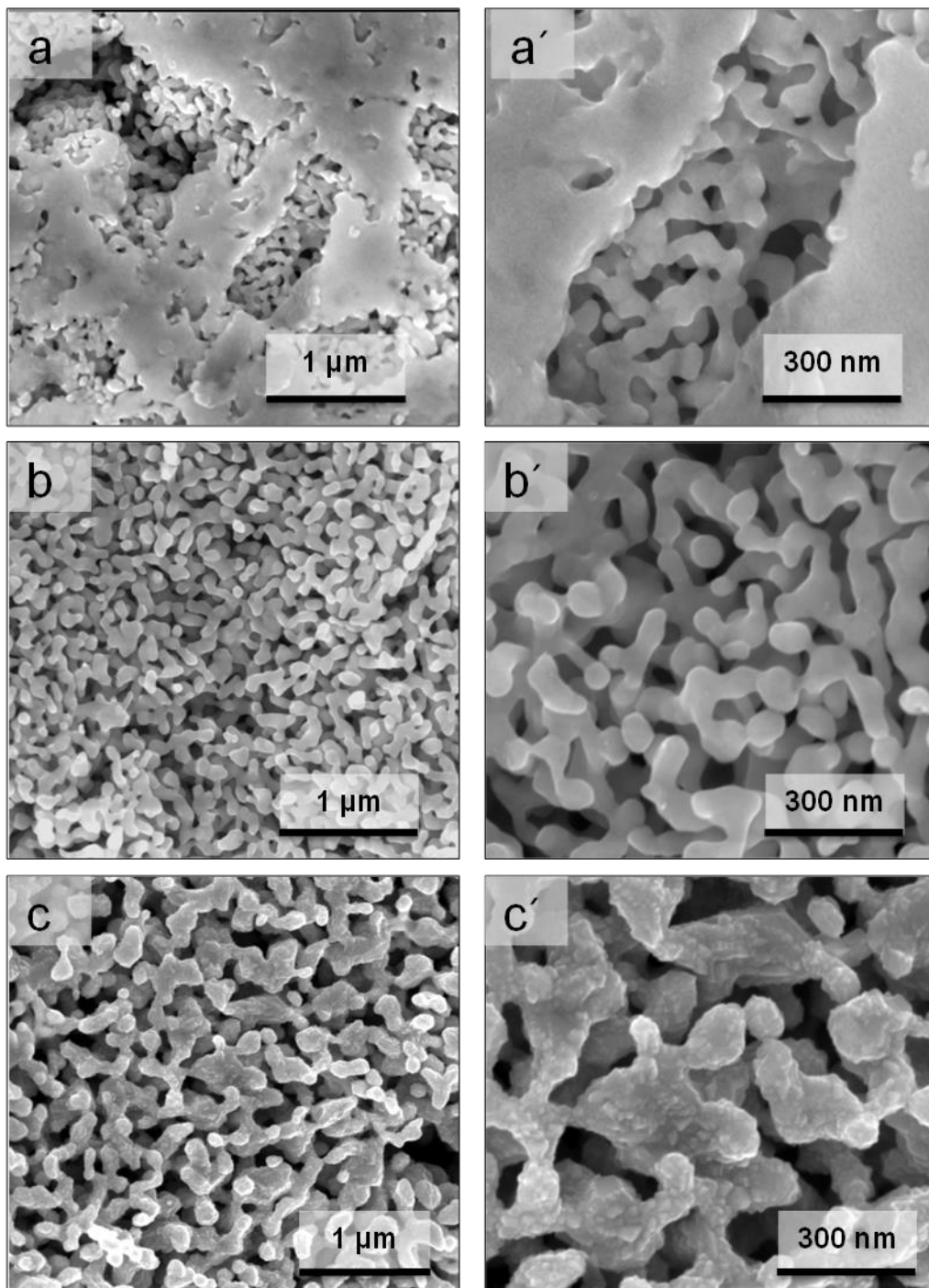
Figure 28: *Series of low (right) and high (left) magnification SEM micrographs of $Zn_{80}Cu_{20}$ ribbons (a, a´) after 3.5 h, (b, b´) 24 h, and (c, c´) 312 h (13 days) of dealloying time in 0.1 M HCl at 25°C under Ar atmosphere. Figure reprinted with permission from ref. 52.*

Figure 28c – c´ display the low and high resolution SEM micrographs of the np-Cu after dealloying time of 312 h (13 days) in 0.1 M HCl at 25°C under Ar atmosphere. The np-Cu (HCl, 312 h) shows ligaments with larger size and rough ligament surfaces compared to np-Cu (HCl, 24 h). The visible coarsening of the porous structure can be attributed to the rapid surface diffusion of Cu at the surface–electrolyte interface over time induced by the presence of adsorbed chloride anions and by the tendency for surface energy reduction.[203,204] This contrary observation can be explained by the different initial thicknesses and homogeneity of pristine $Zn_{80}Cu_{20}$ master alloys used in our previous dealloying experiments. The time-resolved changes in ligament size and chemical composition of np-Cu will be discussed later in more detail.

Dealloying of the ribbons in alkaline solution shows a different behavior to that observed in acidic environment. **Figure 29** displays a series of low and high resolution SEM micrographs of np-Cu after various dealloying times (8, 24, 92, and 312 h) in 1.3 M NaOH at 25°C under Ar atmosphere. **Figure 29a – a´** show the increased appearance of micro-cracks, forming along the grain boundaries of $Zn_{80}Cu_{20}$ alloy ribbons after 8 h of dealloying time. Beside the micro-cracks, ligaments with smaller size and less intense in depth compared to those in np-Cu (HCl) are formed within the grain. It is noted that no ligament formation is observed below a dealloying time of 8 h in NaOH. With increasing dealloying time, the structure and distribution of ligaments in np-Cu (NaOH, 24 h) are similar to those observed after 8 h dealloying time, in **Figure 29b – b´**. Only the cracks appear much deeper with increasing dealloying time in alkaline media. The extent of the dealloying time up to 92 h leads to larger ligaments with more depth to the porous structure, as shown in the SEM micrograph of the dealloyed ribbons (**Figure 29c**). Interestingly, octahedral crystals with different sizes appear at the surface of the np-Cu (NaOH, 92 h). Further XRD and XPS analysis could identify the structure and composition of these crystals to be Cu(I)oxide (see **Figure 30d**). These crystals grew in frequency and size by increasing the dealloying time in alkaline solution. After 312 h (13 days), the surface of the dealloyed ribbons is entirely covered with μm-sized Cu_2O crystals, as shown in **Figure 29d**. Based on the SEM analysis, we suggest that the surface diffusion process at the alloy–electrolyte

interface during dealloying might control the propagation of the three-dimensional bicontinuous ligament pore structure. This will be discussed in more detail later.
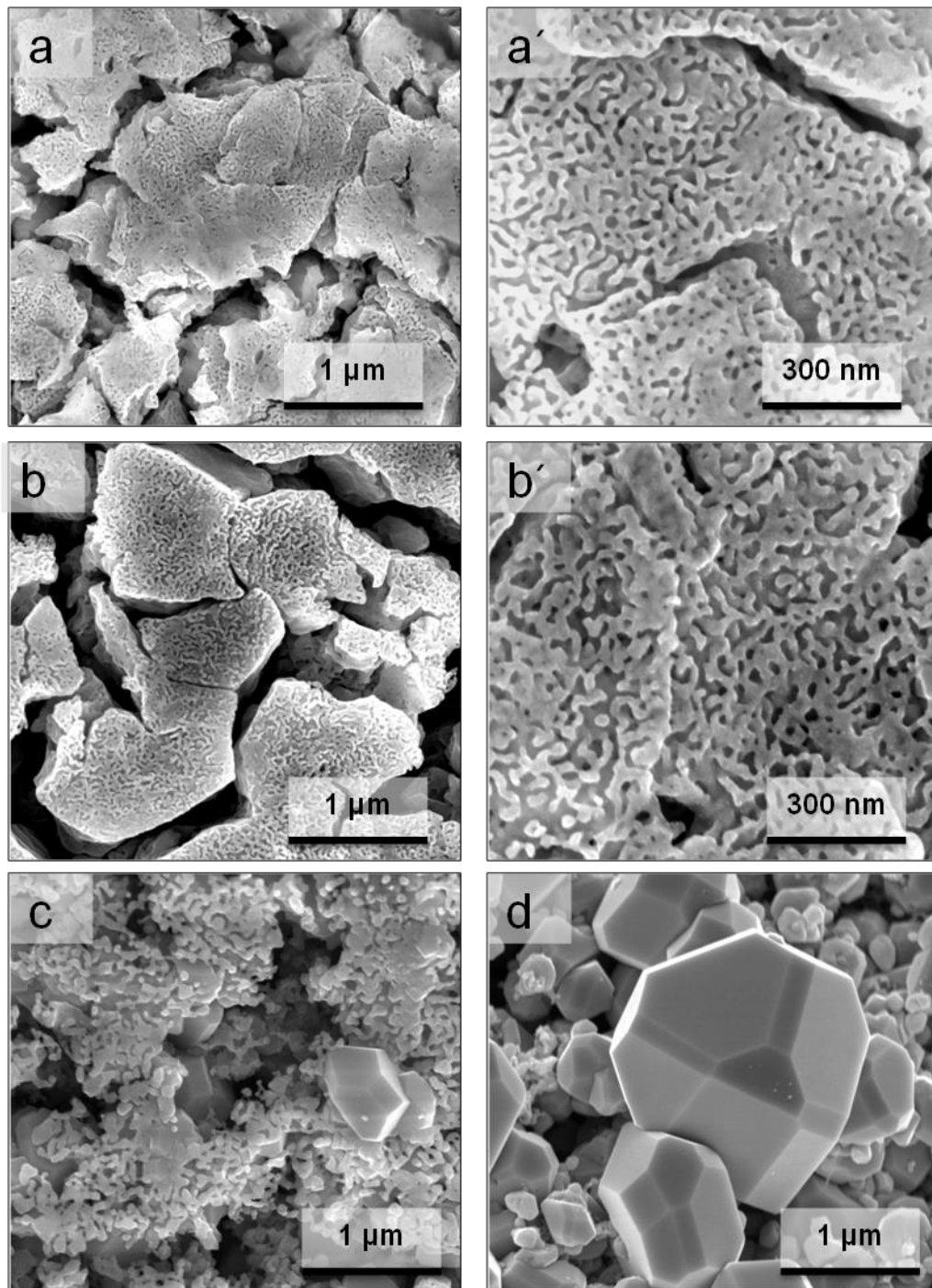
Figure 29: *Series of low (right) and high (left) magnification SEM micrographs of $Zn_{80}Cu_{20}$ ribbons after dealloying time of (a, a´) 8 h, (b, b´) 24 h, (c) 92 h, and (d) 312 h (13 days) in 1.3 M NaOH at 25 °C under Ar atmosphere. Figure reprinted with permission from ref. 52.*

To correlate the morphological alterations from the SEM analysis with the changes in crystallographic phase structure and composition, XRD investigations and quantitative Rietveld analysis on treated ribbons were performed after various dealloying times in HCl and NaOH. In **Figure 30a,** the XRD profile of the np-Cu (HCl, 24 h) shows 2θ reflexes at 34.9°, 37.9°, 43.2°, 48.0°, 50.5°, 52.6°, 62.8°, 64.7°, 72.2°, 75.8°, 79.2°, and 89.6°, ascribing to the cubic $Cu_{38}Zn_{62}$ (COD[182], reference pattern ID: #1100057) with a space group of I-43m. In fact, the dissolution of zinc is accompanied by the changes in crystal structure from hexagonal $Cu_{20}Zn_{80}$ phase (P6₃/mmc) to cubic $Cu_{38}Zn_{62}$ (I-43m). Additional 2θ reflexes at 43.3°, 50.5°, and 74.1° are detected for the np-Cu (HCl, 24 h), corresponding to the face-centered cubic (fcc) Cu phase with Fm-3m (COD[182], pattern ID: 4105040). Quantitative Rietveld refinement indicates 84.4 ± 0.9 wt.% and 15.6 ± 0.9 wt.% for $Cu_{38}Zn_{62}$ and pure Cu, respectively. The contribution of the pure Cu crystal phase grows by increasing dealloying time, indicating the successive loss of Zn from the bulk ribbons. Finally, after dealloying time of 312 h in HCl (**Figure 30b**), the Cu amount reaches 84.6 ± 1.0 wt.% and the $Cu_{38}Zn_{62}$ phase contributes to only 15.4 ± 1.0 wt.%.

In alkaline media, however, the XRD patterns of dealloyed ribbons were found to be strongly different. Two crystal phases, $Cu_{20}Zn_{80}$ and $Cu_{38}Zn_{62}$, were observed in np-Cu (NaOH, 24 h), shown in **Figure 30c**, with contribution of 30.7 ± 0.5 wt.% and 69.3 ± 0.5 wt.%, respectively. The octahedral crystals observed in the SEM micrographs of np-Cu (NaOH, 312 h; **Figure 29d**) are also confirmed as Cu(I)oxide (COD[182], ID pattern: 1000063, space group Pn-3m) by XRD. The Cu_2O phase is represented by 2θ reflexes at 29.5°, 36.4°, 42.3°, 61.4°, 73.5°, and 77.4°. Quantitative Rietveld analysis reveals 81.7 ± 3.4 wt.% and 18.3 ± 3.4 wt.% for Cu_2O and Cu, respectively. The wavy background in the XRD profiles is caused by the plexiglass used as sample holder (see **Figure S3**) due to the low sample quantities available for these measurements.
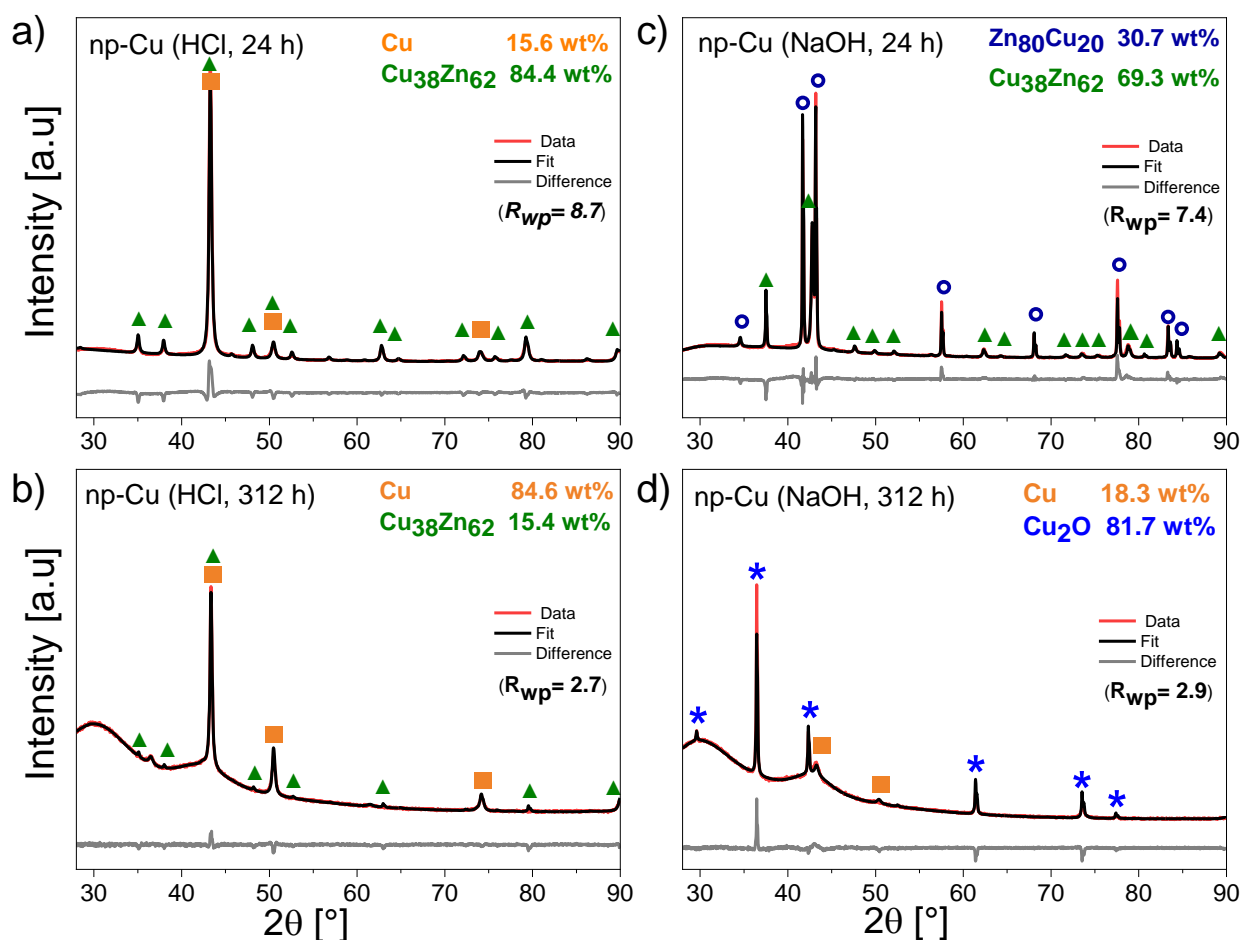
Figure 30: *XRD profiles for np-Cu materials dealloyed in 0.1 M HCl for (a) 24 h and (b) 312 h as well as in 1.3 M NaOH for 24 h (c) and (d) 312 h at 25°C under Ar atmosphere. The wavy background stems from the plexiglass used as a substrate for dealloyed samples. Rietveld analysis: (i) hexagonal $Cu_{20}Zn_{80}$ phase ($P6_3/mmc$), $a = 2.734 \pm 0.001$ Å, $c = 4.293 \pm 0.001$ Å, crystallite size of 165 ± 4 nm; (ii) cubic $Cu_{38}Zn_{62}$ phase (I-43m), $a = 8.881 \pm 0.002$ Å, crystallite size 38 ± 1 nm; (iii) Fcc Cu phase (Fm-3m), $a = 3.616 \pm 0.002$ Å, crystallite size 29 ± 3 nm;(iv) Cu_2O phase (Pn-3m), $a = 4.269 \pm 0.001$ Å, crystallite size 96 ± 3 nm. The following reference pattern IDs from the COD[182] were taken: blue hollow circles (ID: #1524894) for $Zn_{80}Cu_{20}$, green triangles (ID: #1100057) for $Cu_{38}Zn_{62}$, orange squares (ID: #4105040) for Cu, and blue stars (ID: #1000063) for Cu_2O. Difference profiles are denoted in grey line. The R_{wp} is the weighted profile residuals as a quality of the fit. Figure reprinted with permission from ref. 52.*

In **Figure 31**, the compositional changes obtained from EDX are correlated with the dealloying time in HCl and NaOH. It also shows the trend, by which the ligament size alters with respect to the Zn content and dealloying time. First, we will describe the loss of Zn as a function of the dealloying time in 0.1 M HCl (**Figure 31a**). As the dealloying rate is associated with the dissolution rate of less noble metal from master alloy, it is obvious that the Zn content continuously decreases in HCl over time. The dissolution rate of Zn from the ribbon surface is very fast in the first hours of dealloying process. Within the first 3.5 h of dealloying time, the Zn content drops drastically from 77 ± 1 at.% (pristine) to 56 ± 3 at.%. After 24 h dealloying time, the remaining Zn content is still 32 ± 5 at.% and continues to decline to 16 ± 4 at.% after 48 h. Finally, the Zn content was found to be 3 ± 2 at.% after 168 h and it remains almost constant until 312 h of dealloying time. The corresponding SEM micrographs of np-Cu (**Figure 28c – c´**) reveals that 2 – 3 at.% of Zn is still sufficient to retain the ligament structure. An entire loss of zinc leads to a loss of ligament structure and results in a polycrystalline solid film.[7]

In **Figure 31b**, the dealloying of ribbons in 1.3 M NaOH shows a decrease in Zn content over time. At the beginning, the residual Zn content for np-Cu (NaOH, 3.5 h) was found to be similar to np-Cu (HCl, 3.5 h) with amount of 55-60 at.%. After that, the process became much slower in alkaline media. The amount of residual Zn dropped to 50 ± 9 at.% after 24 h, and 37 ± 11 at.% after 48 h, until it had reached 1 – 2 at.% after 312 h (13 days). An important finding to notice in alkaline medium is the detection of large amount of oxygen that increased strongly from 24 ± 10 at.% (after 92 h) to 45 ± 19 at.% (after 312 h). The correlation of O, Cu and Zn contents over dealloying time in NaOH is shown in **Figure S4** of the **Supporting information for Chapter 4.** As the atomic Cu:O ratios obtained over time deviate from Cu_2O, we suggest that the formation of Zn and Cu (hydr)oxide surface species occurs during the dealloying process in alkaline corrosive environment.

It is also important to clarify how the ligament size in the np-Cu materials changes over dealloying time in HCl and NaOH at 25°C. The mean ligament size was determined by analyzing of at least 200 ligaments from several SEM micrographs. **Figure 31a** displays the changes in ligament size as a function of dealloying time in 0.1 M HCl. In fact, the

formed ligaments of np-Cu materials were found to become larger and rougher over dealloying time. More precisely, the mean ligament size increases from 55 ± 12 nm (3.5 h) to 73 ± 14 nm (24 h) and finally to 128 ± 27 nm (312 h) in HCl. Due to coarsening of the ligaments in contact with a strong acid, the size distribution becomes broader as illustrated in **Figure S5** of the **Supporting information for Chapter 4**. In this context, the residual Zn content decreases concurrently from 56 ± 3 at.% to 32 ± 5 at.% and finally to 3 ± 1 at.%. Thus, a reverse correlation is observed between the ligament size and residual Zn content in np-Cu by dealloying in HCl.

Contrary to the dealloying behavior in acid, the ligament size of np-Cu remains almost unchanged with a size of 21 ± 4 nm until 48 h of dealloying time in 1.3 M NaOH, see **Figure 31b**. It is noted that the ligament size distributions are very narrow (see **Figure S6**). After that, a slight increase of the mean ligament size up to 36 ± 11 nm (1.7 fold) is observed. Obviously, the ligament size formed during dealloying in NaOH is much smaller than those in HCl.

Due to its very high solubility in HCl as well as NaOH, we suggest that a supersaturation of soluble Zn compounds, e.g. $ZnCl_2$ or $Zn(OH)_4^{2-}$ might not be reached in these electrolyte solutions, because no precipitation of Zn salts and no alteration of surface diffusion rate at the alloy–electrolyte interface have been observed. As shown in **Figure 29d**, only large Cu(I)oxide crystals via continuous re-deposition form and mainly cover the entire surface after 312 h of dealloying time in 1.3 M NaOH. We can sum up that the ligament size is independent from residual Zn content in the first 48 h of dealloying in alkaline media because of the lower diffusivity of Cu atoms by forming hyr(oxide) species along the alloy–electrolyte interface. This information is particularly useful for systematic studies of np-Cu materials in heterogeneous and electrochemical catalysis.
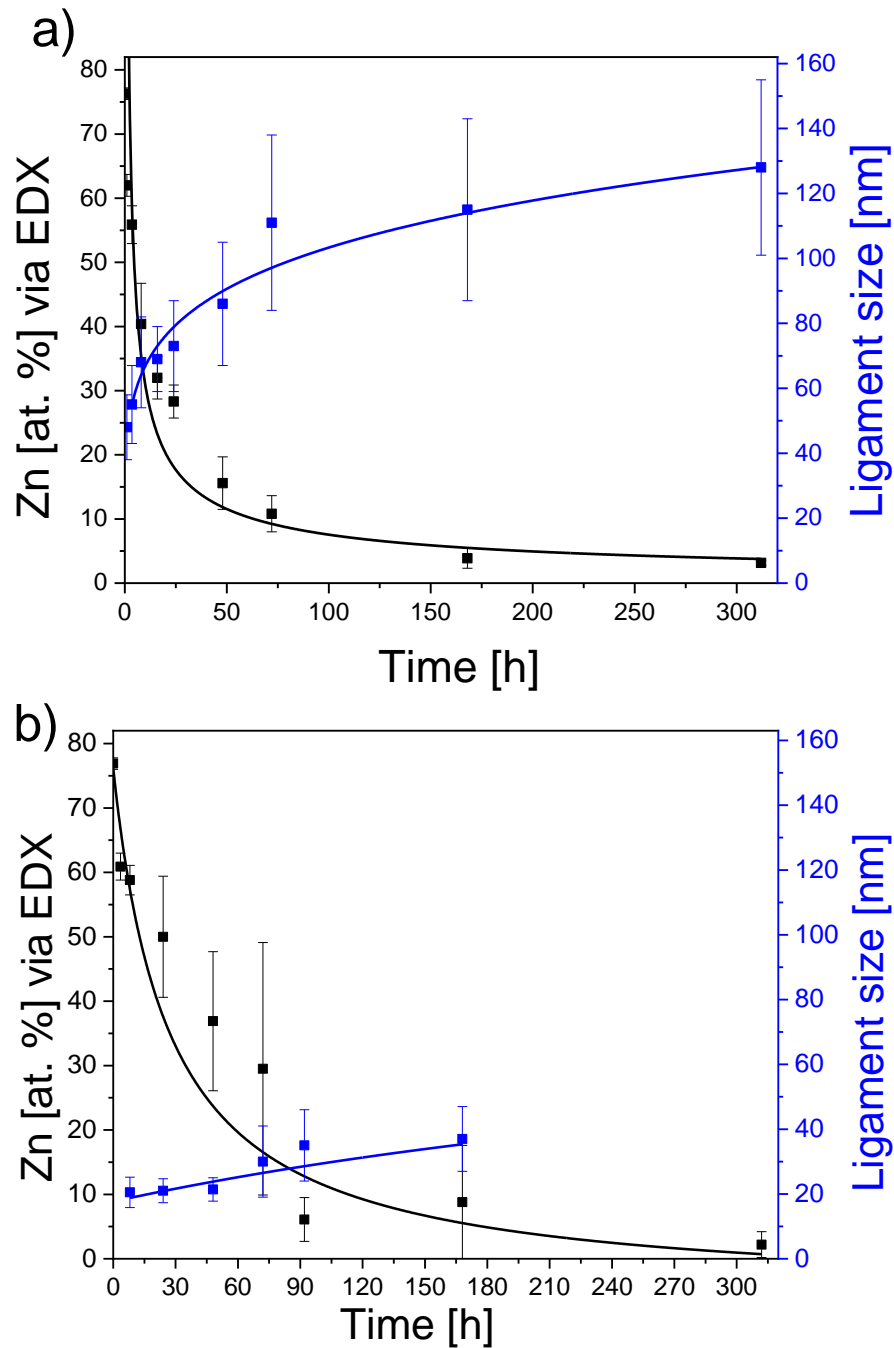
Figure 31: *Dependence on dealloying time, residual Zn content, and ligament size after chemical dealloying of Zn₈₀Cu₂₀ ribbons in (a) 0.1 M HCl and (b) 1.3 M NaOH at 25°C under Ar atmosphere. The EDX quantification of chemical composition was determined from at least three sample areas at low magnification, while at least 200 ligaments from several SEM micrographs were analyzed to establish the mean ligament size. Each measurement was repeated at least three times for each sample. Figure reprinted with permission from ref. 52.*

We wanted to mention that in all experiments a Cu substrate was attached to the pristine $Zn_{80}Cu_{20}$ ribbons during dealloying in 1.3 M NaOH. This was found to be essential for initiating and accelerating the dealloying process on Zn-rich surface. The high overpotential of the cathodic hydrogen evolution reaction (HER) as an opposite reaction hinders the oxidative dissolution of Zn and thus slows down the dealloying process by passivation. More precisely, the residual Zn content of dealloyed ribbons in 1.3 M NaOH for 312 h (13 days) was found to be 62 ± 2 at.% (SEM micrographs, **Figure S7**). When the ribbons, however, were attached to a Cu substrate, the Zn dissolution process was enhanced and dropped to 61 ± 2 at.% after only 3.5 h of dealloying time. The iR-corrected HER polarization curves for pristine $Zn_{80}Cu_{20}$ ribbons and monometallic compounds are displayed in **Figure S8**, signifying a decrease of the overpotential for HER in the order of: pure Cu < $Zn_{80}Cu_{20}$ < pure Zn in 1.3 M NaOH. Thus, the passivation layer of a Zn-rich ribbon surface can break down in strong alkaline environment, when an electrochemical cathodic reaction like HER on more active metal surface with lower activation barrier (overpotential) is offered. This is also visible by the hydrogen bubble formation on the attached Cu foil, but not on the ribbons alone (**Figure S9**).

4.3. Effects of dealloying temperature, electrolyte agitation and de-aeration on the structure of np-Cu

The effect of electrolyte agitation on the pore-ligament evolution of np-Cu ribbons during the first 24 h of dealloying in de-aerated 0.1 M HCl at room temperature was studied to point out any mass transport restrictions based on the electrolyte solution within the pores. **Figure S10** summarizes the results from the dealloyed samples with and without agitation evaluated by SEM-EDX measurements in the top and cross-sectional view. A similar dealloying behavior is observed in stagnant and agitated HCl solutions. The chemical composition, ligament size as well as the dealloying depth over the first 24 hours (see **Figure S10c**) are very similar with and without stirring. A slight difference of the residual Zn content was observed after dealloying for more than 8 hours. We explained this observation by the different formation of laminar film resistance on the

ribbon surface with and without convection as mass transport resistance. To sum up, agitation of the electrolyte during dealloying does not have a significant influence on the structure since the mass transport of electrolyte into the pores is not the rate-limiting step in the dealloying process.

The effect of de-aeration of the electrolyte was also investigated in HCl. **Figure S11** and **Table S1** in the **Supporting information for Chapter 4** show very similar results of the np-Cu ribbons in aerated and de-aerated 0.1 M HCl at room temperature. We can point out that the de-aeration of HCl solution has no influence on microstructure evolution characteristics of np-Cu ribbons during dealloying. However, the de-aeration of aggressive electrolyte solution is important when the dealloying takes place in alkaline media, where soluble zinc species reacts with carbon dioxide from the air to form zinc carbonate. Zinc carbonate is insoluble in water, thus it precipitates on the surface of the ribbons and terminates the dealloying process.

The dealloying temperature is very important parameter that influences the structure of np-Cu. Thus, the $Zn_{80}Cu_{20}$ ribbons were dealloyed for 24 h in 0.1 M HCl at 15°, 25° and 50°C. **Figure S12a** and **Figure S12b** in the **Supporting information for Chapter 4** display the changes in residual Zn content and ligaments size with the dealloying temperature. The EDX analysis shows Zn content of 17 ± 3 at.% at 50°C, compared to 32 ± 5 at.% at 25°C. The mean ligament size increases with higher dealloying temperature from 64 ± 12 nm, to 73 ± 14 nm, to 84 ± 15 nm at 15°C, 25°C and 50°C, respectively. The observed ligament size growth is related to the temperature-dependent surface diffusion rates of Cu atoms, as reported in the literature.[70,73,205] Surface diffusivity of Cu along the alloy-electrolyte interface (D_s) is estimated from the following equation: [69-75]

$$D_s = \frac{d(t)^4 KT}{32\, \gamma t \alpha^4} \qquad\qquad \textit{Equation (12)}$$

where d(t) in [m] is the ligament size at given dealloying time t, K is the Boltzmann constant (1.3806 x 10^{-23} J K^{-1}), T in [K] is the dealloying temperature, γ is the surface energy of Cu (1.79 J m^{-2})[69,70,74], t in [s] is the dealloying time and α is the lattice

parameter of Cu (3.616 x 10^{-10} m). The calculated D_s values of Cu in 0.1 M HCl were found to be 7.9 x 10^{-19} m^2 s^{-1}, 1.4 x 10^{-18} m^2 s^{-1} and 2.6 x 10^{-18} m^2 s^{-1} at 15°C, 25°C and 50°C, respectively. Our results are in good agreement with the reported values from Aburada et al.[71] in HCl and Erlebacher et al.[62] in vacuum.

Since the nanostructure is dependent on the dealloying time and temperature, measurement of the activation energy (E_a) is necessary to better understand the dealloying mechanism. An Arrhenius plot in **Figure S12c** shows a linear relationship between lnD_s and 1000/T based on our experimental data. The slope of the fitted line equals to -E_a/R, where R is the gas constant (8.3145 J mol^{-1} K^{-1}).[70,72] In this work, E_a was determined to be 25.8 kJ mol^{-1}. Zhang et al.[75] have reported an E_a value of 36.6 kJ mol^{-1} for Cu in 0.1 M HCl, which is comparable to our result. E_a values between 17 and 62 kJ mol^{-1} were reported in NaOH, H_2SO_4 and HF solutions.[70,72,75,205]

Based on our experimental data, the surface diffusivity of Cu in 1.3 M NaOH at 25°C was estimated to be 9.4 x 10^{-21} m^2 s^{-1}, which is three orders slower than the diffusivity in 0.1 M HCl at 25°C (1.4 x 10^{-18} m^2 s^{-1}). Therefore, smaller ligament sizes in alkaline media are attributed to the slower surface mobility of Cu atoms along the alloy–electrolyte interface. This allows controlling the Zn content from 59 ± 3 at.% (NaOH, 8 h) to 37 ± 11 at.% (NaOH, 48 h) independent from the ligament size. Very interestingly, the ligament size could not be increased by simply adding NaCl into 1.3 M NaOH. An opposite trend is even observed, so that the ligament size becomes smaller. This observation is not yet fully understood and further investigations are required. We can sum up that the nature of electrolyte and dealloying temperature have a strong influence on the surface diffusion of Cu atoms and hence on microstructure evolution characteristics of np-materials.

4.4.   Spatial distribution of residual Zn atoms in the ligaments

Further investigations of the spatial distribution of residual Zn atoms within the ligaments of np-Cu were verified using high resolution STEM-EDX technique. EDX mappings of Cu (red) and Zn (green) within a single ligament of np-Cu ribbon (HCl, 168 h) are displayed in **Figure 32**. The average Zn content of the entire ligament (**Figure 32a**) was

found to be 3 at.%, which is in excellent agreement with the SEM-EDX analysis in **Figure 31**. Very interestingly, the overlaid EDX mapping (**Figure 32b**) clearly shows an Zn enrichment up to ca. 12 at.% in these regions, while Zn-poor regions only contain 1 – 2 at.%. Separate EDX mappings of Cu and Zn are also shown in **Figure 32c** and **Figure 32d**, respectively.
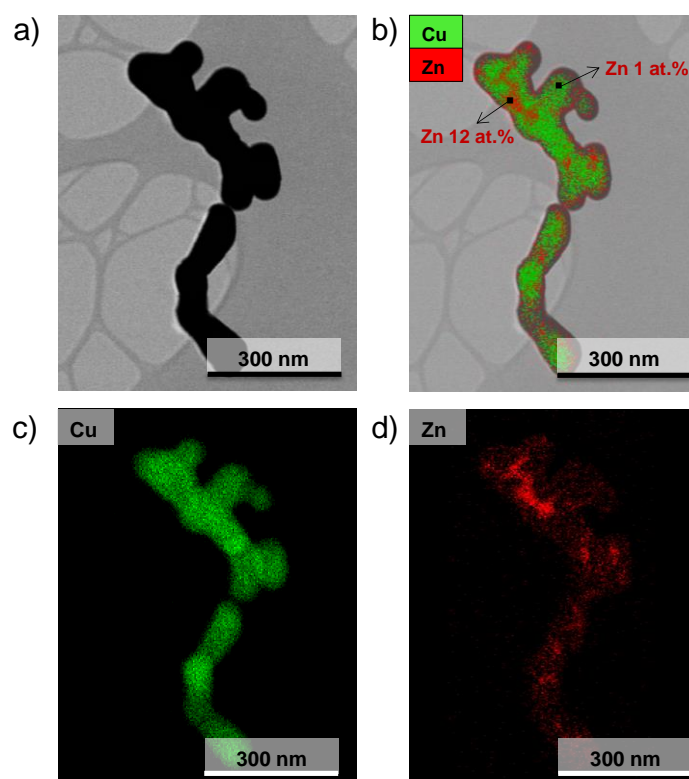
Figure 32: *Elemental EDX mappings of Zn and Cu atoms inside single ligaments of np-Cu materials (HCl, 168 h) probed by STEM-EDX. (a) Bright-field STEM micrograph of single ligaments prepared by dispersion of the np-Cu (HCl, 168 h) in propan-2-ol; (b) Overlaid EDX mapping of Cu (in green) and Zn (in red) of the respective sample area, showing Zn-rich and Zn-poor regions; separate EDX mappings of Cu (c) and Zn (d). Figure reprinted with permission from ref. 52.*

This heterogeneous distribution of the less noble metal has also been reported in np-Au showing Ag rich domains within the ligaments.[206,207] The formation of Ag-rich regions is very likely related to the critical interplay between the Ag dissolution rates and the remaining Au surface diffusion rates. The remaining Au surface atoms might trap the near-surface Ag atoms and prevent their exposure to the corrosive electrolyte for dissolution. This trapping of Zn atoms near the surface by passivation of more noble Cu

surface atoms might explain the appearance of Zn-rich regions inside the np-Cu materials. Thus, we suggest that the residual Zn atoms are located in the relics of the master alloy. Obviously, the average concentration of Zn in the whole ligament is only an approximation, obtained from the bulk EDX, as the local Zn concentration differs within the ligaments. To sum up, the distribution of Zn atoms inside the ligaments of np-Cu materials is heterogeneous and, as a consequence, the appearance of Zn-rich regions near the surface might influence their catalytic properties, e.g. for electrochemical CO_2 reduction reaction.

4.5. Cross-section analysis of np-Cu ribbons

Until now, the porosity of np-Cu ribbons was analyzed by SEM from the plane view (see **Figure 28** and **Figure 29**). To evaluate the dealloying front propagation within the relatively thick ribbons, cross-sectional SEM-EDX analysis of np-Cu ribbons treated at various dealloying time at constant temperature (25 °C) were performed.

Figure 33 displays the cross-sectional SEM micrographs of a selection of np-Cu after dealloying for 24 h and 168 h in HCl and for 24 h in NaOH. As an overview, **Table 5** lists the comparison between the obtained chemical compositions and ligament sizes of np-Cu in the plane and cross-sectional view of the SEM-EDX measurements. In **Figure 33a – a´**, the cross-sectional SEM micrographs of the np-Cu (HCl, 24 h) show a homogeneous porous micro-structure near the surface (comparable to the SEM micrographs in the plane view, (**Figure 28b – b´**), while the inner part is partially solid and dense. Interestingly, the ligaments formed near the surface were found to be smaller with higher Zn content compared to those on the surface. In the cross-sectional and plane view, the mean ligament size and the Zn content for np-Cu (HCl, 24 h) are 56 ± 15 nm at 52 ± 6 at.% and 73 ± 14 nm at 32 ± 5 at.%, respectively. It is noted that the residual Zn content and ligament size measured in the inner part of dealloyed ribbons correspond to the surface composition and ligament size of np-Cu (HCl, 3.5 h). Altogether, we can distinguish three regions for the np-Cu (HCl, 24 h).
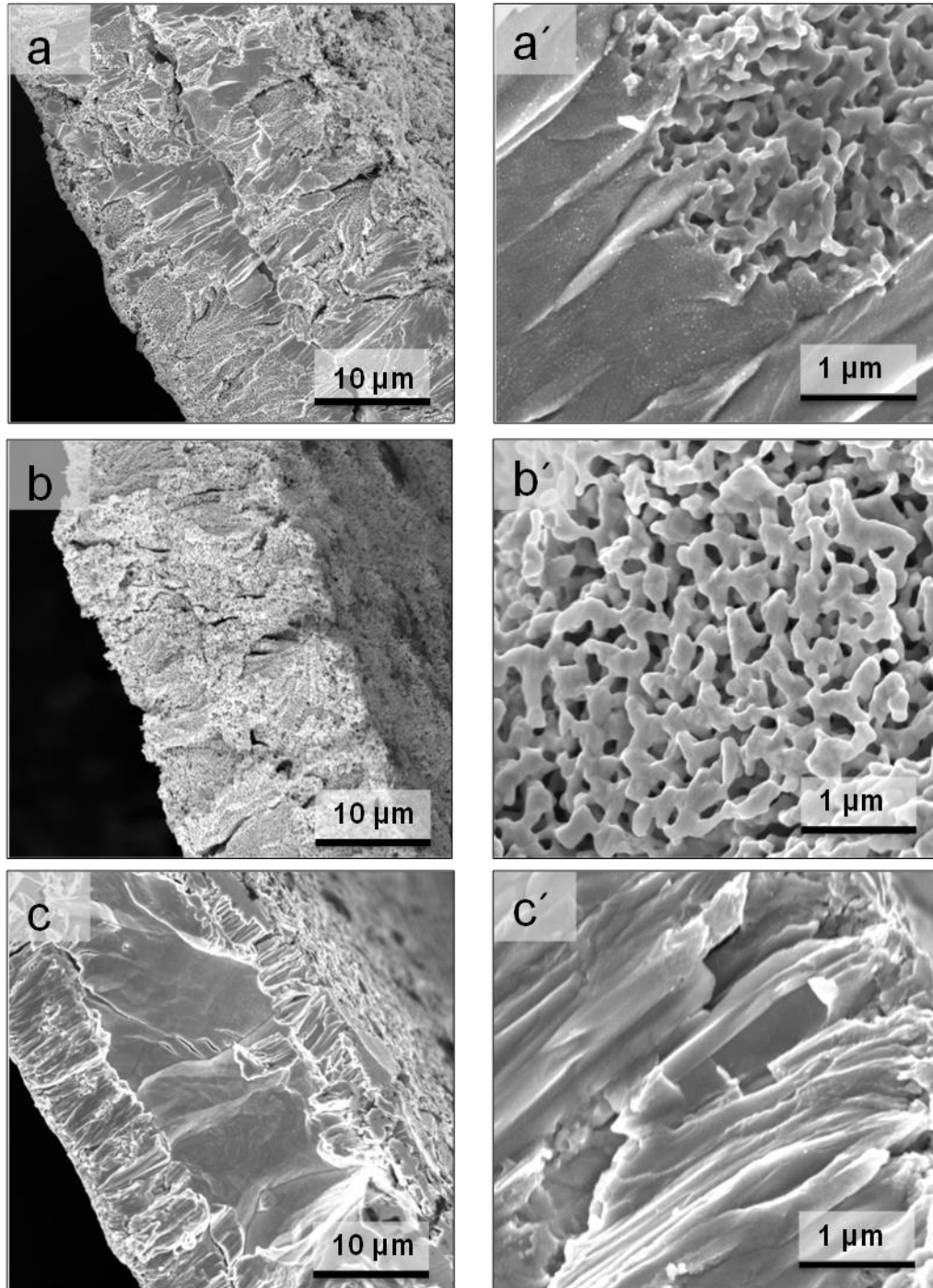
Figure 33: *Low (right) and high (left) magnification cross-sectional SEM micrographs of Zn$_{80}$Cu$_{20}$ ribbons dealloyed in (a, a´) for 24 h and (b, b´) 168 h (7 days) in 0.1 M HCl or (c, c´) for 24 h in 1.3 M NaOH, respectively. Figure reprinted with permission from ref. 52.*

Region I: The surface of the dealloyed ribbons is exposed to the electrolyte all the time and thus commences to coarsen within the 24 hours, resulting in larger ligament size and lower residual Zn content.

Region II: Micro-structure with smaller ligament size and higher Zn content form near the surface of dealloyed ribbons based on the dealloying front propagation within the master alloy ribbons and less exposure time to the highly aggressive electrolyte.

Region III: The center of the master alloy showing dense and solid structure is further unaffected from any dealloying process under free corrosion. Thus, the middle part of the dealloyed ribbons signifies the same composition like the starting alloy ribbons.

With increasing dealloying time, e.g. for 168 h = 7 days, we observed a homogenous pore network in the cross-sectional SEM micrograph of dealloyed ribbons, as shown in **Figure 33b − b´**. The composition of the np-Cu (HCl, 168 h) in the plane and cross-sectional view was found to be very similar (around 3 ± 1 at.%), while the mean ligament sizes is a bit smaller, yet, not very different taking the error bars into account. Therefore, dealloying for longer period enables to form porous network structure that is controlled by varying the nature of electrolyte solution, pH value, dealloying time and temperature.

To have a better understanding of the microstructure evolution characteristics and dealloying front propagation of $Zn_{80}Cu_{20}$ master alloy ribbons during dealloying process in 0.1 M HCl, the dealloying depth during the first 24 h was investigated. It is noted that the total thickness of the ribbons is decreasing during dealloying due to the shrinkage associated with dissolution of large amounts of Zn and phase transformation from hexagonal to cubic structure. More precisely, the total thickness strongly decreased about 45 %, from 35 ± 3 μm to 19 ± 1 μm, after 24 h of dealloying (see **Figure 34a**). **Figure 34b** shows a plot of normalized dealloying depth vs dealloying time. Such a strong shrinkage was also reported for np-Co, where cross-section thickness is decreased by 55% after dealloying.[198] To consider the strong shrinkage of the ribbons, the dealloying depth was normalized by dividing its value by the total thickness of the ribbons at each dealloying time. In **Figure 34b**, we observed a linear relationship between normalized dealloying depth and dealloying time, indicating that the rate of dealloying front propagation is constant. This suggests that the dealloying is controlled

by the interfacial processes.[11,73,208-210] If the mass-transport of electrolyte (diffusion of corrosive electrolyte solution in and out of the porous layers) would be the rate-limiting step, we would have seen slower dealloying front propagation over the dealloying period. Therefore, we conclude that the microstructure of np-Cu is controlled by the interfacial process, which is occurring at the interface between the alloy and electrolyte.

Based on the plane-view SEM micrographs in **Figure 29**, we assumed that the ligaments mainly form at and near the surface of the ribbons dealloyed for 24 h in 1.3 M NaOH. The cross-sectional SEM-EDX analysis (**Figure 33c – c´** and **Table 5**) confirms our observation. Only the surface of the ribbons which is directly exposed to NaOH shows a porous micro-structure, while the inner part is still dense and solid. For the np-Cu (NaOH, 24 h) the content of Zn was found to be 73 ± 3 at.% and 57 ± 9 at.% near the surface (cross-section) and on the surface (in plane), respectively. The solid and dense inner part of the ribbon is very similar in morphology and chemical composition to the starting one (see cross-sectional SEM micrograph of pristine $Zn_{80}Cu_{20}$ ribbons in **Figure S13**). We can sum up that the dealloying process and thus the pore evolution is much slower in alkaline media compared to those in acidic. Since dealloying is an interface-controlled process, Zn dissolution and pore evolution rate control the penetration of the electrolyte and thus the dealloying of the bulk of the ribbons. The small pore network is likely related to the slower surface diffusion rates of the remaining Cu atoms by forming surface (hydr)oxide, which will be discussed in the next section.
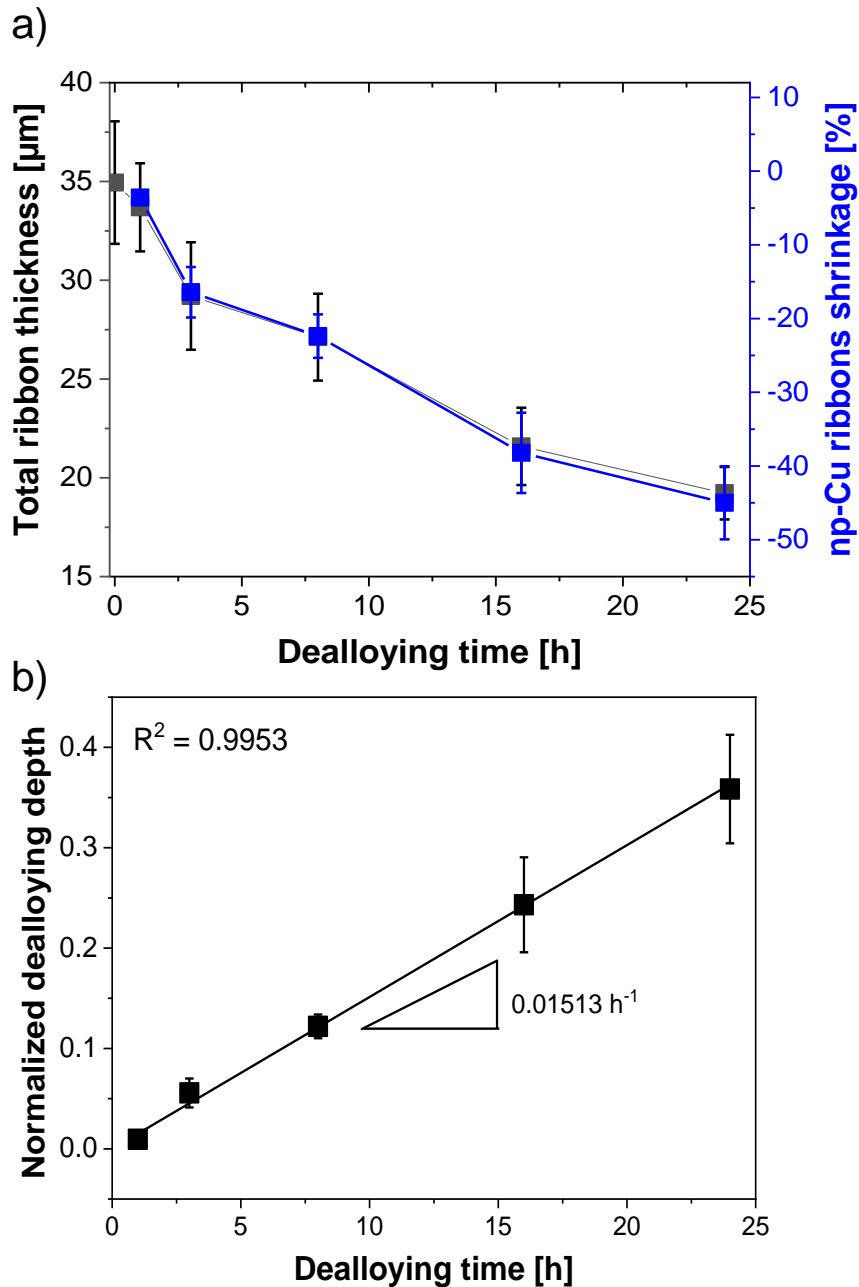
Figure 34: *Shrinkage of ribbons during dealloying and the dealloying rate. (a) Plot of total ribbons thickness at a given time [D_t] in black squares, and np-Cu ribbons shrinkage in thickness [$100x \Delta D/D_0$] in blue vs. dealloying time in 0.1 M HCl at 25°C under Ar atmosphere. D_0 is the thickness of the ZnCu alloy ribbons before dealloying, and the change of thickness was calculated by $\Delta D = D_t - D_0$. (b) Plot of normalized dealloying depth vs. dealloying time in 0.1 M HCl at room temperature under Ar atmosphere. The normalized dealloying depth was calculated by dividing the dealloying depth by the ribbon thickness at a given time (D_t) due to its shrinkage. Each measurement was repeated three times for each sample. Figure reprinted with permission from ref. 52.*

4.6.   Dealloying of $Zn_{80}Cu_{20}$ ribbons in phosphoric acid [not published]

The choice of electrolyte anion during the dealloying process has a significant impact on the formation and properties of the nanoporous structure. The effect of adsorbed chloride anions in enhancing the Cu surface diffusion was clearly observed during dealloying in 0.1 M HCl. On the contrary, previous research reported slower surface diffusion of the noble metal atoms in phosphoric acid (H_3PO_4).[14,23,211] Therefore, in this study, the evolution of ligaments during chemical dealloying of $Zn_{80}Cu_{20}$ alloy ribbons in 15 M H_3PO_4 at 25°C under Ar atmosphere was investigated.
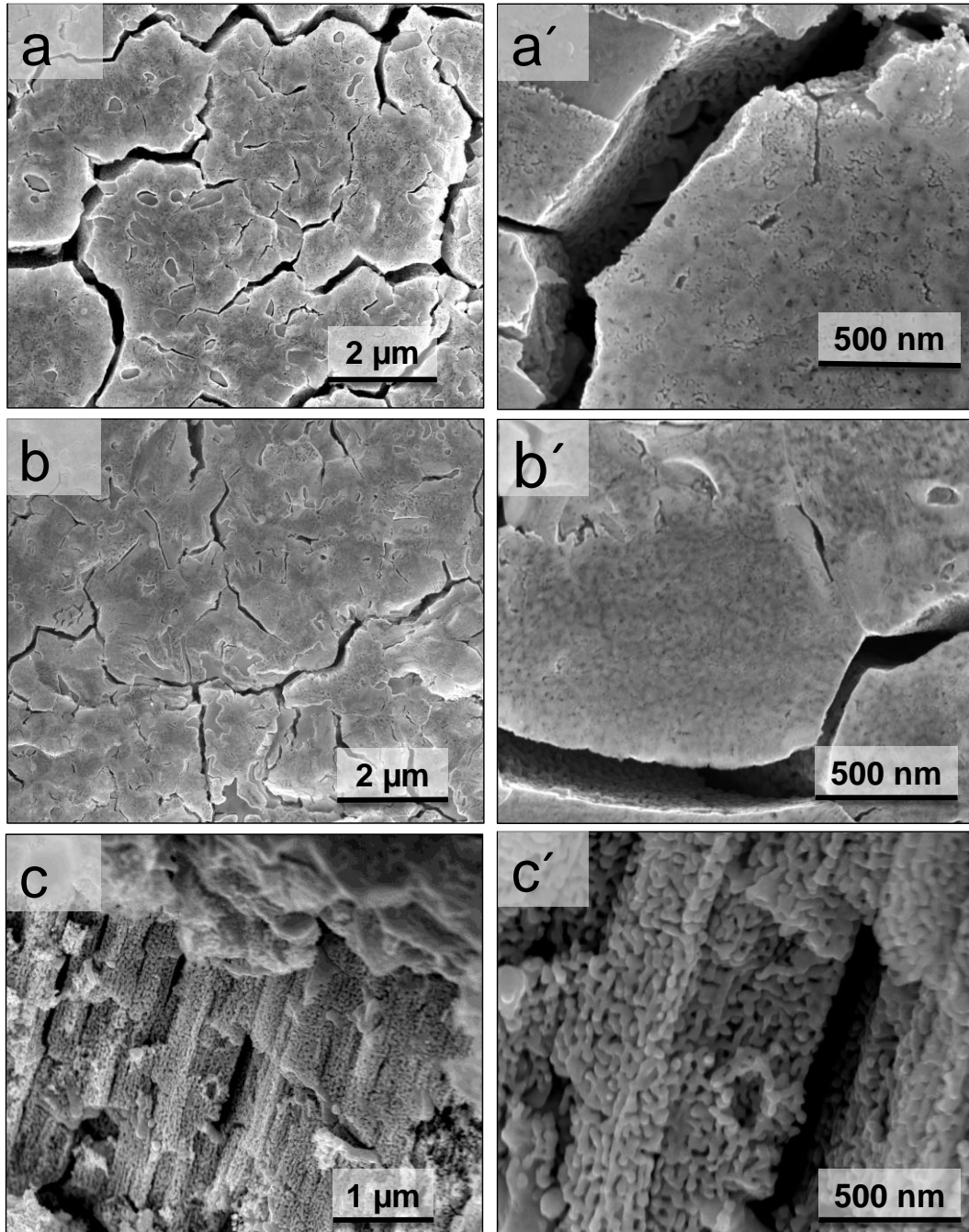
Figure 35: *Series of low (right) and high (left) magnification SEM micrographs of (a, a´, b, b´) plane-view and (c, c´) cross-section of $Zn_{80}Cu_{20}$ ribbons after (a, a´) 3 h and (b, b´, c, c´) 7 h of dealloying in 15 M H_3PO_4 at 25°C under Ar atmosphere.*

Ribbons were taken out from the electrolyte after 3 h of dealloying time, and the formation of several cracks, with width of 276 ± 60 nm, is observed in **Figure 35a**.

During dealloying, significant volume changes occur related to the dissolution of the large amounts of the zinc, causing stress accumulation on the surface of the ribbons and the formation of cracks in the grain boundaries. At higher resolution, the SEM micrographs (**Figure 35a´**) illustrate small ligaments with mean size of 16 ± 3 nm on the surface of the dealloyed ribbons. Interestingly, ligaments were observed within the cracks. When samples were further dealloyed up to 7 h, plane-view SEM images (**Figure 35b – b´**) shows fewer cracks and ligaments. It is expected that the small surface ligaments exposed to the corrosive electrolyte for an extended duration can induce surface stress. In response to this stress, the surface undergoes coarsening as a mechanism to alleviate or reduce surface stress, resulting in surface flattening. On the other hand, the cross-section analysis (**Figure 35c – c´**) displays homogenous micro-structure with ligament size of 37 ± 7 nm. The large cracks formed at an early stage of dealloying allowed the electrolyte to enter the cracks and the dealloying process to proceed into the deeper layers of the ribbons. It is obvious that the ligament-pore structure is remarkably refined compared to dealloyed ribbons in HCl (see **Figure 28** and **Figure 33**), which is in agreement with the literature.[14,211]

To explore the effect of acid concentration, dealloying was carried out in solutions of 5 M H_3PO_4 at 25°C under Ar. **Figure 36a– a´** shows the plane-view of np-Cu ribbons after 7 hours of dealloying, illustrating the presence of cracks, and some pores with no identified ligaments. The cross-section of the dealloyed ribbons (**Figure 36b – b´**) is fully porous with mean ligament size of 44 ± 8 nm. Therefore, a slightly larger ligaments forms in 5 M compared to 5 M H_3PO_4 solutions. This effect is attributed to the influence of phosphate anions on Cu surface diffusivity.

It is well recognized that the adsorption of electrolyte anions on the surface of the ribbons influences the ligament size through its effect on the diffusivity of the noble metal. Surface diffusivity (D_s) of Cu was reported to be 5.49 $\times 10^{-16}$ and 4.75 $\times 10^{-17}$ $m^2 s^{-1}$ in 10 wt.% HCl and H_3PO_4 solutions at 90°C, respectively.[24] Furthermore, the diffusion coefficient of Au and Ag in H_3PO_4 was reported to be 2 – 3 magnitudes lower than in HCl.[23,211] Consequently, the ligament size of np-Cu dealloyed in phosphoric acid is remarkably smaller (see **Table 5**). The higher concentration of phosphoric acid leads to the formation of smaller ligaments (37 ± 7 nm compared to 44 ± 8 nm in 15 M and 5 M

H$_3$PO$_4$, respectively, in the cross-section of the ribbons), due to the additional suppression of the surface diffusion. Here, the pH difference is not expected to play a significant role.[14] Since no precipitation of Zn salts was observed, it is expected that highly soluble zinc dihydrogen phosphate Zn(H$_2$PO$_4$)$_2$ is formed. Therefore, supersaturation of this salt is unlikely to be reached during dealloying in 5 M or 15 M H$_3$PO$_4$ solutions.
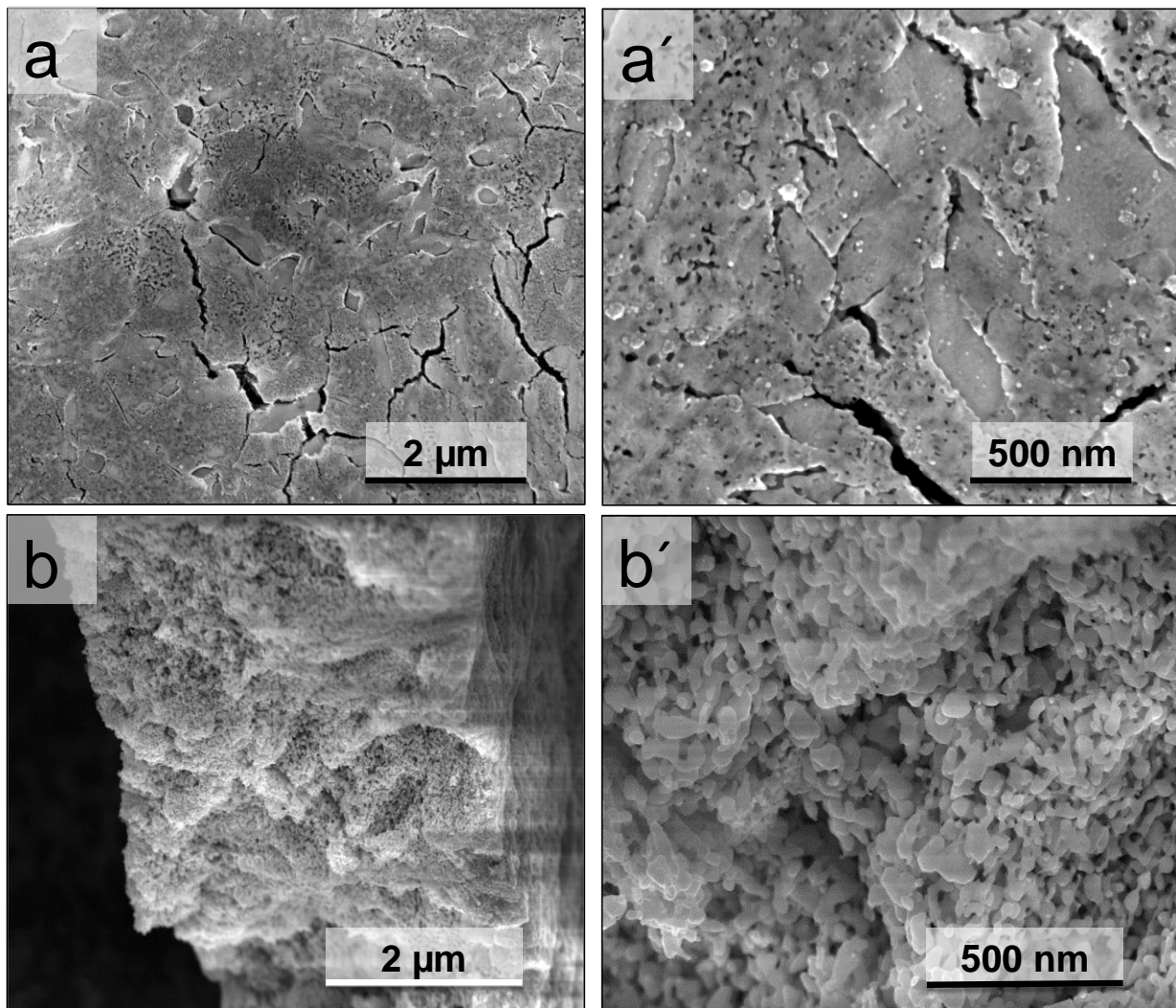
Figure 36: Series of low (right) and high (left) magnification SEM micrographs of (a, a´) plane-view and (b, b´) cross-section of Zn$_{80}$Cu$_{20}$ ribbons after 7 of dealloying in 5 M H$_3$PO$_4$ at 25°C under Ar atmosphere.

The chemical composition of the dealloyed ribbons was investigated with EDX. **Figure 37** displays the changes of Zn content, in plane-view, during dealloying in diluted and concentrated phosphoric acid. During the first 3 hours of dealloying in 15 M H_3PO_4, a drastic drop of Zn content from 77± 1 at.% to 37 ± 6 at.% was observed. Zn content further decreases to 31 ± 4 at. % after 5 h, and reaches 29 ± 3 at.% after 7 h of dealloying. The cross-section of the samples dealloyed for 7 h shows 35 ± 7 at. % Zn, which is comparable to the composition of the plane-view. Similarly, the Zn content in np-Cu dealloyed in 5 M H_3PO_4 was found to be 40 ± 6, 36 ± 5 and 30 ± 4 at.% after 3, 5, and 7 h, respectively. The results indicate that phosphoric acid concentration has only a minor influence on the residual Zn content in the dealloyed ribbons.
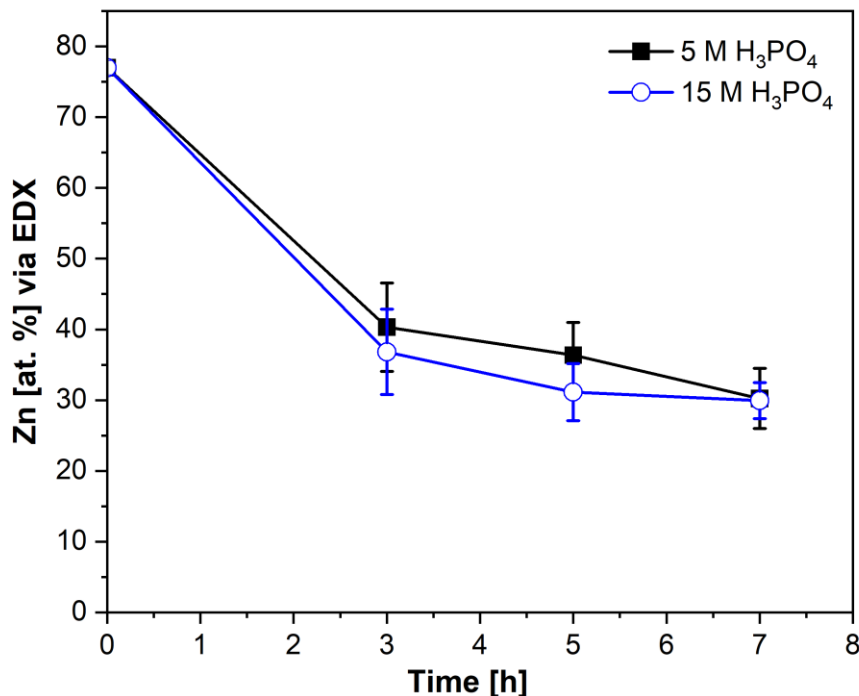
Figure 37: *Residual Zn content after chemical dealloying of $Zn_{80}Cu_{20}$ ribbons for 3, 5, and 7 h in 5 M (black squares) and 15 M (blue hollow circles) H_3PO_4 at 25°C under Ar atmosphere. The EDX quantification of chemical composition was determined from at least three sample areas at low magnification. Each measurement was repeated at least three times for each sample.*

In this study, the distribution of Zn atoms inside the ligaments of np-Cu ribbons dealloyed in H_3PO_4 was not investigated. However, the presence of Zn-rich regions, similar to those observed during dealloying in HCl (**Section 4.4**), is expected. This

heterogenous distribution of Zn is associated with the surface diffusion of Cu atoms during the dealloying process. The formation of islands of Cu atoms results in trapping of some of the near-surface Zn atoms, which cannot be exposed to the electrolyte, and thus cannot be dissolved. The distribution of the less noble metal within the ligaments is not expected to change due to the slower Cu diffusivity in H_3PO_4 compared to HCl solutions.

We conclude that the electrolyte anions play a crucial role in the dealloying process by altering the surface diffusivity of the noble metal. This allows for tailoring of the nanoporous structure by changing the dealloying electrolyte. The coarsening of the surface, resulting in a flattened surface, presents a challenge for the direct application of dealloyed ribbons in H_3PO_4. However, this can be overcome by the preparation of a dispersion of np-Cu that is then drop-casted on a substrate, where the ligaments in the cross-section become available for use. Another approach can be the dealloying in a mixture of HCl and H_3PO_4 to achieve a porous surface with the desired ligament size.

4.7. Understanding ligament evolution in different electrolytes [partially published]

Starting from $Zn_{80}Cu_{20}$ alloy ribbons prepared by melt-spinning, the microstructure evolution characteristics of the np-Cu with highly open and three-dimensional pore network is visualized in **Figure 38**. When the ribbons are immersed in 0.1 M HCl solution, the dealloying process is rapidly initiated by dissolution of Zn atoms from the top Zn-rich surface layer of alloy ribbons. This process leaves the more noble Cu surface atoms unstable and highly low-coordinated. The remaining Cu surface atoms tend to diffuse along the top layers and additional Zn atoms within the near-surface layers are successively exposed to the aggressive electrolyte. Therefore, a critical interplay between Zn dissolution rates and surface diffusion rates of Cu atoms controls the formation of highly porous and well-connected ligament network.

Dealloying is controlled by the interfacial processes mentioned above. In case of using chloride-containing acidic solution, the chloride ions enhance the mobility of Cu surface atoms by 2 – 5 magnitudes compared to a chloride free enviroment.[14,19] Chloride ions

can adsorb on a Cu-based surface, especially at low-coordinated sites and increase its mobility.[19,203] This leads to formation of larger ligaments and pores (**Table 5**). The addition of chloride ions to an alkaline solution showed an opposite effect, which is still not well understood to date. The obtained ligament sizes in this work are in good agreement with the results published from other groups.[14,16,17,20,99,203] An overview about the structural information and its experimental conditions for the formation of np-Cu are listed in **Table 1** (**Section 2.2.1**). The enhanced Cu surface diffusion in HCl allows the dealloying front propagation into the entire ribbons (initial thickness of ribbons of 35 ± 3 µm). Therefore, dealloying in HCl solution allows the formation of homogeneous np-Cu-rich materials.

By immersing the $Zn_{80}Cu_{20}$ alloy ribbons in H_3PO_4, dealloying is rapidly started by dissolution of Zn atoms, followed by surface diffusion of Cu atoms. Contrary to dealloying in HCl, the adsorbed phosphate ions suppress Cu mobility, leading to the formation of smaller ligaments on the surface of the ribbons (16 ± 3 nm after 3 h of dealloying in 5 M H_3PO_4). The diffusion coefficient of Cu, Au and Ag in HCl was reported to be 1 – 3 magnitudes higher than in H_3PO_4.[23,24,211] Consequently, the ligament size of np-Cu dealloyed in phosphoric acid is remarkably smaller than that of HCl (**Table 5**). Moreover, the higher concentration of phosphoric acid leads to more suppression of the surface diffusion and the formation of smaller ligaments (37 ± 7 nm in 15 M compared to 44 ± 8 nm in 5 M H_3PO_4). Very interestingly, the surface undergoes coarsening to reduce surface stress, leading to flattening of the surface. During the initial phase of dealloying, numerous large cracks appeared on the surface as a result of the stress induced by the rapid dissolution of Zn (approximately 30 at. % of Zn was lost within the first 3 hours of dealloying). These cracks allow the corrosive solution to initiate the dealloying into the deeper layer of the ribbons, which over time leads to the a fully porous cross-section. The proposed dealloying mechanism in phosphoric acid is shown in **Figure 38b**.

Table 5: *Comparison of chemical composition and ligament size between the surface (in plane) and cross-section of dealloyed ribbons. Table reprinted with modifications from ref. 52.*

ribbons	Zn [at.%] *via EDX*		Cu [at.%] *via EDX*		ligament size [nm]	
	in plane	cross-sectional	in plane	cross-sectional	in plane	cross-sectional
$Zn_{80}Cu_{20}$ alloy	77 ± 1	78 ± 1	23 ± 1	22 ± 1	-	-
np-Cu (1.3 M NaOH, 24 h)	73 ± 3	57 ± 9	78 ± 3	44 ± 9	21 ± 4	-
np-Cu (0.1 M HCl, 24 h)	32 ± 5	52 ± 6	68 ± 5	48 ± 6	73 ± 14	56 ± 15
np-Cu (0.1 M HCl, 168 h)	3 ± 2	3 ± 1	97 ± 2	97 ± 1	115 ± 28	97 ± 16
np-Cu (5 M H_3PO_4, 7 h)	36 ± 5	-	64 ± 5	-	-	43 ± 8
np-Cu (15 M H_3PO_4, 7 h)	31 ± 4	35 ± 7	69 ± 4	65 ± 7	-	37 ± 7

In alkaline media, the dealloying process is mainly restricted by the slow surface diffusion of Cu (hydr)oxide species, forming when Cu atoms are in exposure to strongly alkaline solution. The surface diffusion coefficient of Cu (hydr)oxide species is suggested to be 2 – 3 magnitudes slower than metallic Cu.[7,17-19] It was also seen from the estimation of the surface diffusivity (D_s) in HCl (1.4 x 10^{-18} m^2 s^{-1}) and NaOH (9.4 x 10^{-21} m^2 s^{-1}) at 25°C in this work. This limits the coarsening process and leads to the formation of smaller ligaments compared to dealloying in acidic media. The slow Cu diffusion and evolution of small ligaments/pores restrict the dealloying front propagation in the thick ribbons. Therefore, the nanoporous structure only forms on the surface and the properties of the original master alloy retain in the bulk. On the other hand, during dealloying in strong alkaline media low-coordinated Cu atoms dissolve in minor concentration and enrich near the alloy surface. We believe that over dealloying time the concentration of soluble Cu species gradually increases until a critical concentration has been achieved. Above this threshold (supersaturation), Cu species commence to re-deposit and grow as Cu(I)oxide crystals at the alloy surface. We suggest that the critical point of the supersaturation is different inside the pores rather than outside of the pores (bulk electrolyte). Therefore, we observed a sudden change in the morphological structure of np-Cu in NaOH due to the formation and growth of Cu(I) oxide seed crystals inside the pores.[7] Both the formation of octahedral Cu_2O crystals and the slow Cu

surface diffusion hinder electrolyte penetration and thus the dealloying of the bulk ribbons.
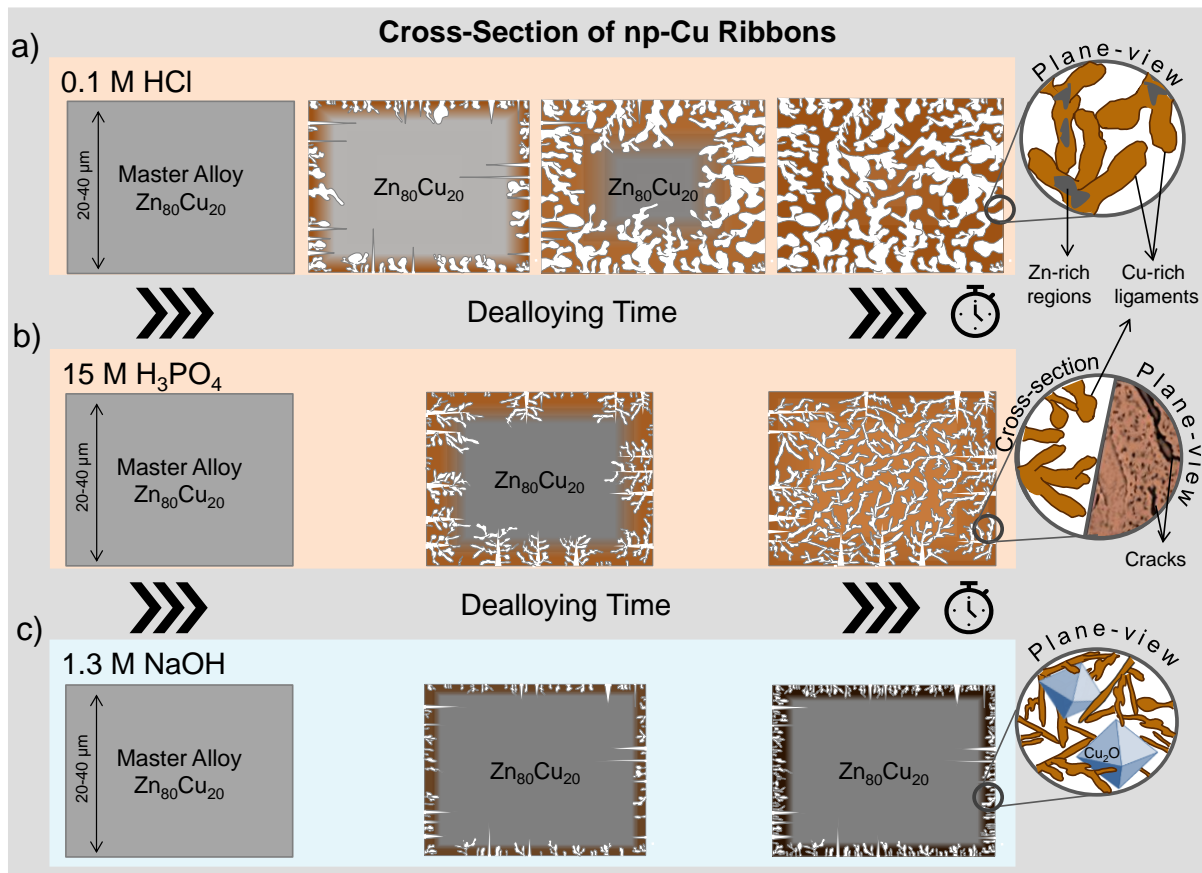
Figure 38: *Schematic of the dealloying front propagation for the pore-ligament evolution of np-Cu ribbons. a) Dealloying in 0.1 M HCl: the first graph represents a cross-section of $Zn_{80}Cu_{20}$ alloy and the next graph displays the formation of cracks and the evolution of ligament on the surface of the ribbons, the following graphs show the dealloying front propagation during the dealloying time. The zoomed graph on the top right represents the plane-view ligaments with Zn-rich regions inside the ligaments. b) Dealloying in 15 M H_3PO_4: the second graph shows the crack formation and evolution of smaller ligaments, the following graph shows the coarsening with flattening the surface and the fully porous cross-section. The zoomed graph on the middle right represents the flattened surface in plane-view and the Cu-rich ligaments in the cross-section. c) Dealloying in 1.3 M NaOH: Over time, ligaments form only on the surface and do not grow into deeper level of the ribbons. The zoomed graph on bottom right shows the plane-view ligaments with octahedral Cu(I)oxide crystals. The master alloy is denoted in grey color, Zn-rich regions in dark-grey, Cu-rich ligaments in brown in acidic media and in brown/black in alkaline media. It is noted that the different dealloying durations were applied in this study, where dealloying in HCl and NaOH was carried out for up to 168 h (13 days), whereas dealloying in H_3PO_4 up to 7 hours. Figure reprinted with modifications from ref. 52.*

We can sum up that the nature of the dealloying electrolyte strongly impacts the dealloying process of thick $Zn_{80}Cu_{20}$ alloy ribbons. Therefore, by controlling the dealloying conditions, like dealloying electrolyte and dealloying time, it is possible to tailor the resulting porous structure and residual Zn content.

4.8.   Summary

This chapter explored the formation of np-Cu by chemical dealloying of $Zn_{80}Cu_{20}$ alloy ribbons in different electrolytes and pH values. The master alloy was prepared by melt-spinning and the obtained alloy ribbons consist of a Zn-enriched surface layer (of ~14 nm), followed by a homogenous sub-surface and bulk composition of 23 ± 1 at.% Cu and 77 ± 1 at. % Zn. The chemical dealloying of the ribbons in 0.1 M HCl, 5 M and 15 M H_3PO_4, and 1.3 M NaOH leads to formation of an extended ligament-pore network with different structural and chemical properties. In particular, the dealloying process in HCl facilitates the Zn dissolution, resulting in a change of the crystal structure from hexagonal $Cu_{20}Zn_{80}$ to cubic $Cu_{38}Zn_{62}$ and finally to cubic Cu. Residuals of Zn of 1 – 2 at.% are enough to preserve the homogeneous ligament structure even after very long dealloying times (13 days). Very interestingly, the distribution of Zn within the single ligaments is inhomogeneous by the formation of local Zn-rich regions near the surface. The appearance of these Zn-rich regions might be very likely related to the passivation behavior of Cu surface atoms and might be relics of the master alloy.

Despite the relatively thick melt-spun ribbons (35 ± 3 µm), kinetics of bicontinuous ligament-pore structure is controlled by the interfacial process instead of the diffusion of corrosive electrolyte solution in and out of the porous layers, referred to as long-range mass transport. Surface diffusivities of Cu at 25°C were determined to be 1.4 x 10^{-18} m^2 s^{-1} and 9.4 x 10^{-21} m^2 s^{-1} in 0.1 M HCl and 1.3 M NaOH, respectively. Therefore, the high Cu surface diffusion rate in HCl enables an enhanced dealloying front propagation into the ribbons, and also coarsening of the ligaments to form larger ligaments. Therefore, in HCl, the ligament size and Zn content are strongly correlated to each other, as the ligament size grows and simultaneously the residual Zn content decreases over the dealloying time. On the contrary, the slow surface diffusion rate of

Cu (hydr)oxide in 1.3 M NaOH solution strongly limits the dealloying process and form smaller ligaments, independent from the residual Zn content.

The anions of the acidic electrolyte have great impact on Cu diffusivity. The observed enhanced Cu mobility in HCl is associated with the adsorbed chloride anions of the low-coordinated Cu atoms, leading to larger ligaments. On the contrary, phosphate anions in H_3PO_4 suppress the surface diffusion coefficient of Cu by 2 – 3 magnitudes compared to HCl, which leads to the formation of smaller ligaments. Furthermore, the effect of different dealloying conditions was also investigated. Agitation and de-aeration of the acidic electrolyte has no significant influence on the structure of np-Cu. On the other hand, dealloying temperature strongly influences the surface diffusivity of Cu, leading to a strong relationship between dealloying temperature and the np-Cu structure.

This study describes the formation of np-Cu materials with tunable ligament size and residual Zn content starting from alloy ribbons, which allows the modification of the structural and chemical properties of np-Cu material for a wide range of possible applications in electrochemical synthesis, sensors and catalysis.

5. Electrosynthesis of cyclic carbonates from epoxide and CO_2 on nanoporous copper cathode

This chapter is reprinted in adapted form from a submitted manuscript to a journal, titled "Nanoporous Copper for the Electrosynthesis of cyclic carbonates from CO_2 and epoxide".

Co-authors contribution: D. Crespo prepared the master alloy. S. Blaseio performed Raman spectroscopy measurements and participated in the discussion of the results. A. Hockmann performed the blank experiment, G. Hilt and M. Oezaslan contributed in the supervision of the whole work, discussion of results and editing the manuscript.

5.1. Morphological and structural characterization of np-Cu/GC

Nanoporous copper (np-Cu) was fabricated by chemical dealloying (free corrosion) of melt-spun $Zn_{80}Cu_{20}$ alloy ribbons in 0.1 M HCl at 25°C in Ar atmosphere. Due to the high mass loss of zinc (from 77 ± 1 to 3 ± 2 atomic%), a volume shrinkage of ~45% was observed after 168 h of dealloying, leading to the evolution of bicontinuous np-Cu ribbons consisted of a ligament-pore network.[52] To produce a practical electrode for the applications in organic electrosynthesis, the np-Cu was drop-casted on a glass carbon (GC) substrate (np-Cu/GC). These preparation steps are displayed in **Figure 15**, and was often reported for other dealloyed ribbons such as silver (np-Ag[212]), boron (np-B[213]), and platinum (np-Pt[214]) electrodes in the literature. Different shapes and dimensions of substrates can be used, which gives huge flexibility for preparing individual porous electrodes with controlled loading.

The morphology of the np-Cu/GC was evaluated by scanning electron microscopy (SEM). The SEM micrographs at low magnification are displayed in **Figure 39a – b**, showing a homogenous spatial distribution of the np-Cu on the GC substrate. No agglomeration of the dispersion was noticed. In the SEM micrographs at higher magnification (**Figure 39c – d**), the porous structure as a network of pores and Cu-rich ligaments is visible. The mean ligament size was estimated by counting at least 200 ligaments from several SEM micrographs and found to be 112 ± 16 nm. It is noted that

the GC substrate surface is not fully covered with np-Cu. Therefore, the coverage was estimated using thresholding method, where pixels with intensity values lower than 45, 52 or 60% were replaced by red pixels, see **Figure 39a' – b'**. From the area of the exposed GC, the mean coverage of the substrate with np-Cu was estimated to be $77 \pm 3\%$. Moreover, the film thickness of the np-Cu was calculated from the mass, coverage, and Cu density (8.96 g·cm^{-3}) to be ~0.9 ± 0.1 μm. Energy-dispersive X-ray spectroscopy (EDX) measurements of the np-Cu/GC show very high carbon content (> 90 atomic%), which is attributed to the elemental analysis of the bulk of the electrode rather than the thin layer of np-Cu on the substrate surface.
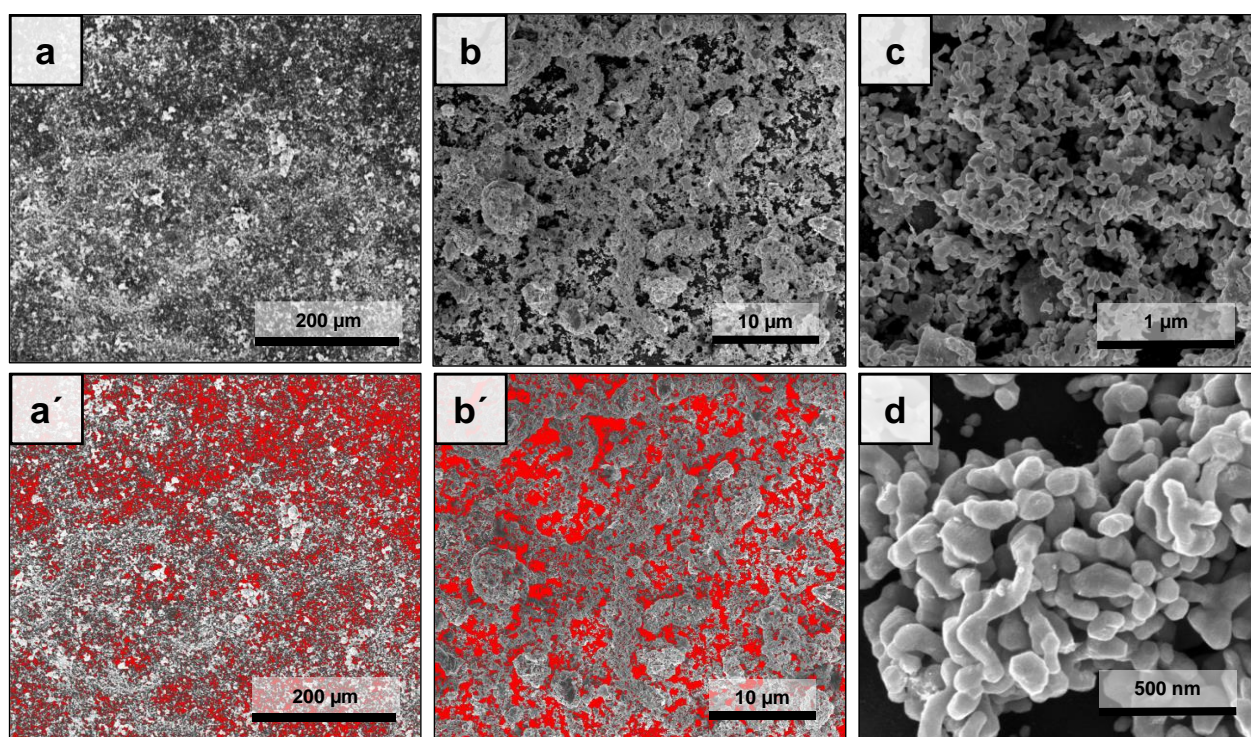
Figure 39: *Series of SEM micrographs of nanoporous Cu drop-casted onto a GC substrate (np-Cu/GC) with different magnifications of (a, a') 250x, (b, b') 3,500 x, (c) 25,000x, and (d) 80,000x. (a', b') Thresholding method was used in ImageJ software, where pixels with intensity lower than 52% were changed to red, indicating a coverage of $77 \pm 3\%$ for the GC surface with np-Cu (loading 1 mg·cm$^{-2}_{geo}$). Figure reprinted from the manuscript submitted to a journal.*

5.2. Estimation of the electrochemically active surface area

5.2.1. Underpotential deposition of lead (Pb-UPD) [not published]

The electrochemically active surface area (ECSA) of the np-Cu/GC was investigated by Pb-UPD method. This technique is based on the unique ability of Pb to form a monolayer on the surface of Cu at potentials positive than those of Pb/Pb^{2+} equilibrium.[192,193,215] Pb-UPD has been successfully applied for the ECSA determination of nanoporous gold (np-Au).[216] The procedure involves analyzing samples of a flat metal surface to get the charge, which is then normalized by the pseudo-capacity obtained from the porous surface of the same metal. Therefore, the Pb-UPD measurements were first tested on polycrystalline Cu by recording CV profiles at a potential range from 0.4 V to 0.0 V vs Pb/Pb^{+2} and a scan rate of 0.01 V s^{-1}, using Pt mesh and Pb wire as counter and reference electrodes, respectively. Blank measurements were done in a solution containing 0.01 M perchloric acid ($HClO_4$) and 0.1 M sodium perchlorate ($NaClO_4$). In the absence of Pb^{+2}, no faradic current occurs, as shown in **Figure 40a** (dotted black line). Thereafter, CV profiles were acquired in solutions containing 0.01 M lead(II) perchlorate hydrate ($Pb(ClO_4)_2$) in addition to 0.01 M $HClO_4$ and 0.1 M $NaClO_4$. In Pb-containing solutions, two broad peaks were observed (**Figure 40a**, blue). The cathodic peak **I**, occurring at approximately 0.08 V vs Pb/Pb^{+2}, represents the deposition of Pb monolayer on the surface of Cu. The anodic peak **II**, observed at 0.19 V vs Pb/Pb^{+2}, demonstrates the stripping of the Pb monolayer.

It is reported that the presence of chloride anions (Cl^-) enhance the kinetics of Pb-UPD on the Cu surface, leading to sharpening and improved reversibility of the peaks.[215,217] The adsorbed chloride layer on the surface of Cu is displaced during Pb-UPD, forming a compact layer of Pb atoms.[217] Consequently, 0.05 M sodium chloride (NaCl) was added to the electrolyte, and the orange-colored CV in **Figure 40a** clearly shows well-defined Pb-UPD features on the polycrystalline Cu surface. In the cathodic scan, peaks **III** and **IV** were observed at 0.12 V and 0.08 V vs Pb/Pb^{+2}, where the deposition of Pb monolayer takes place. This peak split can be attributed to different crystallographic orientations of the Cu surface.[215] The stripping peak **V** in the anodic scan appears at 0.15 V vs Pb/Pb^{+2}, which is slightly shifted compared to chloride-free solution (0.19 V).

Our results are in agreement with the literature[215,217] that the presence of chloride ions in the solution positively impacts the characteristics of the Pb-UPD process.
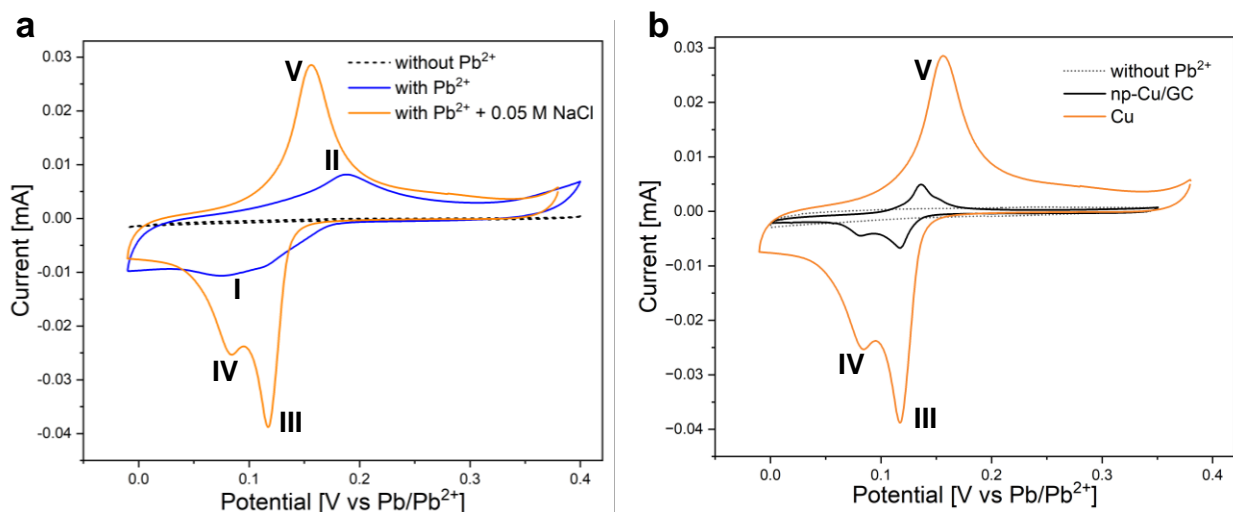
Figure 40: *Pb-UPD measurements, where CV profiles were recorded at 0.01 V s⁻¹ (a) using polycrystalline Cu working electrode in different electrolytes: Pb-free electrolyte (0.01 M HClO₄, and 0.1 M NaClO₄; dotted black), Pb-containing electrolyte (0.01 M HClO₄, 0.1 M NaClO₄, and 0.01 M Pb(ClO₄)₂; blue), and in Pb- and Cl-containing electrolyte (0.01 M HClO₄, 0.1 M NaClO₄, 0.01 M Pb(ClO₄)₂, and 0.05 M NaCl; orange); (b) on np-Cu/GC (solid black) and polycrystalline Cu (orange) in the Pb- and Cl-containing electrolyte. Peaks I, III, and IV correspond to the deposition of Pb monolayer on the surface of the electrode, whereas peaks II and V indicate the subsequent stripping of this monolayer.*

After finding the optimal electrolyte solution, Pb-UPD measurements were performed on the np-Cu/GC. CV profiles were recorded on the np-Cu/GC at potentials from 0.4 to 0.0 V vs Pb/Pb²⁺ at 0.01 V s⁻¹ in Pb- and Cl-containing electrolyte (0.01 M HClO₄, 0.1 M NaClO₄, 0.01 M Pb(ClO₄)₂, and 0.05 M NaCl).

Figure 40b shows the Pb-UPD on np-Cu/GC (solid black) with two deposition peaks at 0.12 V and 0.08 V and a stripping peak at 0.13 V vs Pb/Pb⁺². The averaged integrated charge of deposition and stripping peaks of Pb-UPD, $\bar{Q}_{\text{dep./strip.}}$, was estimated from the CV profiles. The charge, Q, was obtained by dividing $\bar{Q}_{\text{dep./strip.}}$ by the scan rate, v (**Equation (5)** in **section 3.3.2**). The charge was calculated to be 25 and 140 µC for np-Cu/GC and polycrystalline Cu, respectively. These charge values were normalized by the charge of one monolayer of Pb on pure flat Cu (300 µC cm⁻²)[192,193] to give an ECSA

of 0.08 cm^2 for np-Cu/GC and 0.47 cm^2 for polycrystalline Cu. Accordingly, the roughness factor, *RF*, of polycrystalline Cu was determined, by dividing ECSA to the geometric surface area (0.196 cm^2) to be 2.3. This is in agreement with the literature, where RF values of 1.8 were reported for rough polycrystalline Cu.[215]

Surprisingly, the np-Cu/GC shows an extremely low RF value of 0.4, which is probably related to the oxide species on the surface of the electrode, hindering the formation of Pb monolayer. The Cu oxides are formed by contact with air during the preparation of the electrode, i.e., during the drop-casting process used to create a thin film of np-Cu on the GC substrate. To confirm this assumption, the surface of the np-Cu/GC was analyzed by XPS after the Pb-UPD measurement. The electrode was washed well, dried under Ar, and directly transferred to the XPS chamber. **Figure 41** shows the survey and high resolution XPS spectra of Cu 2p, Zn 2p, Pb 4f, O 1s, and C 1s of the np-Cu/GC. In **Figure 41a– b**, the Cu 2p and Zn 2p XPS spectra were deconvoluted and fitted with a doublet for Cu 2p$_{1/2}$ and Cu 2p$_{3/2}$ at 952.3 and 932.5 eV as well as for Zn 2p$_{1/3}$ and 2p$_{3/2}$ at 1045.1 and 1022.1 eV, respectively. The low intensity of the Zn 2p data indicates its minor content on the surface of np-Cu/GC. The Cu satellites observed at about 946 eV (**Figure 41a**, green line) signify the presence of Cu^{2+}.[218,219] Furthermore, the XPS spectrum of oxygen (**Figure 41c**) demonstrates the predominance of metal hydroxides (peak maxima at 532.4, blue line), along with some metal oxides (at 530.4 eV, green line). **Figure 41d** shows the Pb 4f XPS spectrum, which were deconvoluted and fitted with a doublet for Pb 4f$_{5/2}$ and Pb 4f$_{7/2}$ at 138.3 and 143.1 eV, respectively. The XPS spectrum of C 1s (**Figure 41e**) shows the presence of C sp^2, C sp^3 and C-O peaks at 284.4, 285.2, and 586.0 eV, respectively. Quantification analysis was conducted based on the above fitted peaks showed a content of 81.2 at.% C, 15.5 at.% O (among which are 14.5 at.% metal hydroxide), 2.6 at.% Cu (2p), 0.4 at.% Zn (2p), and 0.3 at.% Pb (4f). The high content of carbon comes from the GC substrate of the np-Cu/GC electrode. The high content of oxygen and the presence of Cu^{2+} on the surface of the np-Cu/GC support our assumption that copper (hydr)oxide species impede the formation of Pb monolayer on the surface of np-Cu/GC.
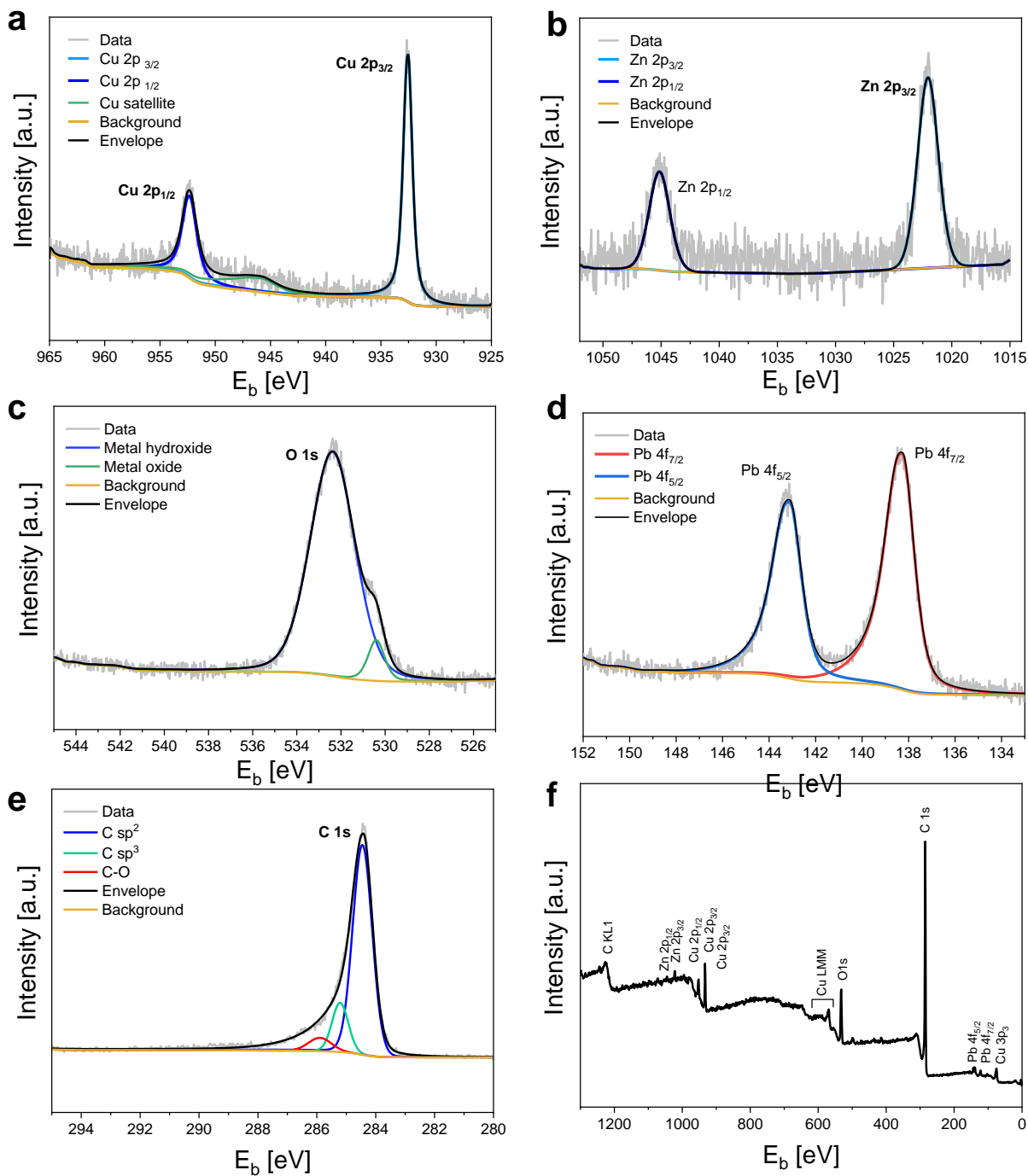
Figure 41*: High resolution XPS spectra of (a) Cu 2p, (b) Zn 2p, (c) O 1s, (d), Pb 4f, (e) C 1s, and (f) survey of the np-Cu/GC surface after Pb-UPD measurement. The experimental data are denoted in grey, the resulting envelope is symbolized in black, and the background is indicated in yellow.*

As an attempt to chemically remove surface Cu oxides, the np-Cu/GC was immersed in concentrated phosphoric acid for few minutes before the Pb-UPD experiments. This step was not enough to remove the surface oxide species, or it is possible that the surface was oxidized during the short exposure to air while handling the sample. This rapid oxidation is attributed to the large surface area of np-Cu. A possible option for future investigations can be the electrochemical reduction of the surface Cu (hydr)oxide species in the same electrolyte, directly before conducting Pb-UPD measurements. In this way, any contact with air is eliminated. To sum up, under the conditions of this study, it is not possible to determine ECSA for np-Cu/GC using the Pb-UPD approach. Consequently, the double-layer capacitance method was investigated for this purpose instead.

5.2.2. Double-layer capacitance

Due to its bicontinuous ligament-pore structure, the np-Cu/GC has a larger surface area than a polycrystalline flat Cu electrode. The electrochemically active surface area (ECSA) of np-materials was determined by the double-layer capacitance method, which has been often reported for oxide-derived Cu foams[195], np-Ag ribbons[212], carbon sphere-loaded Cu nanoparticles[173], and oxide-derived Cu nanorods[220]. In this study, double-layer capacitance measurements were carried out by recording CV profiles in a potential range, where no apparent faradaic processes occur. **Figure 42a – b** shows the CV profiles for the np-Cu/GC and bare GC from –0.1 to –0.2 V vs Ag/AgCl at scan rates of 0.02, 0.04, 0.05, 0.075, 0.10, and 0.15 V·s^{-1} in Ar-saturated 0.1 M aqueous $HClO_4$. It is obvious that for both electrodes only capacitive currents are dominant in this potential range.

In **Equation 13**, the double-layer charging current, i_C, is proportional to the scan rate, v, and electrochemical double-layer capacitance, C.[173,194,195]

$$i_C = v * C \qquad \text{Equation (13)}$$

In **Figure 42c**, for np-Cu/GC and bare GC the i_C values at a potential, E, of –0.15 V vs Ag/AgCl were plotted against the scan rate, v. The double-layer capacitance for the np-

Cu, $C_{np\text{-}Cu}$, was estimated from the slope of the linear fit, calculated from three samples, to be 11.3 ± 1.3 µF. Due to the incomplete coverage, a bare GC was taken as reference and shows a double-layer capacitance, C_{GC}, of 3.8 ± 0.8 µF, see **Figure 42d**. The roughness factor (RF) of the np-Cu/GC was then determined by **Equation 14** to be 3.0 ± 0.7, confirming its enhanced ECSA compared to bare GC.

$$RF = C_{np\text{-}Cu/GC} / C_{GC} \qquad \textbf{Equation (14)}$$
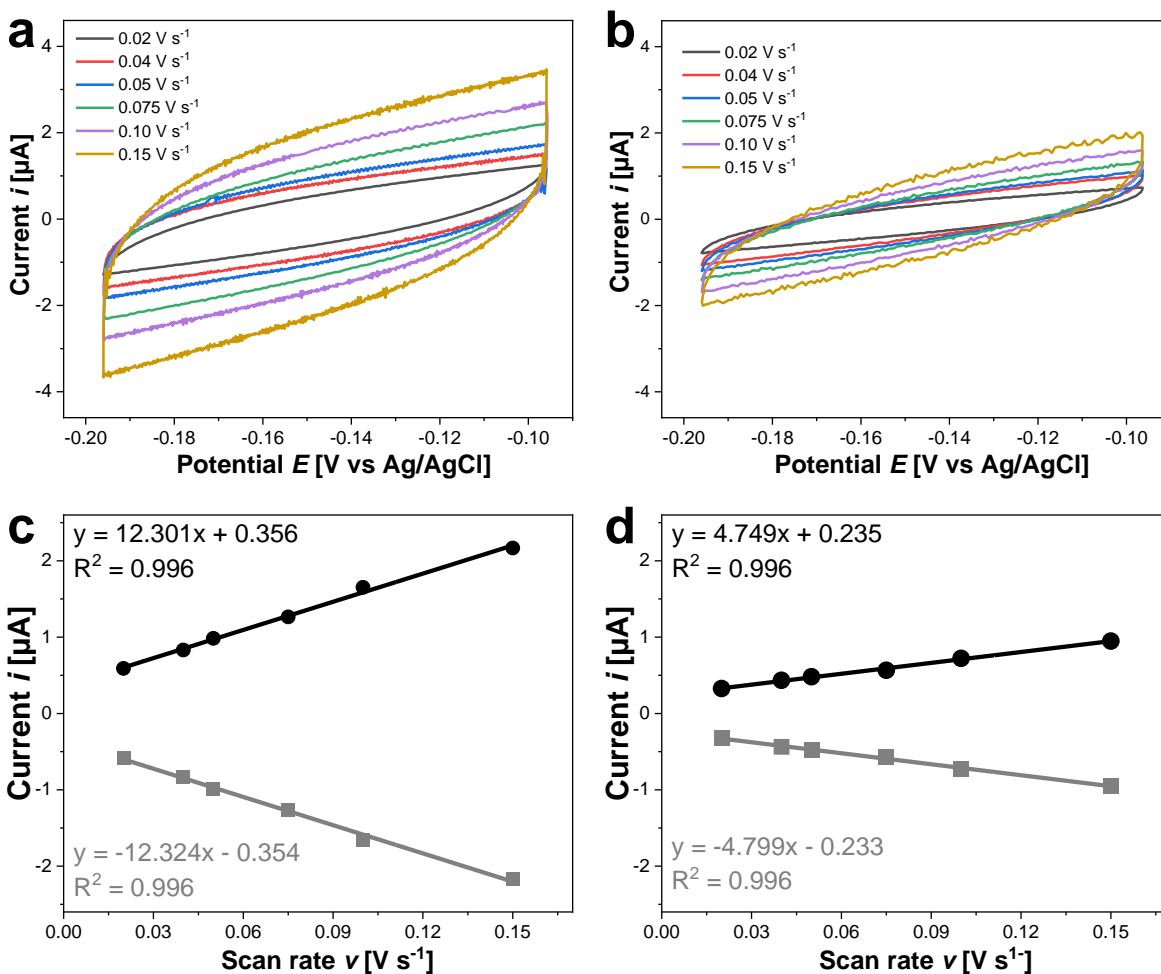
Figure 42: *CV profiles and current i - scan rate v plots of (a, c) np-Cu/GC and (b, d) bare GC at different scan rates, v, in argon-saturated 0.1 M aqueous HClO₄. The data was fitted using the least-squares model, showing a R^2 value of 0.996. The slope of the linear fit gives the double-layer capacitance of the respective electrode material. Figure reprinted from the manuscript submitted to a journal.*

It is noted that the polycrystalline Cu has a much lower double-layer capacitance (0.38 ± 0.04 µF) than that of bare GC (see **Figure 24** in **Section 3.3.3**) and would deliver extremely high ECSA for np-Cu/GC. The above characterizations show interesting features of the np-Cu/GC with a ligament-pore network and large ECSA compared to bare GC.

5.3. Catalytic properties of np-Cu/GC for the electrochemical CO_2 reduction reaction (CO_2RR)

It has been reported that the electrochemical reaction of CO_2 with epoxides is initiated by the formation of the $CO_2^{\bullet-}$ radical species on the electrode surface.[41,42] Therefore, we investigated the electrochemical properties of the np-Cu/GC towards CO_2RR by recording CV profiles in CO_2-saturated 0.07 M TEAI-MeCN between -1.0 and -2.0 V vs Ag/AgCl[iR-corrcted] at 0.02 V s^{-1}, see **Figure 43**. First, a background measurement was carried out in the absence of CO_2, where a CV profile (dotted black, **Figure 43**) was recorded in N_2-saturated electrolyte under similar conditions. In the forward scan, only capacitive currents occur up to -1.9 V vs Ag/AgCl. Thereafter, a small reduction current peak appears, which can be associated with the hydrogen evolution reaction (HER). In the presence of CO_2 (solid black, **Figure 43**), the onset potential is at ca. -1.4 V vs Ag/AgCl, where the current density related to the CO_2RR starts to increase. With increasing overpotential, additional broad current peak between -1.61 and -1.75 V vs Ag/AgCl appears during CO_2 electrolysis. The first reduction peak is ascribed to one electron reduction of CO_2, generating the $CO_2^{\bullet-}$ anion radical.[27,177] The subsequent broad current peak could be due to the further reduction of $CO_2^{\bullet-}$ to form carbon monoxide or hydrocarbons.[44]

The catalytic CO_2RR activity of np-Cu/GC was compared to two reference materials: bare GC (grey) and polycrystalline Cu (orange), see **Figure 43**. The onset potentials for CO_2RR were observed at around -1.7 V and -1.4 V vs Ag/AgCl for bare GC and polycrystalline Cu, respectively. In addition, the CO_2 reduction peak appears at ca. -1.9 V for bare GC, while for the polycrystalline Cu a broad current peak is visible at around -1.6 V. Due to the high overpotential, the GC is less efficient in electrochemically

catalyzing the CO_2. At the upper vertex potential of –2.0 V vs Ag/AgCl, much higher current density was observed for the np-Cu/GC (–2.0 mA·cm^{-2}) compared to polycrystalline Cu (–1.3 mA·cm^{-2}), which is associated with its higher ECSA. In the literature, the CO_2 reduction peaks on Cu nanoparticle-based electrode with particle sizes of 100 and 300 nm were reported at around –1.5 V and –1.6 V vs Ag/AgI in 0.1 M TEAI-MeCN, respectively.[177]

Altogether, our findings demonstrate a higher catalytic CO_2RR activity on the np-Cu/GC compared to polycrystalline Cu and bare GC. Further experiments were carried out to investigate whether the enhanced catalytic activity is directly correlated to the formation of cyclic carbonates from CO_2 and epoxides and will be discussed in **Section 5.4.2**.
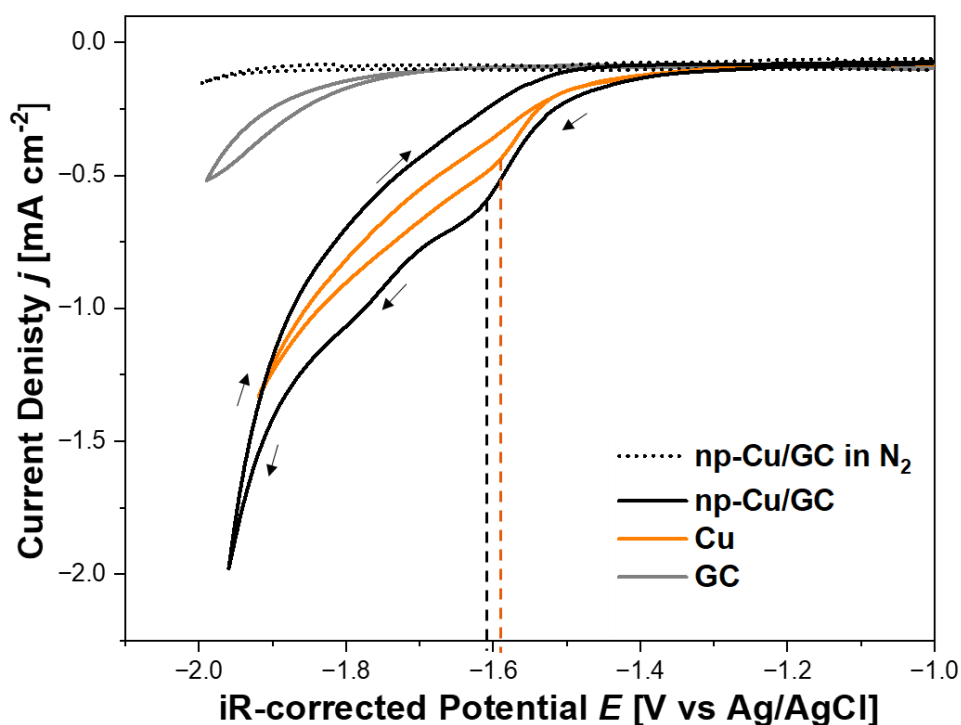
Figure 43: *CV profiles of the np-Cu/GC (solid black), polycrystalline Cu (orange), and bare GC (grey) at scan rate of 0.02 V·s^{-1} in CO_2-saturated 0.07 M TEAI-MeCN. A background measurement was performed on np-Cu/GC in N_2-saturated electrolyte (dotted black). The current density, j, is normalized to the geometric surface area of the working electrode. Figure reprinted from the manuscript submitted to a journal.*

5.4. Organic electrosynthesis of cyclic carbonates

After structural characterization and CO_2RR activity investigations, the np-Cu/GC was used as cathode for the electrosynthesis of cyclic carbonates from CO_2 and epoxides. Based on the literature[38,42,151,172,173,178], a galvanostatic electrosynthesis was performed in an undivided cell, using epoxides as starting material and acetonitrile as solvent. In **Section 5.4.1**, further reaction parameters were experimentally tested to optimize the yield of cyclic carbonates.

5.4.1. Effects of reaction parameters

The influence of various experimental parameters on the yield of cyclic carbonates was explored, including supporting electrolyte, current, charge, anode, and cathode materials. For this work, the formation of 1,2-butylene carbonate (BC) from 1,2-butylene oxide (BO) and CO_2 was used as a model reaction. The results are summarized in **Table 6**, where the upper section shows the reaction with the optimized parameters, and entries 1 - 14 show the variations of the reaction parameters. First, the optimal concentration of BO was identified to being 0.1 M (see **Section 7.4.1.** in the **Supporting information for chapter 5**) No other byproducts were detected by gas chromatography-mass spectroscopy.

5.4.1.1. Blank reaction without applied current

To investigate whether CO_2 activation is essential for the reaction, a control experiment was performed without applying any electric current. A reaction solution of 0.1 M TBAB-MeCN with 0.1 M BO, and 0.02 M dry $MgBr_2$ was left with continuous stirring in an undivided cell under constant flow of CO_2 at room temperature and atmospheric pressure. To mimic the electrosynthesis, polycrystalline Cu and Mg electrodes were also immersed in the solution. Evidently, the GC and GC-MS data show that no product was formed after 18 h reaction time (**Table 6, entry 2**). This observation is in excellent agreement with other studies.[23,27,45] Only a very small amount of the starting material was ring-opened to form 1-bromobutan-2-ol. These findings clearly reveal that the role of the electrochemical process is not only to generate Mg^{2+} cations, but also to activate CO_2. Therefore, the electrochemical CO_2 activation is necessary for the reaction with epoxides under ambient conditions.

5.4.1.2. Influence of supporting electrolyte

The effect of two quaternary ammonium salts, tetraethylammonium iodide (TEAI) and tetrabutylammonium bromide (TBAB), on the yield of BC was investigated. Electrolysis of BO towards BC was conducted using np-Cu/GC cathode and Mg anode in CO_2-saturated 0.07 M TBAB or TEAI in MeCN. After a total charge of 2.0 F was passed, yields of BC of $61 \pm 3\%$ and $70 \pm 4\%$ were formed in 0.07 M TBAB-MeCN and TEAI-MeCN, respectively (**entries 3 – 4** in **Table 6**). The superior performance of TEAI compared to TBAB required further examination of its concentration. Increasing the concentration from 0.07 to 0.1 M TEAI in MeCN resulted in a slight improvement of the yield of BC from $70 \pm 4\%$ to $74 \pm 4\%$. A further increase in the concentration was not possible due to the limited solubility of TEAI in MeCN. Consequently, 0.1 M TEAI-MeCN was used as electrolyte solution in all further experiments.

The improved yield of BC due to the use of TEAI can be related to the stronger nucleophilicity of the halide anions (I⁻), which facilitates the opening of the epoxide ring.[172,174] Zhang et al.[174] observed a direct correlation between the relative strength of the halide in the quaternary ammonium salt (I⁻ > Br⁻ > Cl⁻) and an increase in the yield of propylene carbonate (PC). In addition to the halide, the alkyl chain of the quaternary ammonium salts could also influence the conversion. For example, higher yields were reported for tetraethylammonium bromide (TEAB) compared to TBAB.[174] The use of ethyl groups in the TEA cation enhances their mobility in MeCN, leading to higher conductivity.[174] Therefore, due to the highly nucleophilic nature of iodide and shorter alkaline cation groups, the TEAI is the most suitable supporting electrolyte for the electrosynthesis of BC from BO and CO_2.

Table 6: *Effect of the reaction parameters for the electrosynthesis of 1,2-butylene carbonate (BC). Table reprinted from the manuscript submitted to a journal.*

$+ \quad CO_2$ (1 bar)

np-Cu/GC cathode
Mg anode, RT

0.1 M TEAI-MeCN
2.0 mA·cm^{-2}, 2.0 *F*

Entry	Variation parameter	Yield [a]
1	None	**74 ± 4%**
2	Blank - no current*	-
Supporting electrolyte		
3	0.07 M TBAB	61 ± 3%
4	0.07 M TEAI	70 ± 4%
Current density [mA·cm^{-2}]		
5	2.8	74 ± 2%
6	6.5	28 ± 3%
Charge [*F*]		
7	1.0	48 ± 3%
8	1.5	59 ± 4%
9	2.5	73 ± 3%
10	3.0	72 ± 3%
11	3.5	72 ± 2%
Cathode material		
12	bare GC	19 ± 3%
13	polycrystalline Cu	76 ± 4%
Anode material		
14	polycrystalline Zn	2% [b]
15	bare GC	-

The reactions were performed using np-Cu/GC cathode material in an undivided cell at room temperature. BO: 0.1 M. The electrolyte was saturated with CO_2 for 30 min before the experiment. A balloon filled with CO_2 was used during the experiment. [a] The yield of BC was determined by gas chromatography analysis of the reaction mixture using mesitylene as internal standard. All experiments were repeated at least twice. [b] Experiment was done once. * Blank experiment without applying any electric current was carried out in a reaction solution of 0.1 M BO, 0.02 M dry $MgBr_2$ and 0.1 M TBAB-MeCN together with the inserted Cu and Mg electrodes in an undivided cell for 18 h at room temperature.

5.4.1.3. Influence of current and charge

In galvanostatic electrosynthesis, the current is a key parameter to improve the product yield. Therefore, different current densities of 2.0, 2.8, and 6.5 mA·cm^{-2} were studied in this work. When a current density of 2.0 mA·cm^{-2} was applied, 74 ± 3% of BC was formed. An increase of the current density to 2.8 mA·cm^{-2} resulted in a similar yield of BC (**entry 5** in **Table 1**), whereas higher current density equal or more than 6.5 mA·cm^{-2} drastically decreased the yield to 28 ± 3 % (**entry 6** in **Table 6**). It is expected that at higher currents, undesirable reactions may occur such as a further conversion of $CO_2^{\bullet-}$ to CO and oxalate dianion.[174,177]

The influence of charge passed during electrolysis was also investigated in a range of 1.0 and 3.5 *F*. A linear increase of BC yield was observed when a charge between 1.0 to 2.5 *F* was applied (**Table 6, entries 7 – 9**). After that a plateau was reached, where the yield remained constant with increasing charge up to 3.5 *F* (**Table 6, entries 10-11**). This finding is consistent with previous studies, which often employed a charge between 2.0 and 2.5 *F*.[173,177,178] Based on our results, the optimal parameters for electrosynthesis of BC were determined to be at 2.0 mA·cm^{-2} and 2.0 *F*.

5.4.1.4. Influence of cathode material

The nature of the electrode material can strongly influence the electrochemical activation of CO_2. Therefore, reference experiments were performed on polycrystalline Cu and bare GC electrodes under similar conditions. As shown **Table 6, entry 12 – 13**, the obtained yield of BC was 19 ± 3% and 76 ± 4% for bare GC and polycrystalline Cu electrode, respectively. Despite the higher catalytic activity of np-Cu/GC, confirmed by the CV profile in **Figure 43**, the yields of BC are comparable on both Cu-based electrodes. These findings indicate that the activation of CO_2 is not the rate-limiting step for the cyclic carbonate formation as reported in the literature.[41,42,172] Another possible explanation could be the presence of precipitants formed from the sacrificial Mg anode, which may reduce the available ECSA of np-Cu by blocking the pores. This will be discussed in **Section 5.4.2** and **Section 5.4.3** in detail. Based on these results, we concluded that np-Cu/GC and polycrystalline Cu are suitable cathode materials for the electrosynthesis of BC

5.4.1.5. Influence of anode material

Sacrificial anodes donate electrons to the system and produce metal cations that could play a role in the reaction. Here, we tested the effect of polycrystalline Mg, Zn, and bare GC as anode materials for the reaction of epoxide with CO_2. Mg anode was used initially in this study based on its extensive use reported in the literature [38,151,172,177,178] and good yields of BC ($74 \pm 4\%$) were achieved. The effect of Zn or bare GC as alternative sacrificial anode was investigated, and only 2% of BC or no product was formed (**Table 6, entries 13 – 14**), respectively. This is related to the more negative standard electrode potential of Mg compared to the other metals such as Zn, Al, and Sn.[151] On the other hand, as no product forms using bare GC anode, the Mg^{2+} species from the sacrificial anode play an important role in the reaction of CO_2 with epoxides.

5.4.2. Yields of cyclic carbonates using the optimized parameters

A galvanostatic electrosynthesis was carried out using np-Cu/GC cathode and sacrificial Mg anode in CO_2-saturated 0.1 M TEAI-MeCN. A current of 2.0 mA·cm^{-2} was applied until a total charge of 2.0 F was passed. Very good yields of BC ($74 \pm 4\%$) on np-Cu/GC and Mg were achieved. This is superior to the reported studies that used stainless steel electrodes[172], Cu nanoparticles[177], and Ag nanoparticles[178].

The optimized reaction conditions were applied for another starting material that has one methyl group less than BO. Propylene carbonate (PC) in good yields ($62 \pm 6\%$) was produced from propylene oxide (PO) and CO_2 on np-Cu/GC cathode material using the optimal parameters. For comparison, the yields of BC and PC reported by other studies are summarized in **Table 2** in **Section 2.3.3**.

Figure 44 illustrates an overview of the resulting yields of BC and PC using np-Cu/GC as well as reference cathode materials like polycrystalline Cu and bare GC. It is obvious that the np-Cu/GC achieves very good yields of both products ($74 \pm 4\%$ of BC and $62 \pm 6\%$ of PC), whereas the bare GC gives very low yields ($20 \pm 3\%$ of BC and $14 \pm 3\%$ of PC). As np-Cu only covered around 77% of the GC substrate surface, the contribution of the GC on the yield is neglectable.

When polycrystalline Cu was used as a cathode material, 63 ± 5% of PC and 76 ± 4% of BC were formed. An improvement of the yields of these cyclic carbonates by increasing the surface area and higher catalytic activity for CO_2RR was therefore not observed. This observation is very likely related to the reaction pathway, where the electrochemical CO_2 activation is not the rate-limiting step for cyclic carbonate formation.
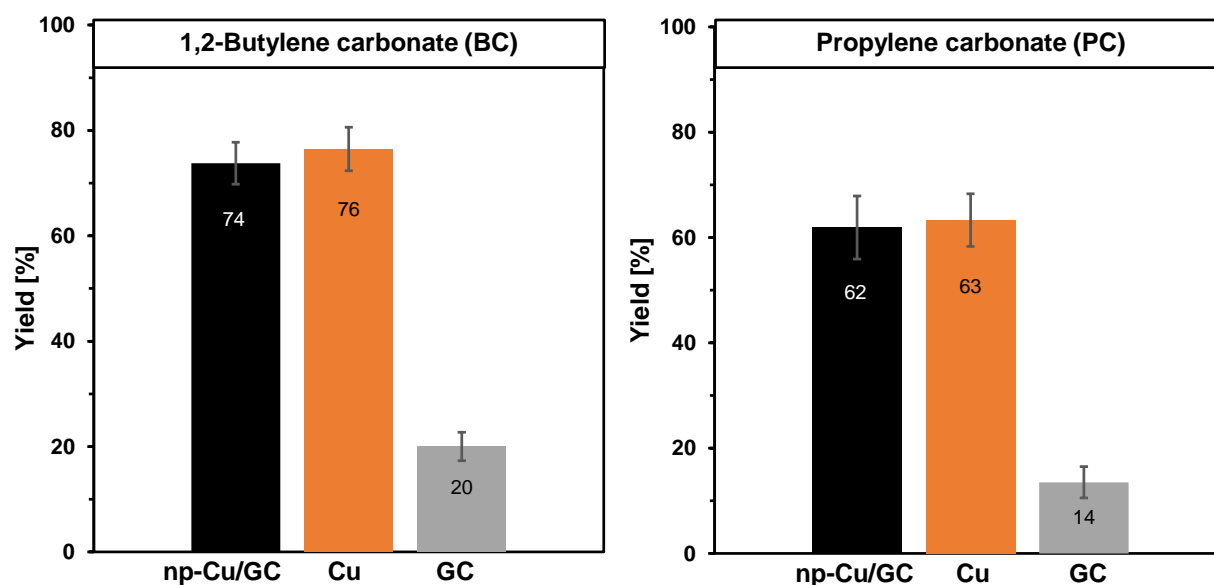
Figure 44: *Bar chart of yield of 1,2-butylene carbonate (BO, left) and propylene carbonate (PC, right) using different cathode materials: np-Cu/GC (black), polycrystalline Cu (orange), and bare GC (grey). Electrolysis conditions: undivided cell, 40 mL CO_2-saturated 0.1 M TEAI-MeCN, 0.1 M starting material, Mg anode, 2.0 mA·cm^{-2}, 2.0 F. Yield was determined by gas chromatography from the reaction mixture using mesitylene as internal standard. Figure reprinted from the manuscript submitted to a journal.*

Another possible reason behind the similar yields obtained could be that during electrosynthesis the nanopores of np-Cu might be blocked by precipitate, probably a magnesium salt formed on the anode, that are visible to the eye. To cover the pores of np-Cu with a pore size of 45 ± 16 nm, the precipitants need to be much smaller and the mass transport within these pores is controlled by diffusion instead of convection, which seems to be unlikely. If this is the case, a gradual loss of ECSA of np-Cu/GC might occur over the electrolysis time. The np-Cu/GC with high ECSA and CO_2RR reactivity is then more suitable in combination with non-sacrificial anodes such as carbon. For instance, electrosynthetic reaction of interest on np-Cu/GC could be electrocarboxylation of dienes[221] or *α,β*-unsaturated esters [222] with CO_2.

5.4.3. Electrochemical Reaction Pathway

Reaction pathway of epoxide with CO_2 has not been fully understood to date. The findings from the blank experiment (**Section 5.4.1.1)** performed using the same conditions, but in the absence of applied current, reveal that the CO_2 activation is necessary for the reaction with epoxides under ambient conditions. Similar results have been reported by other groups.[23,27,45] We strongly believe that the activation process involves the electro-reduction of CO_2 to form $CO_2^{\bullet-}$ radical anion.[39,41,172] Distortion of the commonly linear structure of neutral CO_2 towards a bent structure of the radical anion results in a pronounced activation at the electrophilic center of CO_2, consequently enhancing the efficiency of the reaction with epoxide.[42] However, our results pointed out that the electrochemical CO_2 activation is not the rate-limiting step in the formation of cyclic carbonates. This assumption originates from the similar yields of BC and PC formed on np-Cu/GC and polycrystalline Cu, despite the higher catalytic CO_2RR activity and RF of np-Cu/GC. Perez-Gallant et al.[41] also found no strong effect of the electrode material on the yield, strongly suggesting that CO_2 activation is not the rate-limiting step.

While CO_2 undergoes reduction on the cathode surface, the sacrificial magnesium anode is oxidized, constantly releasing Mg^{2+} ions into the electrolyte. As shown in **Section 5.4.1.5** when Mg anode was replaced with Zn or bare GC, no product ($\leq$ 2%) was detected. Similar results were reported by other groups, where minimal product formation was observed using Pt anode.[172] However, when $MgBr_2$ was added to the reaction mixture in the presence of Pt anode, cyclic carbonates were formed.[172] This experimental observation strongly suggests that Mg^{2+} species play a crucial role in the reaction pathway, which is further supported by theoretical predictions based on density functional (DFT) calculations.[42]

While the significance of Mg^{2+} species in the reaction has been widely acknowledged in the literature, different mechanisms have been proposed to explain its role. Some studies reported the formation of an intermediate, from CO_2 and MgI_2 (I^- from TEAI), that opens the epoxide ring.[172] Others proposed that the halide species from the ionic liquid or supporting electrolyte are responsible for the ring opening, while Mg^{2+} facilitates this

process.[42] Furthermore, it has been suggested that the supporting electrolyte TBAB undergoes deposition, producing tributylamine, which then forms an intermediate with CO_2 and $MgBr_2$ to open the epoxide ring.[180] Since triethylamine was not detected in the reaction mixture in this study, we can exclude the decomposition of the supporting electrolyte as a possible mechanism. Therefore, we concluded that both Mg^{2+} and halide anions (I^-) from the supporting electrolyte play an important role in facilitating the ring opening of the epoxide. Further investigations are required to gain a deeper understanding of the reaction pathway and identify the intermediates involved.

Afterwards, $CO_2^{\cdot-}$ acts as a nucleophile attacking the open oxide, and the cyclic carbonate is obtained by ring closure.[42,172] DFT calculations suggest that the ring closure is the rate-limiting step of the reaction.[42] This aligns with our experimental observations and indicate that enhancing the catalytic activity for CO_2 reduction would not necessarily lead to an increase in the yield of cyclic carbonates.

5.5. Reusability of np-Cu electrode

To investigate the stability and reusability of the porous electrode, np-Cu/GC was employed several times. After each electrolysis run for 15 hours, the np-Cu/GC electrode was washed in highly purified water and propan-2-ol followed by chemically polishing with phosphoric acid. In **Figure 45a – b**, the SEM micrographs show the morphology of the np-Cu/GC electrode after three runs of electrolysis experiments with a total duration time of 45 hours. It is obvious that the ligaments are stable, and the structure is preserved (reference structure before electrolysis in **Figure 39**). No changes in mean ligament size are observed (108 ± 18 nm in comparison with a fresh np-Cu/GC with 112 ± 16 nm).

A slight decrease in the yield of BC was observed after three times of reuse of the np-Cu/GC as shown in **Figure 45c** The yield was determined as 73, 69 and 61% of BC for three successive 15-hour electrolysis experiments. We explain the slight drop of performance by partial detachment of np-Cu dispersion from the GC substrate during handling the electrode between experiments (see **Figure S14** from the **Supporting**

information for chapter 5). This observation supports our hypothesis, that the Mg-based precipitations are not blocking the internal pores of the np-Cu materials, because the diffusion process is very slow. The use of binder can prevent the mechanical loss of materials during a long period of electrolysis. Altogether, our results show that the np-Cu/GC is stable and can be easily reused after a simple washing process.
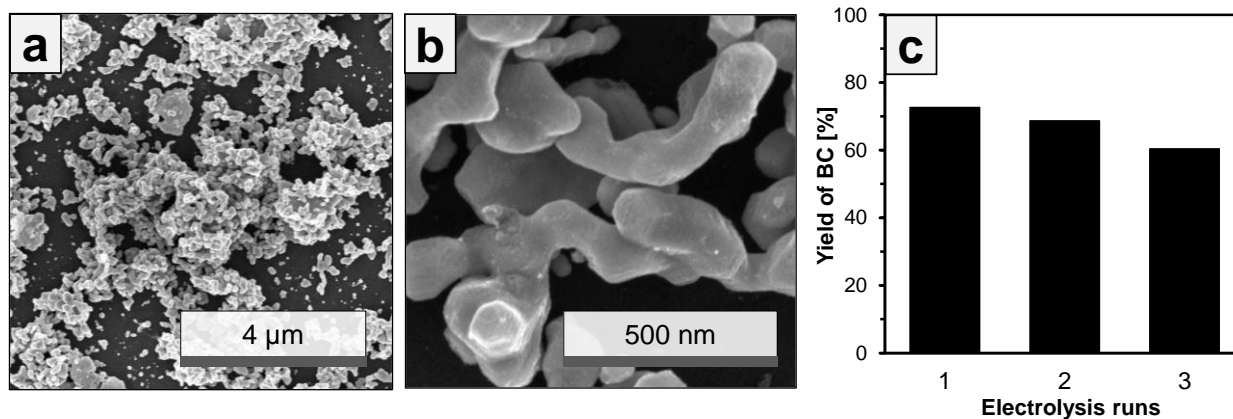
Figure 45: SEM micrographs of np-Cu/GC after the three runs of 15-hour electrolysis at (a) low and (b) high magnification. (c) Bar chart showing yield [%] of 1,2-butylene carbonate (BC) on the reused np-Cu/GC electrode. Electrolysis conditions: undivided cell, 40 mL CO_2-saturated 0.1 M TEAI-MeCN, 0.1 M starting material, Mg anode, 2.0 mA·cm^{-2}, 2.0 F. Figure reprinted from the manuscript submitted to a journal.

5.6. Raman spectroscopy investigations of np-Cu/GC after electrolysis [not published]

After confirming the stability and reusability of the np-Cu/GC, the chemical state of Cu on the electrode surface before and after electrolysis was investigated. Raman spectroscopy is a surface sensitive method and a powerful tool for the analysis of Cu oxide species, where Cu(I) and Cu(II) show distinct different Raman shifts. **Figure 46a – c** show Raman mappings for np-Cu/GC (after electrolysis), np-Cu ribbons (before electrolysis), and polycrystalline Cu. Spectra were recorded for every 1 μm of the sample surface in the wavenumber interval of 100 – 1,000 cm^{-1}, using a 532 nm

laser and a 50x /0.8 objective. Areas with higher ratio of Cu(I) or Cu(II) are presented in the mappings with red or blue pixels, respectively.

Figure 46d show the component spectra of Cu(I) in red and Cu(II) in blue. The measured spectra were compared to reference Raman spectra of Cu_2O (black) and CuO (grey) obtained from the RUFF project Database[186]. The spectrum of Cu_2O shows Raman shifts at 218, 410, and 623 cm^{-1}. It is well-known that the instability of Cu_2O leads to a variety of intrinsic defects and a tendency towards nonstoichiometry.[189,190] Therefore, the observed peaks at 218 cm^{-1} and 410 cm^{-1} are assigned to multiphonon Raman scattering whereas the peak at 623 cm^{-1} corresponds to the IR-active mode T_{1u}, associated with the Cu-O stretching mode.[189-191] On the other hand, the Raman spectrum of CuO shows three Raman peaks at 295, 347, and 630 cm^{-1}, corresponding to the Raman-active vibrational A_g (at 295 cm^{-1}), and B_g (at 347 and 630 cm^{-1}) modes of CuO crystals.[187-189]

For the analysis of the Cu-based samples, Raman peaks at 218 and 295 cm^{-1}, showing the highest intensity, were chosen as distinctive peaks for Cu(I) and Cu(II), respectively. The peaks where fitted with Gauss peak fitting function and the Cu(I):Cu(II) ratio for every spectrum was estimated by dividing the peak area at 218 cm^{-1} by the peak area at 295 cm^{-1}. The mean Cu(I):Cu(II) ratio, estimated from the whole mapping area, was found to be 2.3 ± 1, 3.8 ± 3, and 14.5 ± 9 for np-Cu/GC (after electrolysis), np-Cu ribbons (before electrolysis), and polycrystalline Cu, respectively. It is worth mentioning here that samples were exposed to air for several hours during the measurements. The large error bars are attributed to the disturbance from the florescence of metallic Cu present in the samples and the rough surface of np-Cu. Uneven surfaces can lead to variations in the sampling area, causing inconsistent measurements and fluctuations in signal intensity.

It is apparent that the relevant content of Cu(II) is higher in np-Cu compared to polycrystalline Cu. While the cause of this difference isn't fully understood and requires further investigation, it's plausible to propose an association with the chemical and morphological changes occurring during the dealloying process. Additionally, the high density of surface defects or vacancies in the formed nanoporous structure might also

play a role. The Cu(I):Cu(II) ratio was found to be slightly smaller for the np-Cu/GC after electrolysis compared to np-Cu ribbons, which can be related to the electrode preparation process during horn sonication.
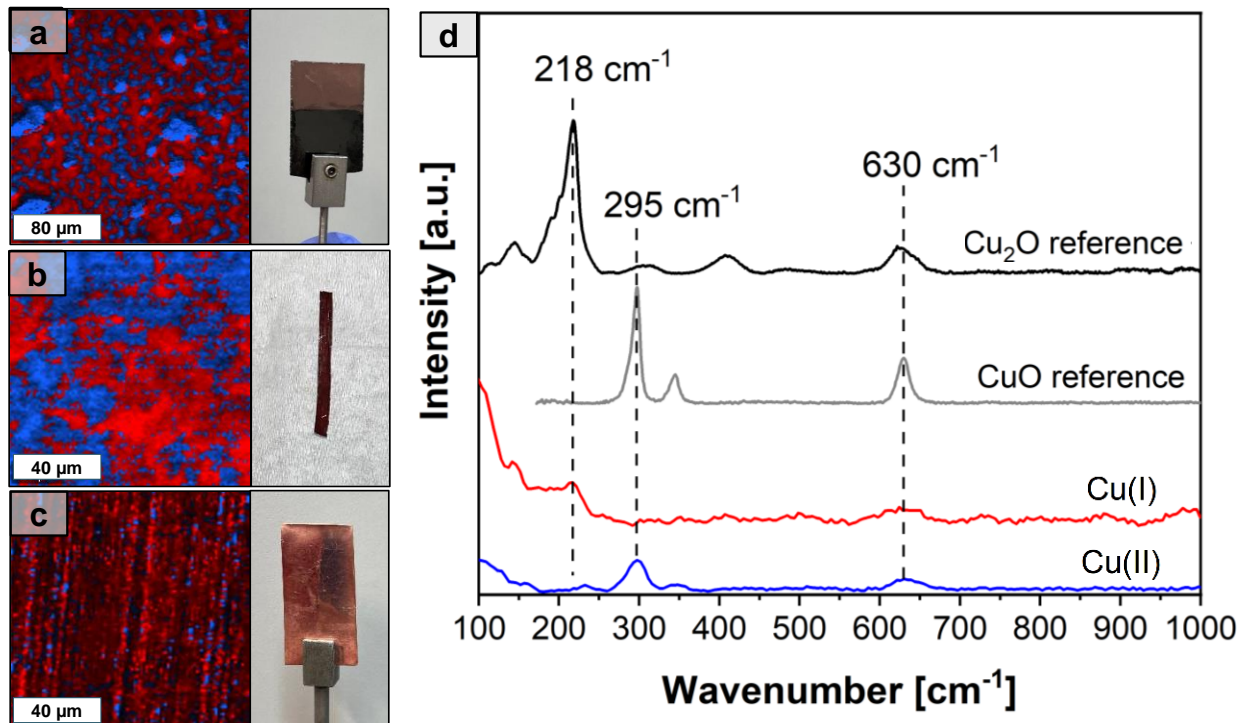
Figure 46: *Raman mappings with corresponding photographs of the investigated Cu-based materials, showing the distribution of Cu(I) in red and Cu(II) in blue in (a) np-Cu/GC after electrolysis, (b) np-Cu ribbons before electrolysis, and (c) polycrystalline Cu. (d) Raman spectra of Cu(I) in red, and Cu(II) in blue for a sample surface area of 1 μm^2 (representing 1 pixel of the mapping) of np-Cu/GC, with the reference spectra of Cu_2O [ID: #R050384] in black, and CuO [ID: #R060978] in grey obtained from the RUFF™ project Database[186].*

During the electrolysis, Cu oxides are expected to be reduced to metallic Cu, which is the active species for CO_2RR.[195,223,224] The higher Cu(II) prevalence in np-Cu/GC can have an influence on the catalytic activity of the cathode. Various studies in the literature have highlighted distinct selectivities for the products obtained during CO_2RR when using different copper oxide (Cu_xO) and metallic Cu electrodes.[225-227] Wang et al.[225] investigated the activity of Cu(II) oxide nanosheet catalysts for CO_2RR in 0.1 M $KHCO_3$. Operando X-ray absorption spectroscopy (XAS) studies show the chemical reduction of CuO and concomitant formation of metallic Cu^0 under reductive CO_2RR conditions (after

scanning to –0.84 V vs RHE). The formation of undercoordinated Cu sites, resulting from CuO nanosheet fragmentation, demonstrates robust chemisorption capabilities, which has been linked to elevated catalytic rates for the conversion of CO_2 into C^{2+} products. The authors also tracked the product formation rates and yields under transient catalytic CO_2RR by differential electrochemical mass spectrometry and found a correlation between the yield of CO, CH_4, C_2H_4 and EtOH and the chemical state of the Cu catalyst. As soon as the metallic Cu^0 catalyst emerged, the rates and yields of CH_4, C_2H_4 and EtOH exhibited an upward trend. A shift in the onset potentials of both C_2H_4 (from –0.57 ± 0.07 to –0.63 ± 0.09 V vs RHE) and CO (from –0.38 ± 0.08 to –0.48 ± 0.05 V vs RHE) was also observed with the reduction of CuO to metallic Cu. Here, the onset potential is defined as the electrode potential where product generation initiates. Therefore, the utilization of this CuO catalyst for CO_2RR offers onset potential benefits towards the formation of C_{2+} products.

The observations from the literature highlight the impact of oxide species on the catalytic performance of Cu electrodes for CO_2RR. Therefore, the enhanced activity of np-Cu/GC compared to polycrystalline Cu, observed in **Section 5.3** (**Figure 43**), could be partially attributed to the Cu(II) oxides formed on the surface of the cathode. Further analysis of the electrode surface before and after electrolysis by XPS can provide more precise estimation of the content of oxide and metallic copper species in the different samples.

5.7. Summary

In this Chapter, we investigated the catalytic activity and stability of np-Cu in the electrosynthesis of cyclic carbonates from CO_2 and epoxides at room temperature and ambient pressure. To overcome the fragility and brittleness of dealloyed ribbons, np-Cu was drop-casted on GC substrate, to form np-Cu/GC electrode, with a total Cu loading of 1 mg cm^{-2}_{geo} (per geometric area). The surface of the electrode is comprised of a thin layer of np-Cu (~0.9 ± 0.1 μm thickness) consisting of a bicontinuous ligament-pore network with a mean ligament size of 112 ± 16 nm. The GC surface coverage with np-Cu was found to be 77 ± 3 %. Np-Cu/GC exhibits a high electrochemically active surface area (ECSA), described by a roughness factor of 3, estimated by double layer

capacitance measurements. Determination of ECSA using Pb-UPD technique was found not suitable, due to unavoidable oxide formation on the electrode surface during its preparation process. The higher ECSA resulted in an improved catalytic activity for electrochemical CO_2 reduction reaction (CO_2RR) compared to polycrystalline Cu. This was supported by observing larger current densities for np-Cu/GC in cyclic voltammetry during CO_2RR.

After analysis of the morphology and catalytic activity, the np-Cu/GC was used as a cathode for a galvanostatic electrolysis of cyclic carbonates from epoxides (1,2-butylene oxide, and propylene oxide) in CO_2-saturated 0.1 M TEAI-MeCN with Mg anode, 2.0 mA cm^{-2} applied current, and 2.0 F mol^{-1} passed charge. Very good yields of 1,2-butylene carbonate (BC, 74 ± 4 %) and propylene carbonate (PC, 62 ± 6 %) were achieved on the np-Cu/GC. Analysis of the porous electrode surface by Raman spectroscopy revealed higher relevant content of Cu(II) than Cu(I) species, which might have an influence on the catalytic activity. After three runs of electrolysis, the np-Cu/GC shows very good stability, where the structure is preserved, and ligament size did not change and good reusability.

When bare GC was employed as cathode, low yields of the products were produced (≥ 20 %), indicating minimal contribution of the GC substrate on the yields. Interestingly, BC and PC yields achieved on polycrystalline Cu were comparable to the yields produced on np-Cu/GC. The reaction pathway is expected to involve the activation of CO_2 to form $CO_2^{\bullet -}$ radical anion as well as the activation epoxide by Mg^{+2} (from the sacrificial anode) and I^- (from the supporting electrolyte). The open epoxide is then nucleophilically attacked by $CO_2^{\bullet -}$, and the cyclic carbonate is obtained by ring closure, which is expected to be the rate-limiting step.

We showed that the np-Cu/GC is an effective cathode material for the electrosynthesis of cyclic carbonates from CO_2 and epoxides under mild conditions. Although the pore-ligament structure is beneficial to enhance the CO_2RR performance, its impact on the yield of cyclic carbonate is minimal, due to the rate-limiting step of the reaction being the ring closure of the final intermediate. Therefore, the application of np-Cu/GC in other

reactions such as the electrocarboxylation of styrene, dienes or α,β-unsaturated esters with CO_2 should be investigated.

6.   Conclusions and outlook

6.1. Conclusions

The evolution of a three-dimensional porous structure varies significantly for master alloys prepared by different techniques, due to differences in crystal phase structures, homogeneities and thicknesses. In addition to the master alloy, dealloying conditions such as electrolyte, time, and temperature remarkably influence the resulting dealloyed structure. Deeper understanding of the dealloying process and ligament evolution allows for preparation of nanoporous materials with tailored properties for the desired applications. In this context, the objective of this study was twofold: first, to offer a comprehensive analysis of the development of ligament-pore network by chemical dealloying of melt-spun $Zn_{80}Cu_{20}$ ribbons in different electrolytes. Second, demonstrate the applicability and stability of the prepared np-Cu for the electrosynthesis of cyclic carbonates from CO_2 and epoxides at room temperature and ambient pressure.

The results are presented and discussed in Chapters 4 and 5 of this dissertation. **Chapter 4** provided in depth insights into the ligament evolution during chemical dealloying of melt-spun $Zn_{80}Cu_{20}$ ribbons in 0.1 M HCl, 5 M and 15 M H_3PO_4, and 1.3 M NaOH solutions. Despite the relatively thick melt-spun ribbons (35 ± 3 µm), kinetics of the bicontinuous ligament-pore structure is controlled by the interfacial process instead of the diffusion of corrosive electrolyte solution in and out of the porous layers. The surface diffusivity of Cu atoms is strongly influenced by the nature of the dealloying conditions. Adsorbed chloride anions from HCl enhance the surface diffusion of Cu, leading to larger ligament size (73 ± 14 and 115 ± 28 nm after dealloying for 24 h and 168 h in 0.1 M HCl at 25°C). The higher Cu mobility also results in a strong correlation between ligament size and residual Zn content of the porous structure, as the ligament size grows and simultaneously the residual Zn content decreases over the dealloying time. Surface diffusivities of Cu at 25°C were determined to be 1.4 x 10^{-18} m^2 s^{-1} and 9.4 x 10^{-21} m^2 s^{-1} in 0.1 M HCl and 1.3 M NaOH, respectively. The slower Cu mobility in H_3PO_4 and in NaOH leads to the formation of smaller ligaments (21 ± 14 nm after dealloying for 24 h in 1.3 M NaOH and 43 ± 8 nm and 37 ± 7 after dealloying for 7 h

in   5 M and 15 H_3PO_4, respectively). Dealloying in alkaline media allows the control of Zn content independent of the ligament size.

Moreover, a strong relationship between dealloying temperature and the np-Cu structure was found. The mean ligament size increases with higher dealloying temperature from 64 ± 12 nm, to 73 ± 14 nm to 84 ± 15 nm at 15°C, 25°C and 50°C, respectively. This ligament size growth is related to the temperature-dependent surface diffusion rates of Cu atoms, where calculated surface diffusivity values of Cu in 0.1 M HCl were found to be 7.9 x 10^{-19} m^2 s^{-1}, 1.4 x 10^{-18} m^2 s^{-1} and 2.6 x 10^{-18} m^2 s^{-1} at 15°C, 25°C and 50°C, respectively. On the other hand, agitation and de-aeration of the acidic electrolyte shows negligible influence on the process. We can sum up that the nature of electrolyte and dealloying temperature have a strong influence on the surface diffusion of Cu atoms and hence on microstructure evolution characteristics of np-materials.

Chapter 5 investigated the catalytic activity and stability of the prepared np-Cu in the electrosynthesis of cyclic carbonates from CO_2 and epoxides at room temperature and ambient pressure. The cathode material consists of a thin film of np-Cu (~0.9 ± 0.1 µm thick), dealloyed in 0.1 M HCl for 168 h, drop-casted on a glassy carbon substrate (np-Cu/GC). It exhibits a high electrochemically active surface area and an improved catalytic activity for CO_2RR compared to polycrystalline Cu. A galvanostatic electrolysis was carried out using the np-Cu/GC cathode and Mg anode in CO_2-saturated 0.1 M TEAI-MeCN, with 0.1 M 1,2-butylene oxide and propylene oxide as starting materials. Np-Cu/GC cathode material shows very high yields of 1,2-butylene carbonate (74 ± 4%) and propylene carbonates (62 ± 6%). In addition, the pore-ligament structure of np-Cu/GC remains stable after 15-hour electrolysis and can be reused several times. However, similar yields were achieved on polycrystalline copper, implicating that the CO_2 activation to form $CO_2^{\bullet -}$ radical anion is not the rate-limiting step of the reaction, but rather the ring closure of the final intermediate to form cyclic carbonates. The np-Cu/GC shows very good stability and reusability. The findings of this work highlight the interesting properties of np-Cu and provide insights into the reaction mechanism of CO_2 with epoxides. This comprehensive study allows tuning the structural and chemical properties of np-Cu material for a wide range of possible applications in electrochemical synthesis and catalysis.

6.2. Outlook

The knowledge and insights gained from this research can serve as a guide for directing future investigations. It is recommended that upcoming projects focus on: (1) tailoring nanoporous structure by chemical dealloying in different electrolytes with mixtures of anions such as various proportions of HCl and H_3PO_4, or by electrochemical dealloying; (2) np-Cu/GC as electrode material for other reactions, like electrocarboxylation of dienes or α,β-unsaturated esters with CO_2; (3) the effect of ligament size and Zn residual content, and (4) surface oxides on np-Cu activity for CO_2RR.

6.2.1. Tailoring nanoporous structure by chemical dealloying in electrolyte mixtures or electrochemical dealloying

The distinct characteristics of np-Cu formed during chemical dealloying in H_3PO_4 and HCl opens the opportunity to better tailor the nanoporous structure for the desired applications. There have been very limited studies on dealloying in mixtures of acids. The addition of chloride anions enhances the Cu surface diffusion whereas phosphate anions suppress it. As a result, varying the ratios of chloride to phosphate anions in electrolytes during dealloying could offer a better control over ligament size and Zn content. For instance, the preparation of electrolytes with varying proportions of HCl and H_3PO_4, or the addition of NaCl to H_3PO_4, could be explored. Such an approach may help overcome the coarsening of the surface of dealloyed ribbons in phosphoric acid.

Although chemical dealloying of $Zn_{80}Cu_{20}$ alloy ribbons is the scope of this work, electrochemical dealloying is known to provide better control over the np structure. Therefore, it can be a powerful technique for a more precise tailoring of the ligament size and residual Zn content of np-Cu ribbons.

6.2.2. Np-Cu/GC as electrode material for other reactions

Our findings indicate that the activation of CO_2 on the np-Cu/GC cathode is not the rate-limiting step of the reaction of epoxides with CO_2. Therefore, the enhanced catalytic activity for CO_2RR and the large ECSA of np-Cu are not fully utilized for this reaction. The employment of this interesting electrode material for other reactions in organic

electrosynthesis would be of great interest. For example, the np-Cu/GC can be suitable cathode material for the electrocarboxylation of styrene with CO_2 to produce phenyl succinic acid.[228] Another possible reaction is the electrocarboxylation of dienes or *α,β*-unsaturated esters with CO_2, where copper shows higher selectivity towards δ-monocarboxylated alkene.[221]

6.2.3. Effect of ligament size and Zn content on np-Cu catalytic performance

The specific effects of ligament size on the electrocatalytic performance of np-Cu electrodes in CO_2RR remain an area that requires deeper exploration. It is uncertain whether a smaller ligament size, which results in a larger ECSA, would directly lead to improved activity of the np-Cu electrode for CO_2RR and better yields of the desired products. Further investigations are required to thoroughly understand the correlation between ligament and the activity of np-Cu. Similarly, dealloying permits control over the residual content of the less noble metal. This advantage is not yet fully utilized due to the poor understanding of the role of residual Zn on the activity of np-Cu for CO_2RR. By systematically examining the impact of different Zn contents on np-Cu electrodes with similar ligament sizes, researchers can elucidate the specific role of residual Zn and its correlation with the catalytic activity of np-Cu. This knowledge can then inform the design of tailored structures of np-Cu prepared through dealloying, potentially offering significant advantages for CO_2RR processes.

6.2.4. Effect of surface oxide species

In this work, np-Cu was freshly used after preparation or chemically polished by concentrated phosphoric acid between experiments. This originates from the traditional concept that metallic copper is active. Recently, copper oxide electrodes are becoming widely used.[190,223,225,229,230] For examples, oxide-derived copper catalyst showed unique reactivity for CO_2RR, with three times selectivity towards CO than for electropolished Cu foil.[227] Our Raman spectroscopy measurements showed higher relative content of Cu(II) oxide species on the surface of np-Cu left in contact with air for few hours compared to as-received polycrystalline Cu. Therefore, it would be interesting and beneficial to have a better understanding of the surface oxides of non-polished np-Cu by XPS analysis,

and investigations of its activity in non-aqueous electrolytes for organic electrosynthesis. This could provide significant impact of the activity or selectivity of oxide-derived np-Cu. Furthermore, skipping the polishing steps and vacuum storage would provide an easier approach for the electrode handling and preparation.

7. Appendix

7.1. Abbreviations

BC	1,2-butylene carbonate
$[C_4C_1Im][Br]$	1-butyl-3 methylimidazolium bromide
CO_2	carbon dioxide
CO_2RR	CO_2 reduction reaction
COD	crystallography open database
CV	cyclic voltammetry
DFT	density functional theory
ECSA	electrochemically active surface area
EDX	energy dispersive X-ray spectroscopy
EtOH	ethanol
fcc	face-centered cubic
FIB	focused ion beam
GC	glassy carbon
hcp	hexagonal close packed
HER	hydrogen evolution reaction
HR-TEM	high resolution transmission electron microscopy
MeCN	acetonitrile
NHE	normal hydrogen electrode
np	nanoporous
np-Cu	nanoporous copper
np-Cu/GC	nanoporous copper drop-casted on glassy carbon

Pb-UPD	underpotential deposition of lead
PC	propylene carbonate
RF	roughness factor
RHE	reversible hydrogen electrode
R_{wp}	weighted profile residual
SEM	scanning electron microscopy
SERS	surface-enhanced Raman spectroscopy
TBAB	tetrabutylammonium bromide
TEAI	tetraethylammonium iodide
XAS	X-ray absorption spectroscopy
XPS	X-ray photoelectron spectroscopy
XRD	X-ray diffraction

7.2. Symbols

Symbol	Acceptation	Unit
$\bar{Q}_{\text{dep./strip.}}$	averaged integrated charge	µC
$\bar{E}$	reversible potential for the flat surface	V
ΔD	change of ribbon thickness	µm
a	lattice paramter	Å
Å	Ångstrom	
A_{geo}	geometric surface area	cm^2
at.	atomic	%
C	electrochemical double-layer capacitance	µF
C_{GC}	double-layer capacitance for bare GC	µF
$C_{np\text{-}Cu}$	double-layer capacitance for the np-Cu	µF
d(t)	ligament size at a given time	nm
D_0	thickness of ZnCu alloy ribbons before dealloying	µm
D_s	surface diffusivity	$m^2\,s^{-1}$
D_t	thickness of ribbons at a given time	µm
E_a	activation energy	$kJ\,mol^{-1}$
E_b	binding energy	eV
E_c	dealloying critical potential	V
i	current	µA
i_C	double layer charging current	µA
K	Boltzmann constant (1.3806×10^{-23})	$J\,K^{-1}$
Q	charge	C

R	gas constant (8.3145 J mol^{-1} K^{-1})	J mol^{-1} K^{-1}
T	temperature	K
v	scan rate	V s^{-1}
vol.%	volume	%
wt.%	weight	%
γ	surface energy of the more noble metal	J m^{-2}
θ	Bragg angle	°
p	atom fraction of less noble component	
$\eta(x)$	overpotential for the dissolution process	V

This Appendix lists the supporting information reprinted in adapted form from ref. 52 with permission from the Journal of Physical chemistry C, copyright 2022 American Chemical Society.
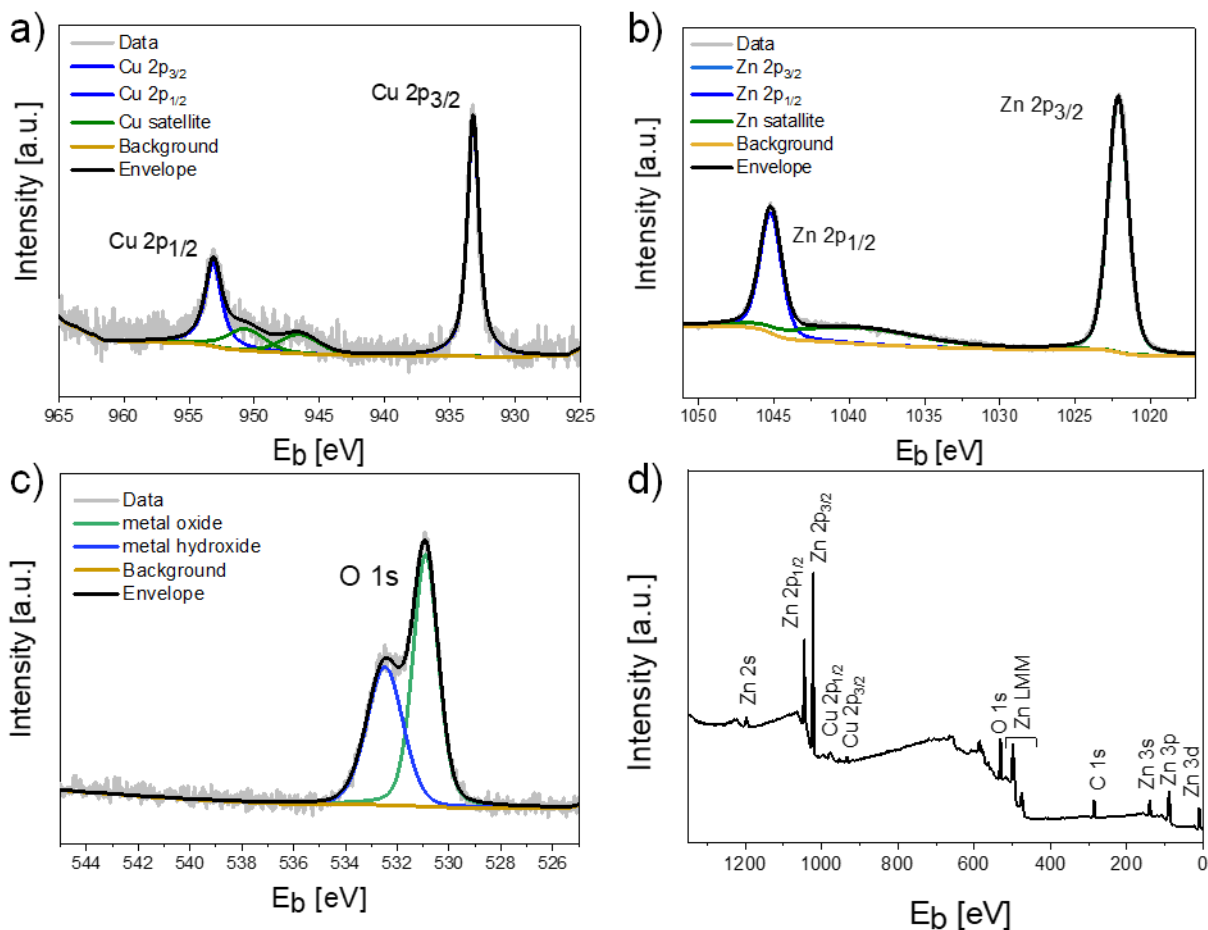
Figure S1: *High resolution XPS spectra of (a) Cu 2p, (b) Zn 2p, (c) O 1s and (d) survey of $Zn_{80}Cu_{20}$ ribbon surface prepared by melt-spinning. The experimental data are denoted in grey, the resulting envelope is symbolized in black, and the background is indicated in yellow. Figure reprinted with permission from ref. 52.*
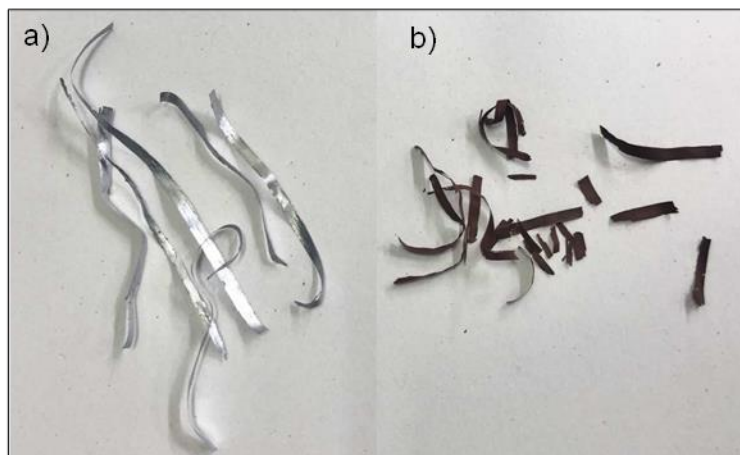
Figure S2: *Photographs of Zn$_{80}$Cu$_{20}$ ribbons (a) before and (b) after dealloying in 0.1 M HCl (24 h) at 25°C under Ar atmosphere. After dealloying, metallic grey ribbons changed color to brown. Figure reprinted with permission from ref. 52.*
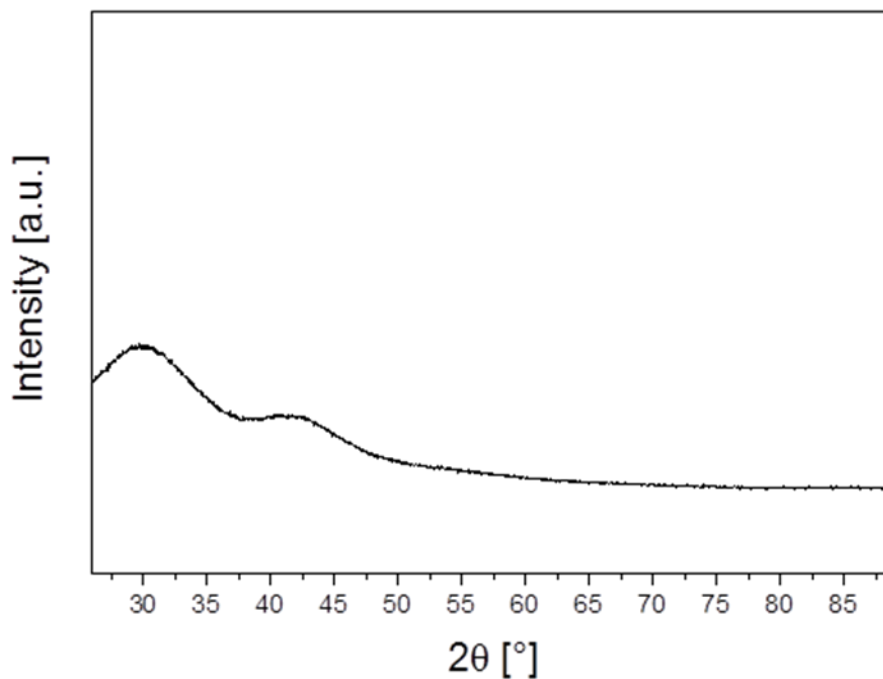
Figure S3: *XRD pattern of the plexiglass used as sample holder due to the low sample quantities available for the measurement. The wavy background stems from the amorphous structure of plexiglass. Figure reprinted with permission from ref. 52.*
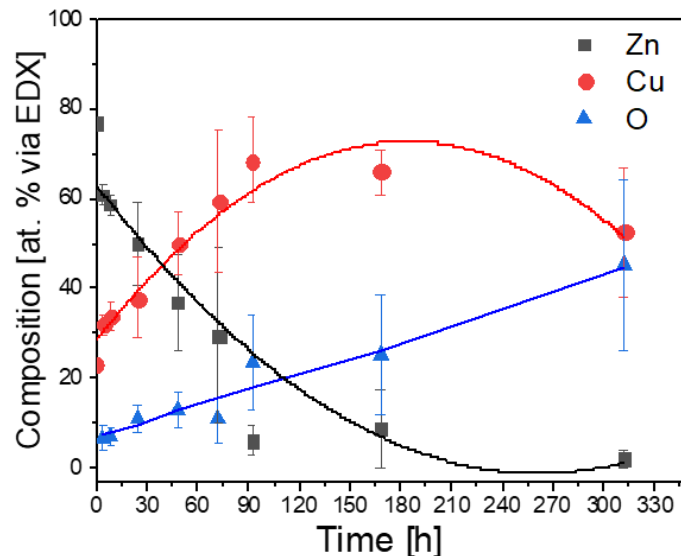
Figure S4: *Time-resolved course of the chemical composition of Zn, Cu and O for Zn₈₀Cu₂₀ alloy ribbons dealloyed in 1.3 M NaOH. Each EDX measurement was repeated at least three times for each sample. Figure reprinted with permission from ref. 52.*
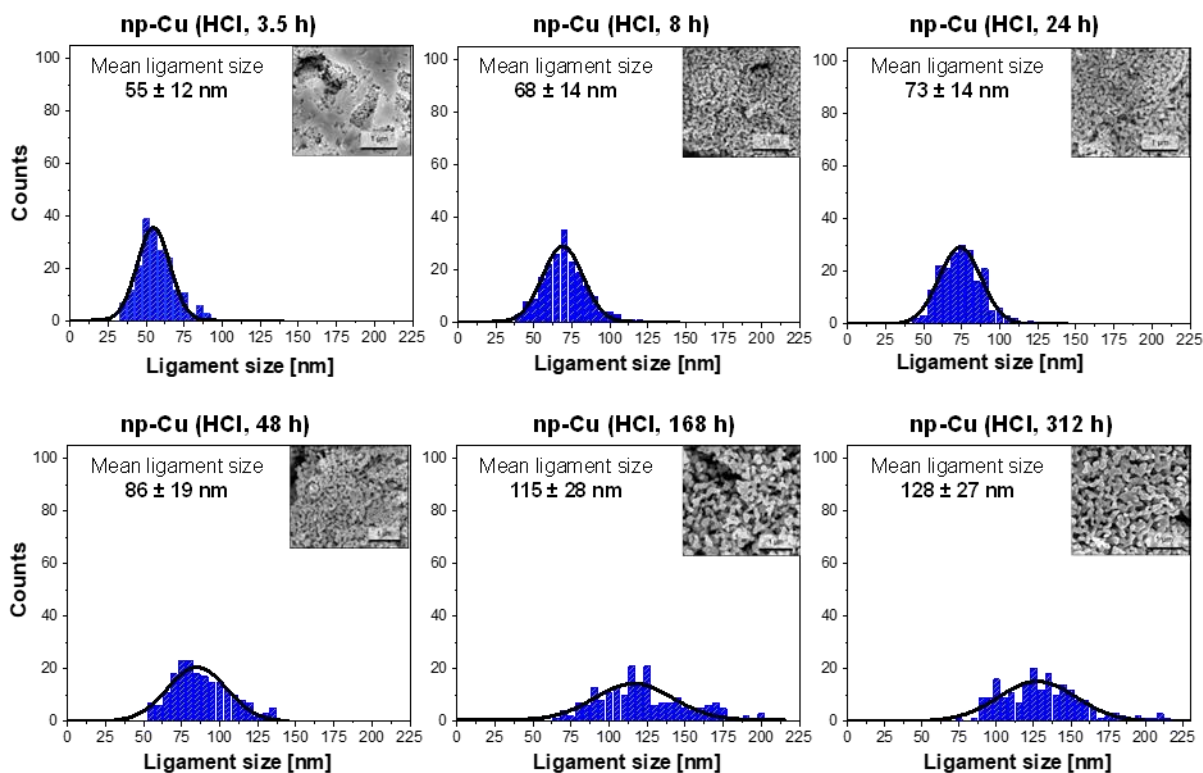
Figure S5: *Ligament size distributions of np-Cu ribbons prepared by dealloying at different times in 0.1 M HCl at 25 °C under Ar atmosphere. For the analysis 200 ligaments from three different samples were used. Figure reprinted with permission from ref. 52.*
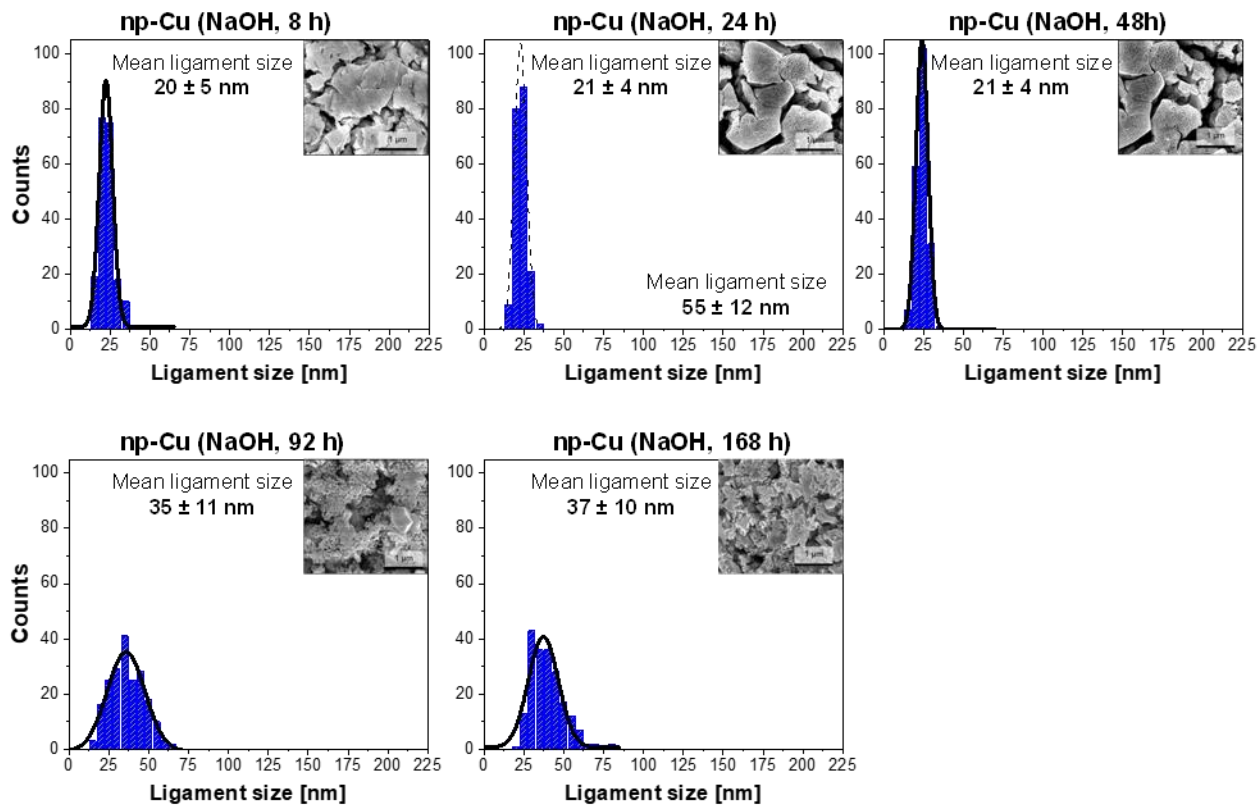
Figure S6: *Ligament size distributions of np-Cu ribbons prepared by dealloying at different times in 1.3 M NaOH at 25 °C under Ar atmosphere. For the analysis 200 ligaments from three different samples were used. Figure reprinted with permission from ref. 52.*
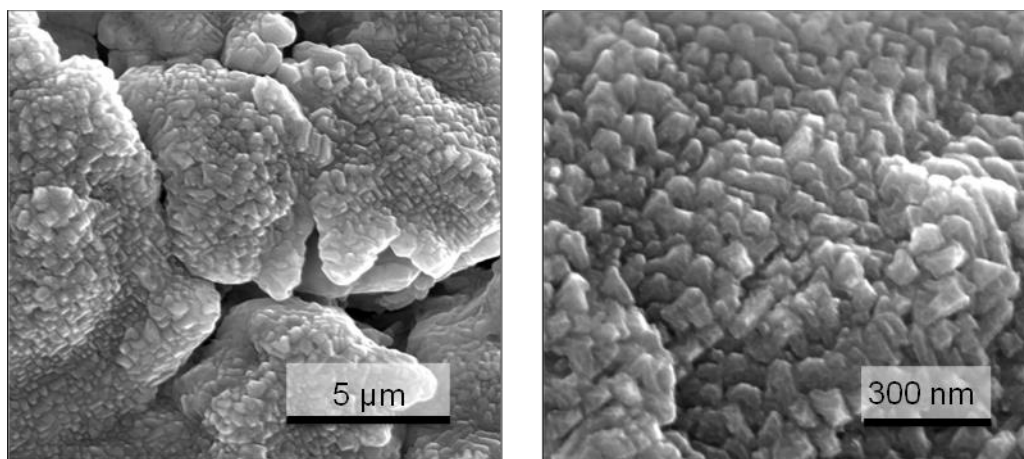
Figure S7: *Low (left) and high magnification (right) SEM micrographs of "freely" dealloyed $Zn_{80}Cu_{20}$ ribbons (without any attachment to Cu substrate) for 312 h (13 days) in 1.3 M NaOH at 25°C under Ar atmosphere, showing the absence of ligament formation. Figure reprinted with permission from ref. 52.*
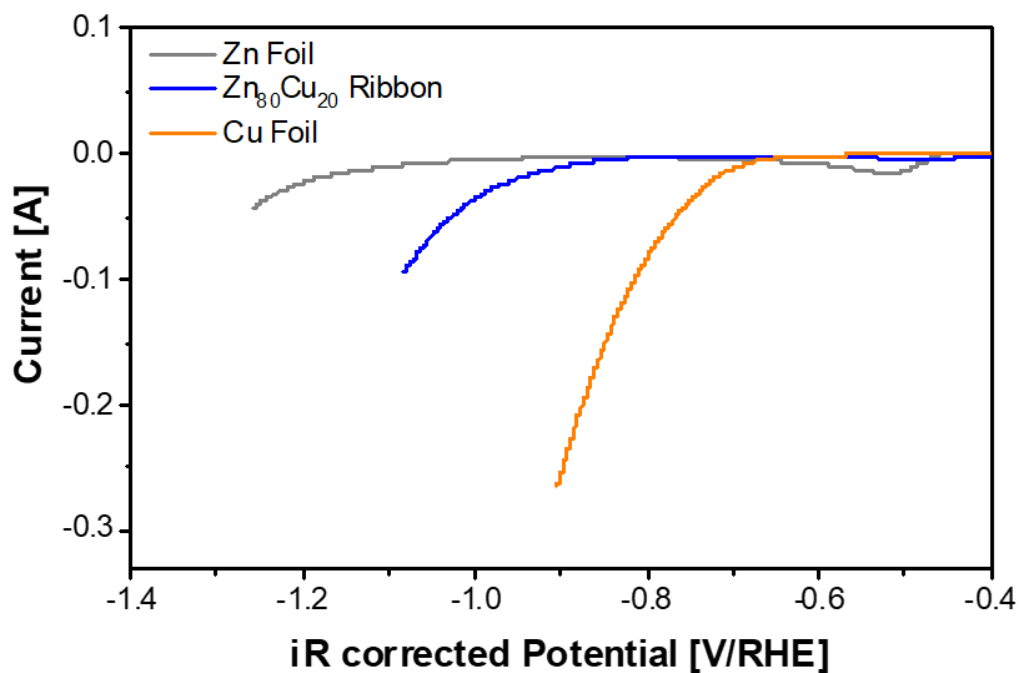
Figure S8: *iR-corrected polarization curves for hydrogen evolution reaction (HER) on pure Cu (orange line), Zn (grey line), and $Zn_{80}Cu_{20}$ alloy ribbon (blue line) at a scan rate of 50 mV s^{-1} in 1.3 M NaOH. Figure reprinted with permission from ref. 52.*

Figure S9: *Dealloying of $Zn_{80}Cu_{20}$ alloy ribbons in 1.3 M NaOH, showing hydrogen bubble formation on the Cu substrate (left image) and the absence of hydrogen bubbles on the pure ribbon surface without Cu attached (right image). Figure reprinted with permission from ref. 52.*
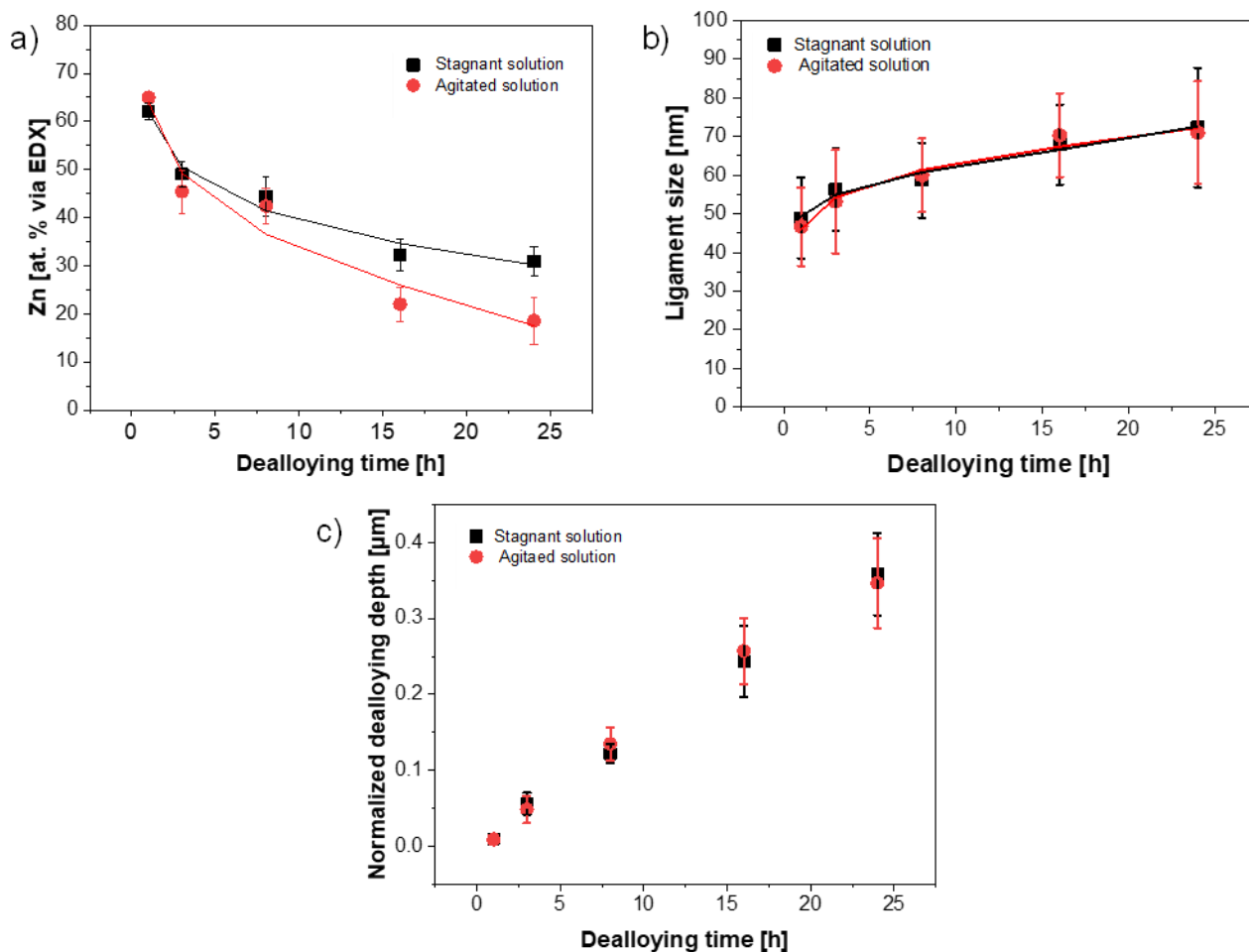
Figure S10: *Comparison of the microstructure of np-Cu ribbons during dealloying process in stagnant (black squares) and agitated (red circles) 0.1 M HCl solutions at room temperature under Ar atmosphere. Agitated solution was stirred at speed rate of 150 rpm (revolution per minute). Dealloying time is plotted against (a) residual Zn content at the surface of the treated ribbons via EDX, (b) ligament size and (c) normalized dealloying depth (dealloying depth divided by the total thickness of the ribbons at each dealloying time) measured from cross-sectional SEM images. Each measurement was repeated at least three times for each sample and at least 200 ligaments from several cross-sectional SEM micrographs were analyzed to establish the mean ligament size. Figure reprinted with permission from ref. 52.*
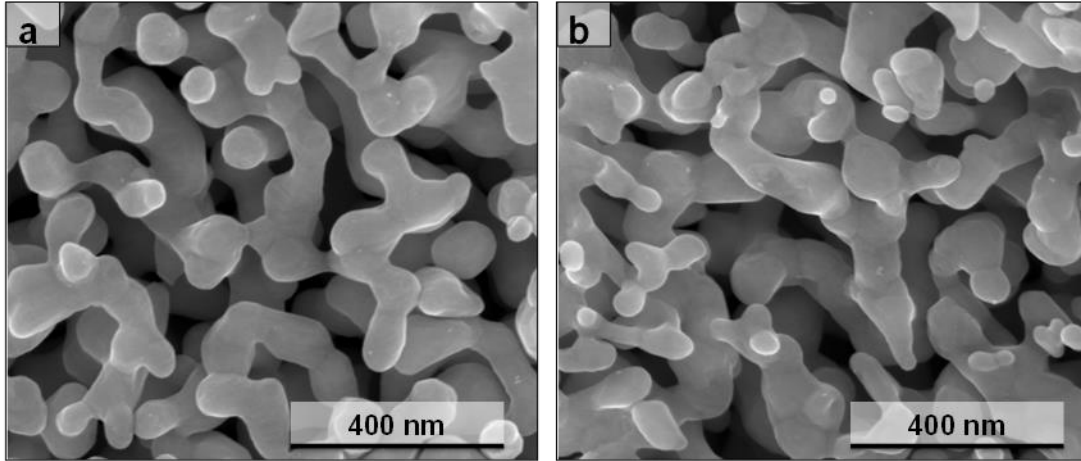
Figure S11: *High resolution SEM micrographs of np-Cu ribbons after 48 h dealloying time in (a) aerated and (b) de-aerated 0.1 M HCl at 25°C, acquired from the top view. Figure reprinted with permission from ref. 52.*

Table S1: *Comparison between chemical composition, ligament size and dealloying depth of np-Cu (HCl, 48 h) dealloyed in (a) aerated and (b) de-aerated 0.1 M HCl at 25°C obtained from SEM-EDX. Table reprinted with permission from ref. 52.*

		aerated 0.1 M HCl	de-aerated 0.1 M HCl
top view	Zn [at.%]	13 ± 2	14 ± 2
	Cu [at.%]	82 ± 3	80 ± 2
	O [at. %]	5 ± 1	5 ± 1
	ligament size [nm]	83 ± 12	86 ± 19
cross-section	Zn [at.%]	22 ± 11	21 ± 12
	Cu [at.%]	71 ± 13	74 ± 12
	O [at. %]	7 ± 1	5 ± 1
	total thickness [nm]	19.7 ± 1.8	20.4 ± 2.1
	dealloying depth [nm]	9.1 ± 1.4	8.9 ± 2.0
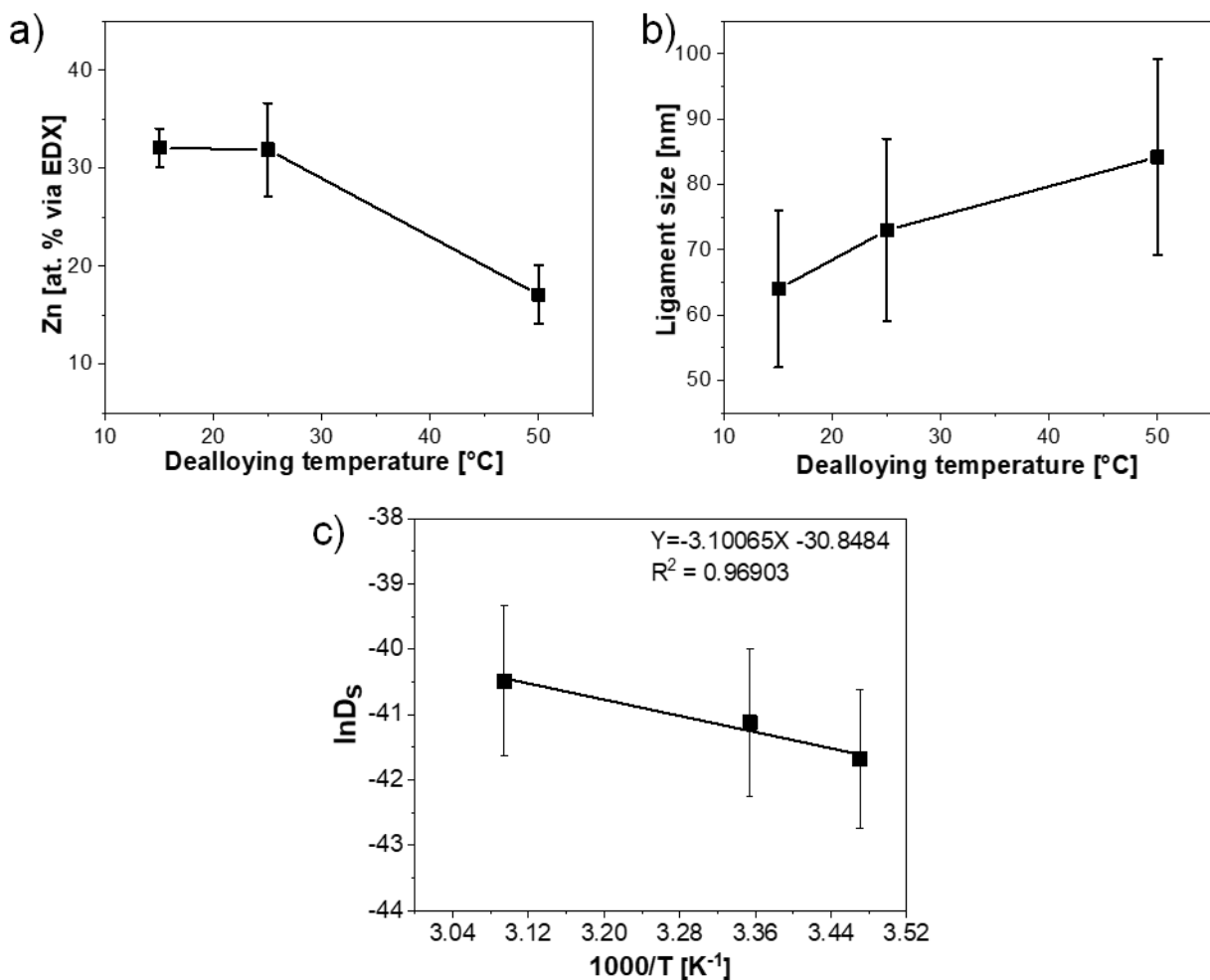
Figure S12: *Effect of dealloying temperature (15°, 25 and 50°C) on the microstructure of np-Cu ribbons during dealloying process in 0.1 M HCl under Ar atmosphere. Plot of (a) residual Zn content and (b) ligament size vs. dealloying temperature. (c) Arrhenius plot of ln D_s vs 1000/T, with error range calculated from the error of ligament size. Figure reprinted with permission from ref. 52.*
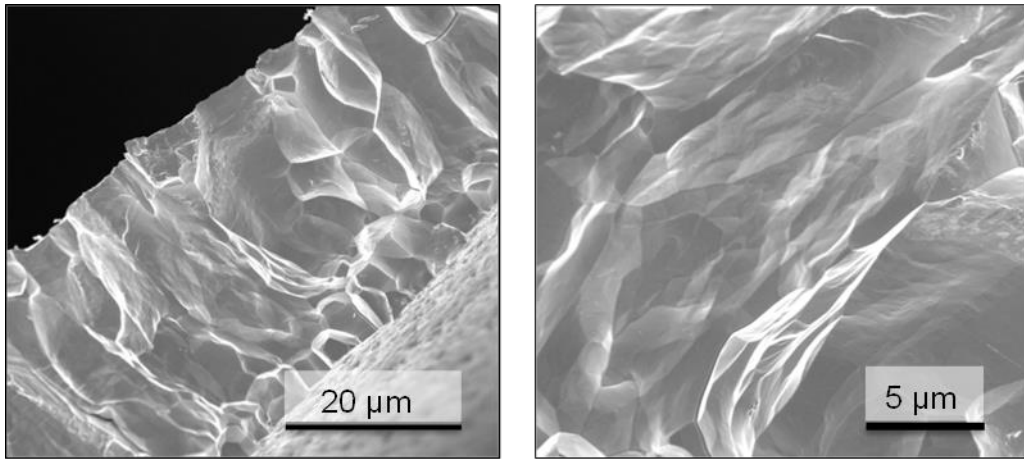
Figure S13: *Low (left) and high (right) magnification SEM micrographs of pristine Zn$_{80}$Cu$_{20}$ alloy ribbon in the cross-sectional view. Figure reprinted with permission from ref. 52.*

7.4. Supporting information for Chapter 5

This Appendix lists the supporting information reprinted in adapted form from the submitted manuscript to ChemElectoChem.

7.4.1. Influence of starting material concentration on the yield of 1,2-butylene carbonate (BC)

The concentration of the starting material affects the speed and extent of the reaction. Studies on the optimal concentration of 1,2-butylene oxide (BO) were carried out on polycrystalline Cu cathode and Mg anode in CO_2-saturated 0.07 M TEAI-MeCN. The yields of BC were 69 ± 3 %, 73 ± 3 %, and 73 ± 3 % for 0.05, 0.10, and 0.15 M of BO, respectively, which is in agreement with the literature[178]. At low concentrations, lower yields are attributed to the slower reaction kinetics.[45,178] However, high concentration of the starting material might lead to increase in electrolysis time and the formation of byproducts. Based on these results, 0.1 M of BO was used for all further electrolysis experiments.
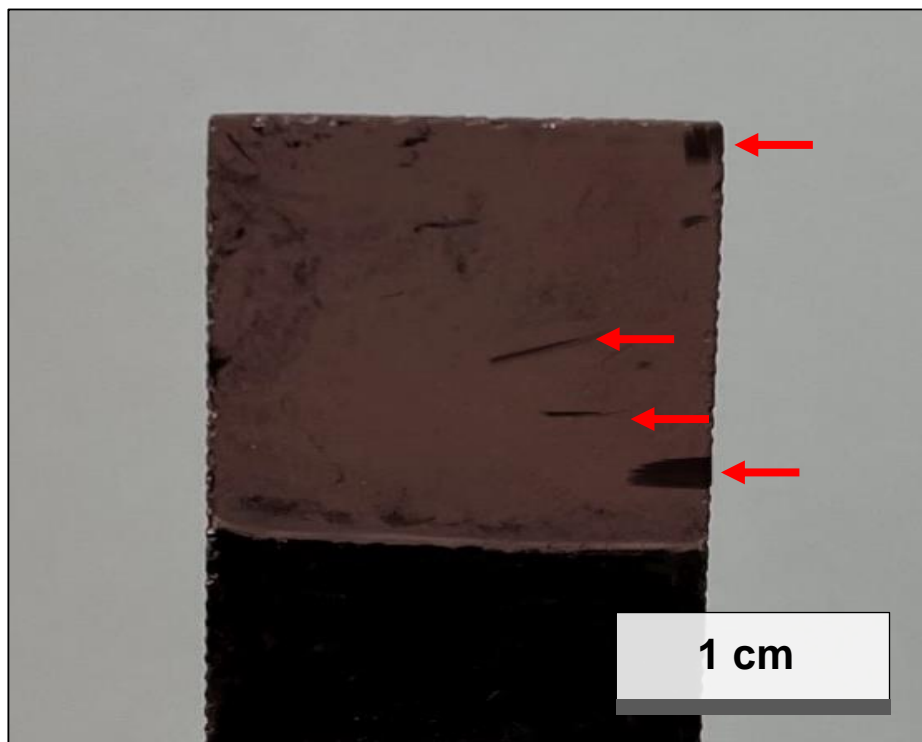
Figure S14: *Np-Cu/GC electrode after three runs of 15-hour electrolysis, showing mechanical detachment of the ligament from the GC substrate during handling between measurements. Figure reprinted from the manuscript submitted to a journal.*

References

1. McCue, I.; Benn, E.; Gaskey, B.; Erlebacher, J. Dealloying and Dealloyed Materials. *Annu. Rev. Mater* **2016**, *46* (1), 263-286. DOI: 10.1146/annurev-matsci-070115-031739.

2. Juarez, T.; Biener, J.; Weissmüller, J.; Hodge, A. M. Nanoporous metals with structural hierarchy: A review. *Advanced Engineering Materials* **2017**, *19* (12), 1700389.

3. Wittstock, A.; Biener, J.; Bäumer, M. Surface Chemistry and Catalysis. In *Nanoporous Gold: From an Ancient Technology to a High-Tech Material*, RSC Nanoscience & Nanotechnology, No. 22, 2012; pp 167-198.

4. Kim, S. H. Nanoporous gold: Preparation and applications to catalysis and sensors. *Current Applied Physics* **2018**, *18* (7), 810-818. DOI: 10.1016/j.cap.2018.03.021.

5. Badwe, N.; Chen, X.; Sieradzki, K. Mechanical properties of nanoporous gold in tension. *Acta Materialia* **2017**, *129*, 251-258. DOI: 10.1016/j.actamat.2017.02.040.

6. Xiao, X.; Si, P.; Magner, E. An overview of dealloyed nanoporous gold in bioelectrochemistry. *Bioelectrochemistry* **2016**, *109*, 117-126. DOI: 10.1016/j.bioelechem.2015.12.008.

7. Hecker, B.; Dosche, C.; Oezaslan, M. Ligament evolution in nanoporous Cu films prepared by dealloying. *The Journal of Physical Chemistry C* **2018**, *122* (46), 26378-26384.

8. Zhu, D.; Xia, C.; Yang, Z.; Wang, X.; Yang, T.; Liang, C.; Yin, F.; Li, Q. Fabrication of non-enzyme glucose sensor via dealloying amorphous Zr-Cu alloy and anodic oxidation. *Materials Letters* **2019**, *245*, 49-52. DOI: 10.1016/j.matlet.2019.02.095.

9. Liu, W.; Chen, L.; Yan, J.; Li, N.; Shi, S.; Zhang, S. Nanoporous copper from dual-phase alloy families and its technology application in lithium ion batteries. *Corrosion Reviews* **2015**, *33* (5), 203-231.

10. Song, T.; Yan, M.; Qian, M. The enabling role of dealloying in the creation of specific hierarchical porous metal structures—A review. *Corrosion Science* **2018**, *134*, 78-98. DOI: 10.1016/j.corsci.2018.02.013.

11. Erlebacher, J.; Aziz, M. J.; Karma, A.; Dimitrov, N.; Sieradzki, K. Evolution of nanoporosity in dealloying. *Natur* **2001**, *410* (6827), 450-453. DOI: 10.1038/35068529.

12. Weissmüller, J.; Newman, R. C.; Jin, H.-J.; Hodge, A. M.; Kysar, J. W. Nanoporous Metals by Alloy Corrosion: Formation and Mechanical Properties. *MRS Bulletin* **2009**, *34* (8), 577-586. DOI: 10.1557/mrs2009.157.

13. Zhang, Z.; Wang, Y.; Qi, Z.; Zhang, W.; Qin, J.; Frenzel, J. Generalized Fabrication of Nanoporous Metals (Au, Pd, Pt, Ag, and Cu) through Chemical Dealloying. *The Journal of Physical Chemistry C* **2009**, *113* (29), 12629-12636. DOI: 10.1021/jp811445a.

14. Egle, T.; Barroo, C.; Janvelyan, N.; Baumgaertel, A. C.; Akey, A. J.; Biener, M. M.; Friend, C. M.; Bell, D. C.; Biener, J. Multiscale Morphology of Nanoporous Copper Made from Intermetallic Phases. *ACS Applied Materials & Interfaces* **2017**, *9* (30), 25615-25622. DOI: 10.1021/acsami.7b05648.

15. Zhang, L.; Chen, L.; Liu, H.; Hou, Y.; Hirata, A.; Fujita, T.; Chen, M. Effect of Residual Silver on Surface-Enhanced Raman Scattering of Dealloyed Nanoporous Gold. *The Journal of Physical Chemistry C* **2011**, *115* (40), 19583-19587. DOI: 10.1021/jp205892n.

16. Hayes, J.; Hodge, A.; Biener, J.; Hamza, A.; Sieradzki, K. Monolithic nanoporous copper by dealloying Mn–Cu. *Journal of Materials Research* **2006**, *21* (10), 2611-2616.

17. Liu, W. B.; Zhang, S. C.; Li, N.; Zheng, J. W.; Xing, Y. L. Facile One-Pot Synthesis of Nanoporous Copper Ribbons with Bimodal Pore Size Distributions by Chemical Dealloying. *Journal of The Electrochemical Society* **2011**, *158* (10), D611. DOI: 10.1149/1.3622288.

18. Li, M.; Zhou, Y.; Geng, H. Fabrication of nanoporous copper ribbons by dealloying of Al-Cu alloys. *Journal of Porous Materials* **2012**, *19* (5), 791-796.

19. Liu, W.; Chen, L.; Yan, J.; Li, N.; Shi, S.; Zhang, S. Dealloying solution dependence of fabrication, microstructure and porosity of hierarchical structured nanoporous copper ribbons. *Corrosion Science* **2015**, *94*, 114-121. DOI: 10.1016/j.corsci.2015.01.043.

20. Jia, F.; Yu, C.; Deng, K.; Zhang, L. Nanoporous Metal (Cu, Ag, Au) Films with High Surface Area: General Fabrication and Preliminary Electrochemical Performance. *The Journal of Physical Chemistry C* **2007**, *111* (24), 8424-8431. DOI: 10.1021/jp071815y.

21. Qi, Z.; Zhao, C.; Wang, X.; Lin, J.; Shao, W.; Zhang, Z.; Bian, X. Formation and Characterization of Monolithic Nanoporous Copper by Chemical Dealloying of Al−Cu Alloys. *The Journal of Physical Chemistry C* **2009**, *113* (16), 6694-6698. DOI: 10.1021/jp810742z.

22. Dan, Z.; Qin, F.; Sugawara, Y.; Muto, I.; Hara, N. Fabrication of nanoporous copper by dealloying amorphous binary Ti–Cu alloys in hydrofluoric acid solutions. *Intermetallics* **2012**, *29*, 14-20. DOI: 10.1016/j.intermet.2012.04.016.

23. Wang, X.; Zhang, Z.; Ji, H.; Xu, J.; Huang, X.; Ma, Y. Dealloying of single-phase Al2Au to nanoporous gold ribbon/film with tunable morphology in inorganic and organic acidic media. *Applied Surface Science* **2012**, *258* (22), 9073-9079. DOI: 10.1016/j.apsusc.2012.05.165.

24. Ma, H.; Zhao, B.; Ding, K.; Zhang, Y.; Wu, G.; Gao, Y. Influence of dealloying solution on the microstructure of nanoporous copper through chemical dealloying of Al 75 Cu 25 ribbons. *Journal of Materials Research* **2020**, 1-10.

25. Li, A.; Geng, H.; Zhou, Y.; Ding, L. Fabrication of nanoporous copper ribbons by dealloying of Mn70Cu30 alloy and fractal characterization of their porosity. *Rev. Adv. Mater. Sci* **2013**, *33*, 50-60.

26. Scaglione, F.; Rizzi, P.; Battezzati, L. De-alloying kinetics of an Au-based amorphous alloys. *Journal of Alloys and Compounds* **2012**, *536*, S60-S64. DOI: 10.1016/j.jallcom.2011.11.087.

27. Wang, X. Y.; Liu, S. Q.; Huang, K. L.; Feng, Q. J.; Ye, D. L.; Liu, B.; Liu, J. L.; Jin, G. H. Fixation of CO_2 by electrocatalytic reduction to synthesis of dimethyl carbonate in ionic liquid using effective silver-coated nanoporous copper composites. *Chin Chem Lett* **2010**, *21* (8), 987-990. DOI: 10.1016/j.cclet.2010.04.022.

28. Wu, L.-X.; Sun, Q.-L.; Yang, M.-P.; Zhao, Y.-G.; Guan, Y.-B.; Wang, H.; Lu, J.-X. Highly Efficient Electrocatalytic Carboxylation of 1-Phenylethyl Chloride at Cu Foam Cathode. *Catalysts* **2018**, *8* (7), 273.

29. Regiart, M.; Kumar, A.; Gonçalves, J. M.; Silva Junior, G. J.; Masini, J. C.; Angnes, L.; Bertotti, M. An Electrochemically Synthesized Nanoporous Copper Microsensor for Highly Sensitive and Selective Determination of Glyphosate. *ChemElectroChem* **2020**, *7* (7), 1558-1566. DOI: 10.1002/celc.202000064.

30. Heßelmann, C.; Wolf, T.; Galgon, F.; Körner, C.; Albert, J.; Wasserscheid, P. Additively manufactured RANEY®-type copper catalyst for methanol synthesis. *Catalysis Science & Technology* **2020**, *10* (1), 164-168.

31. Chen, G.; Pan, Y.; Lu, T.; Wang, N.; Li, X. Highly catalytical performance of nanoporous copper for electro-oxidation of methanol in alkaline media. *Materials Chemistry and Physics* **2018**, *218*, 108-115. DOI: 10.1016/j.matchemphys.2018.07.034.

32. Yang, Z.; Chou, X.; Kan, H.; Xiao, Z.; Ding, Y. Nanoporous copper catalysts for the fluidized electrocatalytic hydrogenation of furfural to furfuryl alcohol. *ACS Sustainable Chemistry & Engineering* **2022**, *10* (22), 7418-7425.

33. Guo, L.; Lamb, K. J.; North, M. Recent developments in organocatalysed transformations of epoxides and carbon dioxide into cyclic carbonates. *Green Chem* **2021**, *23* (1), 77-118. DOI: 10.1039/D0GC03465G.

34. North, M.; Pasquale, R.; Young, C. Synthesis of cyclic carbonates from epoxides and CO_2. *Green Chem* **2010**, *12* (9), 1514-1539. DOI: 10.1039/C0GC00065E.

35. Kamphuis, A. J.; Picchioni, F.; Pescarmona, P. P. CO_2-fixation into cyclic and polymeric carbonates: principles and applications. *Green chem* **2019**, *21* (3), 406-448. DOI: 10.1039/C8GC03086C.

36. Tyagi, P.; Singh, D.; Malik, N.; Kumar, S.; Singh Malik, R. Metal catalyst for CO_2 capture and conversion into cyclic carbonate: Progress and challenges. *Mater. Today* **2023**. DOI: 10.1016/j.mattod.2023.02.029.

37. Buckley, B. R.; Patel, A. P.; Wijayantha, K. G. U. 'Ring-expansion addition' of epoxides using applied potential: an investigation of catalysts for atmospheric pressure carbon dioxide utilization. *RSC Advances* **2014**, *4* (102), 58581-58590, 10.1039/C4RA09837D. DOI: 10.1039/C4RA09837D.

38. Yang, H.; Gu, Y.; Deng, Y.; Shi, F. Electrochemical activation of carbon dioxide in ionic liquid: synthesis of cyclic carbonates at mild reaction conditions. *ChemComm* **2002**, (3), 274-275. DOI: 10.1039/B108451H.

39. Wu, L.-X.; Wang, H.; He, L.; Wu, L.; Zhang, A.-J.; Kajiura, H.; Li, Y.-M.; Lu, J.-X. Direct electrosynthesis of organic carbonates from CO_2 with alcohols under mild condition. *Int. J. Electrochem* **2012**, *7* (6), 5616-5625. DOI: 10.1016/S1452-3981(23)19648-9.

40. Zhang, L. Y.; Niu, D.; Zhang, K.; Zhang, G.; Luo, Y.; Lu, J. Electrochemical activation of CO_2 in ionic liquid ($BMIMBF_4$): synthesis of organic carbonates under mild conditions. *Green Chem* **2008**, *10*, 202-206. DOI: 10.1039/B711981J.

41. Perez Gallent, E.; Figueiredo, C.; Koper, M. T. Mechanistic study of the electrosynthesis of propylene carbonate from propylene oxide and CO_2 on copper electrodes. *ChemElectroChem* **2019**, *6* (11), 2917-2923. DOI: 10.1002/celc.201900653.

42. Gallardo-Fuentes, S.; Contreras, R.; Isaacs, M.; Honores, J.; Quezada, D.; Landaeta, E.; Ormazábal-Toledo, R. On the mechanism of CO_2 electro-cycloaddition to propylene oxides. *J. CO_2 Util* **2016**, *16*, 114-120. DOI: 10.1016/j.jcou.2016.06.007.

43. Nitopi, S.; Bertheussen, E.; Scott, S. B.; Liu, X.; Engstfeld, A. K.; Horch, S.; Seger, B.; Stephens, I. E.; Chan, K.; Hahn, C. Progress and perspectives of electrochemical CO_2 reduction on copper in aqueous electrolyte. *Chem. Rev* **2019**, *119* (12), 7610-7672. DOI: 10.1021/acs.chemrev.8b00705.

44. Figueiredo, M. C.; Ledezma-Yanez, I.; Koper, M. T. M. In Situ Spectroscopic Study of CO_2 Electroreduction at Copper Electrodes in Acetonitrile. *ACS Catal* **2016**, *6* (4), 2382-2392. DOI: 10.1021/acscatal.5b02543.

45. Wang, H.; Wu, L.-X.; Zhao, J.-Q.; Li, R.-N.; Zhang, A.-J.; Kajiura, H.; Li, Y.-M.; Lu, J.-X. Synthesis of cyclic carbonates from CO_2 and diols via electrogenerated cyanomethyl anion. *Greenhouse. Gas. Sci. Technol.* **2012**, *2* (1), 59-65. DOI: 10.1002/ghg.42.

46. Wang, H.; Wu, L.-X.; Lan, Y.-C.; Zhao, J.-Q.; Lu, J.-X. Electrosynthesis of cyclic carbonates from CO_2 and diols in ionic liquids under mild conditions. *Int. J. Electrochem. Sci* **2011**, *6* (9), 4218-4227. DOI: 10.1016/S1452-3981(23)18322-2.

47. Rebbecchi, T. A.; Chen, Y. Template-based fabrication of nanoporous metals. *Journal of Materials Research* **2018**, *33* (1), 2-15. DOI: 10.1557/jmr.2017.383 From Cambridge University Press Cambridge Core.

48. Zhang, L.; Jaroniec, M. Strategies for development of nanoporous materials with 2D building units. *Chem. Soc. Rev* **2020**, *49* (16), 6039-6055, 10.1039/D0CS00185F. DOI: 10.1039/D0CS00185F.

49. Jiang, H.; Cong, N.; Jiang, H.; Tian, M.; Xie, Z.; Fang, H.; Han, J.; Ren, Z.; Zhu, Y. Dynamic hydrogen bubble template electrodeposition of Ru on amorphous Co support for electrochemical hydrogen evolution. *International Journal of Hydrogen Energy* **2023**, *48* (57), 21599-21609. DOI: 10.1016/j.ijhydene.2023.03.077.

50. Vesztergom, S.; Dutta, A.; Rahaman, M.; Kiran, K.; Zelocualtecatl Montiel, I.; Broekmann, P. Hydrogen Bubble Templated Metal Foams as Efficient Catalysts of CO_2 Electroreduction. *ChemCatChem* **2021**, *13* (4), 1039-1058. DOI: 10.1002/cctc.202001145.

51. Erlebacher, J.; Aziz, M. J.; Karma, A.; Dimitrov, N.; Sieradzki, K. Evolution of nanoporosity in dealloying. *Nature* **2001**, *410* (6827), 450-453. DOI: 10.1038/35068529.

52. Ibrahim, S.; Dworzak, A.; Crespo, D.; Renner, F. U.; Dosche, C.; Oezaslan, M. Nanoporous Copper Ribbons Prepared by Chemical Dealloying of a Melt-Spun ZnCu Alloy. *J. Phys. Chem. C* **2022**, *126* (1), 212-226. DOI: 10.1021/acs.jpcc.1c08258.

53. Zhang, Z.; Wang, Y.; Qi, Z.; Somsen, C.; Wang, X.; Zhao, C. Fabrication and characterization of nanoporous gold composites through chemical dealloying of two phase Al–Au alloys. *Journal of Materials Chemistry* **2009**, *19* (33), 6042-6050, 10.1039/B904052H. DOI: 10.1039/B904052H.

54. Rurainsky, C.; Manjón, A. G.; Hiege, F.; Chen, Y.-T.; Scheu, C.; Tschulik, K. Electrochemical dealloying as a tool to tune the porosity, composition and catalytic activity of nanomaterials. *Journal of Materials Chemistry A* **2020**, *8* (37), 19405-19413, 10.1039/D0TA04880A. DOI: 10.1039/D0TA04880A.

55. Song, T.; Yan, M.; Shi, Z.; Atrens, A.; Qian, M. On the Electrochemical Dealloying of Binary Al-Cu and Ternary Al-Cu-Sn Alloys. *ECS Meeting Abstracts* **2015**, *MA2015-01* (43), 2269. DOI: 10.1149/MA2015-01/43/2269.

56. Cattarin, S.; Kramer, D.; Lui, A.; Musiani, M. M. Preparation and Characterization of Gold Nanostructures of Controlled Dimension by Electrochemical Techniques. *The Journal of Physical Chemistry C* **2007**, *111* (34), 12643-12649. DOI: 10.1021/jp072405c.

57. Luan, C.; Chen, L.; Li, B.; Zhu, L.; Li, W. Electrochemical Dealloying-Enabled 3D Hierarchical Porous Cu Current Collector of Lithium Metal Anodes for Dendrite Growth Inhibition. *ACS Applied Energy Materials* **2021**, *4* (12), 13903-13911. DOI: 10.1021/acsaem.1c02696.

58. Wittstock, G.; Bäumer, M.; Dononelli, W.; Klüner, T.; Lührs, L.; Mahr, C.; Moskaleva, L. V.; Oezaslan, M.; Risse, T.; Rosenauer, A.; Staubitz, A.; Weissmüller, J.; Wittstock, A. Nanoporous Gold: From Structure Evolution to Functional Properties in Catalysis and

Electrochemistry. *Chem. Rev* **2023**, *123* (10), 6716-6792. DOI: 10.1021/acs.chemrev.2c00751.

59. Li, Y.; Ngo-Dinh, B.-N.; Markmann, J.; Weissmüller, J. Evolution of length scales and of chemical heterogeneity during primary and secondary dealloying. *Acta Materialia* **2022**, *222*, 117424. DOI: 10.1016/j.actamat.2021.117424.

60. Ye, X.-L.; Lu, N.; Li, X.-J.; Du, K.; Tan, J.; Jin, H.-J. Primary and Secondary Dealloying of Au(Pt)-Ag: Structural and Compositional Evolutions, and Volume Shrinkage. *Journal of The Electrochemical Society* **2014**, *161* (12), C517. DOI: 10.1149/2.0131412jes.

61. Pickering, H.; Wagner, C. Electrolytic dissolution of binary alloys containing a noble metal. *Journal of the Electrochemical Society* **1967**, *114* (7), 698.

62. Erlebacher, J. An atomistic description of dealloying: porosity evolution, the critical potential, and rate-limiting behavior. *Journal of the Electrochemical Society* **2004**, *151* (10), C614.

63. Sieradzki, K.; Corderman, R. R.; Shukla, K.; Newman, R. C. Computer simulations of corrosion: Selective dissolution of binary alloys. *Philosophical Magazine A* **1989**, *59* (4), 713-746. DOI: 10.1080/01418618908209817.

64. Chen, Q.; Sieradzki, K. Mechanisms and Morphology Evolution in Dealloying. *Journal of The Electrochemical Society* **2013**, *160* (6), C226. DOI: 10.1149/2.064306jes.

65. Nakajima, H. The discovery and acceptance of the Kirkendall Effect: The result of a short research career. *JOM* **1997**, *49* (6), 15-19. DOI: 10.1007/BF02914706.

66. Hsiao, H.-Y.; Liu, C.-M.; Lin, H.-w.; Liu, T.-C.; Lu, C.-L.; Huang, Y.-S.; Chen, C.; Tu, K. N. Unidirectional Growth of Microbumps on (111)-Oriented and Nanotwinned Copper. *Science* **2012**, *336* (6084), 1007-1010. DOI: doi:10.1126/science.1216511.

67. Zeng, K.; Stierman, R.; Chiu, T.-C.; Edwards, D.; Ano, K.; Tu, K. N. Kirkendall void formation in eutectic SnPb solder joints on bare Cu and its effect on joint reliability. *Journal of Applied Physics* **2004**, *97* (2). DOI: 10.1063/1.1839637 (acccessed 12/30/2023).

68. Geng, K.; Sieradzki, K. Dealloying at High Homologous Temperature: Morphology Diagrams. *Journal of The Electrochemical Society* **2017**, *164* (6), C330. DOI: 10.1149/2.0061707jes.

69. Dan, Z.; Qin, F.; Muto, I.; Hara, N.; Chang, H. Elaboration of Nanoporous Copper via Chemical Composition Design of Amorphous Precursor Alloys. *New Uses of Micro and Nanomaterials* **2018**, 39.

70. Dan, Z.; Qin, F.; Sugawara, Y.; Muto, I.; Hara, N. Dependency of the formation of Au-stabilized nanoporous copper on the dealloying temperature. *Microporous and mesoporous materials* **2014**, *186*, 181-186.

71. Aburada, T.; Fitz-Gerald, J. M.; Scully, J. R. Synthesis of nanoporous copper by dealloying of Al-Cu-Mg amorphous alloys in acidic solution: The effect of nickel. *Corrosion Science* **2011**, *53* (5), 1627-1632.

72. Wang, Y.; Wang, Y.; Zhang, C.; Kou, T.; Zhang, Z. Tuning the ligament/channel size of nanoporous copper by temperature control. *CrystEngComm* **2012**, *14* (24), 8352-8356.

73. Qian, L.; Chen, M. Ultrafine nanoporous gold by low-temperature dealloying and kinetics of nanopore formation. *Applied Physics Letters* **2007**, *91* (8), 083105.

74. Lee, Y.-Z.; Zeng, W.-Y.; Cheng, I.-C. Synthesis and characterization of nanoporous copper thin films by magnetron sputtering and subsequent dealloying. *Thin Solid Films* **2020**, *699*, 137913.

75. Zhang, X.-m.; Li, Y.-x.; Zhang, H.-w.; Yuan, L. Evolution of porous structure with dealloying corrosion on Gasar Cu–Mn alloy. *Transactions of Nonferrous Metals Society of China* **2015**, *25* (4), 1200-1205.

76. Zhang, Z.; Wang, Y.; Wang, Y.; Wang, X.; Qi, Z.; Ji, H.; Zhao, C. Formation of ultrafine nanoporous gold related to surface diffusion of gold adatoms during dealloying of Al_2Au in an alkaline solution. *Scripta Materialia* **2010**, *62* (3), 137-140. DOI: 10.1016/j.scriptamat.2009.10.018.

77. Zhang, S.; Chen, H.; Qian, Y.; Zhao, Y.; Suo, L.; Zhang, B.; Li, W. Effect of dealloying temperature on microstructure and tensile properties of self-supporting nanoporous copper foil fabricated in situ. *Journal of Porous Materials* **2023**, *30* (1), 267-276. DOI: 10.1007/s10934-022-01318-x.

78. Sieradzki, K.; Kim, J. S.; Cole, A. T.; Newman, R. C. The Relationship Between Dealloying and Transgranular Stress-Corrosion Cracking of Cu-Zn and Cu-Al Alloys. *Journal of The Electrochemical Society* **1987**, *134* (7), 1635. DOI: 10.1149/1.2100726.

79. Weissmüller, J.; Sieradzki, K. Dealloyed nanoporous materials with interface-controlled behavior. *MRS Bulletin* **2018**, *43* (1), 14-19. DOI: 10.1557/mrs.2017.299.

80. Sieradzki, K.; Dimitrov, N.; Movrin, D.; McCall, C.; Vasiljevic, N.; Erlebacher, J. The Dealloying Critical Potential. *Journal of The Electrochemical Society* **2002**, *149* (8), B370. DOI: 10.1149/1.1492288.

81. Li, Y.; Dinh Ngô, B.-N.; Markmann, J.; Weissmüller, J. Topology evolution during coarsening of nanoscale metal network structures. *Physical Review Materials* **2019**, *3* (7), 076001. DOI: 10.1103/PhysRevMaterials.3.076001.

82. Erlebacher, J. Mechanism of Coarsening and Bubble Formation in High-Genus Nanoporous Metals. *Physical Review Letters* **2011**, *106* (22), 225504. DOI: 10.1103/PhysRevLett.106.225504.

83. Sharp, D. H. An overview of Rayleigh-Taylor instability. *Physica D: Nonlinear Phenomena* **1984**, *12* (1-3), 3-18.

84. Vivegnis, S.; Delhalle, J.; Mekhalif, Z.; Renner, F. Copper–zinc alloy electrodeposition mediated by triethanolamine as a complexing additive and chemical dealloying. *Electrochimica Acta* **2019**, *319*, 400-409.

85. Mao, R.; Liang, S.; Wang, X.; Yang, Q.; Han, B. Effect of preparation conditions on morphology and thermal stability of nanoporous copper. *Corrosion Science* **2012**, *60*, 231-237. DOI: 10.1016/j.corsci.2012.03.032.

86. Zhang, C.; Yue, H.; Wang, H.; Ding, G.; Xiaolin, Z. Nanoporous Copper Films with High Surface Area Formed by Chemical Dealloying from Electroplated CuZn Alloy. *Micro and Nanosystems* **2016**, *8* (1), 13-18. DOI: 10.2174/1876402908666161014092842.

87. Tuan, N. T.; Park, J.; Lee, J.; Gwak, J.; Lee, D. Synthesis of nanoporous Cu films by dealloying of electrochemically deposited Cu–Zn alloy films. *Corrosion Science* **2014**, *80*, 7-11. DOI: 10.1016/j.corsci.2013.11.043.

88. Yue, X.; Hu, R.; Qi, J.; He, Y.; Meng, Q.; Wei, F.; Ren, Y.; Sui, Y. Fabrication and Degradation Properties of Nanoporous Copper with Tunable Pores by Dealloying Amorphous Ti-Cu Alloys with Minor Co Addition. *Journal of Materials Engineering and Performance* **2021**, *30* (3), 1759-1767. DOI: 10.1007/s11665-021-05491-z.

89. Park, B.; Le Han, D.; Saito, M.; Mizuno, J.; Nishikawa, H. Fabrication and characterization of nanoporous copper through chemical dealloying of cold-rolled and annealed Mn–Cu alloy. *Journal of Porous Materials* **2021**, *28* (6), 1823-1836. DOI: 10.1007/s10934-021-01128-7.

90. Wang, J.; Yang, Y.; Zhang, M.; Yang, S. Microstructure Evolution of Nanoporous Copper Fabricated by Electrochemical Dealloying Mn–Cu Alloy. In *Advanced Functional Materials*, Singapore, 2018//, 2018; Han, Y., Ed.; Springer Singapore: pp 919-926.

91. Zhao, C.; Qi, Z.; Wang, X.; Zhang, Z. Fabrication and characterization of monolithic nanoporous copper through chemical dealloying of Mg–Cu alloys. *Corrosion Science* **2009**, *51* (9), 2120-2125. DOI: 10.1016/j.corsci.2009.05.043.

92. Luo, X.; Li, R.; Liu, Z.; Huang, L.; Shi, M.; Xu, T.; Zhang, T. Three-dimensional nanoporous copper with high surface area by dealloying Mg–Cu–Y metallic glasses. *Materials Letters* **2012**, *76*, 96-99. DOI: 10.1016/j.matlet.2012.02.028.

93. Lee, S.-Y.; Baek, S.-M.; Gwak, E.-J.; Kang, N.-R.; Kim, J.-Y.; Kim, S.-H.; Lee, J. G.; Park, S. S. Fabrication of high-strength duplex nanoporous Cu by dealloying a dual-

phase Mg–Cu precursor alloy. *Journal of Magnesium and Alloys* **2020**, *8* (3), 910-916. DOI: 10.1016/j.jma.2020.02.015.

94. Peng, Z.; Ogle, K. The Corrosion of Copper and Copper Alloys. 2017.

95. *ASM Alloy Phase Diagram Database*. 2023. www.matdata.asminternational.org (accessed 01.12.2023).

96. Miodownik, A. Cu-Zn (Copper-Zinc). In *Binary Alloy Phase Diagrams*, Vol. 2; ASM International, 1990; pp 1508-1510.

97. Pedeferri , P. Pourbaix Diagrams. In *Corrosion Science and Engineering*, Springer International Publishing, 2018; pp 57-72.

98. Liu, W.; Zhang, S.; Li, N.; An, S.; Zheng, J. Formation of monolithic nanoporous copper with ultrahigh specific surface area through chemical dealloying of Mg-Cu alloy. *Int. J. Electrochem. Sci* **2012**, *7*, 9707-9716.

99. Wang, J.; Yang, S. Nanoporous copper fabricated by dealloying Mn–Cu precursors with minor nickel element addition and heat treatment coarsening. *Nano* **2018**, *13* (05), 1850058.

100. Liu, W.; Cheng, P.; Yan, J.; Li, N.; Shi, S.; Zhang, S. Temperature-induced surface reconstruction and interface structure evolution on ligament of nanoporous copper. *Scientific Reports* **2018**, *8* (1), 447. DOI: 10.1038/s41598-017-18795-9.

101. Majidi, M. R.; Ghaderi, S. Hydrogen bubble dynamic template fabrication of nanoporous Cu film supported by graphene nanaosheets: A highly sensitive sensor for detection of nitrite. *Talanta* **2017**, *175*, 21-29. DOI: 10.1016/j.talanta.2017.07.020.

102. Sattayasamitsathit, S.; Thavarungkul, P.; Thammakhet, C.; Limbut, W.; Numnuam, A.; Buranachai, C.; Kanatharana, P. Fabrication of Nanoporous Copper Film for Electrochemical Detection of Glucose. *Electroanalysis* **2009**, *21* (21), 2371-2377. DOI: 10.1002/elan.200904697.

103. Tian, C.; Zhang, S.; Wang, H.; Chen, C.; Han, Z.; Chen, M.; Zhu, Y.; Cui, R.; Zhang, G. Three-dimensional nanoporous copper and reduced graphene oxide composites as enhanced sensing platform for electrochemical detection of carbendazim. *Journal of Electroanalytical Chemistry* **2019**, *847*, 113243. DOI: 10.1016/j.jelechem.2019.113243.

104. Chen, L. Y.; Lang, X. Y.; Fujita, T.; Chen, M. W. Nanoporous gold for enzyme-free electrochemical glucose sensors. *Scripta Materialia* **2011**, *65* (1), 17-20. DOI: 10.1016/j.scriptamat.2011.03.025.

105. Diao, F.; Xiao, X.; Luo, B.; Sun, H.; Ding, F.; Ci, L.; Si, P. Two-step fabrication of nanoporous copper films with tunable morphology for SERS application. *Applied Surface Science* **2018**, *427*, 1271-1279. DOI: 10.1016/j.apsusc.2017.08.117.

106. Chen, L.-Y.; Yu, J.-S.; Fujita, T.; Chen, M.-W. Nanoporous Copper with Tunable Nanoporosity for SERS Applications. *Advanced Functional Materials* **2009**, *19* (8), 1221-1226. DOI: 10.1002/adfm.200801239.

107. Song, R.; Zhang, L.; Zhu, F.; Li, W.; Fu, Z.; Chen, B.; Chen, M.; Zeng, H.; Pan, D. Hierarchical Nanoporous Copper Fabricated by One-Step Dealloying Toward Ultrasensitive Surface-Enhanced Raman Sensing. *Advanced Materials Interfaces* **2018**, *5* (16), 1800332. DOI: 10.1002/admi.201800332.

108. Li, M.; Su, Y.; Zhao, J.; Geng, H.; Zhang, J.; Zhang, L.; Yang, C.; Zhang, Y. One-pot preparation of thin nanoporous copper foils with enhanced light absorption and SERS properties. *CrystEngComm* **2015**, *17* (6), 1296-1304, 10.1039/C4CE01967A. DOI: 10.1039/C4CE01967A.

109. McPherson, D. J.; Dowd, A.; Arnold, M. D.; Gentle, A.; Cortie, M. B. Electrochemical energy storage on nanoporous copper sponge. *Journal of Materials Research* **2022**, *37* (13), 2195-2203. DOI: 10.1557/s43578-022-00535-z.

110. Mirzaee, M.; Dehghanian, C. Synthesis of nanoporous copper foam-applied current collector electrode for supercapacitor. *Journal of the Iranian Chemical Society* **2019**, *16* (2), 283-292. DOI: 10.1007/s13738-018-1505-x.

111. Du, X.; Xia, C.; Li, Q.; Wang, X.; Yang, T.; Yin, F. Facile fabrication of CuxO composite nanoarray on nanoporous copper as supercapacitor electrode. *Materials Letters* **2018**, *233*, 170-173. DOI: 10.1016/j.matlet.2018.09.009.

112. Guo, F.; Wu, C.; Chen, S.; Ai, X.; Zhong, F.; Yang, H.; Qian, J. Flaky and Dense Lithium Deposition Enabled by a Nanoporous Copper Surface Layer on Lithium Metal Anode. *ACS Materials Letters* **2020**, *2* (4), 358-366. DOI: 10.1021/acsmaterialslett.0c00001.

113. Zhang, S.; Xing, Y.; Jiang, T.; Du, Z.; Li, F.; He, L.; Liu, W. A three-dimensional tin-coated nanoporous copper for lithium-ion battery anodes. *Journal of Power Sources* **2011**, *196* (16), 6915-6919. DOI: 10.1016/j.jpowsour.2010.12.021.

114. Li, Z. B.; Wang, J.; Liu, X. J.; Li, R.; Wang, H.; Wu, Y.; Wang, X. Z.; Lu, Z. P. Self-supported NiCoP/nanoporous copper as highly active electrodes for hydrogen evolution reaction. *Scripta Materialia* **2019**, *173*, 51-55. DOI: 10.1016/j.scriptamat.2019.07.035.

115. Shi, H.; Zhou, Y.-T.; Yao, R.-Q.; Wan, W.-B.; Zhang, Q.-H.; Gu, L.; Wen, Z.; Lang, X.-Y.; Jiang, Q. Intermetallic Cu_5Zr Clusters Anchored on Hierarchical Nanoporous Copper as Efficient Catalysts for Hydrogen Evolution Reaction. *Research* **2020**, *2020*. DOI: doi:10.34133/2020/2987234.

116. Zeng, W.-Y.; Lai, J.-H.; Cheng, I.-C. Effect of Dealloying Time and Post-Annealing on the Surface Morphology and Electrocatalytic Behavior of Nanoporous Copper Films for CO_2 Reduction Reaction. *Journal of The Electrochemical Society* **2021**, *168* (12), 123501.

117. Qi, Z.; Biener, M. M.; Kashi, A. R.; Hunegnaw, S.; Leung, A.; Ma, S.; Huo, Z.; Kuhl, K. P.; Biener, J. Scalable fabrication of high activity nanoporous copper powders for electrochemical CO_2 reduction via ball milling and dealloying. *Journal of CO_2 Utilization* **2021**, *45*, 101454. DOI: 10.1016/j.jcou.2021.101454.

118. Zeng, W.-Y.; Tsai, J.-H.; Cheng, I.-C. Effect of Atmospheric-Pressure Helium Plasma-Jet Treatment on Electrocatalysis of CO_2 Reduction Reaction using Nanoporous Copper Films. *Journal of The Electrochemical Society* **2021**, *168* (9), 096506.

119. Sen, S.; Liu, D.; Palmore, G. T. R. Electrochemical Reduction of CO_2 at Copper Nanofoams. *ACS Catalysis* **2014**, *4* (9), 3091-3095. DOI: 10.1021/cs500522g.

120. Tang, W.; Peterson, A. A.; Varela, A. S.; Jovanov, Z. P.; Bech, L.; Durand, W. J.; Dahl, S.; Nørskov, J. K.; Chorkendorff, I. The importance of surface morphology in controlling the selectivity of polycrystalline copper for CO_2 electroreduction. *Physical Chemistry Chemical Physics* **2012**, *14* (1), 76-81, 10.1039/C1CP22700A. DOI: 10.1039/C1CP22700A.

121. Hoang, T. T. H.; Ma, S.; Gold, J. I.; Kenis, P. J. A.; Gewirth, A. A. Nanoporous Copper Films by Additive-Controlled Electrodeposition: CO_2 Reduction Catalysis. *ACS Catalysis* **2017**, *7* (5), 3313-3321. DOI: 10.1021/acscatal.6b03613.

122. Lv, J.-J.; Jouny, M.; Luc, W.; Zhu, W.; Zhu, J.-J.; Jiao, F. A Highly Porous Copper Electrocatalyst for Carbon Dioxide Reduction. *Advanced Materials* **2018**, *30* (49), 1803111. DOI: 10.1002/adma.201803111.

123. Woldu, A. R.; Huang, Z.; Zhao, P.; Hu, L.; Astruc, D. Electrochemical CO_2 reduction (CO_2RR) to multi-carbon products over copper-based catalysts. *Coordination Chemistry Reviews* **2022**, *454*, 214340. DOI: 10.1016/j.ccr.2021.214340.

124. Kortlever, R.; Shen, J.; Schouten, K. J. P.; Calle-Vallejo, F.; Koper, M. T. M. Catalysts and Reaction Pathways for the Electrochemical Reduction of Carbon Dioxide. *The Journal of Physical Chemistry Letters* **2015**, *6* (20), 4073-4082. DOI: 10.1021/acs.jpclett.5b01559.

125. Bagger, A.; Ju, W.; Varela, A. S.; Strasser, P.; Rossmeisl, J. Electrochemical CO_2 Reduction: A Classification Problem. *ChemPhysChem* **2017**, *18* (22), 3266-3273. DOI: 10.1002/cphc.201700736.

126. Kuhl, K. P.; Hatsukade, T.; Cave, E. R.; Abram, D. N.; Kibsgaard, J.; Jaramillo, T. F. Electrocatalytic Conversion of Carbon Dioxide to Methane and Methanol on Transition Metal Surfaces. *Journal of the American Chemical Society* **2014**, *136* (40), 14107-14113. DOI: 10.1021/ja505791r.

127. Peterson, A. A.; Abild-Pedersen, F.; Studt, F.; Rossmeisl, J.; Nørskov, J. K. How copper catalyzes the electroreduction of carbon dioxide into hydrocarbon fuels. *Energy & Environmental Science* **2010**, *3* (9), 1311-1315, 10.1039/C0EE00071J. DOI: 10.1039/C0EE00071J.

128. Ooka, H.; Figueiredo, M. C.; Koper, M. T. M. Competition between Hydrogen Evolution and Carbon Dioxide Reduction on Copper Electrodes in Mildly Acidic Media. *Langmuir* **2017**, *33* (37), 9307-9313. DOI: 10.1021/acs.langmuir.7b00696.

129. Xu, Y.; Li, C.; Xiao, Y.; Wu, C.; Li, Y.; Li, Y.; Han, J.; Liu, Q.; He, J. Tuning the Selectivity of Liquid Products of CO_2RR by Cu–Ag Alloying. *ACS Applied Materials & Interfaces* **2022**, *14* (9), 11567-11574. DOI: 10.1021/acsami.2c00593.

130. Chang, F.; Xiao, M.; Miao, R.; Liu, Y.; Ren, M.; Jia, Z.; Han, D.; Yuan, Y.; Bai, Z.; Yang, L. Copper-Based Catalysts for Electrochemical Carbon Dioxide Reduction to Multicarbon Products. *Electrochemical Energy Reviews* **2022**, *5* (3), 4. DOI: 10.1007/s41918-022-00139-5.

131. Ma, Z.; Yang, Z.; Lai, W.; Wang, Q.; Qiao, Y.; Tao, H.; Lian, C.; Liu, M.; Ma, C.; Pan, A.; Huang, H. CO_2 electroreduction to multicarbon products in strongly acidic electrolyte via synergistically modulating the local microenvironment. *Nature Communications* **2022**, *13* (1), 7596. DOI: 10.1038/s41467-022-35415-x.

132. Tabassum, H.; Yang, X.; Zou, R.; Wu, G. Surface engineering of Cu catalysts for electrochemical reduction of CO_2 to value-added multi-carbon products. *Chem Catalysis* **2022**, *2* (7), 1561-1593. DOI: 10.1016/j.checat.2022.04.012.

133. Li, H.; Jiang, Y.; Li, X.; Davey, K.; Zheng, Y.; Jiao, Y.; Qiao, S.-Z. C^{2+} Selectivity for CO_2 Electroreduction on Oxidized Cu-Based Catalysts. *Journal of the American Chemical Society* **2023**, *145* (26), 14335-14344. DOI: 10.1021/jacs.3c03022.

134. Yang, K. D.; Ko, W. R.; Lee, J. H.; Kim, S. J.; Lee, H.; Lee, M. H.; Nam, K. T. Morphology-Directed Selective Production of Ethylene or Ethane from CO_2 on a Cu Mesopore Electrode. *Angewandte Chemie International Edition* **2017**, *56* (3), 796-800. DOI: 10.1002/anie.201610432.

135. Pounds, T. D.; Benn, E.; Wang, C.; Erlebacher, J. Nanoporous Cu Thin Films for Electrochemical CO_2 Reduction. *ECS Meeting Abstracts* **2017**, *MA2017-02* (45), 2002. DOI: 10.1149/MA2017-02/45/2002.

136. Kolbe, H. Untersuchungen über die Elektrolyse organischer Verbindungen. *Justus Liebigs Annalen der Chemie* **1849**, *69* (3), 257-294. DOI: 10.1002/jlac.18490690302.

137. Francke, R.; Little, R. D.; Inagi, S. Organic Electrosynthesis. *ChemElectroChem* **2019**, *6* (16), 4065-4066. DOI: 10.1002/celc.201901175.

138. Leech, M. C.; Garcia, A. D.; Petti, A.; Dobbs, A. P.; Lam, K. Organic electrosynthesis: from academia to industry. *Reaction Chemistry & Engineering* **2020**, *5* (6), 977-990, 10.1039/D0RE00064G. DOI: 10.1039/D0RE00064G.

139. Francke, R. Concepts for sustainable organic electrosynthesis. *Current Opinion in Electrochemistry* **2022**, *36*, 101111. DOI: 10.1016/j.coelec.2022.101111.

140. Cardoso, D. S. P.; Šljukić, B.; Santos, D. M. F.; Sequeira, C. A. C. Organic Electrosynthesis: From Laboratorial Practice to Industrial Applications. *Organic Process Research & Development* **2017**, *21* (9), 1213-1226. DOI: 10.1021/acs.oprd.7b00004.

141. Danly, D. E. Development and Commercialization of the Monsanto Electrochemical Adiponitrile Process. *Journal of The Electrochemical Society* **1984**, *131* (10), 435C. DOI: 10.1149/1.2115324.

142. Kado, Y. Cathodic Hydrocoupling of Acrylonitrile (Electrosynthesis of Adiponitrile). In *Encyclopedia of Applied Electrochemistry*, Kreysa, G., Ota, K.-i., Savinell, R. F. Eds.; Springer New York, 2014; pp 153-154.

143. Hilt, G. Basic Strategies and Types of Applications in Organic Electrochemistry. *ChemElectroChem* **2020**, *7* (2), 395-405. DOI: 10.1002/celc.201901799.

144. Shatskiy, A.; Lundberg, H.; Kärkäs, M. D. Organic Electrosynthesis: Applications in Complex Molecule Synthesis. *ChemElectroChem* **2019**, *6* (16), 4067-4092. DOI: 10.1002/celc.201900435.

145. Frontana-Uribe, B. A.; Little, R. D.; Ibanez, J. G.; Palma, A.; Vasquez-Medrano, R. Organic electrosynthesis: a promising green methodology in organic chemistry. *Green Chemistry* **2010**, *12* (12), 2099-2119, 10.1039/C0GC00382D. DOI: 10.1039/C0GC00382D.

146. van Melis, C. G. W.; Penny, M. R.; Garcia, A. D.; Petti, A.; Dobbs, A. P.; Hilton, S. T.; Lam, K. Supporting-Electrolyte-Free Electrochemical Methoxymethylation of Alcohols Using a 3D-Printed Electrosynthesis Continuous Flow Cell System. *ChemElectroChem* **2019**, *6* (16), 4144-4148. DOI: 10.1002/celc.201900815.

147. Pletcher, D.; Green, R. A.; Brown, R. C. D. Flow Electrolysis Cells for the Synthetic Organic Chemistry Laboratory. *Chemical Reviews* **2018**, *118* (9), 4573-4591. DOI: 10.1021/acs.chemrev.7b00360.

148. Atobe, M. Organic electrosynthesis in flow microreactor. *Current Opinion in Electrochemistry* **2017**, *2* (1), 1-6. DOI: 10.1016/j.coelec.2016.12.002.

149. Brown, R. C. D. The Longer Route can be Better: Electrosynthesis in Extended Path Flow Cells. *The Chemical Record* **2021**, *21* (9), 2472-2487. DOI: 10.1002/tcr.202100163.

150. Heard, D. M.; Lennox, A. J. J. Electrode Materials in Modern Organic Electrochemistry. *Angewandte Chemie International Edition* **2020**, *59* (43), 18866-18884. DOI: 10.1002/anie.202005745.

151. Buckley, B. R.; Patel, A. P.; Wijayantha, K. G. U. Electrosynthesis of cyclic carbonates from epoxides and atmospheric pressure carbon dioxide. *ChemComm* **2011**, *47* (43), 11888-11890, 10.1039/C1CC15467B. DOI: 10.1039/C1CC15467B.

152. Sakakura, T.; Choi, J.-C.; Yasuda, H. Transformation of Carbon Dioxide. *Chemical Reviews* **2007**, *107* (6), 2365-2387. DOI: 10.1021/cr068357u.

153. Mikkelsen, M.; Jørgensen, M.; Krebs, F. C. The teraton challenge. A review of fixation and transformation of carbon dioxide. *Energy & Environmental Science* **2010**, *3* (1), 43-81, 10.1039/B912904A. DOI: 10.1039/B912904A.

154. Markewitz, P.; Kuckshinrichs, W.; Leitner, W.; Linssen, J.; Zapp, P.; Bongartz, R.; Schreiber, A.; Müller, T. E. Worldwide innovations in the development of carbon capture technologies and the utilization of CO_2. *Energy & Environmental Science* **2012**, *5* (6), 7281-7305, 10.1039/C2EE03403D. DOI: 10.1039/C2EE03403D.

155. Álvarez, A.; Borges, M.; Corral-Pérez, J. J.; Olcina, J. G.; Hu, L.; Cornu, D.; Huang, R.; Stoian, D.; Urakawa, A. CO_2 Activation over Catalytic Surfaces. *ChemPhysChem* **2017**, *18* (22), 3135-3141. DOI: 10.1002/cphc.201700782.

156. Hendy, C. M.; Smith, G. C.; Xu, Z.; Lian, T.; Jui, N. T. Radical Chain Reduction via Carbon Dioxide Radical Anion ($CO_2^{•-}$). *Journal of the American Chemical Society* **2021**, *143* (24), 8987-8992. DOI: 10.1021/jacs.1c04427.

157. North, M. Chapter 1 - What is CO_2? Thermodynamics, Basic Reactions and Physical Chemistry. In *Carbon Dioxide Utilisation*, Styring, P., Quadrelli, E. A., Armstrong, K. Eds.; Elsevier, 2015; pp 3-17.

158. Usman, M.; Rehman, A.; Saleem, F.; Abbas, A.; Eze, V. C.; Harvey, A. Synthesis of cyclic carbonates from CO_2 cycloaddition to bio-based epoxides and glycerol: an overview of recent development. *RSC Advances* **2023**, *13* (33), 22717-22743, 10.1039/D3RA03028H. DOI: 10.1039/D3RA03028H.

159. Wang, H.; Xin, Z.; Li, Y. Synthesis of Ureas from CO_2. *Topics in Current Chemistry* **2017**, *375* (2), 49. DOI: 10.1007/s41061-017-0137-4.

160. Lopes, E. J. C.; Ribeiro, A. P. C.; Martins, L. M. D. R. S. New Trends in the Conversion of CO_2 to Cyclic Carbonates. *Catal* **2020**, *10* (5), 479. DOI: 10.3390/catal10050479.

161. Pescarmona, P. P. Cyclic carbonates synthesised from CO_2: Applications, challenges and recent research trends. *Curr. Opin. Green Sustain* **2021**, *29*, 100457. DOI: 10.1016/j.cogsc.2021.100457.

162. Pyo, S.-H.; Persson, P.; Mollaahmad, M. A.; Sörensen, K.; Lundmark, S.; Hatti-Kaul, R. Cyclic carbonates as monomers for phosgene- and isocyanate-free polyurethanes and polycarbonates. *Pure Appl. Chem* **2011**, *84* (3), 637-661. DOI: 10.1351/PAC-CON-11-06-14.

163. Su, C.-C.; He, M.; Amine, R.; Chen, Z.; Sahore, R.; Dietz Rago, N.; Amine, K. Cyclic carbonate for highly stable cycling of high voltage lithium metal batteries. *Energy Stor. Mater* **2019**, *17*, 284-292. DOI: 10.1016/j.ensm.2018.11.003.

164. Duan, J.; Tang, X.; Dai, H.; Yang, Y.; Wu, W.; Wei, X.; Huang, Y. Building Safe Lithium-Ion Batteries for Electric Vehicles: A Review. *Energy Rev* **2020**, *3* (1), 1-42. DOI: 10.1007/s41918-019-00060-4.

165. Kalhoff, J.; Eshetu, G. G.; Bresser, D.; Passerini, S. Safer Electrolytes for Lithium-Ion Batteries: State of the Art and Perspectives. *ChemSusChem* **2015**, *8* (13), 2154-2175. DOI: 10.1002/cssc.201500284.

166. Nemirowsky, J. Ueber die Einwirkung von Chlorkohlenoxyd auf Aethylenglycol; vorläufige Mittheilung. *Journal für Praktische Chemie* **1883**, *28* (1), 439-440.

167. Yan, T.; Liu, H.; Zeng, Z. X.; Pan, W. G. Recent progress of catalysts for synthesis of cyclic carbonates from CO_2 and epoxides. *Journal of CO_2 Utilization* **2023**, *68*, 102355. DOI: 10.1016/j.jcou.2022.102355.

168. Marciniak, A. A.; Lamb, K. J.; Ozorio, L. P.; Mota, C. J. A.; North, M. Heterogeneous catalysts for cyclic carbonate synthesis from carbon dioxide and epoxides. *Current Opinion in Green and Sustainable Chemistry* **2020**, *26*, 100365. DOI: 10.1016/j.cogsc.2020.100365.

169. Cho, H.-Y.; Yang, D.-A.; Kim, J.; Jeong, S.-Y.; Ahn, W.-S. CO_2 adsorption and catalytic application of Co-MOF-74 synthesized by microwave heating. *Catalysis Today* **2012**, *185* (1), 35-40. DOI: 10.1016/j.cattod.2011.08.019.

170. Khatun, R.; Bhanja, P.; Molla, R. A.; Ghosh, S.; Bhaumik, A.; Islam, S. M. Functionalized SBA-15 material with grafted CO_2H group as an efficient heterogeneous acid catalyst for the fixation of CO_2 on epoxides under atmospheric pressure. *Molecular Catalysis* **2017**, *434*, 25-31. DOI: 10.1016/j.mcat.2017.01.013.

171. Tascedda, P.; Dunãch, E. Novel electrochemical reactivity of Ni(cyclam)Br2: catalytic carbon dioxide incorporation into epoxides. *Journal of the Chemical Society, Chemical Communications* **1995**, (1), 43-44, 10.1039/C39950000043. DOI: 10.1039/C39950000043.

172. Xiao, Y.; Chen, B.-L.; Yang, H.-P.; Wang, H.; Lu, J.-X. Electrosynthesis of enantiomerically pure cyclic carbonates from CO_2 and chiral epoxides. *Electrochem commn* **2014**, *43*, 71-74. DOI: 10.1016/j.elecom.2014.03.012.

173. Zhang, J.-J.; Shan, S.-L.; Shi, Y.; Hou, Y.; Wang, H.; Lu, J.-X. Highly efficient electrocatalysis for the fixation of CO_2 into cyclic carbonates with carbon sphere-loaded copper nanoparticles cathode material. *J. Electroanal* **2021**, *882*, 114962. DOI: 10.1016/j.jelechem.2020.114962.

174. Zhang, J.-J.; Li, S.-M.; Shi, Y.; Hu, Q.-L.; Wang, H.; Lu, J.-X. Biomass-derived Cu/porous carbon for the electrocatalytic synthesis of cyclic carbonates from CO_2 and diols under mild conditions. *New J Chem* **2020**, *44* (27), 11817-11823. DOI: 10.1039/D0NJ01728K.

175. Díaz-Duque, Á.; Sandoval-Rojas, A. P.; Molina-Osorio, A. F.; Feliu, J. M.; Suárez-Herrera, M. F. Electrochemical reduction of CO_2 in water-acetonitrile mixtures on nanostructured Cu electrode. *Electrochemistry Communications* **2015**, *61*, 74-77. DOI: 10.1016/j.elecom.2015.10.003.

176. Piontek, S.; junge Puring, K.; Siegmund, D.; Smialkowski, M.; Sinev, I.; Tetzlaff, D.; Roldan Cuenya, B.; Apfel, U.-P. Bio-inspired design: bulk iron–nickel sulfide allows for efficient solvent-dependent CO_2 reduction. *Chemical Science* **2019**, *10* (4), 1075-1081, 10.1039/C8SC03555E. DOI: 10.1039/C8SC03555E.

177. Wu, L.; Yang, H.; Wang, H.; Lu, J. Electrosynthesis of cyclic carbonates from CO_2 and epoxides on a reusable copper nanoparticle cathode. *RSC Adv* **2015**, *5* (30), 23189-23192. DOI: 10.1039/C4RA17287F.

178. Wu, L.-X.; Yang, H.-P.; Guan, Y.-B.; Yang, M.-P.; Wang, H.; Lu, J.-X. Electrosynthesis of cyclic carbonates from CO_2 and epoxides on compacted silver nanoparticles electrode. *Int. J. Electrochem. Sci* **2017**, *12*, 8963-8972. DOI: 10.1039/C4RA17287F.

179. Yang, H.; Gu, Y.; Deng, Y.; Shi, F. Electrochemical activation of carbon dioxide in ionic liquid: synthesis of cyclic carbonates at mild reaction conditions. *Chemical Communications* **2002**, (3), 274-275, 10.1039/B108451H. DOI: 10.1039/B108451H.

180. Buckley, B. R.; Patel, A. P.; Wijayantha, K. G. U. 'Ring-expansion addition' of epoxides using applied potential: an investigation of catalysts for atmospheric pressure carbon dioxide utilization. *RSC Adv* **2014**, *4* (102), 58581-58590. DOI: 10.1039/C4RA09837D.

181. Lavernia, E. J.; Srivatsan, T. S. The rapid solidification processing of materials: science, principles, technology, advances, and applications. *Journal of Materials Science* **2010**, *45* (2), 287-325. DOI: 10.1007/s10853-009-3995-5.

182. Gražulis, S.; Chateigner, D.; Downs, R. T.; Yokochi, A.; Quirós, M.; Lutterotti, L.; Manakova, E.; Butkus, J.; Moeck, P.; Le Bail, A. Crystallography Open Database–an open-access collection of crystal structures. *Journal of applied crystallography* **2009**, *42* (4), 726-729.

183. Darque-Ceretti, E.; Delamare, F.; Blaise, G. Ion induced surface compositional changes of α brass; a comparative study by AES and sputtered thermal ion mass spectrometry. Application to quantitative AES. *Surface and interface analysis* **1985**, *7* (3), 141-149.

184. Van Ooij, W. Surface composition, oxidation and sulfidation of cold-worked brass and brass-coated steel wire as studied by x-ray photoelectron spectroscopy I. Surface composition of commercial cold-worked brass. *Surface Technology* **1977**, *6* (1), 1-18.

185. Haynes, W. M. CRC handbook of chemistry and physics; CRC press, 2014.

186. Lafuente, B.; Downs, R. T.; Yang, H.; Stone, N. 1. The power of databases: The RRUFF project. In *Highlights in mineralogical crystallography*, De Gruyter (O), 2015; pp 1-30.

187. Wang, X.; Xi, G.; Xiong, S.; Liu, Y.; Xi, B.; Yu, W.; Qian, Y. Solution-phase synthesis of single-crystal CuO nanoribbons and nanorings. *Crystal growth & design* **2007**, *7* (5), 930-934.

188. Goldstein, H.; Kim, D.-s.; Peter, Y. Y.; Bourne, L.; Chaminade, J.; Nganga, L. Raman study of CuO single crystals. *Physical Review B* **1990**, *41* (10), 7192.

189. Debbichi, L.; Marco de Lucas, M. C.; Pierson, J. F.; Krüger, P. Vibrational Properties of CuO and Cu4O3 from First-Principles Calculations, and Raman and Infrared Spectroscopy. *The Journal of Physical Chemistry C* **2012**, *116* (18), 10232-10237. DOI: 10.1021/jp303096m.

190. Meyer, B. K.; Polity, A.; Reppin, D.; Becker, M.; Hering, P.; Klar, P. J.; Sander, T.; Reindl, C.; Benz, J.; Eickhoff, M.; Heiliger, C.; Heinemann, M.; Bläsing, J.; Krost, A.; Shokovets, S.; Müller, C.; Ronning, C. Binary copper oxide semiconductors: From materials towards devices. *physica status solidi (b)* **2012**, *249* (8), 1487-1509. DOI: 10.1002/pssb.201248128.

191. Ho, W. C. J.; Tay, Q.; Qi, H.; Huang, Z.; Li, J.; Chen, Z. Photocatalytic and Adsorption Performances of Faceted Cuprous Oxide (Cu_2O) Particles for the Removal of Methyl Orange (MO) from Aqueous Media. *Molecules* **2017**, *22* (4). DOI: 10.3390/molecules22040677 From NLM.

192. Castillo, E.; Zhang, J.; Dimitrov, N. All-electrochemical synthesis of tunable fine-structured nanoporous copper films. *MRS Bulletin* **2022**, *47* (9), 913-925. DOI: 10.1557/s43577-022-00323-4.

193. Vasilic, R.; Vasiljevic, N.; Dimitrov, N. Open circuit stability of underpotentially deposited Pb monolayer on Cu(111). *Journal of Electroanalytical Chemistry* **2005**, *580* (2), 203-212. DOI: 10.1016/j.jelechem.2005.03.028.

194. McCrory, C. C.; Jung, S.; Peters, J. C.; Jaramillo, T. F. Benchmarking heterogeneous electrocatalysts for the oxygen evolution reaction. *J. Am. Chem. Soc* **2013**, *135* (45), 16977-16987. DOI: 10.1021/ja407115p.

195. Dutta, A.; Rahaman, M.; Hecker, B.; Drnec, J.; Kiran, K.; Zelocualtecatl Montiel, I.; Jochen Weber, D.; Zanetti, A.; Cedeño López, A.; Martens, I.; Broekmann, P.; Oezaslan, M. CO_2 electrolysis – Complementary operando XRD, XAS and Raman spectroscopy study on the stability of Cu_xO foam catalysts. *J. Catal* **2020**, *389*, 592-603. DOI: 10.1016/j.jcat.2020.06.024.

196. Zuo, J.; Erbe, A. Optical and electronic properties of native zinc oxide films on polycrystalline Zn. *Physical Chemistry Chemical Physics* **2010**, *12* (37), 11467-11476.

197. Liu, Y.; Liu, Y.; Yang, Z.; Wang, J. Fenton degradation of 4-chlorophenol using H2O2 in situ generated by Zn-CNTs/O2 system. *RSC Advances* **2017**, *7* (79), 49985-49994, 10.1039/C7RA08634B. DOI: 10.1039/C7RA08634B.

198. Lu, Z.; Li, C.; Han, J.; Zhang, F.; Liu, P.; Wang, H.; Wang, Z.; Cheng, C.; Chen, L.; Hirata, A. Three-dimensional bicontinuous nanoporous materials by vapor phase dealloying. *Nature communications* **2018**, *9* (1), 1-7.

199. Kong, Q.; Lian, L.; Liu, Y.; Zhang, J. Hierarchical porous copper materials: fabrication and characterisation. *Micro & Nano Letters* **2013**, *8* (8), 432-435. DOI: 10.1049/mnl.2013.0113.

200. Lian, L.; Yao, Y.; Liu, Y.; Fang, X. A segmental dealloying for fabricating the gradient nanoporous metal materials. *Journal of Porous Materials* **2017**, *24* (1), 211-215. DOI: 10.1007/s10934-016-0254-4.

201. Morrish, R.; Dorame, K.; Muscat, A. J. Formation of nanoporous Au by dealloying AuCu thin films in HNO3. *Scripta Materialia* **2011**, *64* (9), 856-859.

202. Chung, Y.-C.; Kim, C. K.; Wuensch, B. J. Calculation of the contribution to grain boundary diffusion in ionic systems that arises from enhanced defect concentrations adjacent to the boundary. *Journal of Applied Physics* **2000**, *87* (6), 2747-2752.

203. Liu, W.; Zhang, S.; Li, N.; Zheng, J.; An, S.; Xing, Y. Monolithic nanoporous copper ribbons from Mg-Cu alloys with copper contents below 33 at.%: fabrication, structure evolution and coarsening behavior along the thickness direction. *Int. J. Electrochem. Sci* **2011**, *6*, 5445-5461.

204. Erlebacher, J. An Atomistic Description of Dealloying. *Journal of The Electrochemical Society* **2004**, *151* (10), C614. DOI: 10.1149/1.1784820.

205. Wang, N.; Pan, Y.; Wu, S.; Zhang, E.; Dai, W. Fabrication of nanoporous copper with tunable ligaments and promising sonocatalytic performance by dealloying Cu–Y metallic glasses. *RSC advances* **2017**, *7* (68), 43255-43265.

206. Krekeler, T.; Straßer, A. V.; Graf, M.; Wang, K.; Hartig, C.; Ritter, M.; Weissmüller, J. Silver-rich clusters in nanoporous gold. *Materials Research Letters* **2017**, *5* (5), 314-321.

207. Mahr, C.; Kundu, P.; Lackmann, A.; Zanaga, D.; Thiel, K.; Schowalter, M.; Schwan, M.; Bals, S.; Wittstock, A.; Rosenauer, A. Quantitative determination of residual silver distribution in nanoporous gold and its influence on structure and catalytic performance. *Journal of catalysis* **2017**, *352*, 52-58.

208. Chen-Wiegart, Y.-c. K.; Wang, S.; Lee, W.-K.; McNulty, I.; Voorhees, P. W.; Dunand, D. C. In situ imaging of dealloying during nanoporous gold formation by transmission X-ray microscopy. *Acta materialia* **2013**, *61* (4), 1118-1125.

209. Chen-Wiegart, Y.-c. K.; Wang, S.; McNulty, I.; Dunand, D. C. Effect of Ag–Au composition and acid concentration on dealloying front velocity and cracking during nanoporous gold formation. *Acta Materialia* **2013**, *61* (15), 5561-5570. DOI: 10.1016/j.actamat.2013.05.039.

210. Policastro, S. A.; Carnahan, J. C.; Zangari, G.; Bart-Smith, H.; Seker, E.; Begley, M. R.; Reed, M. L.; Reynolds, P. F.; Kelly, R. G. Surface Diffusion and Dissolution Kinetics in the Electrolyte–Metal Interface. *Journal of The Electrochemical Society* **2010**, *157* (10), C328. DOI: 10.1149/1.3478572.

211. Ji, H.; Wang, X.; Zhao, C.; Zhang, C.; Xu, J.; Zhang, Z. Formation, control and functionalization of nanoporous silver through changing dealloying media and elemental doping. *CrystEngComm* **2011**, *13* (7), 2617-2628, 10.1039/C0CE00900H. DOI: 10.1039/C0CE00900H.

212. Yang, W.; Ma, W.; Zhang, Z.; Zhao, C. Ligament size-dependent electrocatalytic activity of nanoporous Ag network for CO_2 reduction. *Faraday Discuss* **2018**, *210* (0), 289-299. DOI: 10.1039/C8FD00056E.

213. Lan, J.; Peng, M.; Liu, P.; Chen, D.; Xu, X.; Luo, M.; Tan, Y.; Chen, M. Scalable synthesis of nanoporous boron for high efficiency ammonia electrosynthesis. *Mater. Today* **2020**, *38*, 58-66. DOI: 10.1016/j.mattod.2020.04.012.

214. Zhang, X.; Li, G.; Duan, D.; Wang, H.; Sun, Z. Formation and control of nanoporous Pt ribbons by two-step dealloying for methanol electro-oxidation. *Corros Sci* **2018**, *135*, 57-66. DOI: 10.1016/j.corsci.2018.02.030.

215. Sebastián-Pascual, P.; Escudero-Escribano, M. Surface characterization of copper electrocatalysts by lead underpotential deposition. *Journal of Electroanalytical Chemistry* **2021**, *896*, 115446. DOI: 10.1016/j.jelechem.2021.115446.

216. Liu, Y.; Bliznakov, S.; Dimitrov, N. Comprehensive study of the application of a Pb underpotential deposition-assisted method for surface area measurement of metallic nanoporous materials. *The Journal of Physical Chemistry C* **2009**, *113* (28), 12362-12372.

217. Brisard, G. M.; Zenati, E.; Gasteiger, H. A.; Marković, N. M.; Ross, P. N. Underpotential Deposition of Lead on Cu(100) in the Presence of Chloride: Ex-Situ Low-Energy Electron Diffraction, Auger Electron Spectroscopy, and Electrochemical Studies. *Langmuir* **1997**, *13* (8), 2390-2397. DOI: 10.1021/la960999x.

218. Biesinger, M. C.; Lau, L. W. M.; Gerson, A. R.; Smart, R. S. C. Resolving surface chemical states in XPS analysis of first row transition metals, oxides and hydroxides: Sc, Ti, V, Cu and Zn. *Applied Surface Science* **2010**, *257* (3), 887-898. DOI: 10.1016/j.apsusc.2010.07.086.

219. Meda, L.; Cerofolini, G. F. A decomposition procedure for the determination of copper oxidation states in Cu-zeolites by XPS. *Surface and Interface Analysis* **2004**, *36* (8), 756-759. DOI: 10.1002/sia.1757.

220. Chen, C.; Yan, X.; Wu, Y.; Liu, S.; Sun, X.; Zhu, Q.; Feng, R.; Wu, T.; Qian, Q.; Liu, H.; Zheng, L.; Zhang, J.; Han, B. The in situ study of surface species and structures of oxide-derived copper catalysts for electrochemical CO_2 reduction. *Chem. Sci* **2021**, *12* (16), 5938-5943. DOI: 10.1039/d1sc00042j.

221. Sheta, A. M.; Mashaly, M. A.; Said, S. B.; Elmorsy, S. S.; Malkov, A. V.; Buckley, B. R. Selective alpha,delta-hydrocarboxylation of conjugated dienes utilizing CO_2 and electrosynthesis. *Chem Sci* **2020**, *11* (34), 9109-9114. DOI: 10.1039/d0sc03148h.

222. Sheta, A. M.; Alkayal, A.; Mashaly, M. A.; Said, S. B.; Elmorsy, S. S.; Malkov, A. V.; Buckley, B. R. Selective Electrosynthetic Hydrocarboxylation of α, β-Unsaturated Esters with Carbon Dioxide. *Angew. Chem.* **2021**, *133* (40), 22003-22008. DOI: 10.26434/chemrxiv.14381087.v1.

223. Mandal, L.; Yang, K. R.; Motapothula, M. R.; Ren, D.; Lobaccaro, P.; Patra, A.; Sherburne, M.; Batista, V. S.; Yeo, B. S.; Ager, J. W.; Martin, J.; Venkatesan, T. Investigating the Role of Copper Oxide in Electrochemical CO_2 Reduction in Real Time. *ACS Applied Materials & Interfaces* **2018**, *10* (10), 8574-8584. DOI: 10.1021/acsami.7b15418.

224. Lum, Y.; Ager, J. W. Stability of Residual Oxides in Oxide-Derived Copper Catalysts for Electrochemical CO_2 Reduction Investigated with ^{18}O Labeling. *Angewandte Chemie International Edition* **2018**, *57* (2), 551-554. DOI: 10.1002/anie.201710590.

225. Wang, X.; Klingan, K.; Klingenhof, M.; Moller, T.; Ferreira de Araujo, J.; Martens, I.; Bagger, A.; Jiang, S.; Rossmeisl, J.; Dau, H.; Strasser, P. Morphology and mechanism of highly selective Cu(II) oxide nanosheet catalysts for carbon dioxide electroreduction. *Nat Commun* **2021**, *12* (1), 794. DOI: 10.1038/s41467-021-20961-7 From NLM PubMed-not-MEDLINE.

226. Gao, D.; Zegkinoglou, I.; Divins, N. J.; Scholten, F.; Sinev, I.; Grosse, P.; Roldan Cuenya, B. Plasma-Activated Copper Nanocube Catalysts for Efficient Carbon Dioxide Electroreduction to Hydrocarbons and Alcohols. *ACS Nano* **2017**, *11* (5), 4825-4831. DOI: 10.1021/acsnano.7b01257.

227. Mistry, H.; Varela, A. S.; Bonifacio, C. S.; Zegkinoglou, I.; Sinev, I.; Choi, Y.-W.; Kisslinger, K.; Stach, E. A.; Yang, J. C.; Strasser, P.; Cuenya, B. R. Highly selective plasma-activated copper catalysts for carbon dioxide reduction to ethylene. *Nature Communications* **2016**, *7* (1), 12123. DOI: 10.1038/ncomms12123.

228. Quan, Y.; Yu, R.; Zhu, J.; Guan, A.; Lv, X.; Yang, C.; Li, S.; Wu, J.; Zheng, G. Efficient carboxylation of styrene and carbon dioxide by single-atomic copper electrocatalyst. *Journal of Colloid and Interface Science* **2021**, *601*, 378-384.

229. Khan, M.; Hameed, A.; Samad, A.; Mushiana, T.; Abdullah, M. I.; Akhtar, A.; Ashraf, R. S.; Zhang, N.; Pollet, B. G.; Schwingenschlögl, U.; Ma, M. In situ grown oxygen-vacancy-rich copper oxide nanosheets on a copper foam electrode afford the selective oxidation of alcohols to value-added chemicals. *Communications Chemistry* **2022**, *5* (1), 109. DOI: 10.1038/s42004-022-00708-1.

230. Deng, Y.; Handoko, A. D.; Du, Y.; Xi, S.; Yeo, B. S. In Situ Raman Spectroscopy of Copper and Copper Oxide Surfaces during Electrochemical Oxygen Evolution Reaction: Identification of CuIII Oxides as Catalytically Active Species. *ACS Catal* **2016**, *6* (4), 2473-2481. DOI: 10.1021/acscatal.6b00205.

8. Publications

Research articles

- Ibrahim, S. Crespo, D., Blaseio, S., Hilt, G., Oezaslan, M. Nanoporous Copper for the Electrosynthesis of cyclic carbonates from CO_2 and epoxide and Epoxides. *ChemElctroChem* **2023**, Submitted.

- Ibrahim, S., Dworzak, A., Crespo, D., Renner, F. U., Dosche, C., Oezaslan, M. Nanoporous Copper Ribbons prepared by Chemical Dealloying of melt-spun ZnCu Alloy. Journal of Physical Chemistry C **2022**, 126, (1), 212-226.

Poster presentations at national conferences

- Ibrahim, S., Dworzak A., Crespo, D., and Oezaslan, M. Tuning the Porosity of dealloyed ZnCu Ribbons. 3rd Symposium on Chemical Bond Activation, Oldenburg, 08 Mar 2021.

- Ibrahim, S., Crespo, D., and Oezaslan, M. Ligament Evolution in Nanoporous Copper Ribbons by Chemical Dealloying. 2nd Symposium on Chemical Bond Activation, Oldenburg, 09 Mar 2020.

- Ibrahim, S., Crespo, D., Hilt, G., and Oezaslan, M. Preparation and Characterization of Nanoporous Copper Foams. Future Perspective in Catalysis, Bremerhaven, 02 - 06 Sept 2019.

- Ibrahim, S., Hecker, B., Hilt, G., Crespo, D., and Oezaslan, M. Electrochemical Synthesis of Cyclic Carbonates on Nanoporous Copper Foam Electrodes. Beilstein Organic Chemistry Symposium- Electrifying Organic Synthesis, Mainz, 09 - 11 Apr 2019.

- Ibrahim, S., Crespo, D., Hilt, G., and Oezaslan, M. Electrochemical Synthesis of Cyclic Carbonates on Nanoporous Copper Electrodes. Symposium on Chemical Bond Activation, Oldenburg, 11 - 12 Mar 2019.

- Ibrahim, S., Hecker, B., Hilt, G., Crespo, D., and Oezaslan, M. Electrochemical Synthesis of Cyclic Carbonates on Nanoporous Copper Electrodes. GDCH Electrochemistry, Ulm, 24 - 26 Sept 2018.

9. Curriculum Vitae

Personal Data

Name:	Sawsan Ibrahim
Place and date of birth:	Rostock, 28.12.1988
Nationality:	German, Syrian

Education

07.2013 – 01.2016	**M.Sc. Pharmaceutical Chemistry** UCSI University, Kuala Lumpur, Malaysia Thesis: Determination of alendronate sodium in tablets by spectroscopic methods
09.2006 – 07.2011	**B.Sc. Pharmacy and Pharmaceutical Chemistry** Damascus University, Damascus, Syria
09.2003 – 06.2006	**Syrian Baccalaureate** Al-awael High School, Damascus, Syria

Work Experience

02.2022 – today	**Pharmacovigilance Manager** MIT Gesundheit GmbH, Kleve, Germany
03.2021 – 12.2021	**Research Assistant** Technical University Carolo Wilhelm, Braunschweig, Germany, Institute for Technical Chemistry, technical electrocatalysis laboratory
12.2017 – 03.2021	**Research Assistant** Carl von Ossietzky University of Oldenburg, Germany Institute of Chemistry – Physical Chemistry
02.2014 – 04.2016	**Content creator and editor** (voluntary work) Syrian Researchers Initiative, Damascus, Syria

Languages

Arabic (native), English (C1), German (B2/C1), Italian (B2/C1).